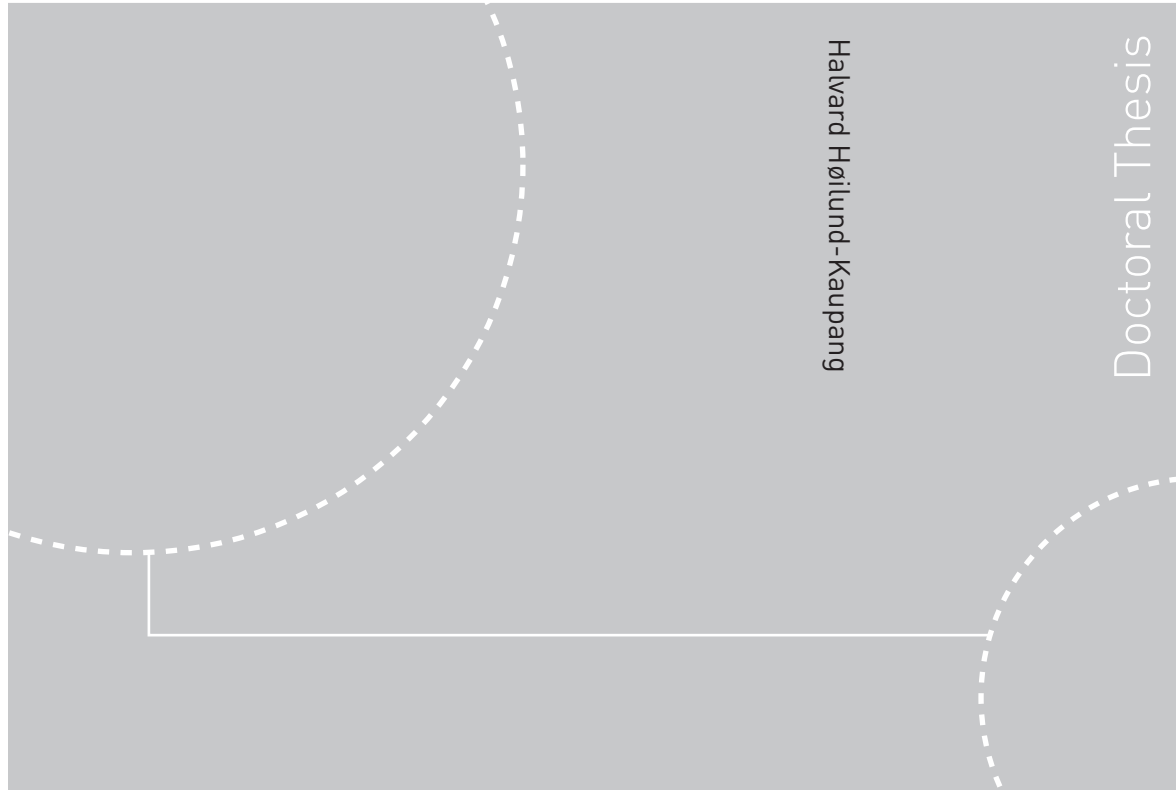


Doctoral theses at NTNU, 2011:217

Halvard Høilund-Kaupang  
**Models and Methods for Investigation  
of Reverberations in Nonlinear  
Ultrasound Imaging**



ISBN 978-82-471-2990-6 (printed ver.)  
ISBN 978-82-471-2991-3 (electronic ver.)  
ISSN 1503-8181

NTNU  
Norwegian University of  
Science and Technology  
Thesis for the degree of  
philosophiae doctor  
Faculty of Medicine  
Department of Circulation and Medical Imaging

Doctoral theses at NTNU, 2011:217

 **NTNU**  
Norwegian University of  
Science and Technology

 NTNU

 **NTNU**  
Norwegian University of  
Science and Technology

Halvard Høiland-Kaupang

# Models and Methods for Investigation of Reverberations in Nonlinear Ultrasound Imaging

Thesis for the degree of philosophiae doctor

Trondheim, August 2011

Norwegian University of  
Science and Technology  
Faculty of Medicine  
Department of Circulation and Medical Imaging



**NTNU**

Norwegian University of  
Science and Technology

**NTNU**

Norwegian University of Science and Technology

Thesis for the degree of philosophiae doctor

Faculty of Medicine

Department of Circulation and Medical Imaging

©Halvard Høiland-Kaupang

ISBN 978-82-471-2990-6 (printed ver.)

ISBN 978-82-471-2991-3 (electronic ver.)

ISSN 1503-8181

Doctoral Theses at NTNU, 2011:217

Printed by Tapir Uttrykk

# Modeller og metoder for studier av reverberasjoner i ikke-lineær ultralydavgivning

Ultralydavgivning skjer ved at en lydimpuls sendes inn i kroppen og reflekteres i overganger mellom ulike type vev og organer. En viktig, men enkel, antagelse er at alle slike overganger bare reflekterer lyden én gang og sender tilbake et *førsteordens* ekko. I virkeligheten reflekteres lyden flere ganger fra slike overganger, og høyere ordens ekko, eller *reverberasjoner*, gir støy og falske ekko i bildet. Slike falske ekko kan skjule viktig informasjon og kan gjøre det vanskeligere å stille en presis diagnose.

Harmonisk avgivning er en teknikk som utnytter ikke-lineariteten i vevselastisiteten til å skape bildet. Denne teknikken har vist seg å redusere mengden akustisk støy, deriblant reverberasjoner, i bildet. Hvor mye bildet forbedres avhenger av avgivningssituasjonen, og en motivasjon for dette arbeidet har vært å forklare hvorfor harmonisk avgivning virker bedre i noen tilfeller enn i andre.

Avhandlingen består av fire artikler som hver presenterer ulike aspekter ved ultralydavgivning og støyyndertrykkelse. En fellesnevner gjennom hele avhandlingen er numeriske beregninger av lydfelt fra ultralydtransdusere. To artikler presenterer ulike måter å gjøre slike beregninger på, og to artikler er viet akustiske fenomener knyttet til vanlig og harmonisk ultralydavgivning.

De to metodeartiklene viser at de dataprogrammene som brukes reproducerer de faktiske forhold tilstrekkelig nøyaktig. Programmene er ulikt bygget opp og baserer seg på forskjellige matematiske modeller, men produserer tilsvarende resultater når de brukes til å løse spesifikke testforsøk.

Resultater fra de to andre artiklene viser at harmonisk avgivning bør føre til lignende forbedring innenfor alle avgivningssituasjoner dersom mediet er homogent. Denne antagelsen er ikke oppfylt, og effekter av heterogene medier er mer uttalt i avgivning med høye frekvenser enn med lave. Dette reduserer forbedringen. Et annet funn er at reverberasjoner alltid opptrer i par. Den bedre bildekvaliteten i harmonisk avgivning skyldes dels bedre undertrykkelse av reverberasjoner, og er en kombinert effekt av et filter som delvis undertrykker den ene av de to reverberasjonene i hvert par og intensiteten til den harmoniske strålen.

Det antydes avslutningsvis at undertrykkelse av akustisk støy i ikke-lineære ultralydavgivning vil kunne bedre både gråtoneavgivning og presisjonen i estimatene som ligger til grunn for annen kvantitativ vevsinformasjon.

Halvard Høiland-Kaupang

Institutt for Sirkulasjon og Bildediagnostikk, NTNU

Veileder: Professor Bjørn Angelsen

Finansieringskilde: Senter for forskningsdrevet innovasjon (Sfi) – «Medical Imaging Laboratory»

*Avhandlingen er funnet verdig til offentlig forsvar for graden Philosophiae Doctor (Ph.D.) i medisinsk teknologi. Disputas finner sted i auditoriet i Medisinsk-teknisk forskningscenter (MTFS), torsdag 25. august kl. 12.15.*



# Abstract

Models and methods for investigation of reverberations in nonlinear imaging techniques are presented in this thesis. Four independent papers provide insight on nonlinear propagation effects, a theoretical description of reverberations and the effects of reverberations on conventional and second-harmonic ultrasound imaging. Two papers, Paper A and C, describe methods used to investigate nonlinear distortion and reverberations, whereas Paper B and D concentrate on acoustic phenomena and performance of conventional and second-harmonic imaging.

Paper A provides a comparison of Field II, the Texas code and Abersim; three freely available simulation tools. If analytic solutions exist, these are used as gold standards for the comparison, and when they do not; high resolution Field II or Texas code simulations are defined to be the gold standard. The comparison suggests that Abersim performs equivalent or better than the two other methods in solving diffraction, attenuation and nonlinear distortion.

In Paper B, the effects of transmit beamforming and safety regulations on second-harmonic generation at two different frequencies are investigated. The safety regulations are imposed through a limitation of the maximum mechanical index of the transmit beam. Abersim is used as the simulation tool. The results suggest that the two frequencies perform equivalently when the transmit beamforming is equal in terms of wavelengths and the medium has a linear-in-frequency attenuation. Nonlinear frequency dependent attenuation and heterogeneous effects are suggested to be the main cause of the reduced improvements of second-harmonic imaging at higher frequencies.

Paper C presents a time-domain Spectral Element Method for nonlinear propagation in a finite spatial domain. The method is shown to perform well when compared with analytic plane wave solutions and in a two-dimensional comparison with Abersim. The Spectral Element Method is suggested to be accurate for heterogeneous media, but this is not investigated or verified.

The last paper concentrate on reverberations. A mathematical description of reverberations is presented along with a classification system. The main

results state that reverberations always act in reciprocal pairs, and that second-harmonic suppression of reverberations is a combined effect of transmit beam intensity and a reverberation weight filter presented in the paper.

The thesis provides insight on the description of reverberations and how they can be investigated. The influence of reverberations on ultrasound imaging is suggested to be more severe in applications where the object of interest is fully submerged in heterogeneous tissue. Deeper understanding of ultrasound acoustics may lead to new nonlinear imaging techniques where the noise contribution can be separated from the first-order echo. In turn, this might provide better gray scale images and ultrasound diagnoses.

# Preface

This thesis has been submitted in partial fulfillment of the requirements for the degree *Philosophiae Doctor* (Ph.D.) at the Faculty of Medicine of the Norwegian University of Science and Technology (NTNU). The research was funded by the *Centre for Research-based Innovation Medical Imaging Laboratory*, and was carried out under the supervision of Professor Bjørn Angelsen at the Department of Circulation and Medical Imaging, NTNU.

## Acknowledgments

First I would like Professor Bjørn Angelsen for supervising this Ph.D. work. Professor Angelsen's energy, interest and continuous flow of ideas and suggestions may seem overwhelming from time to time, but is truly one of the major motivations to do research with him and in his group. He is always available for discussions, and has provided crucial help on the contents of this thesis. I am truly thankful for the years I have worked in his research group.

Among the other members of the group I will especially thank Dr. Svein-Erik Måsøy. He is a true inspiration to work with, and introduced me to the field of phase aberrations and nonlinear effects through my Master's thesis work. The first two papers of this thesis is written in collaboration with Dr. Måsøy and I will thank him for his interest in my work and for the effort of reading and commenting on the manuscripts.

Of the remaining colleagues I will especially thank Dr. Tonni F. Johansen, Dr. Martijn Frijlink, Dr. Trond Varslot, Dr. Marco Voormolen, Øyvind Standal, Dr. Peter Näsholm, Dr. Thor Andreas Tangen, Jochen Deibele and Tarjei Rommetveit. The list of names is rather long, but all of them have shown great interest in my work over the years and have provided valuable insight on the different topics of this thesis. The help and effort of my co-authors Dr. Frijlink, Dr. Tangen and Jochen Deibele is much appreciated. The NTNU has a large and vital group of ultrasound researchers, and I will thank the rest of my colleagues for providing a very good and stimulating work environment. Being

surrounded by so many researchers at different levels and in different aspects of ultrasound reduce the feeling of working alone.

Two more persons deserve an acknowledgement: Director Olav Haraldset of MI Lab and Professor Hans Torp. They were the ones to employ me as a Ph.D. student within the MI Lab environment, and I will thank them for having faith in me and this project.

Although much time has been spent at work, family and friends deserve attention. Being common people in the sense that they don't work with ultrasound research, they have provided many good questions and have encouraged me to explain to them what I really do at work. Their support and interest in my work is highly appreciated, and through trying to explain to them what I do, I become more aware of what I *really* do myself.

Finally, my most heartfelt thank is to my wife, Henriette. Her patience, support and love has really been the most important to me during these years. She has made my days better when the progress seem to move backward, and she reminds me that there is more to life than computers and mathematical models.

# Contents

<b>Introduction</b>	<b>1</b>
I.1 Conventional Ultrasound Imaging . . . . .	1
I.2 Nonlinear Ultrasound Imaging . . . . .	3
I.2.1 Second-Harmonic Imaging . . . . .	3
I.2.2 Other Nonlinear Imaging Techniques . . . . .	5
I.3 Ultrasound Acoustics . . . . .	7
I.3.1 Model Formulation . . . . .	8
I.3.2 Overview of Numerical Methods . . . . .	10
I.3.3 Full Wave Models . . . . .	11
I.3.4 One-Way Wave Models . . . . .	12
I.4 Summary of Contributions . . . . .	13
I.5 Discussion . . . . .	17
I.6 Conclusion . . . . .	20
References . . . . .	21
List of Publications . . . . .	34
<b>A A Comparative Simulation Study on the Radiated Field from Ultrasound Transducers</b>	<b>37</b>
A.1 Introduction . . . . .	38
A.2 Background Theory . . . . .	39
A.3 Methods . . . . .	41
A.4 Results . . . . .	47
A.5 Discussion . . . . .	52
A.6 Conclusion . . . . .	57
References . . . . .	58
<b>B Transmit Beamforming for Optimal Second-Harmonic Gener- ation</b>	<b>61</b>
B.1 Introduction . . . . .	62

B.2	Theory . . . . .	63
B.2.1	Geometric Beam Setup . . . . .	63
B.2.2	Second Harmonic Generation . . . . .	64
B.2.3	Attenuation of Wave Propagation . . . . .	66
B.2.4	Estimation of Transmit Pressure . . . . .	67
B.3	Methods . . . . .	68
B.4	Results . . . . .	70
B.5	Discussion . . . . .	74
B.6	Conclusion . . . . .	79
	References . . . . .	80
<b>C</b>	<b>A Time-Domain Spectral Element Method for Propagation of Pulses in Nonlinear Soft Tissue</b>	<b>83</b>
C.1	Introduction . . . . .	84
C.2	Mathematical Model . . . . .	85
C.2.1	Model Equations . . . . .	85
C.2.2	Spectral Element Discretization . . . . .	86
C.2.3	Time Integration . . . . .	93
C.3	Plane Wave Propagation . . . . .	95
C.3.1	Absorption . . . . .	95
C.3.2	Nonlinear Elasticity . . . . .	99
C.4	Two-Dimensional Propagation . . . . .	101
C.4.1	Case A – Unfocused Transducer . . . . .	102
C.4.2	Case B – Focused Transducer . . . . .	105
C.4.3	Case C – Diagnostic Transducer . . . . .	105
C.5	Summary and Conclusion . . . . .	108
	References . . . . .	108
<b>D</b>	<b>Analysis of Reverberations in Medical Ultrasound</b>	<b>113</b>
D.1	Introduction . . . . .	114
D.2	Reverberation Model . . . . .	114
D.2.1	First-Order Echo . . . . .	115
D.2.2	Higher Order Echo . . . . .	116
D.2.3	Reverberation Classes . . . . .	118
D.2.4	Effect of Nonlinear Propagation . . . . .	119
D.2.5	Received Signal Model . . . . .	120
D.3	Numerical Experiments . . . . .	122
D.3.1	Plane Wave Experiments . . . . .	123
D.3.2	Full 3D Experiment . . . . .	125
D.4	Results . . . . .	126

---

D.4.1	Plane Wave Experiments . . . . .	126
D.4.2	Full 3D Experiment . . . . .	127
D.5	Discussion . . . . .	129
D.5.1	Plane Wave Experiments . . . . .	129
D.5.2	Full 3D Experiment . . . . .	132
D.6	Conclusion . . . . .	133
	References . . . . .	134
	<b>Bibliography</b>	<b>137</b>



# Introduction

Over several decades, ultrasound imaging has been used as a diagnostic tool within the field of medicine. In the early days, the “images” were one-dimensional presentations of the echoes recorded along one scan line, but since the beginning of the seventies, two-dimensional images has been produced. In addition to gray scale images, Doppler techniques are used to detect blood flow and three-dimensional imaging has entered the field of ultrasound.

## I.1 Conventional Ultrasound Imaging

The underlying model for medical ultrasound imaging is based on two simple, but robust, assumptions: A constant speed of sound and the Born approximation stating that all received echoes are first-order echoes. Echoes arise from differences in the equilibrium density and compressibility of the material, and the local speed of sound depends both on these two quantities and the local pressure.<sup>1</sup> Although it is known that both of these assumptions are approximations to the true situation, it is the most robust available model.

Images created under these assumptions are not *true* images. Spatially variant material parameters introduce *clutter*; acoustic noise contributions and artifact echoes in the image. Three main sources of clutter are phase aberration, side-lobe artifacts and reverberations.

Phase aberration, or just aberration, is local refraction (focusing and defocusing) effects caused by spatially variant speed of sound.<sup>2</sup> Aberration is a *forward* effect, and is shown to reduce transmit beam quality through broadening the main-lobe and increasing the side-lobe level.<sup>3-7</sup>

Side-lobes in sound beams are an inevitable effect of diffraction, and side-lobe artifacts are echoes received from scatterers located outside the main lobe. Phase aberration increase the side-lobe level and thus the amount of side-lobe artifacts. Such artifact echoes reduce image contrast, and are observable near vertical boundaries of hypo-echoic cavities where side-lobe echoes from the walls

are interpreted as main-lobe echoes from within the cavity. The reduced contrast complicates detection of smaller hypo- or an-echoic structures. Phase aberration is shown to be more severe in high frequency applications.<sup>7-9</sup> Refraction, or steering, of the beam is also observed.<sup>10</sup>

Theoretically, phase aberration can be modeled as a filter, or a *frequency dependent time-delay and amplitude screen*.<sup>2,11</sup> If this screen is known, the transmit pulse can be corrected such that the aberration effects are “reversed”. The principle of time-reversal is based on this.<sup>2,12,13</sup> The screen can be accurately estimated through the principle of time-reversal, but this requires the presence of a point source, or point scatterer, within the medium.<sup>11-13</sup> This is seldom or never found in diagnostic situations, but it is shown that a time-delay and amplitude correction can be estimated from general back scatter.<sup>14-18</sup>

In a real imaging situation the Born approximation is violated, and the ultrasound system records multiple echoes from the medium. Reverberations have been known for many years, and was early proposed as the most frequent artifact.<sup>19</sup> The signature of a classic reverberation echo is a distinct repetition of a strong scatterer in the image at two, or any integer, times the depth of the first-order echo.<sup>20,21</sup> In addition to this, reverberations introduce a haze in the image especially visible near the proximal boundary of hypo-echoic regions.<sup>20,21</sup>

Both phase aberration and reverberations are said to be effects of heterogeneities close to the transducer surface.<sup>22-24</sup> In deep transcutanial imaging, the body wall acts as the main heterogeneous object, whereas the parenchyma of the organ is more homogeneous. Body habitus may influence the image quality, and in general, obese and over weight patients are shown to produce images of lower quality. In applications such as vascular imaging (carotid artery etc.), breast and small parts imaging, the object of interest is fully submerged in heterogeneous tissue, and the concept of a distinct body wall does not describe the situation adequately.

The degradation of images from heterogeneous effects can be severe, and throughout the years, different techniques have been launched to enhance image quality. One such technique is spatial compounding where several transmit beams are transmitted at an angle to average out artifact echoes and random acoustic noise.<sup>25,26</sup> Another approach in vascular imaging is the use of gas bubbles as a blood pool contrast agent. Bubbles produce strong nonlinear back scatter, and this introduced the concept of nonlinear imaging techniques.

## I.2 Nonlinear Ultrasound Imaging

Nonlinear scattering from gas bubbles submerged in the fluid or tissue is caused by the high compressibility of gases compared to liquids, and produces strong both linear and nonlinear back scatter already at low pressure amplitudes.<sup>2</sup> The nonlinear back scatter of the insonified frequency  $f$ , are the harmonic frequencies  $2f$ ,  $3f$  and so forth. Another source of nonlinear signal contribution are the tissue elasticity. Soft tissue elasticity is a nonlinear relation between the applied force and the local displacement.<sup>2</sup> This introduces a pressure dependent speed of sound. This is widely investigated, and referred to as finite amplitude effects or generation of harmonic frequencies.<sup>2,27,28</sup> The rate of second-harmonic generation is proportional to the square of the total pressure.<sup>2,8</sup>

Bubbles with diameter of a few micrometers show a resonant behavior within the frequency range used in medical ultrasound.<sup>2</sup> The idea is to isolate the bubble response and suppress linear back scatter from the surrounding tissue. Although the back scatter arises from *linear* scatterers, nonlinear *propagation* cause the linear back scatter to contain contributions at the harmonic frequencies. Along with the development of ultrasonic contrast agent detection came the discovery of nonlinear gray scale imaging. Soon it was discovered that nonlinear imaging techniques produced gray scale images superior to those obtained with conventional sonography.<sup>4,6,29</sup>

### I.2.1 Second-Harmonic Imaging

This nonlinear technique was called second-harmonic, tissue harmonic or just harmonic imaging. A second-harmonic image is created by transmitting a pulse at one frequency, and receiving the echoes at the double, or *second-harmonic*, frequency. The transmitted frequency is consequently referred to as the *first-harmonic* frequency. The receive frequency determines the *imaging frequency*, and conventional, or *fundamental*, imaging refers to using the imaging frequency on both transmit and receive.

Second-harmonic gray scale images are usually created using either a filter or a *pulse inversion* scheme. Filtering is used in applications requiring high frame rates such as cardiac imaging. Images created with pulse inversion are based on summation of two receive pulses, where the sign of the second transmit pulse is opposite to the sign of the first. The even harmonic frequencies are invariant under this sign change, and a summation will amplify the even and cancel out the odd harmonic components. Transducer bandwidth limits the received signal to be constructed from the first- and second-harmonic components. The first-harmonic cancel out and the second-harmonic contributes to the image

data. However, *super-harmonic* imaging is proposed, where the third-, fourth- and fifth-harmonic frequencies are isolated with a filter to create the image.<sup>30</sup>

Investigation of the acoustic behavior of second-harmonic transmit beams show that the main lobe is slightly broader than the main lobe of a same-frequency fundamental beam, but the general side-lobe level is lower.<sup>4-6,31</sup> Compared with the first-harmonic beam, the main lobe is narrower. Because the second-harmonic imaging pulse is created from a pulse at half the frequency, the pulse length is longer than a same-frequency fundamental imaging pulse. These two effect reduces both the lateral and range resolution of the image when second-harmonic imaging is compared to fundamental imaging at the same imaging frequency.

Despite the reduced resolution, second-harmonic imaging is clinically shown to provide better diagnostic information in a wide range of applications, and is the preferred imaging technique in cardiac,<sup>22,32-34</sup> liver,<sup>24,35-37</sup> abdominal,<sup>38-41</sup> gall bladder,<sup>35,42</sup> pancreas,<sup>38</sup> kidney,<sup>35,43,44</sup> pelvic,<sup>35,40,41,44</sup> obstetrics and gynecology,<sup>40,42,45</sup> breast,<sup>25,46,47</sup> thyroid,<sup>48</sup> and small parts imaging.<sup>26,40</sup> Reported image improvements are better visualization of details,<sup>36-38,42</sup> hypo- and anechoic cystic lesions,<sup>23,24,39,43</sup> and lumen of cavities due to less influence of clutter.<sup>23,32-34,44</sup> Over all improved image quality<sup>37,40,41,43,46,47</sup> and conspicuity<sup>36,41,43,46,48</sup> are other common improvements.

The reduction of clutter in second-harmonic images is reported as a combined effect of reducing both the influence of phase aberrations, side-lobe artifacts and reverberations.<sup>49</sup> Within the quasilinear approximation, the second-harmonic is generated from the square of the first-harmonic pressure,<sup>8</sup> which implies a shape resemblance between the first- and second-harmonic aberrated beams. The shape resemblance is most prominent when the body wall is thin, and a comparison of aberrated transmit beams shows that the second-harmonic resembles in this case the first-harmonic more than the same-frequency fundamental.<sup>8,9</sup>

Not all improvements are reported to be significant. As a general trend, applications using imaging frequencies in the range 2–5 MHz benefit more from harmonic imaging than those imaging at higher frequencies(6–12 MHz).<sup>22,24,32-44</sup>

In applications using higher frequencies (6–12 MHz), second-harmonic imaging is also reported to improve image quality, but there are fewer published papers.<sup>40,46-48</sup> Two studies on breast<sup>25</sup> and carotid artery imaging<sup>26</sup> compare conventional sonography to spatial compounding. Both conclude that spatial compounding reduce artifacts and improve image quality. Two other studies include second-harmonic in a similar comparison,<sup>23,50</sup> and show that the combination of spatial compounding and second-harmonic imaging produces the

best image. Alone, the two techniques improve image quality when compared with conventional sonography, but spatial compounding produce the better images than second-harmonic imaging. An image of a carotid artery imaged using fundamental and second-harmonic imaging alone is presented in Fig. 1

In short words provides second-harmonic imaging equal or better images than fundamental imaging. Combinations of second-harmonic imaging with other beamforming and signal processing techniques such as spatial compounding, multiple foci etc. can improve the over-all image quality further, and applications using higher frequencies are believed to benefit the most from such combinations.

## I.2.2 Other Nonlinear Imaging Techniques

Assessment of carotid artery plaques, breast and prostate cancer relies on higher imaging frequencies. As described in the previous section, there is not one technique alone that provide the best improvement. Over the recent years, other nonlinear imaging techniques such as ShearWave<sup>TM</sup>Elastography, Differential Tissue Harmonic Imaging and SURF Imaging, or Radial Modulated Imaging, have entered the field of medical ultrasound. These are all techniques exploiting nonlinear effects of wave propagation, but in a different manner than second-harmonic imaging. The first technique is elastography imaging, and the two latter gray scale imaging techniques. SURF Imaging is also a contrast detection method.

### ShearWave<sup>TM</sup>Elastography Imaging

ShearWave<sup>TM</sup>Elastography is an imaging technique developed by SuperSonic Imagine (SSI). Elastography is visualization of the elastic properties of tissue, and SSI has launched a platform for real-time elastography.<sup>51</sup> In normal pulse-echo imaging, differences in acoustic impedance is imaged, and an elasticity model accounting for the *bulk* modulus alone is adequate. Soft tissue elasticity also have a *shear* modulus, and elastography images the differences in shear properties of the material.<sup>1,51</sup>

SSI images shear wave propagation, and utilize acoustic radiation force to induce these waves in the tissue.<sup>52,53</sup> Then, plane wave imaging and software beamforming is employed to create images from just a few scans at ultra high frame rates.<sup>51</sup>

## Differential Tissue Harmonic Imaging

Differential Tissue Harmonic Imaging is similar to second-harmonic imaging, and is developed and implemented by Toshiba.<sup>37,54</sup> In imaging of the liver, Differential Tissue Harmonic Imaging has been shown to perform better than both fundamental and second-harmonic imaging.<sup>37</sup> The technique is similar to pulse inversion harmonic imaging, but uses dual frequency band pulse complexes rather than conventional transmit pulses. The two frequency bands are a few Megahertz apart. Co-propagating pulses interact and create sum and difference frequencies that accumulate over time. Similar to pulse inversion, two receive pulses are needed for each scan line. The sign of the transmitted pulses is inverted in the second pulse, and both the second-harmonic and sum/difference frequencies are invariant under this sign change. The image is created from the echoes of both the harmonic and sum/difference frequencies.<sup>54</sup>

## SURF Imaging

Similar to second-harmonic imaging, SURF Imaging was first developed as a contrast detection method,<sup>55-57</sup> but has later been shown to also improve regular gray scale images.<sup>55,58,59</sup>

The concept of the contrast detection method is to use a low frequency ( $\sim 1$  MHz) manipulation pulse to manipulate the bubbles, and then image the bubbles at two different manipulated states with a high frequency pulse (8–10 MHz). The bubble is *radially modulated*, and Radial Modulated Imaging is another name on this contrast detection method. Using this setup, nonlinear scattering from the bubbles can be distinguished from the linear scattering of the tissue. Typically, the high frequency pulse is positioned at a low frequency wave peak or trough to make the two manipulations as different as possible.

Transmitting dual frequency band pulse complexes, and inverting the phase of the low frequency pulse, SURF Imaging has been shown to provide high quality gray scale images. The low frequency pulse manipulates the tissue, and the manipulation of the first-order echo can be distinguished from that of the reverberations. The result is an efficient reverberation suppression technique capable of visualizing hypo-echoic regions with higher contrast. Figure 1 shows this, and comparing second-harmonic imaging (top right panel) with SURF Imaging (bottom right panel), the lumen of the vessel is better visualized using SURF Imaging.

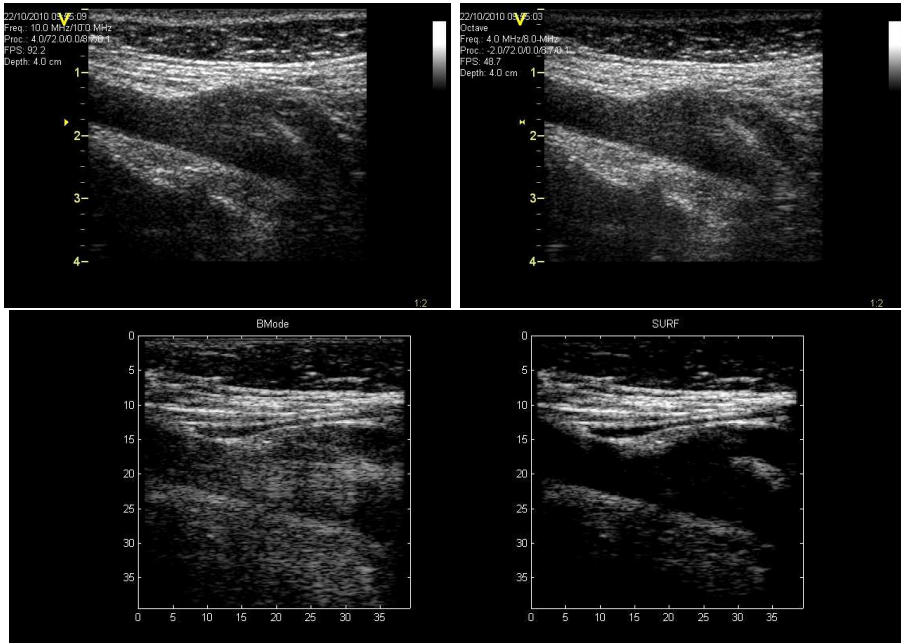


**Figure 1:** Examples of ultrasound gray scale images of the carotid artery. The top row shows a fundamental (left) and second-harmonic (right) image recorded with a GE Logiq E9 scanner (GE Health Care, Milwaukee, USA). The bottom row is from the same patient and is recorded with a Sonix RP scanner (Ultrasonix, Vancouver, Canada) modified for SURF Imaging. The bottom left panel is fundamental imaging and the bottom right SURF Imaging. Clutter is visible in the lumen of the vessel in the fundamental images. The improvement with second-harmonic imaging is hardly visible, but with SURF Imaging, the lumen appears darker and free of clutter near the posterior wall. The histogram of each image is equally compressed to improve the gray scale range in the printed images. The images are reprinted with permission from Svein-Erik Måsøy and Jochen Deibele.

### I.3 Ultrasound Acoustics

To understand the full picture of the acoustics involved in ultrasound imaging, both theoretical and experimental knowledge must be established. Experiments involving the full complex imaging situation provide insight regarding the appearance and existence of physical phenomena. Theoretical models seek to explain them, and simulations to reproduce them.

### I.3.1 Model Formulation

Equations governing acoustic wave propagation arise from three fundamental principles: Conservation of mass, conservation of momentum and a pressure–density relation for compressible fluids. Neglecting body forces, these are stated as<sup>27</sup>

$$\frac{\partial \rho}{\partial t} = \nabla \cdot (\rho \mathbf{u}) \quad (1)$$

$$\frac{d\mathbf{u}}{dt} = \frac{\partial \mathbf{u}}{\partial t} + (\mathbf{u} \cdot \nabla) \mathbf{u} = -\frac{1}{\rho} \nabla p \quad (2)$$

$$p = p(\rho) \quad (3)$$

where  $\rho$  is the density,  $p$ , the pressure and  $\mathbf{u}$  the particle velocity. Assuming the displacements to be small compared to the curvature of the wavefront, the convective term in Eq. (2) can be neglected.<sup>2,60</sup>

The pressure–density relation can be expressed as a Taylor expansion in terms of the density variation,  $\rho'$ , as<sup>2,28</sup>

$$p(\rho) \approx A \left( \frac{\rho'}{\rho_0} \right) + \frac{B}{2} \left( \frac{\rho'}{\rho_0} \right)^2$$

where  $\rho_0$  is the equilibrium density and  $A$  and  $B$  are constants.<sup>2</sup> The relative density change is related to the volume compression,  $\delta V / \Delta V$ , and the divergence of the displacement field,  $-\nabla \cdot \psi$ , and the above equation can be solved with respect to  $\nabla \cdot \psi$  as

$$-\nabla \cdot \psi = \kappa p - \beta_n (\kappa p)^2 + \kappa \mathcal{L} p \quad (4)$$

where  $\beta_n$  is the coefficient of non-linearity  $1+B/2A$ , and attenuation is included through the linear operator  $\mathcal{L}$  in the third term on the right hand side.<sup>2</sup> If attenuation is modeled as pure thermoviscous absorption,  $\mathcal{L}$  is defined as  $\mathcal{L} = \delta / \beta c^3$  where  $\delta$  is the diffusivity of the fluid.<sup>27</sup> For more complex attenuation models,  $\mathcal{L}$  is defined as a temporal convolution operator  $\mathcal{L} p = h *_{\text{t}} p$ .<sup>2</sup>

Introducing the pressure–density relation to Eqs. (1)–(2), two governing equations of acoustic wave propagation are found as

$$\rho \frac{\partial \mathbf{u}}{\partial t} = -\nabla p \quad (5)$$

$$\kappa \frac{\partial p}{\partial t} = -\nabla \cdot \mathbf{u} + \beta_n \kappa^2 \frac{\partial p^2}{\partial t} - \kappa \mathcal{L} \frac{\partial p}{\partial t} \quad (6)$$

where the convective term of Eq. (2) is neglected.

If Eq. (6) is differentiated in time and substituted into (5), a wave equation for the pressure is obtained as

$$\begin{aligned}\kappa \frac{\partial^2 p}{\partial t^2} &= -\nabla \cdot \frac{\partial \mathbf{u}}{\partial t} + \beta_n \kappa^2 \left( p \frac{\partial^2 p^2}{\partial t^2} + \left( \frac{\partial p}{\partial t} \right)^2 \right) + \kappa \mathcal{L} \frac{\partial^2 p}{\partial t^2} \\ &= -\nabla \cdot \left[ -\frac{1}{\rho} \nabla p \right] + \beta_n \kappa^2 \frac{\partial^2 p^2}{\partial t^2} + \kappa \mathcal{L} \frac{\partial^2 p}{\partial t^2}.\end{aligned}$$

This simplifies to the Westervelt equation for the pressure<sup>60</sup>

$$\nabla \cdot \left[ \frac{1}{\rho} \nabla p \right] - \kappa \frac{\partial^2 p}{\partial t^2} - \kappa \mathcal{L} \frac{\partial^2 p}{\partial t^2} = -\beta_n \kappa^2 \frac{\partial^2 p^2}{\partial t^2}. \quad (7)$$

The coupled system of two first-order equations and the second-order Westervelt equation are equivalent formulations of the same problem.

Spatially variant material parameters introduce additional terms to the equations. A material parameter can be modeled with an average and a fluctuating term,  $\rho = \rho_a + \rho_f$  (and similar for  $\kappa$  and  $\beta_n$ ).<sup>1</sup> Inserted in Eq. (7), the average terms are kept on the left hand side and account for forward propagation effects such as nonlinear distortion and phase aberration. The fluctuating terms are multiplied over to the right hand side and act as source terms accounting for local scattering.

The final wave equation accounting for nonlinear propagation and scattering is then

$$\underbrace{\nabla^2 p - \frac{1}{c_a^2} \frac{\partial^2 p}{\partial t^2}}_{\text{Linear propagation}} + \underbrace{\frac{\beta_{na} \kappa_a}{c_a^2} \frac{\partial^2 p^2}{\partial t^2}}_{\text{Nonlinear propagation}} + \underbrace{\frac{1}{c_a^2} \mathcal{L} \frac{\partial^2 p}{\partial t^2}}_{\text{Attenuation}} = \underbrace{\frac{\sigma_1}{c_a^2} \frac{\partial^2 p}{\partial t^2}}_{\text{Linear scattering}} + \nabla \cdot [\gamma \nabla p] + \underbrace{\frac{\sigma_n}{c_a^2} \frac{\partial^2 p^2}{\partial t^2}}_{\text{Nonlinear scattering}} \quad (8)$$

$$c_a^2 = \frac{1}{\rho_a \kappa_a}, \quad \sigma_1 = \frac{\kappa_f}{\kappa_a}, \quad \gamma = \frac{\rho_f}{\rho}, \quad \sigma_n = (2\beta_{na}(2 + \sigma_1)\sigma_1 + \beta_{nf}(1 + \sigma_1)^2) \kappa_a.$$

Fluctuations in compressibility and density cause monopole and dipole scattering respectively.<sup>1</sup> Nonlinear scattering is said to be caused by differences in the coefficient of non-linearity,  $\beta_{nf}$ , but as seen in the above equation, even homogeneously nonlinear materials ( $\beta_{nf}=0$ ) create nonlinear scattering if compressibility fluctuations  $\kappa_f$  are present. Large variations in the elastic properties, where  $\beta_{nf}$  is of the same order as  $\beta_{na}$ , is the dominant contribution to nonlinear back scatter.<sup>2</sup>

### I.3.2 Overview of Numerical Methods

Both theoretical models and simplified laboratory experiments provide the option of isolating the effect of a few chosen physical phenomena. As information technology advances, the use of theoretical models combined with numerical simulations has become more and more popular. One example is the field of transducer research where simulations are used to aid design of transducer arrays in terms of both radiation surfaces, field computations and interaction and behavior of the transducer stack itself.<sup>61–63</sup>

The range of available simulation tools reaches from highly specialized tools tailored for one specific phenomenon to general multiphysics tools for more complex problems. The most general tools are often commercial computer programs with expensive licenses, but simulation tools available free of charge exist.

Available numerical methods for acoustic wave propagation and radiated fields can be separated into two main classes: Those based on the full wave equation and those based on a one-way wave equation. Methods based on the full wave equation are impulse response methods<sup>64,65,68,66,67</sup> or methods integrating the model equations in time within a finite, spatial computational domain.<sup>69–84</sup> Another full wave approach is the Green’s function method proposed by Verweij and Huijssen<sup>85,86</sup> and *Fast ultrasound simulation in k-space* (Fusk) for simulation of pulse–echo imaging.<sup>87</sup>

The one-way wave equation tools are typically based on the parabolic approximation, *i.e.*, the KZK-equation,<sup>88,89</sup> and two well-known tools, the Texas and Bergen codes, solve this equation in the time-domain<sup>93,94,90–92</sup> and frequency domain<sup>97,95,96</sup> respectively. Another approach to solve the one-way wave equation *without* the parabolic approximation is the Angular Spectrum Method<sup>98,99</sup> and variations of this.<sup>102–105,100,101</sup> Both classes contain tools for both linear and nonlinear propagation.

All the mentioned wave models can be expressed in the time-domain or the frequency-domain. Phenomena such as frequency dependent attenuation and impedance boundary conditions of transducer surfaces can be more challenging to handle in the time-domain than in the frequency-domain. Attenuation may be modeled within a frequency range using a finite number of relaxation processes,<sup>1,84,91,106</sup> or through approximation of the formulations presented by Szabo<sup>107</sup> using fractional derivatives.<sup>82</sup> Frequency dependent impedance boundary conditions have been successfully modeled using the  $Z$ -transform in the field of aeroacoustics.<sup>108,109</sup>

### I.3.3 Full Wave Models

Aiming to solve a chosen wave model, approximations are made in the formulation of the numerical model. All methods have a range of validity, and the full wave tools are limited to whatever spatial accuracy they are tailored to satisfy. The spatial accuracy also indicates the maximum spatial frequency the method is able to solve. This limitation makes full wave models in a finite space rather limited to problems where the solution has a smooth resemblance in space over a certain length scale. To capture shocks and discontinuities, the spatial sampling needs to be sufficiently high or methods accounting for discontinuities must be employed.

The spatial domain of a full wave model must be represented in a discrete formulation. The spatial *discretization* usually defines the type of method, and common discretization schemes used in computational acoustics are Finite Differences (FD),<sup>75,81,82,84,110</sup> Finite Elements (FE),<sup>69,111</sup> Spectral Elements (SE),<sup>71,74,76,77</sup> pseudo-spectral<sup>72,73,78</sup> and  $k$ -space methods.<sup>79,80</sup> The difference between pseudo-spectral and  $k$ -space methods is that pseudo-spectral methods use general polynomials (both trigonometric and other) to approximate the solution,<sup>112</sup> whereas “pure”  $k$ -space methods typically are based on the Fourier transform of the model equations.<sup>79,80,113</sup>

Spatial discretization of a wave model results in a system of *semi-discretized* equations, that is: The time is still continuous. Spatial derivatives introduce coupling of the system over a wide range of length scales, or spatial frequencies, and the system is denoted as *stiff*.<sup>114,115</sup> Numerical integration of stiff equations are often limited to *implicit* integration schemes, *i.e.*, schemes where a system of equations must be solved for each step. *Explicit* methods avoid this, but are in general less suited for stiff problems because stability requirements must be met, and these can force the step size to become very small.<sup>114,115</sup> However, some integrators used in wave phenomena are explicit and fully capable of solving such problem as long as the stability requirements are met. The leap-frog (or Störmer-Verlet) scheme is one example along with some of the Newmark schemes.<sup>75,80,83</sup> Other integrators such as Adams-Bashforth and Adams-Moulton schemes are also suggested.<sup>72,73,116</sup>

In the development of the attenuation model in acoustics, thermodynamic approaches are made. Some papers present models where both wave propagation and temperature behavior are accounted for.<sup>70,117–119</sup> The models including both in the simulation itself are the FE-models presented in Refs. 70, 117 and 118. The coupling of the FD-method and a temperature model proposed by Pinton uses two separate models and investigate the temperature response for a pre-simulated wave field.<sup>119</sup>

### I.3.4 One-Way Wave Models

One-way models are in many ways simpler to handle. The wave model is usually formulated in retarded time coordinates and integrated in depth. The one-way wave equation is a second-order differential equation in depth, but a simplification to a first-order formulation through the parabolic approximation ( $\partial^2/\partial z^2 \approx 0$ ) is common. A well-known model within the parabolic approximation is the KZK equation.<sup>88,89</sup> A weakness of the KZK equation is its limited ability to solve wave rays inclined more than  $\sim 15^\circ$  with respect to the  $z$ -axis.<sup>120,121</sup> This limits straight forward use of the KZK equation in problems involving highly focused transducers. However, investigating the field from a highly focused lithotripter, construction of an intermediate source condition is suggested.<sup>122</sup>

Spatial discretization of the transverse spatial dimensions is necessary, and one approach is to use a finite-difference scheme.<sup>93,94,90-92,100,101</sup> Another approximation is the frequency domain solution employed in the Bergen Code,<sup>97,95,96</sup> or the Angular Spectrum approach where the differentiation is solved using the Fourier transform.<sup>99-101</sup> The first is defined for problems in cylinder coordinates and the latter for Cartesian coordinates.

Using the Fourier transform and an Angular Spectrum approach de-couple the equations in space. Employing the Fourier transform in time transforms the model equation into a system of *ordinary* differential equations. In this sense, the one-way wave equation becomes a second-order ordinary differential equation in depth  $z$ . This can be solved without making the parabolic approximation.<sup>100,101</sup>

One-way wave models catch forward effects such as nonlinear distortion and phase aberrations, and this is incorporated into both Abersim<sup>100,101</sup> and the Texas code.<sup>94</sup> Using such tools, the combined effect of these two forward propagation effects can be investigated.<sup>7-9,94,123</sup>

Although one-way wave models are tailored to solve forward effects, *back propagation*, *i.e.*, propagation of a source field in space and back to the transducer, is possible. Using the Angular Spectrum Method in physical rather than retarded time coordinates, enables the use of *back projection* where diffraction effects are reversed.<sup>98</sup> Concentrating on the models formulated in retarded time, one interpretation is that the term *forward* refers to the time of the problem and the term *one-way* to the limitation of only one (spatial) direction of integration at the time. If a problem can be separated into a forward field with a separate (back) scattered field, this can be investigated using one-way wave models. Simultaneous back scatter is, however, not covered by one-way models, and to study more complex, or realistic, back scatter, a full wave model is

preferable.

This limits the one-way tools to simple back scattering problems such as reflection from perfect planes or a few points scatterers. Another possibility for investigation of (first-order) back scatter with one-way tools, is a combination of methods.<sup>124,125</sup> In this fashion, simulation of ultrasound *imaging* similar to available (linear) methods as Field II<sup>66,67</sup> and Fusk<sup>87</sup> can be constructed from components tailored to separate parts of the imaging chain.

A multiphysics environment may be constructed from combinations of several specialized simulation tools. Combining a nonlinear one-way tool with a linear back scatter tool might be faster and require less resources than employing a full wave model. The coupling between the different models and methods may be more approximative in an “in-house” implementation than those employed in commercial multiphysics tools, but can still provide valuable insight in various field of ultrasound research. Another advantage of “in-house” implementations is that they can provide open source code and be free of charge.

## I.4 Summary of Contributions

The four contributions in this thesis present a framework for investigating nonlinear and heterogeneous effects in medical ultrasound imaging through the use of numerical simulations. The included papers are either accepted or submitted for publication, and present the necessary background for each paper. The papers can be read independently and provide a more detailed discussion on each topic. Here, an overview of the thesis as a whole, and the connection between the papers are presented.

The first two chapters are extensions to some of the research activity started off by Dr. Svein-Erik Måsøy and Dr. Trond Varslot on the combined effect of phase aberrations and nonlinear propagation effects. The year between the author’s Master’s degree and start of Ph.D. program (2006–07), was spent on work related to phase aberrations,<sup>123</sup> a new Matlab and parallel C implementation of Abersim, clinical contrast trials with a first generation SURF scanner,<sup>126</sup> and co-supervision of Dr. Måsøy’s Master student on ultrasound contrast agent detection using high frequency SURF Imaging.<sup>127</sup>

Although Paper B was the first work performed in the Ph.D. program, Paper A is presented in the thesis as the first paper to provide an introduction to Abersim; a simulation tool used in the three other papers. Abersim has been developed over many years by members of the author’s research group at NTNU, and was originally tailored to investigate phase aberration; hence the name Abersim. One goal with the re-implementation of Abersim was to make

it more computationally efficient for full three-dimensional problems, and to make it more available.

The comparison performed in Paper A was initialized by Dr. Martijn Frijlink during his post doctoral at NTNU. His research then was mainly on cardiac transducers, and he needed a tool for investigating nonlinear transmit fields. Field II has long been considered the gold standard of field simulations, but Field II is limited to linear elasticity and a linear-in-frequency attenuation model. Abersim was chosen as the tool for nonlinear propagation, and Dr. Frijlink was one of the first to start using the newly implemented parallel C-version of Abersim. Another interest of the authors was to present the developed Generalized Angular Spectrum Method for circular-symmetric problems. Initial results of this comparison was presented at the IEEE International Ultrasonic Symposium 2008 in Beijing, China.<sup>102</sup> Later, the study was extended to include comparisons of nonlinear fields.

In the author's Master's thesis, second-harmonic generation was investigated for different focal depths when the aperture was given. The key results were presented at the IEEE International Ultrasonic Symposium 2006 in Vancouver, Canada.<sup>9</sup> The initial motivation for Paper B was to investigate further the influence of beamforming on second-harmonic generation, and why second-harmonic imaging is reported to be less successful for higher frequencies.

In Ref. 9, the author investigated second-harmonic generation for a few transducer configurations with equal transmit pressure. Higher transmit pressures imply higher generation, but safety limitations are imposed on diagnostic ultrasound scanners to avoid bio-hazards such as too high temperatures or acoustic cavitation. As a consequence, transmit pressure amplitudes must be estimated or measured for each transmit configuration on the scanner. A motivation was to find the optimal transmit configuration for second-harmonic generation given these safety limitations. Paper B provides insight on the combined effects of transmit beamforming and pressure amplitude. For simplicity, the medium was chosen to be homogeneous, and circular-symmetric apertures were chosen to reduce computation time.

The results of Paper B suggest that the degradation caused by heterogeneous effects in second-harmonic images are of least importance when a body wall is the main heterogeneous object. Acoustic noise, or clutter, is assumed to be the main contribution to reduced image quality, and one goal for the Ph.D. program was to develop a software tool for investigation of reverberations, and a full wave model integrated in time was sought.

Through one of the courses included in the Ph.D. program, the author was presented to the field of Spectral Element Methods. Solutions based on Fourier,

or  $k$ -space, discretizations in space such as the methods presented in Ref. 79 and 80 was considered, but an extension to nonlinear tissue was at the time believed to cause too many multidimensional Fourier transforms to be efficient in three dimensions. The use of an initial condition rather than boundary conditions was also considered to be a drawback. Paper C provides a presentation to the basic principles of the spectral element model used in this thesis. The method was first implemented as a one-dimensional test in Matlab, and later C++ for the two-dimensional method.

The last paper concentrates on the effect of reverberations in medical ultrasound. The term reverberations is often referred to, but to the author's knowledge, little or nothing is published on the mathematical description of reverberations. Paper D is included to provide one such description, and to investigate the influence of reverberations from simple scatterers. The reported suppression of clutter through the use of second-harmonic imaging is not fully understood, and effects of second-harmonic imaging on reverberations suppression is investigated in Paper D.

### **Paper A: A Comparative Simulation Study on the Radiated Field from Ultrasound Transducers**

The first paper is a comparison between three publicly available simulation tools: Field II, the Texas code and Abersim. Numerical simulations play an important role in research on transducers and radiated sound fields. The three tools compute radiated sound field, but differ both in the underlying acoustic model and implementation. For many years, Field II has been considered as the gold standard for calculating fields from arbitrary transducer geometries. Along with the development of nonlinear imaging techniques, the need for accurate field simulations including nonlinear effects for arbitrary transducer geometries has become more pronounced. The paper compare each simulation tool with appropriate gold standards. For circular piston transducers the three tools perform equivalently. Abersim is suggested to be more accurate than Field II and KZK based solutions for near field diffraction. The attenuation model employed in Abersim is also superior to the models employed in Field II and the Texas code. A comparison for a cardiac array transducer is made between Field II and Abersim, and shows that Abersim produces radiated fields equivalent to Field II.

*This paper is re-submitted to IEEE Transactions on Ultrasonics, Ferro Electricity and Frequency Control after initial reject from the same journal (old major revision).*

## **Paper B: Transmit Beamforming for Optimal Second-Harmonic Generation**

Second-harmonic imaging is the preferred imaging technique in many applications, and is more often reported to improve image quality at low frequencies than high. A main motivation of the paper was to understand why. Safety regulations impose limitations on the maximum achieved pressure through the *mechanical index*, and a second motivation for this paper was to investigate second-harmonic generation in lieu of transmit beamforming and safety regulations. The transmit pressure is estimated such that the pressure never exceed a mechanical index of 1.2. The main results state that the acoustic model does not indicate that lower frequencies are more favorable if the attenuation is linearly frequency dependent. If the frequency exponent of the attenuation is larger than one, higher frequencies suffer more from this and generate less second-harmonic energy. This, and heterogeneous effects are proposed as the main contributor to different performance of second-harmonic imaging at two different frequencies. A suppression quality factor is suggested to quantify this, and suggests better performance in applications where the heterogeneous structures are located closer to the transducer, *i.e.*, a situation where the body wall is thin in terms of wavelengths.

*This paper is accepted for publication in IEEE Transactions on Ultrasonics, Ferro Electricity and Frequency Control.*

## **Paper C: A Time-Domain Spectral Element Method for Propagation of Pulses in Nonlinear Soft Tissue**

To investigate reverberations and multiple scattering, a full wave time-domain simulation tool is needed. The third paper presents a time-domain Spectral Element Method fulfilling these requirements. The presented method was tailored to handle nonlinear tissue elasticity and frequency dependent power-law attenuation with  $f^1$  and  $f^{1.1}$ . The nonlinear and attenuation models are compared with analytic solutions and verified to provide the desired accuracy in a plane wave environment. Two-dimensional propagation is verified through comparison with Abersim. The discretization itself introduce numerical dispersion in the spatial wave numbers, and this increase the amount of generated harmonic frequencies. This effect is less pronounced when both attenuation and non-linearity are included in the propagation. The author suggests the model to be suited for propagation in heterogeneous materials, but this is not verified.

*This paper is submitted to Journal of the Acoustical Society of America.*

## **Paper D: Analysis of Reverberations in Medical Ultrasound**

The fourth paper presents a mathematical description of reverberations in medical ultrasound, including a classification system. The model is verified through simulations for a plane wave case using the method presented in Paper C and in a full 3D setup using simple reflectors as scatterers in Abersim. The main result states, using spatial reciprocity, that reverberations always act in pairs. This is verified through simulations. A reverberation weight filter is constructed, and suppression of reverberations is discussed in terms of this filter and transmit beam intensity for fundamental and second-harmonic imaging. The suppression obtained in second-harmonic imaging is found to be a combined effect of a more favorable reverberation weight filter and the accumulative effect of harmonic generation.

*This paper is submitted to Journal of the Acoustical Society of America.*

## **I.5 Discussion**

The conclusion of Paper A states that Abersim perform equivalently to Field II in simulating radiation from diagnostic transducers, and possibly better when compared with analytic solutions. A comparison to the Texas code provides another verification of the nonlinear model in Abersim in addition to the results presented in the original papers.<sup>100,101</sup> The first version of Paper A was rejected after review from the IEEE Transactions on Ultrasonics, Ferro Electricity and Frequency Control. One of the reviewers commented that the paper did not include comparisons to measurements, and that small differences were of less interest because the uncertainty of a measurement setup could be much larger. The three tools are previously compared with measurements,<sup>66,67,92,100,101</sup> and a new comparison was not considered to be necessary. In the comparisons made in the revision of Paper A, gold standards are established and the results compared with these.

In Paper B, all transducers are circular-symmetric. Today, most clinical scanners use linear, curved linear and phased array transducers. This is discussed in Paper B, but a few more comments are necessary.

The on-axis radiated field from a circular aperture contains, for a single frequency vibration, perfect constructive and destructive interference. Quadratic or rectangular apertures do not show this behavior, and the interference is less

distinct. Broad-band pulses also reduce the detail of the interference pattern. Comparing quadratic and circular apertures, the area of a quadratic aperture of size  $D \times D$  is larger than the area of a circular aperture of diameter  $D$ . The main lobe of the quadratic aperture is also narrower.<sup>1</sup> These two effects indicate higher second-harmonic generation. Assuming broad-band pulses, modeling the relation between the maximum generated harmonic energy from quadratic and circular aperture through a scaling factor relating the area differences is believed to be possible. This is not investigated.

When the azimuth and elevation apertures become different, the paper, with support from Ref. 97, suggests that rectangular transducers perform worse. Although a scaling factor might be obtainable, the ratio between the azimuth and elevation apertures of diagnostic transducers is not constant. The elevation aperture often is fixed, and the azimuth aperture varies with the application. The effects of variations in this ratio on the optimal choice of transmit beam-forming are not known

The suppression quality factor  $Q$  in Paper B is a suggested measure on the suppression of near field echoes in second-harmonic imaging. Without the knowledge from Paper D, this measure concurs with previously suggested explanations: That the second-harmonic component is generated behind the heterogeneous body wall and suppresses near field echoes originating from within the body wall.<sup>22-24</sup> The suppression factor is determined based on the focal depth of the *transmit* beam, and is not related to the *observation point*, *i.e.*, the receive focal depth.

Introducing some of the concepts from Paper D, the suppression factor  $Q$  describes suppression when the reverberators are located at half the focal depth, and the transmit and receive focal depths are equal. The remaining suppression is, according to Paper D, determined by the amplitude modification introduced by the reverberation weight filter.

The Spectral Element Method in Paper C is suggested as a numerical method for investigation of reverberations. The method is shown to accurately reproduce both plane wave propagation effects and two-dimensional propagation. A weakness of the paper is the missing verification of the indicated ability to solve wave propagation in heterogeneous materials. Effects of heterogeneities are discussed, and also simulated in Paper D, but not verified. Distortion from heterogeneities and non-linearity is a volumetric effect, and the restriction to two-dimensional problem formulations is a drawback in that perspective. An extension to three-dimensional problems requires the method to be implemented in a parallel environment, and at the time this was written; the implemented program could run in parallel, but the extension to three

dimensions was not finished.

The object of Paper D is to provide insight to reverberations in medical ultrasound. The paper presents a mathematical formulation of the multiple scattered wave field, and how the the received signal is influenced by reverberations. Numerical experiments verify the model, and a more detailed discussion is found in the paper itself. In a more holistic perspective, the paper also provides an example on how to use models and methods presented in the three first papers of this thesis. The suppression quality factor  $Q$  from Paper B was not found to be useful in Paper D due to its limited ability to separate the suppression caused by transmit beam intensity differences and the amplitude modification of the reverberation weight filter.

The suppression of reverberations in second-harmonic imaging is suggested to be a combined effect of the accumulation of harmonic energy and an amplitude modification from a reverberation weight filter. The amplitude modification implicitly accounts for transmit beam intensities, and in the situation where near field reverberation echoes arrive simultaneously as a deeper first-order echo, second-harmonic imaging is shown to mainly suppress one out of two (reciprocal) components.

In applications where the object of interest is fully submerged in heterogeneous tissue, plane structures may be present at depths close to the object of interest. The opposite situation is imaging of an organ behind a (thin) body wall. The organ parenchyma is assumed to not contain plane structures, and in this situation the third scatterer will be a collection of diffuse scatterers rather than a reflecting plane. This suggests that reverberations might contribute more to clutter in imaging of fully heterogeneous objects than in applications where distinct body wall is present.

In applications with a body wall and no plane, deep structures, reverberations are suggested to be of less importance at depths larger than approximately twice the thickness of the body wall. Side-lobe artifacts and phase aberrations are believed to be the main sources of clutter in deep regions.

Nonlinear imaging techniques exploiting the accumulative nonlinear distortion of a transmit beam may suppress reverberations similar to second-harmonic imaging. Both Differential Tissue Harmonic Imaging and SURF Imaging create images based on the back scatter from the nonlinear transmit beam. The back scattered signals contain information about the *forward* nonlinear distortion characteristics of the pulse from a certain depth. Nonlinear imaging techniques using the transmit beam intensity as a measure of this distortion are believed to suppress reverberations similar to second-harmonic imaging. This is the case in Differential Tissue Harmonic Imaging,<sup>37</sup> and is also suggested as a method

for SURF Imaging.<sup>59</sup> The SURF image in Fig. 1 is created with proprietary SURF signal processing and not the method suggested in Ref. 59.

Better understanding of the back scattered signal may improve both gray scale images and ultrasound diagnoses. All received echoes are “false” in the sense that they consist of both the true first-order echo and acoustic noise. Estimation of material properties, *e.g.*, tissue and blood velocities, are also influenced by acoustic noise, but the influence is not known. In gray scale images, spatial compounding is shown to reduce clutter, but it is not understood whether the clutter is *suppressed* or if the over-all image quality is a perceptual improvement through better visualization of curved surfaces from the angular dependency of specular reflections.

## I.6 Conclusion

The four papers of the thesis present a framework for investigation of reverberation effects in medical ultrasound through numerical simulations. Both Paper A and C provide insight on possible methods for simulation of different aspects of nonlinear propagation. Abersim has previously been shown to accurately reproduce *forward* nonlinear and heterogeneous effects, and Paper A shows that the transmit beams simulated with Abersim are equivalent to those simulated with the widely used Field II. Paper C presents a Spectral Element Method for simulation of nonlinear wave propagation in back scattering media, and is shown to accurately reproduce forward nonlinear distortion of propagating pulses. Although back scatter is possible to investigate, the accuracy of the method is not verified for heterogeneous materials.

Paper B and D discuss the effects of generation of nonlinear distortion and reverberations in second-harmonic imaging. The first concentrates on second-harmonic generation in diagnostic ultrasound, and the second on suppression of reverberations. Paper B suggests that both low and high frequencies perform equivalently if the medium is homogeneous and has a linear-in-frequency attenuation. Non-linearly frequency dependent attenuation and heterogeneous effects are suggested to be the main reason for lower image improvement in high frequency applications. The suppression of reverberations in second-harmonic imaging is in Paper D suggested to be a combined effect of transmit beam intensity and a reverberation weight filter.

To summarize: Reverberations are a major contributor to clutter in medical ultrasound imaging, and are suggested to contribute more in applications where the object of interest is fully submerged in heterogeneous tissue than in applications imaging an organ behind a body wall. Examples of fully heterogeneous

applications are vascular, breast and small parts imaging at higher frequencies. In applications with a body wall as the main heterogeneous object, reverberations are believed to be less pronounced in (deep) regions of interest, and in these applications, side-lobe artifacts and phase aberrations are believed to be the main sources of clutter. Signal and image processing tailored to conceal clutter may provide better images, but if the *acoustical* model and the information about *forward* propagation effects can be understood and exploited in a better way, separation of true first-order echoes and reverberations might be possible. It is to the author's belief that both gray scale images and clinical ultrasound diagnoses will benefit from such knowledge.

## References

- [1] B. A. J. Angelsen, *Ultrasound Imaging*. Trondheim, Norway: Emantec, 2000, vol. 1.
- [2] ———, *Ultrasound Imaging*. Trondheim, Norway: Emantec, 2000, vol. 2.
- [3] S. H. P. Bly, D. Lee-Chahal, D. R. Foster, M. S. Patterson, F. S. Foster, and J. W. Hunt, "Quantitative Contrast Measurements in B-Mode Images Comparison Between Experiment and Theory," *Ultrasound Med. & Biol.*, vol. 12, pp. 197–208, 1986.
- [4] T. Christopher, "Finite Amplitude Distortion-Based Inhomogenous Pulse Echo Ultrasound Imaging," *IEEE Trans. Ultrason., Ferroelect., Freq. Contr.*, vol. 44, pp. 125–9, 1997.
- [5] ———, "Experimental Investigation of Finite Amplitude Distortion-Based, Second Harmonic Pulse Echo Ultrasound Imaging," *IEEE Trans. Ultrason., Ferroelect., Freq. Contr.*, vol. 45, pp. 158–62, 1998.
- [6] B. Ward, A. C. Baker, and V. F. Humphrey, "Nonlinear Propagation Applied to the Improvement of Resolution in Diagnostic Medical Ultrasound," *J. Acoust. Soc. Am.*, vol. 101, pp. 143–54, 1997.
- [7] K. D. Wallace, M. R. Holland, B. S. Robinson, R. J. Fedewa, C. W. Lloyd, and J. G. Miller, "Impact of Propagation Through an Aberrating Medium on the Linear Effective Apodization of a Nonlinearly Generated Second Harmonic Field," *IEEE Trans. Ultrason., Ferroelect., Freq. Contr.*, vol. 53, pp. 1260–8, 2006.

- [8] T. Varslot, S.-E. Måsøy, T. F. Johansen, and B. A. J. Angelsen, "Aberration in Nonlinear Acoustic Wave Propagation," *IEEE Trans. Ultrason., Ferroelect., Freq. Contr.*, vol. 54, pp. 470–9, 2007.
- [9] H. Kaupang, S.-E. Måsøy, T. Varslot, T. F. Johansen, and B. A. J. Angelsen, "Generation and Aberration of Second-Harmonic Ultrasound Beams in Heterogeneous Tissue," in *IEEE Ultrason. Symp. Proc.*, 2006, pp. 2160–3.
- [10] M. Moshfeghi and R. C. Waag, "In Vivo and In Vitro Ultrasound Beam Distortion Measurements of a Large Aperture and a Conventional Aperture Focused Transducer," *Ultrasound Med. & Biol.*, vol. 14, pp. 415–28, 1988.
- [11] S.-E. Måsøy, T. F. Johansen, and B. Angelsen, "Correction of Ultrasonic Wave Aberration With a Time Delay and Amplitude Filter," *J. Acoust. Soc. Am.*, vol. 113, pp. 2009–20, 2003.
- [12] M. Fink, C. Prada, F. Wu, and D. Cassereau, "Self Focusing in Inhomogeneous Media With Time Reversal Acoustic Mirrors," in *IEEE Ultrason. Symp. Proc.*, 1989, pp. 681–6.
- [13] C. Prada, F. Wu, and M. Fink, "The Iterative Time Reversal Mirror: A Solution to Self-Focusing in the Pulse Echo Mode," *J. Acoust. Soc. Am.*, vol. 90, pp. 1119–29, 1991.
- [14] S.-E. Måsøy, B. A. J. Angelsen, and T. Varslot, "Estimation of Ultrasound Wave Aberration With Signals From Random Scatterers," *J. Acoust. Soc. Am.*, vol. 115, pp. 2998–3009, 2004.
- [15] S.-E. Måsøy, T. Varslot, and B. A. J. Angelsen, "Iteration of Transmit-Beam Aberration Correction in Medical Ultrasound Imaging," *J. Acoust. Soc. Am.*, vol. 117, pp. 450–61, 2005.
- [16] S.-E. Måsøy, B. A. J. Angelsen, and T. Varslot, "Variance Analysis of Arrival Time and Amplitude Estimates From Random Speckle Signal," *J. Acoust. Soc. Am.*, vol. 121, pp. 286–98, 2007.
- [17] T. Varslot, H. Krogstad, E. Mo, and B. A. J. Angelsen, "Eigenfunction Analysis of Stochastic Backscatter for Characterization of Acoustic Aberration in Medical Ultrasound Imaging," *J. Acoust. Soc. Am.*, vol. 115, pp. 3068–76, 2004.

- 
- [18] T. Varslot, B. A. J. Angelsen, and R. C. Waag, "Spectral Estimation for Characterization of Acoustic Aberration," *J. Acoust. Soc. Am.*, vol. 116, pp. 97–108, 2004.
- [19] R. D. Park, T. G. Nyland, J. C. Lattimer, C. W. Miller, and J. L. Lebel, "B-Mode Gray Scale Ultrasound: Imaging Artifacts and Interpretation Principles," *Vet. Rad.*, vol. 22, pp. 204–10, 1981.
- [20] B. D. Sites, R. Brull, V. W. S. Chan, B. C. Spence, J. Gallagher, M. L. Beach, V. R. Sites, and G. S. Hartman, "Artifacts and Pitfall Errors Associated with Ultrasound-Guided Regional Anesthesia. Part I: Understanding the Basic Principles of Ultrasound Physics and Machine Operations," *Reg. Anesth. Pain Med.*, vol. 32, pp. 412–8, 2007.
- [21] B. D. Sites, R. Brull, V. W. S. Chan, B. C. Spence, J. Gallagher, M. L. Beach, V. R. Sites, , S. Abbas, and G. S. Hartman, "Artifacts and Pitfall Errors Associated with Ultrasound-Guided Regional Anesthesia. Part II: A Pictorial Approach to Understanding and Avoidance," *Reg. Anesth. Pain Med.*, vol. 35, pp. S81–S92, 2010, supplement 1.
- [22] J. D. Thomas and D. N. Rubin, "Tissue Harmonic Imaging: Why Does it Work," *J. Am. Soc. Echocar.*, vol. 11, pp. 803–8, 1998.
- [23] D. Ortega, P. N. Burns, D. H. Simpson, and S. R. Wilson, "Tissue Harmonic Imaging Is It a Benefit for Bile Duct Sonography," *Am. J. of Roentgenol.*, vol. 176, pp. 653–9, 2001.
- [24] L. E. Hann, A. M. Bach, L. D. Cramer, D. Siegel, H.-Y. Yoo, and R. Garcia, "Hepatic Sonography: Comparison of Tissue Harmonic and Standard Sonography Techniques," *Am. J. of Roentgenol.*, vol. 173, pp. 201–6, 1999.
- [25] J. Y. Kwak, E.-K. Kim, J. K. You, and K. K. Oh, "Variable Breast Conditions Comparison of Conventional and Real-Time Compound Sonography," *J. Ultrasound Med.*, vol. 23, pp. 85–96, 2004.
- [26] R. Kern, K. Szabo, M. Hennerici, and S. Mairs, "Characterization of Carotid Artery Plaques Using Real-Time Compound B-Mode Ultrasound," *Stroke*, vol. 35, pp. 870–5, 2004.
- [27] A. D. Pierce, *Acoustics - An Introduction to Its Physical Principles and Applications*, 3rd ed. Melville, NY: Acoustical Society of America, 1994.

- [28] M. Hamilton and D. T. Blackstock, *Nonlinear Acoustics*. San Diego: Academic Press, 1997.
- [29] M. A. Averkiou, D. N. Roundhill, and J. E. Powers, “A New Imaging Technique Based on the Nonlinear Properties of Tissues,” in *IEEE Ultrason. Symp. Proc.*, 1997, pp. 1561–6.
- [30] A. Bouakaz and N. de Jong, “Native Tissue Imaging at Superharmonic Frequencies,” *IEEE Trans. Ultrason., Ferroelect., Freq. Contr.*, vol. 50, pp. 496–506, 2003.
- [31] M. A. Averkiou, “Tissue Harmonic Imaging,” in *IEEE Ultrason. Symp. Proc.*, 2000, pp. 1563–72.
- [32] M. Kornbluth, D. H. Liang, A. Paloma, and I. Schnittger, “Native Tissue Harmonic Imaging Improves Endocardial Border Definition and Visualization of Cardiac Structures,” *J. Am. Soc. Echocar.*, vol. 11, pp. 693–701, 1998.
- [33] D. N. Rubin, N. Yazbek, M. J. Garcia, W. J. Stewart, and J. D. Thomas, “Qualitative and Quantitative Effects of Harmonic Echocardiography Imaging on Endocardial Edge Definition and Side-Lobe Artifacts,” *J. Am. Soc. Echocar.*, vol. 13, pp. 1012–8, 2000.
- [34] S. P. Turner and M. J. Monaghan, “Tissue Harmonic Imaging for Standard Left Ventricular Measurements: Fundamentally Flawed?” *Eur. J. of Echocar.*, vol. 7, pp. 9–15, 2005.
- [35] T. S. Desser, R. B. Jeffrey, M. J. Lane, and P. W. Ralls, “Tissue Harmonic Imaging: Utility in Abdominal and Pelvic Sonography,” *J. Clin. Ultrasound*, vol. 27, pp. 135–42, 1999.
- [36] S. Tanaka, O. Oshikawa, T. Sasaki, T. Ioka, and H. Tsukuma, “Evaluation of Tissue Harmonic Imaging for the Diagnosis of Focal Liver Lesions,” *Ultrasound Med. & Biol.*, vol. 26, pp. 183–7, 2000.
- [37] S.-Y. Chiou, F. Forsberg, T. B. Fox, and L. Needleman, “Comparing Differential Tissue Harmonic Imaging With Tissue Harmonic and Fundamental Gray Scale Imaging of the Liver,” *J. Ultrasound Med.*, vol. 26, pp. 1557–63, 2007.
- [38] R. S. Shapiro, J. Wagreich, R. B. Parson, A. Stancato Pasik, H.-C. Yeh, and R. Lao, “Tissue Harmonic Imaging Sonography: Evaluation

- of Image Quality Compared with Conventional Sonography,” *Am. J. of Roentgenol.*, vol. 171, pp. 1203–6, 1998.
- [39] S. Choudhry, B. Gorman, J. W. Charboneau, D. J. Tradup, R. J. Beck, J. M. Kofler, and D. S. Groth, “Comparison of Tissue Harmonic Imaging with Conventional US in Abdominal Disease,” *RadioGraphics*, vol. 20, pp. 1127–35, 2000.
- [40] S. J. Rosenthal, P. L. Jones, and L. H. Wetzel, “Phase Inversion Tissue Harmonic Sonographic Imaging: A Clinical Study,” *Am. J. of Roentgenol.*, vol. 176, pp. 1393–8, 2001.
- [41] S. Ö. Oktar, C. Yücel, H. Özdemir, A. Ulutürk, and S. Isik, “Comparison of Conventional Sonography, Real-Time Compound Sonography, Tissue Harmonic Sonography, and Tissue Harmonic Compound Sonography of Abdominal and Pelvic Lesions,” *Am. J. of Roentgenol.*, vol. 181, pp. 1341–7, 2003.
- [42] F. Tranquart, N. Grenier, V. Eder, and L. Pourcelot, “Clinical Use of Ultrasound Tissue Harmonic Imaging,” *Ultrasound Med. & Biol.*, vol. 28, pp. 889–94, 1999.
- [43] T. Schmidt, C. Hoht, P. Haage, M. Blaum, D. Honnef, C. Weiß, G. Staatz, and R. W. Günther, “Diagnostic Accuracy of Phase-Inversion Tissue Harmonic Imaging Versus Fundamental B-Mode Sonography in the Evaluation of Focal Lesions of the Kidney,” *Am. J. of Roentgenol.*, vol. 180, pp. 1639–47, 2003.
- [44] U. Bartram and K. Darge, “Harmonic vs Conventional Ultrasound Imaging of the Urinary Tract of Children,” *Ped. Radiol.*, vol. 35, pp. 655–60, 2005.
- [45] D. Paladini, M. Vassallo, A. Tartaglione, and P. Martinelli, “The Role of Tissue Harmonic Imaging in Fetal Echocardiography,” *Ultrasound Obstet. Gynecol.*, vol. 23, pp. 159–64, 2004.
- [46] E. L. Rosen and M. S. Soo, “Tissue Harmonic Imaging Sonography of Breast Lesions Improved Margin Analysis, Conspicuity, and Image Quality Compared to Conventional Ultrasound,” *J. Clin. Imaging*, vol. 25, pp. 379–84, 2001.
- [47] K. T. Szopinski, A. M. Pajk, M. Wysocki, D. Amy, M. Szopinska, and W. Jakubowski, “Tissue Harmonic Imaging Utility in Breast Sonography,” *J. Ultrasound Med.*, vol. 22, pp. 479–87, 2003.

- [48] K. T. Szopinski, M. Wysocki, A. M. Pajk, R. Z. Slapa, W. Jakubowski, and M. Szopinska, "Tissue Harmonic Imaging of Thyroid Nodules Initial Experience," *J. Ultrasound Med.*, vol. 22, pp. 5–12, 2003.
- [49] J. J. Dahl, G. F. Pinton, M. Lediju, and G. E. Trahey, "Simulation and Experimental Analysis of Ultrasonic Clutter in Fundamental and Harmonic Imaging," in *Proc. of SPIE*, vol. 7265, 726509, 2009, doi:10.1117/12.813782.
- [50] C.-L. Yen, H.-Y. Chang, S.-Y. Huang, Y.-C. Huang, and C.-M. Jeng, "Combination of Tissue Harmonic Sonography, Real-Time Spatial Compound Sonography and Adaptive Image Processing Technique for the Detection of Carotid Plaques and Intima-Medial Thickness," *Eur. J. of Radiol.*, vol. 71, pp. 11–6, 2009.
- [51] J. Bercoff, "ShearWave Elastography White Paper," Internet page: [http://www.supersonicimagine.fr/product\\_0\\_7\\_white-papers,en.htm](http://www.supersonicimagine.fr/product_0_7_white-papers,en.htm), SuperSonic Imagine, Aix en Provence, France, 2008, last visited: 24. February 2011.
- [52] J. Bercoff, M. Tanter, and M. Fink, "Supersonic Shear Imaging: A New Technique for Soft Tissue Elasticity Mapping," *IEEE Trans. Ultrason., Ferroelect., Freq. Contr.*, vol. 51, pp. 396–409, 2004.
- [53] A. P. Sarvazyan, O. V. Rudenko, S. D. Swanson, J. B. Fowlkes, and S. Y. Emilianov, "Shear Wave Elasticity Imaging: A New Ultrasonic Technology of Medical Diagnostics," *Ultrasound Med. & Biol.*, vol. 24, pp. 1420–35, 1998.
- [54] C. Kollmann, "New Sonographic Techniques for Harmonic Imaging – Underlying Physical Principles," *Eur. J. of Radiol.*, vol. 64, pp. 164–72, 2007.
- [55] R. Hansen and B. Angelsen, "SURF Imaging for Contrast Agent Detection," *IEEE Trans. Ultrason., Ferroelect., Freq. Contr.*, vol. 34, pp. 280–90, 2009.
- [56] E. Cherin, J. Brown, S.-E. Måsøy, H. Shariff, R. Karshafian, R. Williams, P. N. Burns, and F. S. Foster, "Radial Modulated Imaging of Microbubbles Contrast Agents at High Frequency," *Ultrasound Med. & Biol.*, vol. 34, pp. 949–62, 2008.

- 
- [57] S.-E. Måsøy, Ø. Standal, P. Näsholm, T. F. Johansen, B. Angelsen, and R. Hansen, “SURF Imaging: In Vivo Demonstration of an Ultrasound Contrast Detection Technique,” *IEEE Trans. Ultrason., Ferroelect., Freq. Contr.*, vol. 55, pp. 1112–21, 2008.
- [58] R. Hansen, S.-E. Måsøy, T. F. Johansen, and B. Angelsen, “Utilizing Dual Frequency Bnad Transmit Pulse Complexes in Medical Ultrasound Imaging,” *J. Acoust. Soc. Am.*, vol. 127, pp. 579–87, 2010.
- [59] P. Näsholm, R. Hansen, S.-E. Måsøy, T. F. Johansen, and B. Angelsen, “Transmit Beams Adapted to Reverberation Noise Suppression Using Dual-Frequency SURF Imaging,” *IEEE Trans. Ultrason., Ferroelect., Freq. Contr.*, vol. 56, pp. 2124–33, 2009.
- [60] G. Taraldsen, “A Generalized Westerwelt Equation for Nonlinear Medical Ultrasound,” *J. Acoust. Soc. Am.*, vol. 109, pp. 1329–33, 2001.
- [61] X. Ming Lu and T. L. Proulx, “Single Crystals vs. PZT Ceramics for Medical Ultrasound Applications,” in *IEEE Ultrason. Symp. Proc.*, 2005, pp. 227–30.
- [62] D. Bæk, J. A. Jensen, and M. Willatzen, “Testing of a One Dimensional Model for Field II Calibration,” in *IEEE Ultrason. Symp. Proc.*, 2008, pp. 1417–20.
- [63] M. E. Frijlink and H. G. Torp, “Simulation of Acoustic Fields From Arbitrary Transducer Stacks Using a FEM Transducer Model and Nonlinear Wave Propagation,” in *IEEE Ultrason. Symp. Proc.*, 2009, pp. 2340–3.
- [64] J. C. Lockwood and J. G. Willette, “High-Speed Method for Computing the Exact Solution for the Pressure Variations in the Nearfield of a Baffled Piston,” *J. Acoust. Soc. Am.*, vol. 53, pp. 735–41, 1973.
- [65] A. Penttinen and M. Luukkala, “The Impulse Response and Pressure Nearfield of a Curved Ultrasonic Radiator,” *J. Phys. D*, vol. 9, pp. 1547–57, 1976.
- [66] J. A. Jensen, “A Model for the Propagation and Scattering of Ultrasound in Tissue,” *J. Acoust. Soc. Am.*, vol. 89, pp. 182–90, 1991.
- [67] J. A. Jensen and N. B. Svendsen, “Calculation of Pressure Fields from Arbitrary Shaped, Apodized and Exited Ultrasound Transducers,” *IEEE Trans. Ultrason., Ferroelect., Freq. Contr.*, vol. 39, pp. 262–7, 1992.

- [68] J. D'hooge, J. Nuyts, B. Bijmens, B. De Man, P. Suetens, J. Thoen, M.-C. Herregods, and F. van de Werf, "The Calculation of the Transient Near and Far Field of a Baffled Piston Using Low Sampling Frequencies," *J. Acoust. Soc. Am.*, vol. 102, pp. 78–86, 1997.
- [69] G. L. Wojcik, D. K. Vaughan, N. Abboud, and J. C. Mould, "Electromechanical Modeling Using Explicit Time-Domain Finite Elements," in *IEEE Ultrason. Symp. Proc.*, 1993, pp. 1107–12.
- [70] G. L. Wojcik, J. C. Mould, F. Lizzi, Jr., N. Abboud, M. Ostromogilsky, and D. K. Vaughan, "Nonlinear Modeling of Therapeutic Ultrasound," in *IEEE Ultrason. Symp. Proc.*, 1995, pp. 1617–22.
- [71] E. Faccioli, F. Maggio, R. Paolucci, and A. Quarteroni, "2D and 3D Elastic Wave Propagation by a Pseudo-Spectral Domain Decomposition Method," *J. Seism.*, vol. 1, pp. 237–51, 1997.
- [72] G. L. Wojcik, B. Fornberg, R. C. Waag, J. C. Mould, L. Nikodym, and T. Driscoll, "Pseudospectral Methods for Large-Scale Bioacoustic Models," in *IEEE Ultrason. Symp. Proc.*, 1997, pp. 1501–6.
- [73] G. L. Wojcik, J. C. Mould, S. Aytex, and L. M. Carcione, "A Study of Second-Harmonic Generation by Focused Medical Transducer Pulses," in *IEEE Ultrason. Symp. Proc.*, 1998, pp. 1583–8.
- [74] D. Komatitsch and J.-P. Vilotte, "The Spectral Element Method: An Efficient Tool to Simulate the Seismic Response of 2D and 3D Geological Structures," *Bull. Seism. Soc. Am.*, vol. 88, pp. 368–92, 1998.
- [75] X. Yuan, D. Brorup, J. Wisken, M. Berggren, and S. A. Johnson, "Simulation of Acoustic Wave Propagation in Dispersive Media with Relaxation Losses by Using FDTD Method with PML Absorbing Boundary Condition," *IEEE Trans. Ultrason., Ferroelect., Freq. Contr.*, vol. 46, pp. 14–23, 1999.
- [76] D. Komatitsch, C. Barnes, and J. Tromp, "Simulation of Anisotropic Wave Propagation Based upon a Spectral Element Method," *Geophysics*, vol. 65, pp. 1251–60, 2000.
- [77] D. Komatitsch and J. Tromp, "Introduction to the Spectral Element Method for Three-Dimensional Seismic Wave Propagation," *Geophys. J. Int.*, vol. 139, pp. 806–22, 1999.

- 
- [78] Q.-H. Liu, “The Pseudospectral Time-Domain (PSTD) Algorithm for Acoustic Waves in Absorptive Media,” *IEEE Trans. Ultrason., Ferroelect., Freq. Contr.*, vol. 45, pp. 1044–55, 1998.
- [79] T. D. Mast, L. P. Souriau, D.-L. D. Liu, M. Tabei, A. I. Nachman, and R. Waag, “A  $k$ -Space Method for Large-Scale Models of Wave Propagation in Tissue,” *IEEE Trans. Ultrason., Ferroelect., Freq. Contr.*, vol. 48, pp. 341–54, 2001.
- [80] M. Tabei, T. D. Mast, and R. Waag, “A  $k$ -Space Method for Coupled First-Order Acoustic Propagation Equations,” *J. Acoust. Soc. Am.*, vol. 111, pp. 53–63, 2002.
- [81] S. Ginter, M. Liebler, T. Dreyer, and R. E. Riedlinger, “Full-Wave Modeling of Therapeutic Ultrasound: Nonlinear Ultrasound Propagation in Ideal Fluids,” *J. Acoust. Soc. Am.*, vol. 111, pp. 2049–59, 2002.
- [82] M. Liebler, S. Ginter, T. Dreyer, and R. E. Riedlinger, “Full-Wave Modeling of Therapeutic Ultrasound: Efficient Time-Domain Implementation of the Frequency Power-Law Attenuation,” *J. Acoust. Soc. Am.*, vol. 116, pp. 2742–50, 2004.
- [83] E. Zampieri and L. F. Pavarino, “Approximation fo Acoustic Waves by Explicit Newmark’s Schemes and Spectral Element Methods,” *J. Comput. Appl. Math.*, vol. 185, pp. 308–25, 2006.
- [84] G. F. Pinton, J. Dahl, S. Rosenzweig, and G. E. Trahey, “A Heterogeneous Nonlinear Attenuating Full-Wave Model of Ultrasound,” *IEEE Trans. Ultrason., Ferroelect., Freq. Contr.*, vol. 56, pp. 474–88, 2009.
- [85] M. D. Verweij and J. Huijssen, “A Filtered Convolution Method for the Computation of Acoustic Wave Field in Very Large Spatiotemporal Domains,” *J. Acoust. Soc. Am.*, vol. 125, pp. 1868–78, 2009.
- [86] J. Huijssen and M. D. Verweij, “An Iterative Method for the Computation of Wide-Angle, Pulsed Acoustic Fields of Medical Diagnostic Transducers,” *J. Acoust. Soc. Am.*, vol. 127, pp. 33–44, 2010.
- [87] T. Hergum, S. Langeland, E. Remme, and H. Torp, “Fast Ultrasound Imaging Simulation in  $k$ -Space,” *IEEE Trans. Ultrason., Ferroelect., Freq. Contr.*, vol. 56, pp. 1159–67, 2009.
- [88] V. P. Kuznetsov, “Equations of Nonlinear Aacoustics,” *Sov. Phys. Acoust.*, vol. 16, pp. 467–70, 1970.

- [89] E. A. Zabolotksaya and R. V. Khokhlov, “Quasi-Plane Waves in the Nonlinear Acoustics of Confined Beams,” *Sov. Phys. Acoust.*, vol. 15, pp. 35–40, 1969.
- [90] Y.-S. Lee and M. F. Hamilton, “Time Domain Modeling of Pulsed Finite-Amplitude Sound Beams,” *J. Acoust. Soc. Am.*, vol. 97, pp. 906–17, 1995.
- [91] R. O. Cleveland, M. F. Hamilton, and D. T. Blackstock, “Time-Domain Modeling of Finite-Amplitude Sound in Relaxing Fluids,” *J. Acoust. Soc. Am.*, vol. 99, pp. 3312–8, 1996.
- [92] M. A. Averkiou and M. F. Hamilton, “Nonlinear Distortion of Short Pulses Radiated by Plane and Focused Circular Pistons,” *J. Acoust. Soc. Am.*, vol. 102, pp. 2539–48, 1997.
- [93] X. Yang and R. O. Cleveland, “Time Domain Simulation of Nonlinear Acoustic Beams Generated by Rectangular Pistons With Application to Harmonic Imaging,” *J. Acoust. Soc. Am.*, vol. 117, pp. 113–23, 2005.
- [94] Y. Jing and R. O. Cleveland, “Modeling the Propagation of Nonlinear Three-Dimensional Acoustic Beams in Inhomogeneous Media,” *J. Acoust. Soc. Am.*, vol. 122, pp. 1352–64, 2007.
- [95] S. I. Aanonsen, T. Barkve, J. N. Tjøtta, and S. Tjøtta, “Distortion and Harmonic Generation in the Nearfield of a Finite Amplitude Sound Beam,” *J. Acoust. Soc. Am.*, vol. 75, pp. 749–68, 1984.
- [96] J. Berntsen, “Numerical Calculations of Finite Amplitude Sound Beams,” in *Frontiers of Nonlinear Acoustics: Proceedings of 12th ISNA*, M. F. Hamilton and D. T. Blackstock, Eds. Elsevier, 1990.
- [97] A. C. Baker, A. M. Berg, A. Sahin, and J. N. Tjøtta, “The Nonlinear Pressure Field of Plane, Rectangular Apertures: Experimental and Theoretical Results,” *J. Acoust. Soc. Am.*, vol. 97, pp. 3510–7, 1995.
- [98] R. S. C. Cobbold, *Foundations of Biomedical Ultrasound*. New York, NY: Oxford University Press, Inc., 2007.
- [99] R. J. Zemp, J. Tavakkoli, and R. S. Cobbold, “Modeling of Nonlinear Ultrasound Propagation in Tissue from Array Transducers,” *J. Acoust. Soc. Am.*, vol. 113, pp. 139–52, 2003.

- 
- [100] T. Varslot and G. Taraldsen, "Computer Simulation of Forward Propagation in Soft Tissue," *IEEE Trans. Ultrason., Ferroelect., Freq. Contr.*, vol. 52, pp. 1473–82, 2005.
- [101] T. Varslot and S.-E. Måsøy, "Forward Propagation of Acoustic Pressure Pulses in 3D Soft Biological Tissue," *Mod. Ident. Cont.*, vol. 27, no. 3, pp. 181–200, 2006.
- [102] M. E. Frijlink, H. Kaupang, T. Varslot, and S.-E. Måsøy, "Abersim: A Simulation Program for 3D Nonlinear Acoustic Wave Propagation for Arbitrary Pulses and Arbitrary Transducer Geometries," in *IEEE Ultrason. Symp. Proc.*, 2008, pp. 1282–5.
- [103] H. Torp, T. F. Johansen, and J. S. Haugen, "Nonlinear Wavepropagation - A Fast Simulation Method Based on Quasi-Linear Approximation of the Second Harmonic Field," in *IEEE Ultrason. Symp. Proc.*, 2005.
- [104] T. Varslot, S. Dursun, T. F. Johansen, R. Hansen, B. A. J. Angelsen, and H. G. Torp, "Influence of Acoustic Intensity on the Second-Harmonic Beam-Profile," in *IEEE Ultrason. Symp. Proc.*, 2003.
- [105] S. Dursun, T. Varslot, T. F. Johansen, B. Angelsen, and H. Torp, "Fast 3D Simulation of 2nd Harmonic Ultrasound Field From Arbitrary Transducer Geometries," in *IEEE Ultrason. Symp. Proc.*, 2005.
- [106] A. I. Nachman, J. F. Smith, III, and R. C. Waag, "An Equation for Acoustic Propagation in Inhomogeneous Media with Relaxation Losses," *J. Acoust. Soc. Am.*, vol. 88, pp. 1584–95, 1990.
- [107] T. L. Szabo, "Time Domain Equations for Lossy Media Obeying a Frequency Power Law," *J. Acoust. Soc. Am.*, vol. 96, pp. 491–500, 1994.
- [108] C. K. W. Tam and L. Auriault, "Time-Domaing Impedance Boundary Conditions for Computational Aeroacoustics," *AIAA J.*, vol. 34, pp. 917–923, 1996.
- [109] H. Ju and K.-Y. Fung, "Time-Domain Impedance Boundary Conditions with Mean Flow," *AIAA J.*, vol. 39, pp. 1683–90, 2001.
- [110] T.-S. Kang and C.-E. Baag, "An Efficient Finite-Difference Method for Simulating 3D Seismic Response of Localized Basin Structures," *Bull. Seism. Soc. Am.*, vol. 95, pp. 1690–705, 2004.

- [111] M. G. Wismer, “Finite Element Analysis of Broadband Acoustic Pulses Through Inhomogeneous Media with Power-Law Attenuation,” *J. Acoust. Soc. Am.*, vol. 120, pp. 3492–502, 2006.
- [112] B. Fornberg, *A Practical Guide to Pseudospectral Methods*, ser. Cambridge Monographs on Applied and Computational Mathematics. Cambridge University Press, 1996.
- [113] Q.-H. Liu, “Generalization of the  $k$ -Space Formulation to Elastodynamic Scattering Problem,” *J. Acoust. Soc. Am.*, vol. 97, pp. 1373–9, 1995.
- [114] E. Hairer, S. P. Nørsett, and G. Wanner, *Solving Ordinary Differential Equations I*, 2nd ed. Berlin, Heidelberg, New York: Springer, 2000.
- [115] E. Hairer and G. Wanner, *Solving Ordinary Differential Equations II*, 2nd ed. Berlin, Heidelberg, New York: Springer, 2002.
- [116] J. C. Mould, G. L. Wojcik, L. M. Carcione, M. Tabei, T. D. Mast, and R. C. Waag, “Validation of FFT-Based Algorithms for Large-Scale Modeling of Wave Propagation in Tissue,” in *IEEE Ultrason. Symp. Proc.*, 1999, pp. 1551–6.
- [117] G. L. Wojcik, T. L. Szabo, J. C. Mould, L. M. Carcione, and F. Clougherty, “Nonlinear Pulse Calculation & Data in Water and a Tissue Mimic,” in *IEEE Ultrason. Symp. Proc.*, 1999, pp. 1521–6.
- [118] J. Hoffelner, H. Landes, M. Kaltenbacher, and R. Lerch, “Finite Element Simulation of Nonlinear Wave Propagation in Thermoviscous Fluids Including Dissipation,” *IEEE Trans. Ultrason., Ferroelect., Freq. Contr.*, vol. 48, pp. 779–86, 2001.
- [119] G. F. Pinton, J.-F. Aubry, M. Fink, and M. Tanter, “Effects of Nonlinear Ultrasound Propagation on High Intensity Brain Therapy,” *Med. Phys.*, vol. 38, 2011.
- [120] J. N. Tjøtta and S. Tjøtta, “An Analytical Model for the Nearfield of a Baffled Piston Transducer,” *J. Acoust. Soc. Am.*, vol. 68, pp. 334–9, 1980.
- [121] G. F. Pinton and G. E. Trahey, “A Comparison of Time-Domain Solutions for the Full-Wave Equation and the Parabolic Wave Equation for a Diagnostic Ultrasound Transducer,” *IEEE Trans. Ultrason., Ferroelect., Freq. Contr.*, vol. 55, pp. 730–3, 2008.

- 
- [122] M. A. Averkiou and R. O. Cleveland, "Modeling of an Electrohydraulic Lithotripter With the KZK Equation," *J. Acoust. Soc. Am.*, vol. 106, pp. 102–12, 1999.
- [123] H. Kaupang, T. Varslot, and S.-E. Måsøy, "Second-Harmonic Aberration Correction," in *IEEE Ultrason. Symp. Proc.*, 2007, pp. 1537–40.
- [124] Y. Li and J. A. Zagzebski, "Computer Model for Harmonic Ultrasound Imaging," *IEEE Trans. Ultrason., Ferroelect., Freq. Contr.*, vol. 47, pp. 1259–72, 2000.
- [125] M. E. Frijlink, D. E. Goertz, A. Boakaz, and A. F. W. van der Steen, "A Simulation on Tissue Harmonic Imaging With a Single-Element Intravascular Ultrasound Catheter," *J. Acoust. Soc. Am.*, vol. 120, pp. 1723–31, 2006.
- [126] H. Kaupang, K. Helset, O. M. Rygh, S.-E. Måsøy, V. Källskog, C. Nolsøe, H. M. Holden, and R. Hansen, "Contrast Enhanced Ultrasound Sonography of Thyroid Nodules," Symposium of the Norwegian Society of Ultrasound Diagnostics, 2007, Original title: Ultralydkontrastavbildning av knuter i skjoldbruskjertelen.
- [127] E. A. Martinsen, "Detection and Imaging of Micro-Bubbles Using High Frequencies," Master's Thesis, Norwegian University of Science and Technology, 2007, original title: "Deteksjon og avbildning av kontrastbobler ved høye frekvenser.

---

## List of Publications

What follows is a list of scientific publications where I have made significant contributions during my time as a Ph.D. candidate.

### Submitted for Peer Review

**Halvard Høiland-Kaupang**, Martijn E. Frijlink, Svein-Erik Måsøy and Bjørn Angelsen, “A Comparative Simulation Study on the Radiated Field from Ultrasound Transducers,” *Revision submitted to IEEE Transactions on Ultrasonics, Ferroelectrics and Frequency Control* (2011).

**Halvard Høiland-Kaupang**, Jochen Deibele, Thor A. Tangen and Bjørn Angelsen, “Analysis of Reverberations in Medical Ultrasound,” *Submitted to Journal of the Acoustical Society of America* (2011).

Tarjei Rommetveit, Tonni F. Johansen, Jochen Deibele, **Halvard Høiland-Kaupang** and Bjørn Angelsen, “Two-Way Nonlinear Manipulation in Plane Materials using Dual Frequency Band Pulse Complexes,” *Submitted to Journal of the Acoustical Society of America* (2011).

**Halvard Høiland-Kaupang**, and Bjørn Angelsen, “A Time-Domain Spectral Element Method for Propagation of Pulses in Nonlinear Soft Tissue,” *Submitted to Journal of the Acoustical Society of America* (2011).

**Halvard Høiland-Kaupang**, and Svein-Erik Måsøy, “Transmit Beamforming for Optimal Second-Harmonic Generation,” *Accepted for publication in IEEE Transactions on Ultrasonics, Ferroelectrics and Frequency Control* (2010).

### Conference Proceedings

Tarjei Rommetveit, Tonni F. Johansen, Jochen Deibele, **Halvard Kaupang** and Bjørn Angelsen, “Two-Way Nonlinear Manipulation in Plane Materials Using Dual Frequency Pulse Complexes”, in *IEEE Ultrasonic Symposium Proceedings* (2010).

Martijn E. Frijlink, **Halvard Kaupang**, Trond Varslot and Svein-Erik Måsøy, “Abersim: A Simulation Program for 3D Nonlinear Acoustic Wave Propagation for Arbitrary Pulses and Arbitrary Transducer Geometries,” in *IEEE Ultrasonic Symposium Proceedings*, 1282–5 (2008).

---

**Halvard Kaupang**, Trond Varslot and Svein-Erik Måsøy, “Second-Harmonic Aberration Correction,” in *IEEE Ultrasonic Symposium Proceedings*, 1537–40 (2007).

**Halvard Kaupang**, Svein-Erik Måsøy, Trond Varslot, Tonni F. Johansen and Bjørn Angelsen, “Generation and Aberration of Second-Harmonic Ultrasound Beams in Heterogeneous Tissue,” in *IEEE Ultrasonic Symposium Proceedings*, 2160–3 (2006).

## Abstracts and Presentations

Svein-Erik Måsøy, Rune Hansen, Anders Angelsen, **Halvard Kaupang**, Thor Andreas Tangen, Øyvind Standal, Peter Näsholm, Tonni F. Johansen and Angelsen, Bjørn Angelsen, Anders Angelsen, Torbjørn Dahl, Petter Østhus and Kristin Helset, “SURF Imaging – Clinical Examples”, original Norwegian title: “SURF Imaging – Kliniske eksempler,” *Symposium of the Norwegian Society of Ultrasound Diagnostics (NFUD)* (2010).

**Halvard Kaupang** and Bjørn Angelsen, “A Time Domain Spectral Element Method for Propagation of Pulses in Nonlinear Materials,” *IEEE Ultrasonic Symposium* (2009).

Peter Näsholm, **Halvard Kaupang**, Svein-Erik Måsøy, Rune Hansen and Bjørn Angelsen, “A Simulation Study of SURF Reverberation Suppression in an Aberrating Medium,” *Symposium of the Norwegian Society of Ultrasound Diagnostics (NFUD)* (2008).

Svein-Erik Måsøy, **Halvard Kaupang**, Thor Andreas Tangen, Øyvind Standal, Peter Näsholm, Tonni F. Johansen, Rune Hansen and Bjørn Angelsen, “SURF Imaging – In vivo Demonstration of an Ultrasound Contrast Detection Technique in Patients with Prostate Cancer and Thyroid Nodules,” *IEEE Ultrasonic Symposium* (2007).

**Halvard Kaupang**, Kristin Helset, Ola M. Rygh, Svein-Erik Måsøy, Vendela Källskog, Christian Nolsøe, Hans Martin Holden and Rune Hansen, “Contrast Enhanced Ultrasound Sonography of Thyroid Nodules,” original Norwegian title: “Ultraløydkontrastavbildning i skjoldbruskkjertelen,” *Symposium of the Norwegian Society of Ultrasound Diagnostics (NFUD)* (2007).

Peter Näsholm, **Halvard Kaupang**, Svein-Erik Måsøy and Bjørn Angelsen, “Simulation of Ultrasound Wave Propagation in Soft Tissue,” original

---

Norwegian title: “Simulering av ultralydforplantning i bløtvev,” *Symposium of the Norwegian Society of Ultrasound Diagnostics (NFUD)* (2007).

# A Comparative Simulation Study on the Radiated Field from Ultrasound Transducers

Halvard Høiland-Kaupang, Martijn E. Frijlink, Svein-Erik Måsøy and  
Bjørn Angelsen

Department of Circulation and Medical Imaging, NTNU, Trondheim, Norway

## Abstract

A comparative simulation study is performed to benchmark three freely available ultrasound simulation programs: Field II, the Texas code and Abersim. The two latter handle both linear and nonlinear propagation. A Generalized Angular Spectrum Method for calculating the radiated field in circular-symmetric geometries is proposed and implemented in Abersim. Five transducer test cases are investigated; three circular-symmetric piston transducers, one plane wave attenuation comparison and one cardiac array transducer. Each program's ability to solve diffraction, attenuation or nonlinear effects is compared. The comparisons suggest that the Angular Spectrum Method performs better than Field II for equal spatial and temporal sampling when solving near field diffraction. The frequency domain implementation of the attenuation model in Abersim is shown to be superior to the models implemented in Field II and the Texas code. In the nonlinear comparison, the Texas code and Abersim produce equivalent results when resolution and sampling frequencies are equal. In highly nonlinear media, both tools show the same behavior when acoustic shock formation takes place, and both indicate the need of very high sampling frequencies if acoustic shock phenomena are to be investigated. For the array transducer, Abersim is shown to accurately reproduce the Field II solution from plane transducer surfaces. For curved surfaces, some discrepancies are found.

## A.1 Introduction

Acoustic field simulations are used to investigate radiation patterns from arbitrary transducer geometries. These investigations can be useful for deeper understanding of acoustical phenomena and for the design of ultrasound transducers. The effect on the generated field of different excitation pulses, array geometries, system electronics, choice of piezoelectric material, etc., can be simulated using different simulation tools or combinations of them.<sup>1-4</sup> For diagnostic applications which include higher harmonics, it is necessary to include accurate nonlinear field simulations. Combinations of a simulation program for nonlinear forward propagation with a linear back scattering algorithm, can provide insight in specific harmonic imaging applications.<sup>5,6</sup> The simulation program Field II<sup>7</sup> is based on summation of impulse responses from small surfaces to calculate linear pressure fields from arbitrary shaped transducers in materials with linear frequency dependent attenuation.

Nonlinear forward wave propagation can be modeled using the KZK equation.<sup>8,9</sup> The KZK equation is a parabolic approximation to the one-way wave equation in retarded time coordinates. The parabolic approximation neglects diffraction effects in the depth direction, *i.e.*,  $\partial^2 p / \partial z^2 \approx 0$ . This approximation makes the KZK equation inaccurate for highly focused transmit beams.<sup>10</sup> The KZK equation accounts for nonlinear and thermoviscous absorption effects.<sup>8,9</sup> Two well-known tools tailored for the KZK equation are the Bergen code<sup>11</sup> and the Texas code.<sup>12-14</sup> The Bergen code solves the KZK equation through a frequency domain implementation while the Texas code is a time domain implementation. These tools are shown to perform very well when compared with measurements and/or analytical solutions.<sup>11-13</sup>

The computer package Abersim is a software package developed at the Norwegian University of Science and Technology and is designed to solve nonlinear forward wave propagation.<sup>15-17</sup> Contrary to KZK based tools like the Bergen and Texas codes, Abersim avoids the parabolic approximation when simulating three-dimensional (3D) propagation. Abersim solves the one-way wave equation for (forward) propagating waves in retarded time coordinates using an operator splitting approach and the Angular Spectrum Method (ASM). Optionally, for circular-symmetric cases, Abersim uses the parabolic approximation and solves the diffraction using a Finite-Difference Time-Domain solution. The attenuation term is solved in the frequency domain and is shown to handle arbitrary power-law attenuation. Abersim has previously been validated through comparisons with an analytic solution to the viscous Burgers' equation for nonlinear plane wave propagation in materials with thermoviscous absorption, and experimental measurements of the nonlinear wave field from an annular array probe

in water,<sup>15</sup> and a linear array transducer.<sup>16</sup>

In this paper, forward propagating fields from simulation programs Field II, the Texas code and Abersim are compared. The aforementioned programs are used to simulate radiated fields from transducers and all are available free of charge (see Refs. 18–20 for Internet pages). The validity of the KZK equation in the near field is discussed. A Generalized Angular Spectrum Method is proposed for circular-symmetric problems to improve near field performance and reduce computational complexity. The method is compared with the already existing methods used in the different programs.

## A.2 Background Theory

One model for wave propagation in nonlinear materials is the Westervelt equation<sup>21</sup>

$$\nabla^2 p - \frac{1}{c^2} \frac{\partial^2 p}{\partial t^2} - \frac{1}{c^2} h *_t \frac{\partial^2 p}{\partial t^2} = -\frac{\beta_n \kappa}{c^2} \frac{\partial^2 p^2}{\partial t^2}, \quad (\text{A.1})$$

where  $p$  is the pressure,  $c$  the speed of sound in the medium, and  $h$  the kernel of a convolution operator accounting for attenuation.

Introducing retarded time coordinates  $\tau = t - z/c$ , Eq. (A.1) transforms to<sup>15,16</sup>

$$\frac{\partial p}{\partial z} = \underbrace{\frac{c}{2} \int_{-\infty}^{\tau} \nabla_{\perp}^2 p + \frac{\partial^2 p}{\partial z^2} d\tau'}_{\text{Diffraction}} - \underbrace{\frac{1}{2c} h *_\tau \frac{\partial p}{\partial \tau}}_{\text{Attenuation}} + \underbrace{\frac{\beta_n \kappa}{2c} \frac{\partial p^2}{\partial \tau}}_{\text{Non-linearity}}. \quad (\text{A.2})$$

Approximating  $\frac{\partial^2 p}{\partial z^2} \approx 0$  and employing pure thermoviscous absorption yields the KZK equation.<sup>8,9,15,16</sup> In Abersim, the above equation is solved using operator splitting where each term on the right hand side can be solved separately.<sup>15,16</sup> How to solve attenuation and non-linearity is considered to be known, and relevant methods for this paper are presented in Refs. 7,12–16.

The diffraction operator is separated into two parts,  $\frac{\partial^2}{\partial z^2}$  and  $\nabla_{\perp}^2$  accounting for differentiation in  $z$  and transverse space (the plane perpendicular to  $z$ ) respectively. In Cartesian coordinates,  $\nabla_{\perp}^2 = \frac{\partial^2}{\partial x^2} + \frac{\partial^2}{\partial y^2}$ , and for cylindrical coordinates  $\nabla_{\perp}^2 = \frac{\partial^2}{\partial r^2} + \frac{1}{r} \frac{\partial}{\partial r} + \frac{1}{r^2} \frac{\partial^2}{\partial \theta^2}$ . If attenuation and non-linearity in Eq. (A.2) are neglected, the equation reduces to the linear wave equation in a homogeneous, non-absorbing medium in retarded time coordinates.

## Classical Angular Spectrum Method

Applying the Fourier transform in time, the diffraction term in Eq. (A.2) becomes

$$\frac{\partial \hat{p}}{\partial z} = \frac{c}{2i\omega} \left( \frac{\partial^2 \hat{p}}{\partial z^2} + \nabla_{\perp}^2 \hat{p} \right) \quad (\text{A.3})$$

where  $\hat{p}$  denotes the temporal Fourier transform of the pressure.

In 3D Cartesian space, Eq. (A.3) can be discretized in space with the Fourier transform as<sup>15,16</sup>

$$\frac{\partial^2 P}{\partial z^2} + 2ik_t \frac{\partial P}{\partial z} - (k_x^2 + k_y^2)P = 0 \quad (\text{A.4})$$

where  $k_t = \omega/c$  and  $P$  is the spatial Fourier transform of  $\hat{p}$  over  $x$  and  $y$ . Equation (A.4) is the basis for the classical Angular Spectrum Method (ASM) presented by Zemp *et al.*<sup>22</sup> expressed in retarded time coordinates. A solution of this equation is referred to as the ‘‘pseudo-differential model’’.<sup>15,16</sup>

## Generalized Angular Spectrum Method

The classical ASM is, however, limited to Cartesian coordinate systems. Circular-symmetric problems are often defined in cylinder coordinates to reduce the number of dimensions of the problem. With the angular dependency removed, circular symmetry implies a Neumann-type boundary condition where  $\frac{\partial p}{\partial r} = 0$  at  $r=0$ . Another representation of  $\nabla_{\perp}^2$  is through a matrix discretization operator,  $A$ , such that  $A\hat{p} \approx \nabla_{\perp}^2 \hat{p}$ , where  $A$  is constructed from a finite difference scheme. Assuming  $p=0$  at the outer boundary ( $r=r_{\max}$ ), the matrix operator  $A$  is invertible.<sup>23,24</sup> Then,  $A$  can be diagonalized as

$$A = Q\Lambda Q^{-1}$$

where  $Q$  is the diagonalizing matrix, and  $\Lambda$  a diagonal matrix containing the eigenvalues of  $A$ . Another representation of Eq. (A.3) is then found as

$$\frac{\partial^2 \hat{p}}{\partial z^2} + 2ik_t \frac{\partial \hat{p}}{\partial z} + Q\Lambda Q^{-1} \hat{p} = 0$$

where  $k_t = \omega/c$  as before.

The Laplacian is an elliptic differential operator and a matrix discretization of the Laplacian will be negative definite with only negative eigenvalues.<sup>23,24</sup> The Fourier discretization presented in Eq. (A.4) also obeys this, with its eigenvalues being the spatial wave numbers  $-(k_x^2 + k_y^2)$ .

Using the relation  $QQ^{-1}=I$ , where  $I$  is the identity matrix, and the transform pair  $\hat{p}=Q\rho \Leftrightarrow \rho=Q^{-1}\hat{p}$ , the above expression can be written as

$$Q \left( \frac{\partial^2 \rho}{\partial z^2} + 2ik_t \frac{\partial \rho}{\partial z} - |\lambda| \rho \right) = 0. \quad (\text{A.5})$$

Because  $Q$  is constant, the equation within the parentheses is equivalent to Eq. (A.4), and is fully de-coupled in both time and transverse space. This equation may be solved for  $\rho$ , and  $\hat{p}$  is retrieved from  $\hat{p}=Q\rho$ .

Defining a general spatial wave number,  $k_\xi$ , as either  $(k_x^2+k_y^2)$  or  $|\lambda|$  for the Fourier and general matrix discretization respectively, Eqs. (A.4) and (A.5) are second-order *ordinary* differential equations in  $z$ . This type of equation has two solutions, but to investigate directive sound beams, only one is needed.<sup>15,16,25</sup> Disregarding one component, the other represent the linear field at depth  $z$  and is

$$P(z) = e^{i\kappa(z-z_0)} P(z_0) \quad (\text{A.6})$$

where  $\kappa$  is a wave number operator defined as previously presented<sup>15,16</sup>

$$\kappa = \begin{cases} \sqrt{k_t^2 - k_\xi^2} - k_t & k_t^2 \geq k_\xi^2 \\ -i\sqrt{k_\xi^2 - k_t^2} - k_t & k_t^2 < k_\xi^2. \end{cases}$$

Note that Eq. (A.5) is more general than Eq. (A.4) because the Fast Fourier Transform utilized in Eq. (A.4) is merely an efficient implementation of the Discrete Fourier Transform where the matrix  $Q$  in Eq. (A.5) is the Fourier matrix.<sup>26</sup> Any spatial discretization resulting in an invertible diagonalizable matrix operator  $A$  can be used within this framework. An example of such a discretization is a finite element discretization where the mesh is adapted to an arbitrary radiation surface with spatially variable accuracy in terms of element size. The practical use of such discretizations is limited due to the fact that the diagonalization requires the eigenvalues of a rather large system of equations to be found, and the dimension of the full matrix  $Q$  will grow rapidly in three dimensions. In the Cartesian case with  $N=N_x=N_y$ , the diagonalization requires  $\mathcal{O}(N^4)$  operations with a general matrix  $Q$ , and  $\mathcal{O}(N^2 \log 2N)$  with the Fast Fourier Transform. A finite element scheme with adaptive radial accuracy is possible for circular-symmetric problems.

## A.3 Methods

Three computer programs; Field<sup>7</sup>, the Texas code<sup>12-14</sup> and Abersim,<sup>15-17</sup> are compared for five test cases in solving diffraction, attenuation or nonlinear

effects, or combinations of these. A gold standard is established for each case, and the appropriate simulation results are compared with this. The parameters used for each case are presented in Table A.1. Unless specified otherwise, the speed of sound, density and transmit pressure amplitude is  $1540 \text{ m s}^{-1}$ ,  $1050 \text{ kg m}^{-3}$  and  $1 \text{ MPa}$  respectively.

**Table A.1:** Transducer and material parameters for the five cases. The abbreviations “PLW” and “TV” denote plane wave simulation and thermoviscous absorption respectively.

Case	1	2	3	4	5
Shape	Circ.	Circ.	PLW	Circ.	Rect.
Center freq., MHz	2	2	2	2	2
Bandwidth, %	3.3	50	100	50	50
Sampl. freq., MHz	60	40	Var.	100	40
Focal depth, mm	$\infty$	60	—	60	60
Aperture, mm	18.6	18.6	—	18.6	$18.6 \times 13$
# of elements	1	1	—	1	$64 \times 1$
f-number	$\infty$	3.22	—	3.22	$3.22 \times 4.62$
Non-linearity, $\beta_n$	—	—	—	3.48	—
Attenuation	—	—	Var.	TV	Linear

Soft tissue obeys power-law attenuation models of the form  $\alpha(f)=af^b$ , where  $b \in [1, 2]$ .<sup>27</sup> In the presence of only thermoviscous absorption;  $b=2$ . A common approximation for soft tissue is a linear frequency dependence with  $b=1$ , and this assumption is used in Field.<sup>7</sup> The Texas code time-domain implementation cannot handle general power-law attenuation directly, but an approximation can be obtained within a certain frequency range using a finite number of relaxation processes.<sup>14</sup> In this paper, only the thermoviscous absorption of the Texas code is used. Abersim solves the attenuation term in the frequency domain, and handles general power-law attenuation.<sup>15,16</sup>

Nonlinear elasticity is incorporated in both the Texas code and Abersim.<sup>12,15,16</sup> Both use operator splitting to solve the model equation. The Texas code uses a fixed step size and first-order Gudonov splitting scheme for each operator.<sup>12</sup> Abersim uses a second-order Strang splitting for the nonlinear distortion and attenuation where an adaptive step size control is employed to avoid shock formation.<sup>15,16</sup> Field II handles only linearly elastic media.<sup>7</sup>

Field II defines the problem in 3D Cartesian space. Abersim can solve the radiated field from circular apertures in three different ways; through the one-way wave equation in retarded time and Cartesian coordinates with the Clas-

sical Angular Spectrum Method (CASM), or using cylindrical coordinates and either the Generalized Angular Spectrum Method (GASM) or a time-domain solution of the KZK equation (KZKA). The Texas code solves the KZK equation and is only used for circular-symmetric field computations.

The initial field for Abersim corresponds to a field radiated from a transducer embedded in a pressure release baffle because the pressure is assumed to be zero outside the active transducer surface.<sup>25,27</sup> This transducer model is also chosen for the Field II simulations. The Texas code is specified to use a source from a rigid baffle.<sup>12</sup>

The error,  $\varepsilon$ , is measured in the  $L^2$ -norm using

$$\varepsilon = \frac{\|x_{\text{ref}} - x\|_2}{\|x_{\text{ref}}\|_2} \quad (\text{A.7})$$

where  $x_{\text{ref}}$  is the appropriate gold standard and  $x$  the solution to be tested.

**Table A.2:** The acronyms used for the different solutions with their corresponding program and underlying acoustic model. The baffle condition is denoted “r.b.” and “p.r.” for the rigid and pressure release baffle respectively. The bottom section indicate the resolution, normal (N) or high (H), used to calculate the solution in each case.

Acronym:	Field II	CASM	GASM	KZKA	Texas
Program	Field II	Abersim	Abersim	Abersim	Texas code
Wave mod.	Full	One-way	One-way	KZK	KZK
Baffle	r.b./p.r.	p.r.	p.r.	p.r.	r.b.
Case 1	N/H	N	N	N	—
Case 2	N/H	N	N	N	—
Case 3	H	N	—	—	H
Case 4	—	N	N	N	N/H
Case 5	H	N	—	—	—

### Case 1 — Plane Piston Transducer

A plane transducer as specified in Table A.1 is simulated to compare near field performance in Field II and Abersim. The gold standards are the analytic expressions for continuous wave (CW) on-axis fields from rigid and pressure

release baffles as defined in Eq. (3.23) in Ref. 25

$$|p_{\text{rb}}(r=0, z)|^2 = 2p_0^2 [1 - \cos(k(r_e - z))] \quad (\text{A.8})$$

$$|p_{\text{pr}}(r=0, z)|^2 = p_0^2 \left[ 1 + \frac{z}{r_e} [1 - 2\cos(k(r_e - z))] \right] \quad (\text{A.9})$$

where  $p_{\text{rb}}$  and  $p_{\text{pr}}$  are the pressure fields from a transducer embedded in a rigid and a pressure release baffle respectively,  $r_e = \sqrt{z^2 + a^2}$ ,  $p_0 = \rho_0 c_0 v_0$ , and  $v_0$  is the normal vibration velocity on the transducer surface. The Fourier coefficients of the initial pulse and Eqs. (A.8)–(A.9) are combined to an analytic solution in the pulsed wave case.

The low bandwidth (3.3%) is chosen to benchmark the ability to correctly reproduce the on-axis interference pattern in the near field. The radiated field is simulated up to a distance of 52.9 mm which corresponds to an inclination angle of  $\sim 10^\circ$  with respect to the  $z$ -axis. The rays propagating from the edge of the transducer to the  $z$ -axis will because of this for the most be outside the validity of the KZK equation.<sup>10</sup> The Field II and Abersim CASM and GASM solutions are based on the one-way wave equation and are not limited by this. The solution is found for 100 equidistant points over the interval  $[0, 52.9]$  mm, resulting in a step size  $\Delta z = 0.53$  mm.

The Field II and Abersim CASM solutions require the circular aperture to be represented in Cartesian coordinates. A perfect circular shape cannot be obtained, and an approximation to this is made in Field II using 31 428 mathematical elements. This corresponds to 200 elements across the transducer along the  $x$  or  $y$  axis, and an element size of  $\Delta x = 93 \mu\text{m}$ . The high-resolution Field II simulation use 800 elements across the diameter (8 042 516 elements in total and  $\Delta x = 23.3 \mu\text{m}$ ) and sampling frequency 240 MHz. Field II has the option of choosing baffle condition, and both a rigid and pressure release condition is simulated.

In Abersim, the points for the CASM solution are chosen such that the center point corresponds to the origin, and the aperture measures 201 points across ( $\Delta x = 92.4 \mu\text{m}$ ). In the GASM and KZKA solutions, the transducer is defined with the same resolution and 101 radial points distributed over one half aperture.

The Field II and Abersim CASM, GASM and KZKA solutions are compared with the analytic solution [Eq. (A.9)] for a pressure release baffle and on-axis  $L^2$ -errors are estimated using Eq. (A.7). A comparison of the rigid baffle solution in Field II and the analytic solution from Eq. (A.8) is also made.

### Case 2 — Focused Piston Transducer

Case 2 is very similar to Case 1, but now; the circular piston is focused. Transducer and material parameters are given in Table A.1. A similar analytic on-axis solution is found for a transducer embedded in a rigid baffle. From Eqs. (5.229) and (5.236) in Ref. 27, the frequency response of a focused circular piston is

$$p_{\text{foc}}(r=0, z, \omega) = p_0 F \frac{e^{-i\omega z} - e^{-i\omega r_a}}{F - z} \quad (\text{A.10})$$

where  $r_a = \sqrt{z^2 + 2 \left( F - \sqrt{F^2 - a^2} \right) (F - z)}$ .

A high-resolution Field II solution equivalent to the one described for Case 1 with 800 elements across the transducer and a sampling frequency of 160 MHz is compared with Eq. (A.10) for radiation from a rigid baffle. The high-resolution pressure release baffle Field II solution is assumed to be of the same order of accuracy as in Case 1, and is used as gold standard in the comparison with the normal resolution Field II solution and the Abersim CASM, GASM and KZKA solutions. The  $L^2$ -errors for the depth interval  $[0, 80]$  mm and the radial interval  $r \in [0, 10]$  mm are found with Eq. (A.7).

The excitation pulse is a typical cardiac 2 MHz pulse with 50% fractional bandwidth. Spatial dimensions and resolutions are the same as for Case 1 in the transverse directions. In depth, the field is simulated up to 96 mm and exported at 80 equidistant points ( $\Delta z = 1.2$  mm).

### Case 3 — Attenuation

A plane wave setup is chosen to benchmark the attenuation model in each tool. Both Abersim and the Texas code enable the use of plane wave setups through switching off diffraction effects. The attenuation is estimated from the frequency spectrum of the pulse at the transducer and at 10 mm depth.

Field II requires the transducer to have finite physical dimensions, and is considered to be most accurate in the far field.<sup>7</sup> A plane (spherical) wave is constructed in Field II using a small piston transducer with 50 points across an  $50 \mu\text{m}$  aperture. The attenuation is estimated from the solutions from two depths in the far field (100 and 110 mm).

The initial pulse is a 2 MHz sinusoidal vibration with a Gaussian envelope and 100% bandwidth. In the verification of the Field II attenuation model, the attenuation of the material is  $0.5 \text{ dB cm}^{-1} \text{ MHz}^{-1}$  with  $f^1$ . The sampling frequency is 160 MHz in the Field II simulation and 40 MHz in the Abersim simulation.

In the verification of the thermoviscous absorption in the Texas code, water at 20°C is used with  $c_0=1482\text{ m s}^{-1}$  and  $\rho_0=998\text{ kg m}^{-3}$ . The absorption in water at this temperature is  $25\cdot 10^{-3}\text{ Np m}^{-1}$  ( $2.2\cdot 10^{-3}\text{ db cm}^{-1}$ ) at 1 MHz and with frequency dependence  $f^2$ . The sampling frequencies are 400 MHz and 100 MHz in the Texas code and Abersim simulations respectively.

From the simulated results, the frequency dependent attenuation is estimated within the frequency range 0.1–4 MHz (−24 dB bandwidth), and compared with the analytic power-law attenuation  $\alpha f^\beta$ .

### **Case 4 — Nonlinear Propagation**

The radiated field from a focused circular piston transducer identical to the one in Case 2 (see Table A.1) is simulated in water using Abersim and the Texas code to compare both diffraction, nonlinear and thermoviscous absorption effects. A high-resolution Texas code solution is used as the gold standard. The resolution of this simulation uses 401 points over one half aperture ( $\Delta x=23.1\ \mu\text{m}$ ), and a sampling frequency of 400 MHz. To verify the diffraction behaviour of this solution, a simulation in water without non-linearity and absorption is compared with the analytic solution in Eq. (A.10).

The material parameters are the same as specified for water in Case 3. The excitation pulse is a 2 MHz sinusoidal vibration with a Gaussian envelope and 50 % bandwidth, and the transmit amplitude is reduced to 0.5 MPa. The simulation use 101 points over one half aperture and a sampling frequency of 100 MHz.

The nonlinear comparison is performed for the first three harmonic on-axis and focal profiles. To obtain the harmonic components, the simulated field is temporally filtered around each harmonic component with a band-pass filter with 1.5 MHz bandwidth. To avoid noise arising from the non-periodic boundaries of the Texas code, a temporal Tukey window with  $R=0.1$  is applied before filtering to taper each endpoint to zero.

The Abersim CASM, GASM, KZKA and a normal resolution Texas code solutions are compared with the gold standard in the full, nonlinear simulation.

### **Case 5 — Array Transducer**

The radiated linear field from a cardiac array transducer as specified in Table A.1 is simulated. The attenuation of the material is  $0.5\text{ dB cm}^{-1}\text{ MHz}^{-1}$ . Each transducer element is subdivided into  $3\times 134$  mathematical elements resulting in a spatial resolution in the azimuth and elevation directions of  $\Delta x=96.9\ \mu\text{m}$  and  $\Delta y=96.3\ \mu\text{m}$  respectively. No kerf between elements is used.

In the high-resolution Field II simulation, the spatial resolutions are refined with a factor four and the sampling frequency is 160 MHz.

In the azimuth direction, electronic element delay focusing is used. In the elevation direction, there are three ways of specifying focusing of an array in Field II; as a concave element (denoted focused array), through assigning focus delays to each mathematical element in the elevation direction (denoted linear array), or through specification of a full 2D matrix array (denoted matrix array) with electronic elevation focusing. The desired model is chosen by calling either `xdc_foc_array`, `xdc_lin_array` or `xdc_2d_array` respectively. All three possibilities are investigated. The two latter corresponds to the focusing used in Abersim where the transducer surface is assumed to be plane in the elevation direction.

## A.4 Results

Results pertaining to the five cases are presented in this section. RMS denotes the root mean square intensity of a signal.

### Case 1 — Plane Piston Transducer

The on-axis RMS and maximum pressure envelope profiles for Case 1 are presented in Fig. A.1. The Field II, Abersim CASM and GASM solutions show the same behavior as the frequency response solution obtained with Eq. (A.9). The peaks of the interference pattern match well, but there are small amplitude differences ( $<1.5$  dB) in the peaks closest to the transducer. The dips are lower for the simulated results than for the analytic. The KZKA solution has the interference lobes shifted outwards; a shift that decreases as the depth increases. This agrees with the limited ability of the KZK equation to accurately solve waves propagating with a steep inclination angle with respect to the  $z$ -axis.

Table A.3 presents the  $L^2$ -errors of the Case 1 and 2 simulations, and show that the high-resolution Field II simulation provides an error slightly lower, but of the same magnitude, as the normal resolution. A check on the performance of Field II and radiation from a transducer embedded in a rigid baffle is provided in the table, and the error is lower for a rigid than for a pressure release baffle.

### Case 2 — Focused Piston Transducer

Figure A.2 presents the RMS and maximum pressure envelope on-axis and focal plane beam profiles for the focused piston transducer in Case 2. The on-axis interference pattern is not as pronounced as in Case 1 due to the shorter

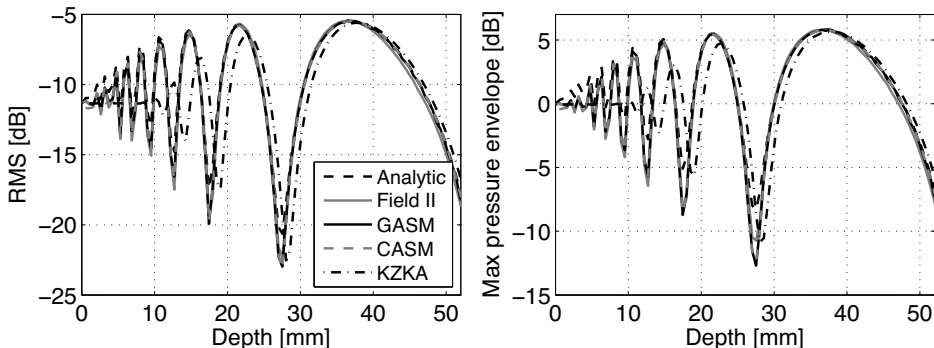


**Figure A.1:** On-axis RMS (left) and maximum pressure envelope (right) beam profiles as a function of depth for the plane piston transducer in Case 1. The line styles apply to both panels.

**Table A.3:**  $L^2$ -errors for the Case 1 and 2 simulations when compared to the appropriate gold standard. The abbreviations “ax” and “foc” denote on-axis and focal field errors respectively, and “HR” and “RB” denote the high-resolution and rigid baffle solutions in Field II. All numbers are to the order of  $10^{-3}$ .

	Case 1 ax.		Case 2 ax.		Case 2 foc.	
	RMS	MAX	RMS	MAX	RMS	MAX
Field II	60	78	10	15	9	16
Field II HR	56	74	—	—	—	—
Field II RB HR	28	63	28	25	—	—
CASM	41	62	16	19	11	12
GASM	40	62	35	38	13	13
KZKA	232	220	77	62	23	17

excitation pulse. All solutions catch the last interference lobe before the on-axis main lobe, and show good agreement beyond 20 mm. Up to 20 mm, some discrepancies are visible in the RMS profiles when compared to the analytic solution from Eq. (A.10). This effect is seen for the Field II, CASM and GASM solutions up to 20 mm. The KZKA solution is even lower. In the absolute pressure value the differences are visually smaller for all solutions.

The focal plane beam profiles of the Case 2 transducer in Fig. A.2 show that the different solutions overlap very well. Both the level and the radial location of the first side-lobe is visible for all solutions. The RMS value of the KZKA solution is lower towards the out-skirts of the domain, and the maximum

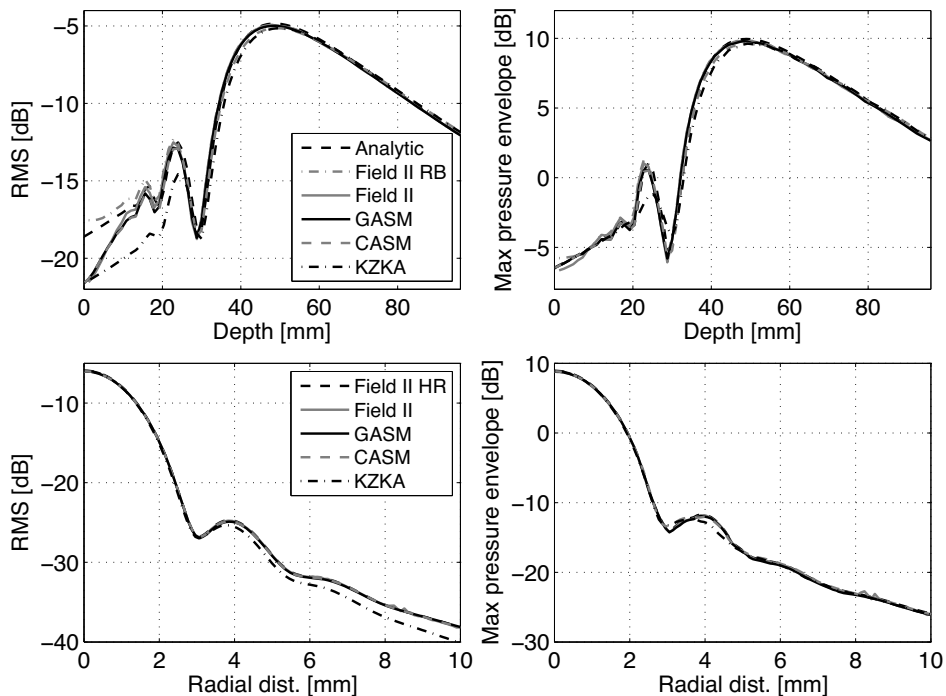


**Figure A.2:** Top row: On-axis RMS (left) and maximum pressure envelope (right) beam profiles as a function of depth for the focused piston transducer in Case 2. Bottom row: Focal plane radial RMS (left) and maximum pressure envelope (right) beam profiles for the same transducer. The legends apply to both panels in each row.

pressure profile shows small discrepancies around the first side-lobe.

The on-axis  $L^2$ -errors (Table A.3) for the high-resolution rigid baffle Field II solution are of the same magnitude for Case 1 and 2. The high-resolution pressure release baffle Field II solution is chosen as the gold standard for the other comparisons, and the error of this with respect to the true solution is assumed to be of the same magnitude as the error for the high-resolution pressure release Field II solution in Case 1. The normal resolution Field II solution provides the lowest error.

### Case 3 — Attenuation

Results for the plane wave attenuation test are presented in Fig. A.3. The visual match between the linear-in-frequency attenuation in Field II and the analytic

expression with  $0.5 \text{ dB cm}^{-1} \text{ MHz}^{-1}$  is excellent, and the  $L^2$ -error is  $64 \cdot 10^{-6}$ . However, the errors for the CASM curves are of the order  $10^{-15}$ . Visually, the thermoviscous absorption in the Texas code is lower than the analytic  $\alpha_0 f^2$ , but the  $L^2$ -error is still low:  $331 \cdot 10^{-6}$ .

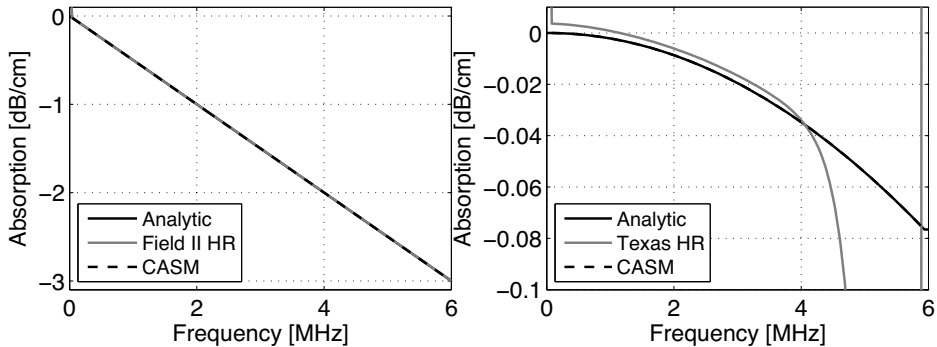


**Figure A.3:** Estimated frequency dependent attenuation over 1 cm propagation in a plane wave setup (Case 3). The left panel shows the result for Field II and Abersim in a material with standard  $0.5 \text{ dB cm}^{-1} \text{ MHz}^{-1}$  attenuation, and the right panel the Abersim and Texas code solutions in water (thermoviscous absorption with  $f^2$ ).

#### Case 4 — Nonlinear Propagation

Figure A.4 presents the graphical results for the nonlinear Case 4 setup. The analytic solution [Eq. (A.10)] is displayed together with the on-axis profiles, and the  $L^2$ -errors between this and a linear, high-resolution Texas code solution are  $20 \cdot 10^{-3}$  and  $6 \cdot 10^{-3}$  for the RMS and maximum pressure envelope respectively. This comparison is performed to verify the high resolution Texas code simulation as the gold standard for the following comparisons. Remind that Field II does not handle non-linearly elastic materials and is left out of this comparison.

In the near field, the Texas code solutions make a small jump around 5–10 mm. Both the level and shape of the three harmonic profiles agree well for the Abersim and Texas code solutions in the on-axis beam profiles. The radial focal plane beam profiles show that the KZKA solution has a slightly lower RMS value outside the first side-lobe. This is also seen for the normal resolution Texas code simulation in the second- and third-harmonic focal plane profiles. The CASM and GASM solutions do not show this tendency in the side-lobe region, however, all solutions have a slightly reduced amplitude within the main lobe when compared with the gold standard.

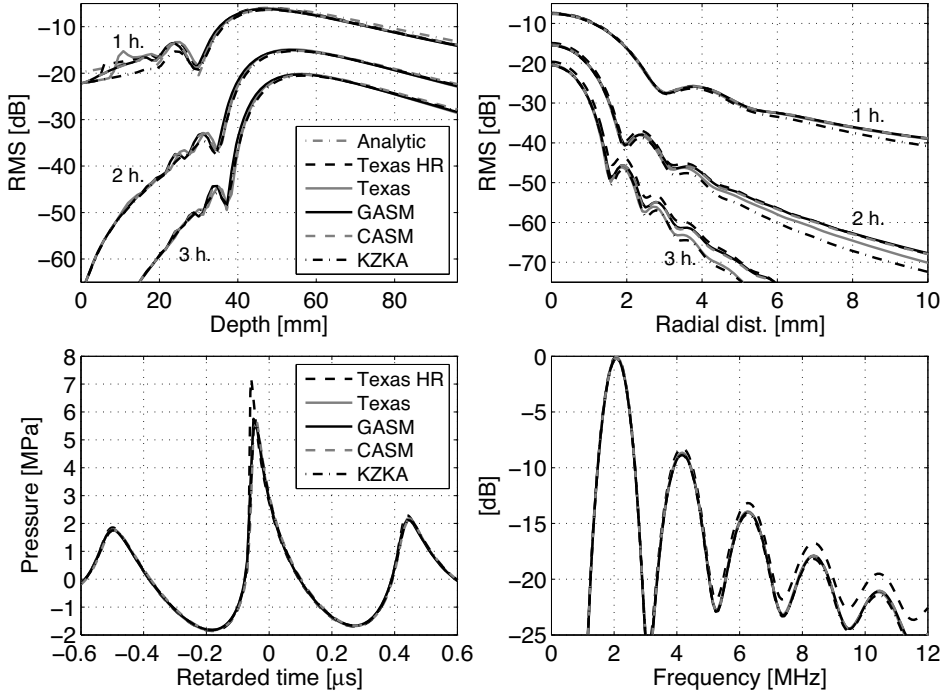


**Figure A.4:** On-axis (top left) and focal plane (top right) RMS beam profiles for the focused piston transducer in a nonlinear medium (Case 4). The bottom row shows the focal point pulse in time (left) and its frequency spectrum (right). Line styles apply to each row.

The temporal wave forms show an amplitude difference of  $\sim 1.5$  MPa between the high-resolution and normal resolution simulations, and its frequency spectrum shows that the amplitude of the harmonic components of the normal resolution simulations are lower than those of the gold standard. The  $L^2$ -errors of the on-axis and radial profiles for Case 4 are presented in Table A.4.

### Case 5 — Array Transducer

The relative RMS  $L^2$ -errors of the CASM solution when compared to the high-resolution Field II solution for the linear, focused and matrix array transducers are presented for the azimuth, elevation and focal planes in Fig. A.5. In the bright areas of each panel (toward the outskirts of each beam), the error approaches the same magnitude as the radiated field, but stays lower than  $-6$  dB. The contours indicate that in these areas, the RMS of the radiated field is lower

**Table A.4:**  $L^2$ -errors for the nonlinear propagation comparison in Case 4. Errors for the first three harmonic components are shown for the on-axis (“ax”) and focal plane (“foc”) RMS and maximum pressure envelope profiles. All values are to the order of  $10^{-3}$ .

Harm.	Texas		CASM		GASM		KZKA	
	RMS	MAX	RMS	MAX	RMS	MAX	RMS	MAX
1 ax.	33	20	40	38	36	33	75	46
2 ax.	58	62	72	75	63	66	88	90
3 ax.	100	107	103	110	98	104	126	131
1 foc.	18	21	23	26	24	26	27	27
2 foc.	66	74	69	72	70	78	79	83
3 foc.	117	128	116	118	117	129	130	134
pulse	42	217	54	200	55	199	57	225

than  $-20$  dB relative to the on-axis maximum RMS.

In the azimuth direction, the Abersim CASM solution compares well with both the Field II linear and matrix array solutions, whereas the errors for the focused array solution are larger close to the transducer. Elevation direction profiles show some of the same tendencies, but the linear and matrix array profiles are different in the sense that the errors of the linear array are larger close to the edges of the transducer.

On-axis and focal plane profiles are shown in Fig. A.6. The two baffle conditions produce in this case very similar profiles, and the CASM solution matches both well. The focal profiles in Fig. A.6 show that the CASM solution reproduce the focal field in both azimuth and elevation direction well when compared with the high-resolution matrix array Field II simulation.

## A.5 Discussion

### Case 1 — Plane Piston Transducer

Inaccuracies are found for all solutions in the extreme near field. Neither Abersim nor Field II claims to be programs well suited for this type of computations, but a short discussion is provided. Field II requires the field point to be in the far field of each mathematical element. For a small circular small element with area  $\Delta x^2$ , this limit is  $2\Delta x^2/\pi\lambda \approx 0.44 \mu\text{m}$ , and is not considered to be the source of error. The small difference in  $L^2$ -error between the normal and high-resolution Field II simulations indicates that the main source of error might come from the choice and/or implementation of the underlying model. The er-

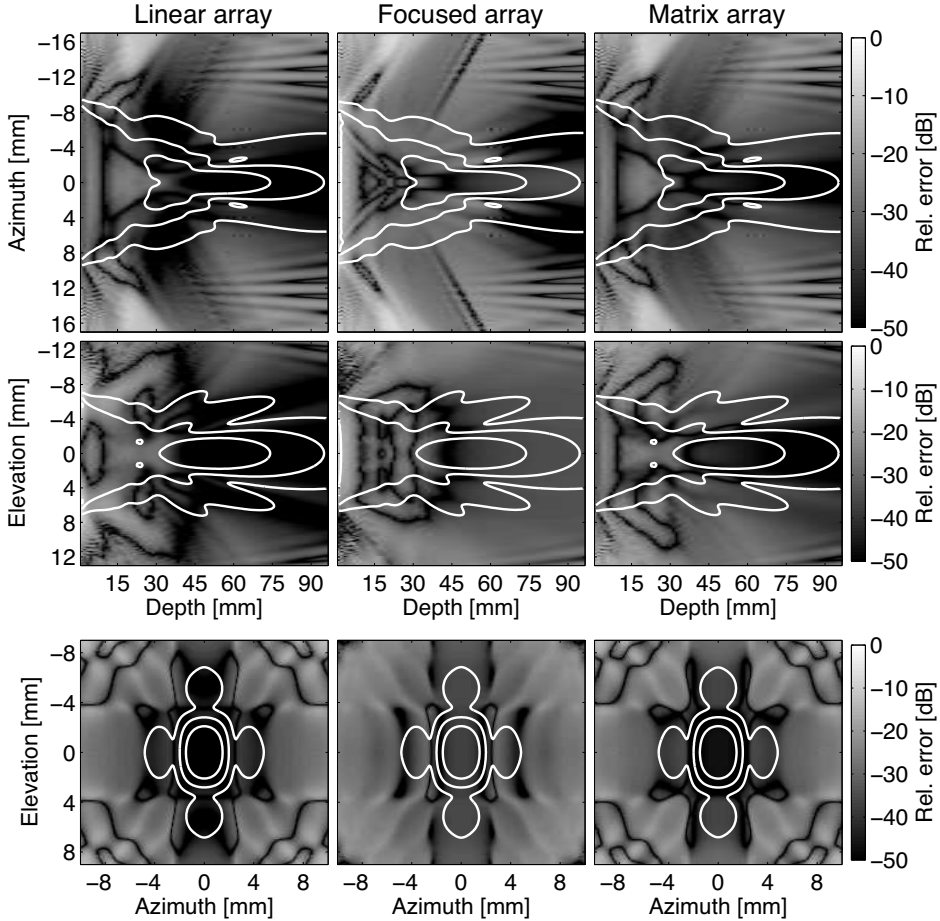


**Figure A.5:** Relative  $L^2$ -errors for the azimuth, elevation and focal plane profiles for the Abersim solution in the array transducer comparison in Case 5. The gold standard of each column is the high-resolution Field II simulation for the linear (left), focused (center) and matrix array (right) transducers. The contours indicate the  $-6$ ,  $-12$  and  $-20$  dB RMS beam profiles for the Field II simulation.

ror of the high-resolution rigid baffle solution is lower than the pressure release solution, and the implementation of the pressure release condition is believed to be one such source of error.

The lowest errors in the pressure release comparison are found for the Abersim CASM and GASIM solutions. This indicates that an Angular Spectrum approach might be better suited for pressure release conditions. Cobbold states

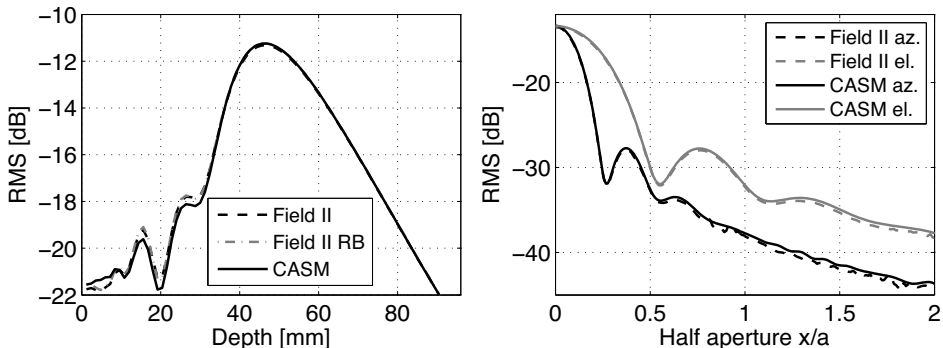


**Figure A.6:** The on-axis (left) and focal plane (right) pressure profiles for the array transducer in Case 5. The on-axis profile for a rigid baffle is included in the left panel. The right panel shows the azimuth and elevation profiles over the normalized axis  $x/a$ , where  $a = D/2$  and  $D$  is the aperture in either azimuth or elevation direction.

in Ref. 25 that the classical ASM is inaccurate up to  $\sim 3\lambda \approx 2.3$  mm, and this might cause the mismatch in amplitude very close to the transducers. The spatial resolution of the CASM and GASM solutions is four times lower than the high-resolution Field II simulations, and yet, the CASM and GASM solutions produce lower errors. This suggests that an ASM based solution is preferable if accurate near field diffraction is considered important. Abersim was originally developed as a tool for aberration studies, and the near field accuracy shown in this study indicates that ASM based methods are well suited for local interference and focusing effects.

The largest error is found for the KZKA solution, but this is the only solution where the validity of the underlying model is violated. The inclination angle with respect to the  $z$ -axis is higher than  $15^\circ$  this close to the transducer, and outside the validity of the KZK equation. Another cause of this is the too slow build-up of edge waves and erroneous near field interference.

## Case 2 — Focused Piston Transducer

The difference between the rigid and the pressure release baffle is visually more prominent in the Case 2 results. The on-axis analytic solution is a combination of the center wave and the edge waves, and in the rigid baffle case, the amplitude of the edge wave equals the amplitude of the center wave. A pressure release baffle provides a lower amplitude in the edge waves close to the transducer, and this influences the RMS value. The maximum pressure envelope is

less influenced because the center wave amplitude is invariant under the baffle condition. The even lower on-axis RMS in the KZKA solution arises from the limitations of the KZK model. The edge ray is inclined  $\sim 17^\circ$  relative to the  $z$ -axis at 30 mm depth, and this corresponds visually to where the KZKA solution catches up with the rest.

In the focal plane profiles, the different solutions match each other excellent. The errors are lower than the on-axis errors, which indicates that the two tools are more accurate in the focal and far field of the transducer rather than the near field. The lower RMS of the KZKA solution is visible in the focal profiles in Fig. A.2, and is believed to arise from the limitations of the KZK model. At the focal point, the inclination angle with respect to the  $z$ -axis from the farthest edge to a radial point reaches  $15^\circ$  at  $r=6.7$  mm.

### Case 3 — Attenuation

Abersim solves the attenuation term in the frequency domain, which suggest that this should be the best match to a general frequency dependent power-law attenuation. This is shown in Case 3. The Field II and Texas code solutions both provide errors of the order  $10^{-6}$ , but the error for the Abersim simulations are much lower. The setups used in this case are plane wave setups, and both Abersim and the Texas code solve the attenuation term using a plane wave approximation. The sub steps used in the operator splitting scheme are assumed to be short enough such to ensure that plane-wave approximations are valid for radiation of diffractive fields.

### Case 4 — Nonlinear Propagation

The reported jump in the Texas code profiles occur when the edge waves enter the computational domain. As depth increases, it is clear that the Texas code solution matches the analytic solution of a rigid baffle excellently. The measured error verifies this, and is lower than that found for the Field II simulation in Case 2. Contrary to Case 2, the maximum pressure envelope error is lower than the RMS error, which arises from the influence of edge waves on the RMS solution. Abersim show the same tendencies as in Case 2 for the first-harmonic on-axis beam.

In the algorithm for solving the nonlinear term, both Abersim and the Texas code perform a re-sampling operation and an interpolation error interpreted as an artificial, numerical absorption is introduced.<sup>12,14</sup> Varslot and Taraldsen report this to be negligible.<sup>15</sup> This error grows as the sampling-to-center frequency ratio drops, and is more clearly visible in the frequency spectrum of the

focal point pulse (bottom right panel of Fig. A.4).

The shape of the temporal wave form indicates the presence of an acoustic shock. Acoustic shock formation occurs for higher transmit pressures in water. The full depth of the simulation is shorter than the plane wave shock length for this setup (148 mm), but focused waves can form shocks earlier than this. The focal point pulse shows that high temporal sampling is necessary when the medium is highly nonlinear. An up-sampling of the normal resolution temporal wave form shows that the reduced amplitude is an effect of the incorrect generation of the harmonic contents of the pulse and not the temporal sampling alone. This result is not visualized. The artificial numerical absorption is the source of this error. The  $L^2$ -errors in Table A.4 are more pronounced in the maximum pressure envelope than the RMS value because the relative error is largest for frequencies with very low amplitude.

Although the transmit pressure amplitude is in the range used for diagnostic purposes, attenuation in soft tissue is much higher than that of water and will attenuate the pulse, and especially higher frequencies, such that shock formation is not present. If one wants to study shock formation, high sampling frequencies are crucial — both to ensure the correct frequency content of the pulse, and the ability to present the correct temporal wave forms.

### Case 5 — Array Transducer

Consistent with the other error measures in this paper, the relative error is presented in Fig. A.5. In the regions where the relative errors are high, *i.e.*, approaches the same magnitude as the field itself, the transmit field is very low in amplitude.

The focused transducer has a curved geometry in the elevation direction, and the impulse response from a plane vs. a curved surface are different. The impulse response of each element has a field pattern accounting for directivity, and a curved surface makes the elements towards the edge to be pointing inward. This causes the near field differences in the focused array azimuth profiles. The differences in the elevation direction between the linear and matrix arrays are not understood fully by the authors, but is believed to arise from how Field II handles electronic focusing vs. assigning focusing delays for each mathematical element. The *source code* of Field II is not publicly available, and this is not investigated further. The differences seen in the main lobe of the elevation plane indicate that this influence the edge wave contributions and hence the diffraction of the radiated beam.

Differences in the on-axis field caused by the baffle condition is smaller for Case 5 than the other cases. The CASM solution matches both baffle conditions

well, and indicate that Abersim is well suited for calculation of transmit fields from diagnostic transducers in both types of baffles. A limitation is still the requirement of a plane transducer surface, and in applications using highly curved transducers, the baffle directivity can influence the focal field if the transducer is modeled as a plane surface. Field II is not limited by this, but does not account for eventual reflections from the transducer surface itself nor non-linearity of the medium. To catch both of these phenomena a general Finite Element tool is believed to be a better solution.

Another approach is the development of an equivalent source condition as used by Averkiou and Cleveland<sup>28</sup> where the shock wave from a lithotripter is simulated using the KZK equation. The lithotripter has the shape of a focused bowl and the initial field used in the KZK model, *i.e.*, the pressure field at the mouth of the lithotripter, is calculated using geometrical acoustics within the bowl.

Forward propagation tools as Abersim and the Texas code do not handle back scattering well, and a vital part of diagnostic ultrasound is the back scatter information. Combination of several tools are suggested,<sup>5,6</sup> and such a combination can be obtained by simulating the transmit field from a diagnostic transducer using a forward tool, and the back scattered field using a linear tool, *e.g.*, Field II.

## A.6 Conclusion

Radiated fields computed with three simulation programs are compared for five test cases. Four cases benchmark the programs in solving diffraction, attenuation or nonlinear effects, and one case is a comparison for a cardiac array transducer. The compared tools can be downloaded free of charge, and the source codes for the Texas code and Abersim are publicly available.<sup>18-20</sup>

Both Field II and Abersim reproduce accurate near and focal field diffraction for unfocused and focused circular piston transducers. A high resolution Field II solution is used as the gold standard where analytic solutions are not available, but estimated  $L^2$ -errors suggest that the Abersim CASM and GASM solutions are more accurate.

The presented Generalized Angular Spectrum Method (GASM) utilize the symmetry of the problem to reduce computational complexity from  $N^2 \log 2N$  to  $N^2$ , and perform equivalently to the classic ASM (CASM), and better than the Abersim KZKA solution for circular-symmetric apertures.

The attenuation model used in Abersim provides lower errors than the one in Field II and the thermoviscous absorption model in the Texas code.

In the nonlinear case, both Abersim and the Texas code provide equivalent results. High sampling frequencies are crucial if shock phenomena are to be investigated, and the two tools perform similar for equal sampling.

The radiated field computed with Abersim matches the solution from Field II for a linear or matrix array transducer model with a plane surface best. Curved transducer surfaces introduce higher errors in the near field, and the focal and far field errors are in the order of  $-20$  to  $-30$  dB, which is higher than the  $<-50$  dB error found for the linear and matrix arrays.

## Acknowledgements

The authors would like to thank Trond Varslot and Marco Voormolen for providing insight and experience in the use of the presented tools. This project is funded by the Norwegian Research Council.

## References

- [1] R. Krimholtz, D. A. Leedom, and G. L. Matthaei, “New Equivalent Circuits for Elementary Piezoelectric Transducers,” *Electron. Lett.*, vol. 6, pp. 398–9, 1970.
- [2] X. Ming Lu and T. L. Proulx, “Single Crystals vs. PZT Ceramics for Medical Ultrasound Applications,” in *IEEE Ultrason. Symp. Proc.*, 2005, pp. 227–30.
- [3] D. Bæk, J. A. Jensen, and M. Willatzen, “Testing of a One Dimensional Model for Field II Calibration,” in *IEEE Ultrason. Symp. Proc.*, 2008, pp. 1417–20.
- [4] M. E. Frijlink and H. G. Torp, “Simulation of Acoustic Fields From Arbitrary Transducer Stacks Using a FEM Transducer Model and Nonlinear Wave Propagation,” in *IEEE Ultrason. Symp. Proc.*, 2009, pp. 2340–3.
- [5] Y. Li and J. A. Zagzebski, “Computer Model for Harmonic Ultrasound Imaging,” *IEEE Trans. Ultrason., Ferroelect., Freq. Contr.*, vol. 47, pp. 1259–72, 2000.
- [6] M. E. Frijlink, D. E. Goertz, A. Boakaz, and A. F. W. van der Steen, “A Simulation on Tissue Harmonic Imaging With a Single-Element Intravascular Ultrasound Catheter,” *J. Acoust. Soc. Am.*, vol. 120, pp. 1723–31, 2006.

- 
- [7] J. A. Jensen and N. B. Svendsen, "Calculation of Pressure Fields from Arbitrary Shaped, Apodized and Exited Ultrasound Transducers," *IEEE Trans. Ultrason., Ferroelect., Freq. Contr.*, vol. 39, pp. 262–7, 1992.
- [8] E. A. Zabolotksaya and R. V. Khokhlov, "Quasi-Plane Waves in the Nonlinear Acoustics of Confined Beams," *Sov. Phys. Acoust.*, vol. 15, pp. 35–40, 1969.
- [9] V. P. Kuznetsov, "Equations of Nonlinear Acoustics," *Sov. Phys. Acoust.*, vol. 16, pp. 467–70, 1970.
- [10] J. N. Tjøtta and S. Tjøtta, "An Analytical Model for the Nearfield of a Baffled Piston Transducer," *J. Acoust. Soc. Am.*, vol. 68, pp. 334–9, 1980.
- [11] S. I. Aanonsen, T. Barkve, J. N. Tjøtta, and S. Tjøtta, "Distortion and Harmonic Generation in the Nearfield of a Finite Amplitude Sound Beam," *J. Acoust. Soc. Am.*, vol. 75, pp. 749–68, 1984.
- [12] Y.-S. Lee and M. F. Hamilton, "Time Domain Modeling of Pulsed Finite-Amplitude Sound Beams," *J. Acoust. Soc. Am.*, vol. 97, pp. 906–17, 1995.
- [13] M. A. Averkiou and M. F. Hamilton, "Nonlinear Distortion of Short Pulses Radiated by Plane and Focused Circular Pistons," *J. Acoust. Soc. Am.*, vol. 102, pp. 2539–48, 1997.
- [14] R. O. Cleveland, M. F. Hamilton, and D. T. Blackstock, "Time-Domain Modeling of Finite-Amplitude Sound in Relaxing Fluids," *J. Acoust. Soc. Am.*, vol. 99, pp. 3312–8, 1996.
- [15] T. Varslot and G. Taraldsen, "Computer Simulation of Forward Propagation in Soft Tissue," *IEEE Trans. Ultrason., Ferroelect., Freq. Contr.*, vol. 52, pp. 1473–82, 2005.
- [16] T. Varslot and S.-E. Måsøy, "Forward Propagation of Acoustic Pressure Pulses in 3D Soft Biological Tissue," *Mod. Ident. Cont.*, vol. 27, no. 3, pp. 181–200, 2006.
- [17] M. E. Frijlink, H. Kaupang, T. Varslot, and S.-E. Måsøy, "Abersim: A Simulation Program for 3D Nonlinear Acoustic Wave Propagation for Arbitrary Pulses and Arbitrary Transducer Geometries," in *IEEE Ultrason. Symp. Proc.*, 2008, pp. 1282–5.

- 
- [18] “Field II Ultrasound Simulation Program,” Internet page: <http://server.electro.dtu.dk/personal/jaj/field/>, last visited: 18. January 2011.
- [19] “Texas KZK Time Domain Code,” Internet page: <http://people.bu.edu/robinc/kzk/index.html>, last visited: 18. January 2011.
- [20] “Abersim — Ultrasound Simulation Software,” Internet page: <http://www.ntnu.no/isb/abersim>, last visited: 18. January 2011.
- [21] G. Taraldsen, “A Generalized Westervelt Equation for Nonlinear Medical Ultrasound,” *J. Acoust. Soc. Am.*, vol. 109, pp. 1329–33, 2001.
- [22] R. J. Zemp, J. Tavakkoli, and R. S. Cobbold, “Modeling of Nonlinear Ultrasound Propagation in Tissue from Array Transducers,” *J. Acoust. Soc. Am.*, vol. 113, pp. 139–52, 2003.
- [23] L. C. Evans, *Partial Differential Equations*. Providence, RI: American Mathematical Society, 1998.
- [24] G. H. Golub and C. F. Van Loan, *Matrix Computations*, 3rd ed. Baltimore, London: Johns Hopkins University Press, 1996.
- [25] R. S. C. Cobbold, *Foundations of Biomedical Ultrasound*. New York, NY: Oxford University Press, Inc., 2007.
- [26] C. Gasquet and P. Witomski, *Fourier Analysis and Applications*. Berlin, Heidelberg, New York: Springer, 1999.
- [27] B. A. J. Angelsen, *Ultrasound Imaging*. Trondheim, Norway: Emantec, 2000, vol. 1.
- [28] M. A. Averkiou and R. O. Cleveland, “Modeling of an Electrohydraulic Lithotripter With the KZK Equation,” *J. Acoust. Soc. Am.*, vol. 106, pp. 102–12, 1999.

# Transmit Beamforming for Optimal Second-Harmonic Generation

Halvard Høilund-Kaupang and Svein-Erik Måsøy

Department of Circulation and Medical Imaging, NTNU, Trondheim, Norway

## Abstract

A simulation study of transmit ultrasound beams from several transducer configurations is conducted to compare second-harmonic imaging at 3.5 MHz and 11 MHz. Second-harmonic generation and the ability to suppress near field echoes are compared. Each transducer configuration is defined by a chosen f-number and focal depth, and the transmit pressure is estimated not to exceed a mechanical index of 1.2. The medium resembles homogeneous muscle tissue with nonlinear elasticity and power-law attenuation. To improve computational efficiency, the KZK equation is utilized, and all transducers are circular-symmetric. Previous literature shows that second-harmonic generation is proportional to the square of the transmit pressure, and that transducer configurations with different transmit frequencies, but equal apertures and focal depths in terms of wavelengths, generate identical second-harmonic fields in terms of shape. Results verify this for a medium with attenuation  $\mathbf{f}^1$ . For attenuation  $\mathbf{f}^{1.1}$ , deviations are found, and the high frequency perform subsequently worse than the low. The ability to suppress near field echoes in the presence of a heterogeneous body wall is suggested to perform worse for high frequencies than low.

## B.1 Introduction

Conventional ultrasound scanners assume the body to consist of a homogeneous material with a constant speed of sound.<sup>1</sup> For soft tissue, the speed of sound is both dependent on the type of tissue and the local acoustic pressure.<sup>2</sup> This pressure dependence is a nonlinear effect of the tissue elasticity, and gave birth to an imaging technique referred to as second-harmonic, tissue-harmonic or just harmonic imaging. Harmonic imaging was first developed as a contrast detection technique,<sup>3</sup> but has later been shown to improve image quality for several applications such as cardiac,<sup>4,5</sup> liver,<sup>6-8</sup> abdominal,<sup>6,7,9</sup> obstetrics,<sup>7,8,10</sup> small parts<sup>8</sup> and carotid<sup>11,12</sup> imaging.

Harmonic imaging is also studied and verified through technical studies.<sup>13-20</sup> These have reported that the second-harmonic beam generally has a lower side-lobe level and improved contrast resolution when compared with a same-frequency fundamental beam.<sup>15,17,18</sup> The axial and lateral resolution is somewhat reduced because the second-harmonic signal is generated from a pulse of half the frequency: the first-harmonic.<sup>15,17</sup> Harmonic generation also depends on the shape of the aperture.<sup>13,14,16,19</sup> For power-law attenuation, a higher frequency exponent reduces the amount of second-harmonic generated.<sup>20</sup>

For heterogeneous materials, the tissue has spatially dependent acoustic parameters, which causes phase aberrations and reverberations.<sup>1,2</sup> The aberration characteristics of the second-harmonic beam resemble the aberration characteristics for the first-harmonic more than the fundamental for typical cardiac frequencies.<sup>21,22</sup> Reverberations, or multiple echoes of the pulse, appear in the image as repetitions of a strong scattering object or as ghost noise. Reverberation noise is especially seen in the lumen of vessels and fluid filled chambers. Harmonic imaging of deeper-lying structures and organs is shown to be less influenced by these two effects because the near field intensity is very low.<sup>4-8,10,18</sup>

Imaging of structures located closer to the skin surface uses a higher imaging frequency. The number of studies performed on higher frequencies (6–12 MHz) are not as numerous as those performed on 3–4 MHz. One abdominal study performed on children<sup>9</sup> and two carotid studies<sup>11,12</sup> show an improvement in image quality with harmonic imaging, but it is less than the one gained for lower frequencies. Rosenthal *et al.* presents in Ref. 8 a study that includes breast and biliary artery imaging, and show mainly equal performance of harmonic imaging compared to fundamental for normal tissue and a slight improvement for pathological tissue.

This study will present the theoretical framework for a suggested shape invariance of the second-harmonic field when the transmit measures are in terms

of wavelengths and an algorithm for estimation of transmit pressure. Plane wave attenuation is assumed. Simulations of a series of transducer configurations with varying focal depths and f-numbers are performed to compare second-harmonic to fundamental imaging for a low frequency of 3.5 MHz and a high frequency of 11 MHz. To avoid running simulations using several types of attenuation, a method for attenuation compensation is introduced and verified.

In terms of wavelengths, the transducer configurations are chosen to be equal for the two frequencies. This enables comparison of generation effects across frequency differences. Second-harmonic generation will be discussed in relation to the differences in transmit pressure and attenuation characteristics of the medium. A quality factor for the second-harmonic's ability to suppress near field echoes is suggested and discussed.

Throughout the paper, the second-harmonic is said to be generated from the first-harmonic transmitted at half the frequency of the second-harmonic. The fundamental is transmitted at the second-harmonic frequency.

## B.2 Theory

### B.2.1 Geometric Beam Setup

A focused ultrasound beam can be divided into three main depth regions: The near field, the focal region and the far field (see Fig. B.1). These geometric

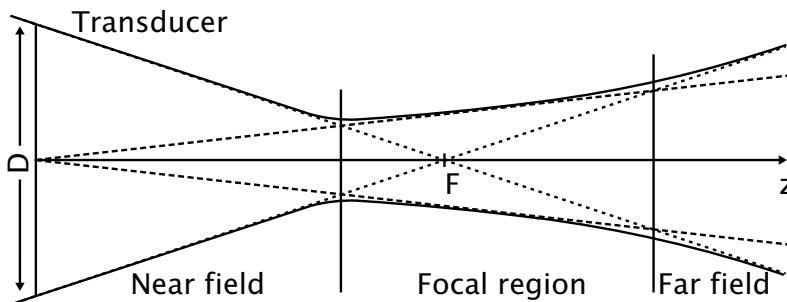


**Figure B.1:** A focused ultrasound beam with the different regions indicated.

regions are related to the frequency, aperture size and focal depth.<sup>1</sup>

Lateral resolution of a transmit beam is determined by the frequency and the f-number,  $f/\#$ . The f-number also determines the length of the focal region, and is closely connected to the Fresnel number,  $S$ , a measure determining the diffraction behavior of a focused ultrasound beam.<sup>1</sup> The f-number and Fresnel

number are

$$f/\# = \frac{F}{D}, \quad (\text{B.1})$$

$$S = \frac{2\lambda}{\left(4F - \sqrt{4F^2 - D^2}\right)} \approx \frac{4\lambda f/\#}{D}. \quad (\text{B.2})$$

Here,  $F$  is the depth of the geometric focal point,  $D$  the aperture size, and  $\lambda$  the wavelength. The approximation of the Fresnel number is valid for apertures where  $D \gg \lambda$ .<sup>1</sup>

Diffraction causes the maximum on-axis pressure to be shifted closer to the transducer surface than the geometric focal point, and this shift is proportional to the f-number and Fresnel number.<sup>1</sup> An optimal transmit beam combines a narrow focal region, a high intensity within the focal region and a low intensity outside this region. The latter to reduce unwanted multiple reflections originating in the near field.

## B.2.2 Second Harmonic Generation

Human tissue exhibits a nonlinear elasticity function, and the simplest nonlinear approximation of tissue elasticity is a second-order Taylor expansion of the pressure-density relation.<sup>2,23</sup> Simplifying and re-ordering the relative volume compression is given with quadratic pressure dependence as

$$\frac{\delta V}{\Delta V} = -\nabla \cdot \psi = \kappa p - \beta_n (\kappa p)^2,$$

where  $\nabla \cdot \psi$  is the divergence of the particle displacement in Lagrangian coordinates,  $\kappa$  the compressibility of the medium, and  $\beta_n$  the coefficient of non-linearity given as  $\beta_n = 1 + \frac{B}{2A}$ , where  $B$  and  $A$  are the coefficients from the Taylor expansion and often referred to as the parameter “ $B/A$ ”.<sup>2,23</sup> The forward non-linear distortion in a diffractive beam cause the wave peaks to have a higher absolute value amplitude than the wave troughs.<sup>2,23</sup>

Taraldsen showed that nonlinear propagation in soft tissue may be modeled using the generalized Westervelt equation.<sup>24</sup> In order to compare wave propagation across frequency differences, the Westervelt equation must be scaled and written on dimensionless form. The scales are chosen such that space is expressed in terms of wavelengths and that the speed of sound,  $c$ , and characteristic frequency,  $f_c$ , equals one. The scales are presented in Table B.1. The

scaled and dimensionless Westervelt equation is<sup>24</sup>

$$\begin{aligned} \nabla^2 p - \frac{1}{c^2} \frac{\partial^2 p}{\partial t^2} - \frac{1}{c^2} h * \frac{\partial^2 p}{\partial t^2} &= -\epsilon_s \epsilon_n \frac{\partial^2 p^2}{\partial t^2}, \\ \epsilon_s &= p_s \kappa_s, \quad \epsilon_n = \frac{\beta_n \kappa}{c^2}, \end{aligned} \quad (\text{B.3})$$

where  $h$  is a convolution operator accounting for attenuation.

**Table B.1:** Appropriate linear scales for physical variables. The tilde denotes the physical variable.

Physical variable	Symbol	Scale value
Space	$x = \tilde{x}/x_s$	$x_s = \lambda_c$
Speed of sound	$c = \tilde{c}/c_s$	$c_s = c_{\text{tissue}}$
Pressure	$p = \tilde{p}/p_s$	$p_s = 10^6 \text{ Pa}$
Compressibility	$\kappa = \tilde{\kappa}/\kappa_s$	$\kappa_s = 400 \cdot 10^{-12} \text{ Pa}^{-1}$
Time	$t = \tilde{t}/t_s$	$t_s = \frac{x_s}{c_s} = \frac{1}{f_c}$

Varslot *et al.* assume the pressure to be separable into a linear and a non-linear part such that the governing equations in the frequency domain are<sup>21</sup>

$$p = p_l + p_{\text{nl}}, \quad (\text{B.4})$$

$$\nabla^2 \hat{p}_l + k^2 [1 + H] \hat{p}_l = 0, \quad (\text{B.5})$$

$$\nabla^2 \hat{p}_{\text{nl}} + k^2 [1 + H] \hat{p}_{\text{nl}} = \epsilon_s \epsilon_n k^2 \hat{p}_* \hat{p}_*, \quad (\text{B.6})$$

where  $k = \omega/c = 2\pi f/c$ ,  $\epsilon_s = p_s \kappa_s$ ,  $\epsilon_n = \beta_n \kappa/c^2$  and  $H$  the temporal Fourier transform of  $h$  in Eq. (B.3).

At the time of transmit,  $t_0$ , the nonlinear part of  $p$  is zero. The vibration on the transducer is modeled as a separable function  $f(t)U_0 u_n(\xi)$  where  $f(t)$  is the temporal variation,  $U_0$  the maximum normal vibration velocity and  $u_n$  a normalized apodization function over the transducer surface with coordinates  $\xi = [x, y]^T$ . Varslot *et al.* show in Ref. 21 that the radiated linear pressure field in Eq. (B.5) in the frequency domain is expressed through the Rayleigh integral as

$$\hat{p}_l(\xi, z, \omega) = \rho c U_0 \hat{f}(\omega) H_1(\xi, z, \omega) \quad (\text{B.7})$$

and

$$H_1(\xi, z, \omega) = ik \int_{S_0} 2\hat{g}(\xi - \xi_0, z, \omega) u_n(\xi_0) d\xi_0 \quad (\text{B.8})$$

where  $g$  is a Green's function that accounts for attenuation and baffle directivity.

Using the quasilinear approximation,  $|\hat{p}_{\text{nl}}| \ll |\hat{p}_1|$ , and a plane wave conversion  $P_0 = \rho c U_0$  for the pressure, an expression similar to Eq. (10) in Ref. 21 is

$$\begin{aligned} \hat{p}_{\text{nl}}(\xi, z, \omega) &= \epsilon_s \epsilon_n k^2 \int_0^z \int_{\mathbb{R}^2} g(\xi - \xi_1, z - z_1, \omega) \\ &\quad \times \left( \hat{p}_1 *_{\omega} \hat{p}_1 \right) (\xi_1, z_1, \omega) d\xi_1 dz_1, \\ &= P_0^2 H_{\text{nl}}(\xi, z, \omega) \end{aligned} \quad (\text{B.9})$$

where  $H_{\text{nl}}$  is a source function defined as

$$\begin{aligned} H_{\text{nl}}(\xi, z, \omega) &= \epsilon_s \epsilon_n k^2 \int_0^z \int_{\mathbb{R}^2} g(\xi - \xi_1, z - z_1, \omega) \\ &\quad \times \left( \hat{f} H_1 *_{\omega} \hat{f} H_1 \right) (\xi_1, z_1, \omega) d\xi_1 dz_1, \end{aligned} \quad (\text{B.10})$$

where  $\hat{f}$  and  $H_1$  are the normalized temporal variation and linear spatial frequency response from Eqs. (B.7) and (B.8). Although both  $H_1$  and  $H_{\text{nl}}$  in Eqs. (B.8) and (B.10) explicitly depend on  $k$  and  $\omega$ , recall that frequency related variables are in terms of scaled variables. Independently of the physical frequency, the scaled characteristic frequency is one.

Equation (B.9) shows that the generation of the nonlinear part of the pressure is shape invariant of the physical frequency. The amplitude of the second-harmonic field is proportional to the square of the transmit pressure  $P_0$ .

### B.2.3 Attenuation of Wave Propagation

For wave propagation in homogeneous media, power-law attenuation,  $\tilde{\alpha}(f)$ , following  $\tilde{\alpha}_{\text{dB}}(f) = \tilde{\alpha}_0 \tilde{f}^\beta$  is modeled into the frequency space representation of the convolution operator  $h$  in Eq. (B.3).<sup>1</sup> An attenuation coefficient  $\tilde{\alpha}_{\text{dB}} = \alpha_0 \tilde{f}^\beta$  will on scaled and dimensionless form be

$$\alpha_{\text{dB}} = \frac{100}{(f_s^1)^\beta} x_s f_s^\beta \alpha_0 f^\beta = \frac{100 c_s}{(2\pi)^2 f_s^1} \bar{f}_c^\delta \alpha_0 \omega^\beta = \gamma \bar{f}_c^\delta \alpha_0 \omega^\beta \quad (\text{B.11})$$

where  $\alpha_0$  is the attenuation coefficient in  $\text{dB cm}^{-1} \text{MHz}^{-\beta}$ ,  $f_s^1 = 1 \text{ MHz}$  and  $\bar{f}_c = f_s / f_s^1$  is the characteristic frequency scaled to megahertz and  $\delta = \beta - 1$  or the deviation from a linear frequency dependence. The dependence on  $\bar{f}_c^\delta$  implies that the attenuation per wavelength varies with frequency if  $\beta \neq 1$ .

For low curvature wave fronts, plane wave attenuation is assumed<sup>1</sup> as

$$\begin{aligned} \hat{p}_{1a}(\xi, z, \omega) &= P_0 \hat{f}(\omega) e^{-\alpha_e \bar{f}_c^\delta \omega^\beta z} H_1(\xi, z, \omega) \\ &= A(\alpha_0, \bar{f}_c^\delta, z, \omega) \hat{p}_1(\xi, z, \omega) \end{aligned} \quad (\text{B.12})$$

where  $\alpha_e = \ln 10 / 20 \gamma \alpha_0$  and  $A(\alpha_0, \bar{f}_c^\delta, z, \omega)$  is an attenuation function. For the linear pressure in Eq. (B.7) the attenuated pressure is the non-attenuated pressure multiplied with the attenuation function  $A$ . For the nonlinear pressure in Eq. (B.9), the attenuation function will be within both the integral in  $z_0$  and the convolution over  $\omega$ . For  $\beta=1$ , the convolution is independent of  $A$ .

Throughout the paper three definitions of attenuation will be used: Regular, linear and conservative. Regular attenuation uses muscle tissue attenuation with  $\alpha_0 = 0.52 \text{ dB cm}^{-1} \text{ MHz}^{-\beta}$  and  $\beta = 1.1$ .<sup>25,26</sup> Linear attenuation is a linearized tissue attenuation with  $\alpha_0 = 0.52 \text{ dB cm}^{-1} \text{ MHz}^{-1}$  and  $\beta = 1$ .<sup>25</sup> Conservative attenuation is the assumed attenuation defined by the safety regulations. This is used for estimating transmit pressure and mechanical index, and uses  $\alpha_0 = 0.3 \text{ dB cm}^{-1} \text{ MHz}^{-1}$  and  $\beta = 1$ .<sup>27</sup> The units of  $\alpha_0$  will be omitted for the rest of the paper.

Plane-wave attenuation in Eq. (B.12) can be compensated for by switching the sign of the parameter  $\alpha_0$  such that  $A(\alpha_0, \bar{f}_c^\delta, z, \omega)A(-\alpha_0, \bar{f}_c^\delta, z, \omega) = 1$ . Compensation between different plane wave attenuation models are also possible through the equation

$$C_{1 \rightarrow 2}(z) = A(-\alpha_{01}, \bar{f}_c^\delta, z, \omega)A(\alpha_{02}, \bar{f}_c^\delta, z, \omega) \quad (\text{B.13})$$

where  $C_{1 \rightarrow 2}$  denotes compensation from attenuation type 1 to attenuation type 2.

### B.2.4 Estimation of Transmit Pressure

High peak negative pressure values may cause cavitation and rupture of tissue fibres and structures.<sup>2,23</sup> To prevent this, safety regulations are employed through introduction of the mechanical index. The mechanical index is defined in standard IEC 62359<sup>27</sup> as

$$\text{MI} = \frac{|p_{\text{neg}}|}{C\sqrt{\tilde{f}_{\text{aw}}}}, \quad C = 1 \text{ MPa MHz}^{-1/2} \quad (\text{B.14})$$

where  $\tilde{f}_{\text{aw}}$  is the physical acoustic working frequency and  $p_{\text{neg}}$  is the peak negative pressure.

To prevent the pressure from exceeding the limit induced by the mechanical index, the transmit pressure is estimated in this study using the on-axis continuous-wave field. The radiated continuous-wave field from a circular focused bowl transducer with uniform vibration amplitude  $U_0$  in a linear and non-attenuating medium is given by the Rayleigh integral as  $\hat{p}_c(z, \omega) = 2\pi \hat{f}(\omega) H_{1c}(\xi, z, \omega)$ ,

where (Ref. 1, p. 5.67)

$$\begin{aligned} H_{1c}(\xi=0, z, \omega) &= i\omega F \frac{e^{-ikz} - e^{-ikr_e(z)}}{ik(F-z)} \\ &= cF \frac{e^{-ikz} - e^{-ikr_e(z)}}{(F-z)} \end{aligned} \quad (\text{B.15})$$

and  $r_e(z) = \sqrt{z^2 + 2(F - \sqrt{F^2 - R^2})(F - z)}$  is the distance from the outer edge of the transducer bowl to a point  $z$  on the center axis, and  $R=D/2$  the radius of the transducer. A plane wave conservative attenuation ( $\alpha=0.3, \beta=1$ ) is then introduced, and the transmit pressure is estimated using Eqs. (B.12), (B.14) and (B.15) to be

$$P_0 = \frac{\text{MI}_t \sqrt{f_c}}{\max_z |H_{1c}(z, \omega) A(0.3, 1, z, \omega)|} \quad (\text{B.16})$$

where  $\text{MI}_t$  is the maximum desired mechanical index.

### B.3 Methods

A numerical simulation experiment is performed to compare second-harmonic with fundamental imaging for two separate imaging frequencies and several combinations of f-numbers ( $f/\#$ ) and focal depths ( $F$ ). The two chosen frequencies are 3.5 MHz and 11 MHz. For second-harmonic imaging, the transmit frequency is half the imaging frequency, or 1.75 MHz and 5.5 MHz respectively. The transducer configuration is defined by a chosen f-number and focal depth, and the aperture is calculated according to Eq. (B.1).

The simulations are performed using the free and open-source computer package Abersim.<sup>28,29</sup> Abersim is capable of solving three-dimensional, directional, nonlinear wave propagation in both homogeneous and heterogeneous tissue. In this study, all simulations are performed in a homogeneous medium using the parabolic approximation of Eq. (B.3) presented in Eq. (3) in Ref. 29. Even though most diagnostic transducers today are rectangular array transducers, circular apertures are chosen both to reduce computational complexity and to avoid the use of different f-number and focal depth in azimuth and elevation. References 14, 16 and 29 all verify that parabolic approximations agree well with physical measurements. The pseudo-differential diffraction model presented in Ref. 29 requires the wave field to be specified in three dimensions, and are because of this much slower than the parabolic approximation that enables the use of circular symmetry in the computation.

The range of f-number and focal depths used for the simulations are presented in both mm and wavelengths in Table B.2. In terms of wavelengths, the focal depths for each frequency are identical. This, and the f-number, ensures that also the aperture, in terms of wavelengths, and Fresnel number of each configuration are identical.

**Table B.2:** Parameter ranges used in the simulations. The apertures are chosen to be realistic in mm, which result in different ranges in terms of wavelengths.

	Low	High
Imaging frequency, $f_c$	3.5 MHz	11 MHz
MI limit	1.2	
F-numbers	1–7	
Focal depths ( $n \lambda$ )	20–300	
Apertures ( $n \lambda$ )	8–90	8–180
Focal depths (mm)	9–133	3–43
Apertures (mm)	3.5–39.9	1.1–25.4
Typical thickness of body wall (mm)	20–30	15–25
Typical thickness of body wall ( $n \lambda$ )	30–60	110–170

The transmit pressure amplitudes are estimated to not exceed a mechanical index limit of 1.2 using Eq. (B.16). The simulations are performed using regular attenuation ( $\alpha_0=0.52$ ,  $\beta=1.1$ ). The sampling frequency is  $20f_i$  where  $f_i$  is the imaging frequency. For each simulation the maximum temporal pressure envelope and the total acoustic energy are calculated from the fundamental, first- and second-harmonic components.

The filtered wave field is considered similar to a linear wave field, where the peak negative pressure is similar to the peak positive pressure in magnitude. Throughout the paper, a measure referred to as the frequency-scaled pressure (FSP) will be used. The FSP is similar to the mechanical index for narrow-band, linear pulses, and is defined as

$$\text{FSP}(z, f_c) = \frac{p_{\max}(z)}{\tilde{C} f_c^{n/2}}, \quad \tilde{C} = 1 \text{ MPa MHz}^{-n/2}, \quad (\text{B.17})$$

where  $f_c$  is the center frequency of the pulse, and  $n=1, 2$  and denotes either the first- or second-harmonic frequency. The dependence on the harmonic components ensures that the FSP of the second-harmonic field is invariant of the physical frequency for equal transmit FSP.

**Table B.3:** The transducer configurations for the three case studies for the two frequency situations.

Case	f/#	Low freq.				High freq.	
		<i>F</i>	<i>D</i>	<i>F</i>	<i>D</i>	<i>F</i>	<i>D</i>
		$n\lambda$	$n\lambda$	$mm$	$mm$	$mm$	$mm$
1	1.5	40	26.7	17.6	11.7	5.6	3.7
2	3.0	120	40.0	52.8	17.6	16.8	5.6
3	4.5	220	48.9	96.8	21.5	30.8	6.8

The total acoustic energy is calculated as the sum of the square of the pressure in both the radial and temporal direction as

$$E(z) = \frac{2\pi}{\rho c} \int_{\mathbb{R}} \int_{-\infty}^{\infty} |p(r, z, t)|^2 dt r dr, \quad (\text{B.18})$$

where the  $2\pi$  accounts for the rotational part of the volume integral due to circular symmetry. To enable direct comparison of the energy, the spatial extensions of the domain is equal for all simulations.

The method for attenuation compensation in Eq. (B.13) is used to compare effects of attenuation *without* running all the simulations for several values of  $\alpha_0$  and  $\beta$ . This method is validated for three specific case studies. The three cases are simulated both with equal transmit pressure and equal transmit FSP. The two options in transmit pressure are presented to verify Eq. (B.10)

In Table B.2 a body wall thickness is indicated. Although no results from simulation in heterogeneous media will be presented, near field intensity and ability to suppress near field echoes will be discussed. Suppression of near field echoes is quantified using a quality factor  $Q$  based on the energy characteristics of the transmit beam. This  $Q$ -factor for suppression of near field echoes up to a given depth  $z_{\text{supp}}$  is defined as

$$Q = 10 \log_{10} \left( \frac{E_C(F)}{E_C(z_{\text{supp}})} \right) \quad (\text{B.19})$$

where  $E_C$  is the energy compensated to no attenuation and  $F$  the geometric focal point.

## B.4 Results

Figure B.2 and Table B.4 present results pertaining to the validation of the compensation for attenuation through Eq. (B.13). Figure B.2 presents the

frequency-scaled pressure, or FSP, for case study 2. Table B.4 presents in numbers the same information for all three case studies.

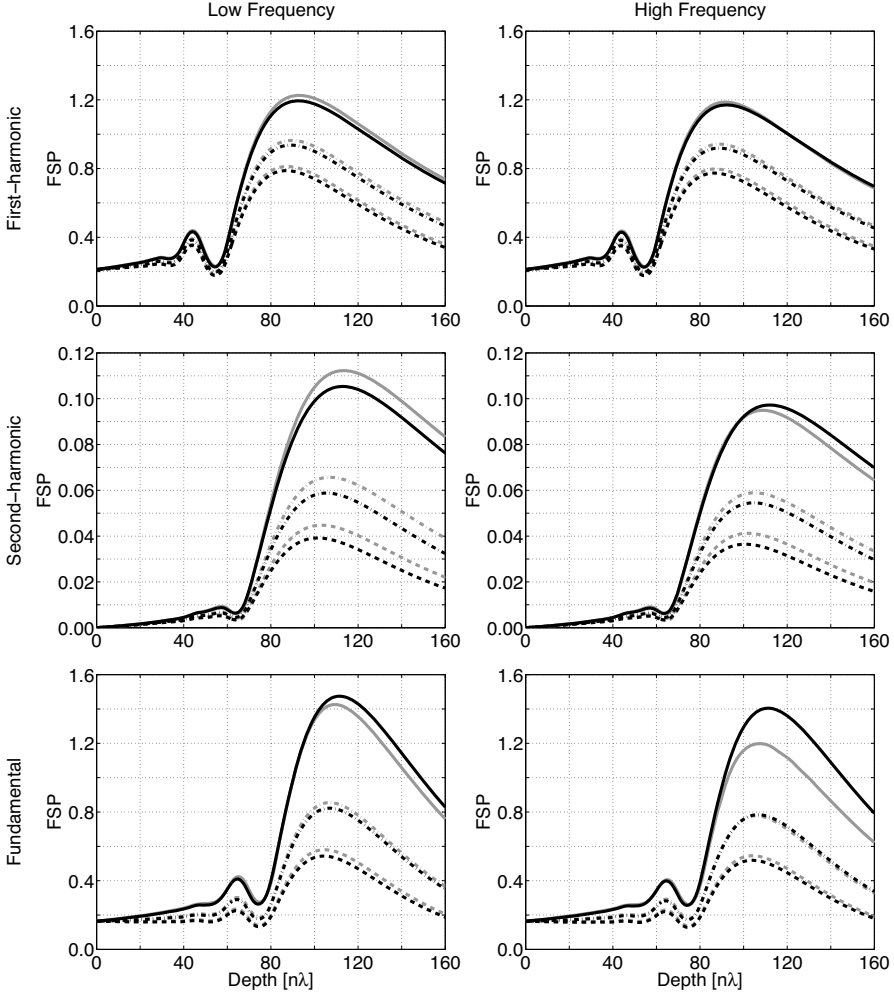


**Figure B.2:** On-axis maximum FSP for case study 2. The black lines indicate the FSP compensated to no (solid), conservative (dash-dot) and linear (dashed) attenuation. The gray lines indicate the FSP when *simulated* with the three types of attenuation (the same line styles apply).

Figure B.3a shows that the wave field does not achieve pressure values at any point in depth that may challenge the mechanical index limit. This type of plot will show one parameter related to the radiated beam, as a function of the transmit f-number and focal depth. The image represents a surface plot where

**Table B.4:** The mean dB deviation between the compensated and simulated on-axis FSP values for all three cases.

		Low freq. Cases			High freq. Cases			
		Comp	1	2	3	1	2	3
1. H.	No	-0.13	-0.38	-0.19	-0.13	-0.38	-0.17	
	Con.	-0.13	-0.53	-0.22	-0.14	-0.54	-0.23	
	Lin.	-0.13	-0.63	-0.26	-0.14	-0.66	-0.27	
2. H.	No	-0.17	-0.35	0.14	-0.04	0.15	0.74	
	Con.	-0.22	-0.66	-0.27	-0.17	-0.45	-0.02	
	Lin.	-0.24	-0.83	-0.45	-0.24	-0.76	-0.36	
Fund.	No	-0.01	0.03	1.59	0.46	1.95	3.12	
	Con.	-0.27	-0.80	-0.04	-0.07	-0.07	0.65	
	Lin.	-0.37	-1.32	-0.62	-0.31	-1.05	-0.35	

the gray scale denotes the magnitude of the parameter.

Compared with the maximum *mechanical index*, the maximum FSP in the three cases deviates in both harmonic and fundamental mode by  $-0.6$  to  $1.3$  dB for the low, and  $-0.4$  to  $1.4$  dB for the high frequency. The dB ranges are valid for all attenuation models used in this study.

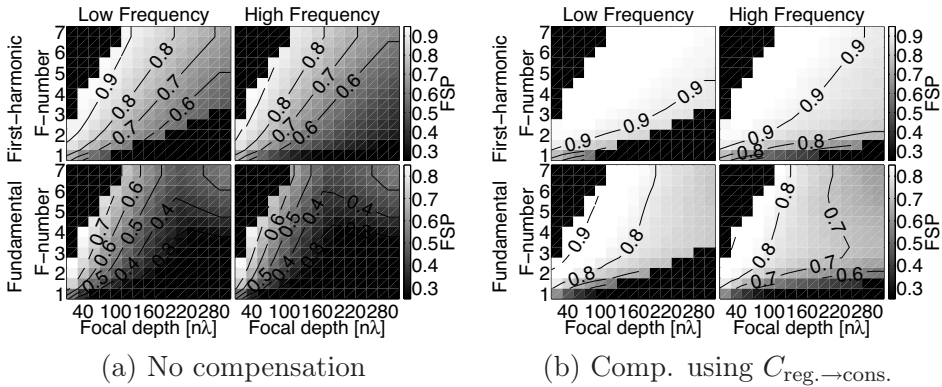


**Figure B.3:** Maximum obtained on-axis FSP.

The estimation algorithm in Eq. (B.16) assumes the attenuation to be conservative ( $\alpha_0=0.3$ ,  $\beta=1$ ). To verify that this algorithm performs equally well for all transducer configurations, the on-axis FSP is compensated to conservative attenuation. The maximum obtained compensated FSP is presented in Fig. B.3b.

Figure B.4 shows the focal point FSP for the *second*-harmonic component for each simulation. The focal point FSP of the harmonic component is used as a qualitative description of the signal-to-noise ratio within the focal region. The absolute signal-to-noise ratio is not quantified itself in this study. In Fig. B.4, dashed lines representing the Fresnel number for each configuration are overlaid the FSP data.

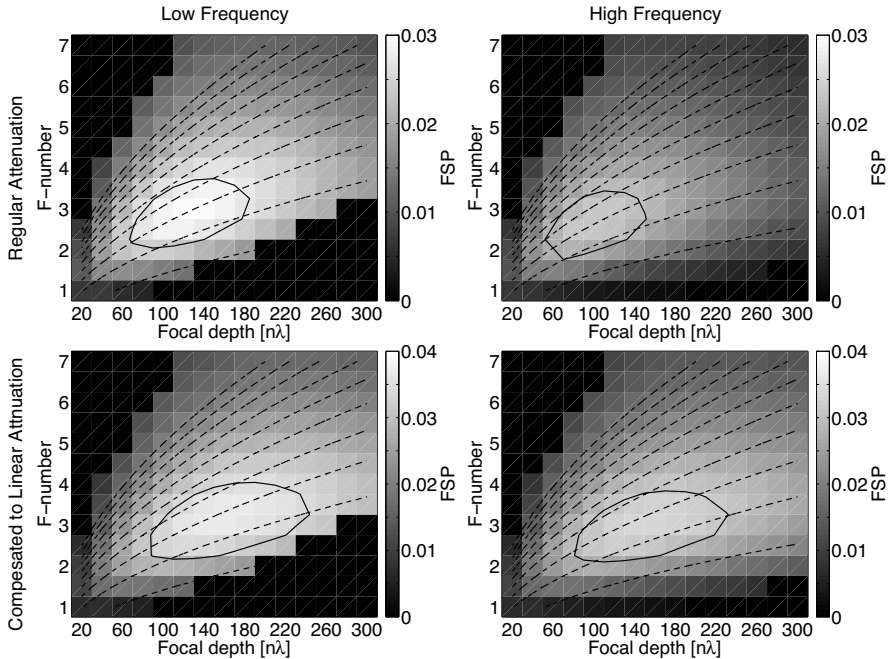


**Figure B.4:** Focal point second-harmonic FSP. The solid contour marks out the top 90% of the FSP. The dashed lines are the Fresnel numbers ranging from 0.1 to 0.9 in steps of 0.1 starting at 0.1 closest to the  $x$ -axis.

The maximum obtained axial second-harmonic FSP increases for increasing  $f$ -number and focal depth due to the increased transmit pressure. The increase is steepest for low  $f$ -numbers.

In order to verify Eq. (B.10), the generated pressure or FSP for the three case studies must be compared. This comparison is presented in Fig. B.5 for the three case studies as the fraction of the high frequency pressure (or FSP) relative to the low frequency pressure (or FSP) as a function of depth.

Suppression  $Q$ -factors for the harmonic beams for both frequencies and up to two depths are presented in Fig. B.6.

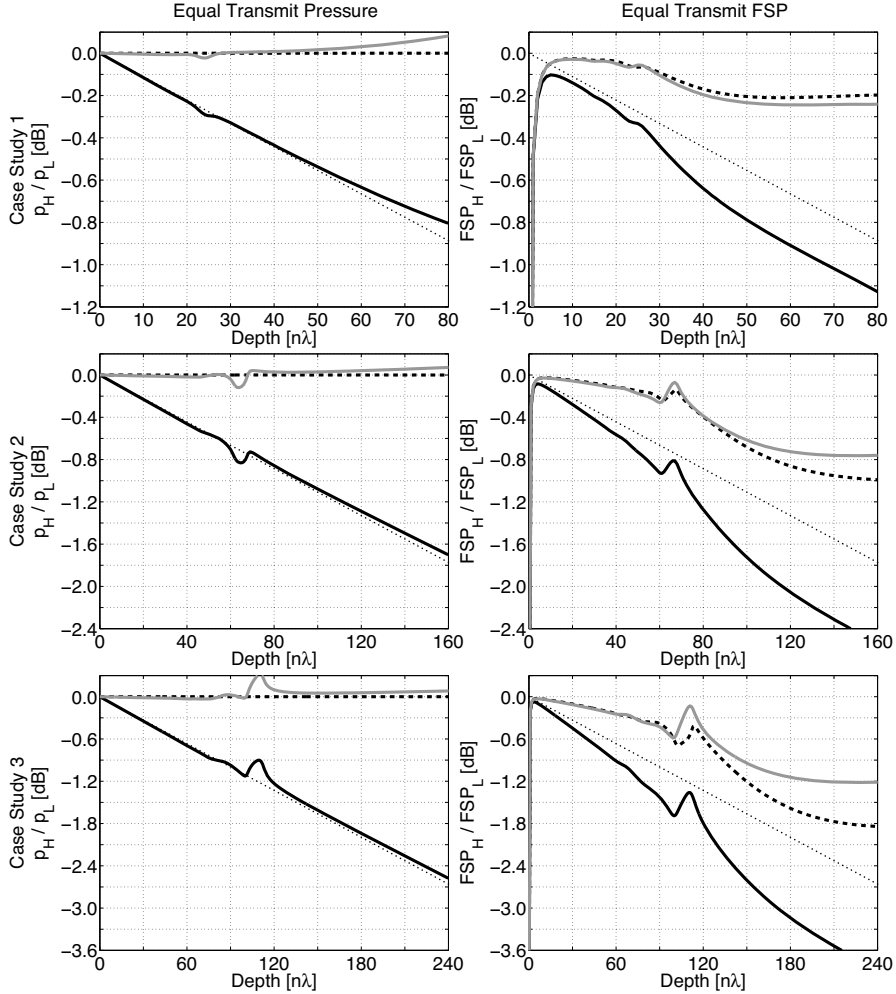


**Figure B.5:** On-axis relative high over low frequency second-harmonic pressure and FSP. Black lines are simulations run with regular (solid) and linear (dashed) attenuation. The solid gray line is the relative pressure or FSP compensated to linear attenuation. The dotted black line is the dB-linear theoretical relative second-harmonic attenuation, *i.e.*,  $-\gamma\alpha_0z\omega^\beta(\bar{f}_{c,hi}^\delta - \bar{f}_{c,lo}^\delta)$ , from Eq. (B.11).

## B.5 Discussion

Application of Eq. (B.13) to *a posteriori* compensate between different plane-wave attenuation models sufficiently accurately reproduce simulation results

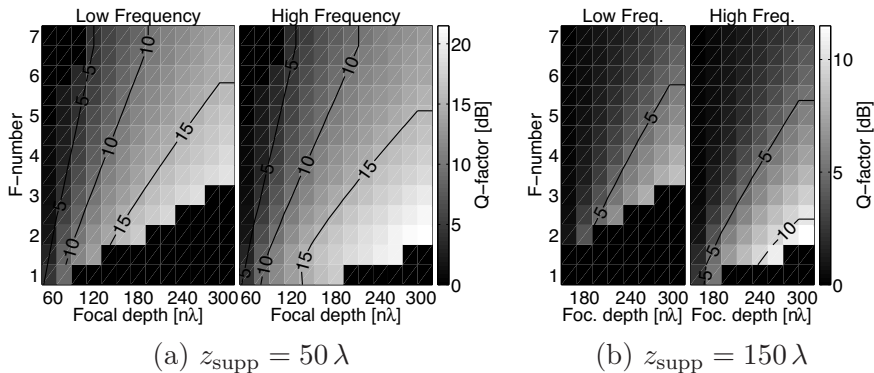


**Figure B.6:** Second-harmonic  $Q$ -factor values for near field suppression up to depth  $z_{\text{supp}}$ .

from media with the desired attenuation model. For the linear field, *i.e.*, the first-harmonic and fundamental, the compensation should be correct given a plane-wave attenuation model as in Eq. (B.12), but this is not the case for all three cases. Different values for  $\alpha_0$  and  $\beta$  influence the generation of higher harmonics, and this should cause the compensation to over-estimate the actual values. This is, however, not the case. The plane wave distance is given as the depth  $z$ , but this is also the distance to the closest point on the transducer, and contributions from off-axis transducer points are more attenuated than the center point.

When acoustic shock formation is present, the FSP value rapidly decreases. A compensation then overestimates the FSP value, and the numbers in Table B.4 are positive. This is the case for the fundamental and second-harmonic beam in both the low and high frequency setting when no attenuation is present. For the high frequency case, the fundamental beam shows shock formation when conservative attenuation is chosen.

The compensation tends to underestimate slightly, and more for higher frequencies. Over all, the compensation framework is consistent for compensation between smaller differences in the attenuation parameters  $\alpha_0$  and  $\beta$ .

Figure B.3 shows that the transmit pressure estimation in Eq. (B.16) performs equally well for a wide range of transducer configurations. The FSP of the second-harmonic beam is too low to challenge the safety regulations.

The maximum obtained FSP using regular attenuation ( $\alpha_0=0.52$ ,  $\beta=1.1$ ) are not above the limit for the mechanical index for any transducer configuration. In a non-linearly distorted wave field, diffraction causes the peak negative pressure to be lower than the peak positive pressure.<sup>2,23</sup> For a linear pulse,

the amplitude difference between the positive and negative peak pressure is small, and the maximum FSP of the filtered first-harmonic and fundamental pulse provides an estimate for the obtained mechanical index. The difference between the maximum FSP and the mechanical index is within  $-0.6$  to  $1.4$  dB for all three cases in both imaging modes, both frequency situations and all attenuation models used.

The estimation algorithm assumes conservative attenuation, and if the radiated beams are compensated to this, a constant value of the maximum FSP is expected. Fig. B.3 shows this effect. Some discrepancies are present: The estimation performs worse for low f-numbers and deep focal depths, and the maximum FSP is generally lower for the fundamental than the first-harmonic component for both frequencies.

The first is either related to the parabolic approximation in the KZK equation or the plane-wave attenuation model. A low f-number results in a high focusing gain,<sup>14,16,19</sup> and the parabolic approximation erroneously resolve waves with a steep inclination angle relative to the  $z$ -axis. This can cause unresolved edge waves and reduced focus gain. Plane-wave attenuation compensation of low f-number beams can also cause deviations because the distance to the edge of the transducer is relatively much longer than the depth coordinate  $z$ . The second effect is caused by a higher attenuation per wavelength for the fundamental frequency. The general level of the maximum FSP is approximately 20% lower than the mechanical index limit, and indicate that the transmit pressure estimation is conservative.

The signal-to-noise ratio of harmonic imaging is low compared to that of fundamental imaging, and therefore, it is even more important to optimize the signal-to-noise ratio for harmonic imaging. The focal point second-harmonic FSP in Fig. B.4 is a measure for the signal-to-noise ratio, and show that an optimal transducer configuration for both frequencies will result in approximately the same amount of harmonic FSP for identical transducer configurations. The general level of the low frequency FSP is slightly higher than the high frequency.

The most optimal configuration for second-harmonic generation in the low frequency situation has a f-number of 3, aperture of  $40 \lambda$  (18 mm) and is focused at  $120 \lambda$  (53 mm). For a typical cardiac setup, transducers seldom have larger apertures than 20 mm, and this limit is determined by the distance between the ribs. For deep abdominal imaging at the same frequency, the aperture may be larger, but this does not result in more second-harmonic generation. For the high frequency situation, the optimal configuration has a f-number of 2.5, aperture of  $40 \lambda$  (6 mm) and a focal depth of  $100 \lambda$  (14 mm). The values are lower for the high frequency due to the higher attenuation per wavelength.

For  $\beta=1$ , the two frequencies perform equally well when compensated to linear attenuation. The general level of the low frequency focal point FSP is slightly higher than the high frequency's, but this difference is not affected by the compensation. For  $\beta \neq 1$ , the generation of second-harmonic is reduced, and the reduction is larger for the high than the low frequency. This agrees with previous literature.<sup>20</sup>

Dashed curves indicating the Fresnel number of each beam in Fig. B.4 show that the optimal Fresnel number lies between 0.1 and 0.4. This agrees with previous literature.<sup>1</sup>

The *maximum* obtained second-harmonic FSP is also a qualitative measure of the signal-to-noise ratio, but does not provide any new insight unless the position where the maximum occurs is provided. The maximum level increases with increasing f-number and focal depth, and the general level of the maximum second-harmonic FSP is lower for the high frequency situation because of the higher attenuation. This result is not visualized.

The position of the maximum pressure relative to the focal depth ( $z_{\max}/F$ ) decreases for a constant f-number when the focal depth and Fresnel number is increased. This agrees with previous literature.<sup>1</sup> Attenuation causes a shift of the maximum further towards the transducer. The relative position for low f-number configurations is above one. This indicates that the second-harmonic achieves its maximum value beyond the geometric focal point. The same configuration shows this effect also for the first-harmonic and fundamental beam, and is an example of an artifact from the parabolic approximation in the KZK equation as the outward shift of the position of the maximum reported by Pinton and Trahey.<sup>30</sup>

All apertures in this study are circular. It is plausible that quadratic apertures will perform similarly.<sup>16,19</sup> Rectangular apertures with large difference in azimuth and elevation apertures will perform worse than quadratic for equal transmit pressure.<sup>13</sup> However, a smaller footprint of the transducer allows higher transmit pressure. The estimation used in this study for the transmit pressure may be inadequate for rectangular transducers.

According to Eq. (B.9), the generation of second-harmonic is invariant to transmit frequency for two identical setups in terms of wavelengths. Figure B.5 shows that this holds when the attenuation model is linear in frequency. When  $\beta \neq 1$ ,  $\bar{f}_c^\delta$  in Eq. (B.11) becomes different from one, and the generated fields are different. The differences are caused by the inclusion of the attenuation function  $A$  from Eq. (B.12) in both the Green's function in the integral over  $z_0$  in Eq. (B.10) and in the convolution  $(\hat{f}H_{1a}) *_{\omega} (\hat{f}H_{1a})$ . The relative pressure follows a straight decline with a dB-slope proportional to  $\bar{f}_{c,hi}^\delta - \bar{f}_{c,lo}^\delta$ , which indicates the

existence of an approximate plane-wave attenuation for the second-harmonic field  $p_{\text{nla}}=A(\alpha_0, \bar{f}_c^\delta, z, \omega)p_{\text{nl}}$  similar to Eq. (B.12) for the first-harmonic.

Different attenuation per wavelength will also cause the two frequency situations to have different shifts in center frequency. This will cause the diffraction for the two frequency situations to be different, and is a possible source of the visible ripple in Fig. B.5. Another indication on this being a diffraction phenomenon is the location of the ripple for the second case study. The ripple is located around  $60 \lambda$ , which corresponds to the location of the on-axis interference of the second-harmonic beam profiles in Fig. B.2.

For different transmit pressures, but equal transmit FSP, the shape of the field should according to Eq. (B.10) be identical, but the pressure level different. The relative second-harmonic FSP is, however, equal from the definition in Eq. (B.17). For linear attenuation, the relative FSP in the three case studies does not follow the 0dB line as well as the simulations with equal transmit pressures. The visible ripple is again caused by diffraction effects. The overall decline of the the relative FSP originates from how Abersim handles either the diffraction term or the nonlinear term of Eq. (3) in Ref. 29. Attenuation is solved using linear operators and should not introduce any amplitude dependent errors that do not cancel out when a relative measure is presented as in Fig. B.5. An error in the attenuation term would also result in a similar behavior for the equal transmit pressure panels in the left column of Fig. B.5. Both the parabolic diffraction model and nonlinear model can be susceptible to pressure dependent errors due to their iterative and nonlinear nature.<sup>29</sup>

Compensated, the simulations run with regular attenuation reproduce approximately the FSP-curves run with linear attenuation. The compensated curves are for case study 1 slightly lower and for case study 2 and 3 slightly higher than the actual result. From Table B.4 the numbers presenting the compensation errors, this behavior is as expected.

The suppression  $Q$ -factor is for all fundamental beams close to zero or slightly negative. In fundamental imaging, the compensated total energy of a plane at depth  $z$  will always be equal to or lower than the initial total energy transmitted through the transducer surface.

For two equal transducer setups in terms of wavelengths, the performance in suppression of near field echoes of the two frequencies (Fig. B.6) are similar. The suppression  $Q$ -factor assumes approximately the same value for a body-wall of either  $50 \lambda$  and  $150 \lambda$  for the two frequencies, and both setups perform best with a relatively thin body wall.

In physical measures, the body wall for the low and high frequency situation is approximately equally thick for non-obese patients, but is in terms of

wavelengths in the low frequency situation about one third of the one in the high frequency situation. Because of this, it is suggested that second-harmonic imaging at higher frequencies does not provide the same suppression as for low frequencies. This is one possible explanation why the improvement in image quality for carotid imaging is not as pronounced as it is for cardiac and abdominal imaging.<sup>4-12</sup>

Figure B.6 also shows that the  $Q$ -factor increases for low  $f$ -numbers and deep focal depths. For such a configuration, the near field first-harmonic pressure and second-harmonic generation are very low. When entering the short focal region, both the first- and second-harmonic pressure increases rapidly, but because of the short focal region, the total amount of second-harmonic generation is still rather low when looking at Fig. B.4.

## B.6 Conclusion

Transmit beams from a range of transducer configurations for a low and high frequency situation are compared to evaluate second-harmonic generation and suppression of near field echoes. The transmit pressure is estimated to not violate safety regulations for each configuration, and the estimation algorithm utilized has been shown to perform equally well for a wide range of  $f$ -numbers and focal depths, but is conservative.

According to previous literature, the second-harmonic is shown to be identical for equal transmit pressures and linear-in-frequency attenuation. For power-law attenuation  $f^\beta$  with  $\beta > 1$ , equal transmit pressures generate almost shape invariant second-harmonic fields, but some discrepancies related to diffraction are found. Equal transmit FSP produces some shape variations. These variations are either related to approximations made in the model for diffraction or second-harmonic generation.

The optimal configurations for a high signal-to-noise ratio are for a medium with regular attenuation a  $f$ -number in the range 2–3.5 and a focal depth of  $100 \lambda$ – $180 \lambda$  (45–80 mm) for the low frequency situation and  $80 \lambda$ – $140 \lambda$  (11–19 mm) for the high.

In the presence of a body wall, it is suggested that the ability to suppress near field echoes is equal for the two frequency situations when the body wall is equally thick in terms of wave lengths. The body wall is in non-obese patients approximately equally thick in terms of millimeters. Because of this, the body wall is thinner in terms of wavelengths for low frequency applications, and the suggested suppression  $Q$ -factor is higher. A previously presented<sup>22</sup> higher sensitivity to phase aberrations for higher frequencies cohere with the argument that

high frequency applications may be more vulnerable to heterogeneous effects than low frequency applications.

## Acknowledgements

The authors would like to thank the Norwegian Research Council for funding and Trond Varslot for fruitful discussions and valuable input related to the theory section of this paper.

## References

- [1] B. A. J. Angelsen, *Ultrasound Imaging*. Trondheim, Norway: Emantec, 2000, vol. 1.
- [2] —, *Ultrasound Imaging*. Trondheim, Norway: Emantec, 2000, vol. 2.
- [3] B. Schrope, V. Newhouse, and V. Uhlendorf, “Simulated Capillary Blood Flow Measurement Using a Nonlinear Ultrasonic Contrast Agent,” *Ultrasound. Im.*, vol. 14, pp. 134–58, 1992.
- [4] J. D. Thomas and D. N. Rubin, “Tissue Harmonic Imaging: Why Does it Work,” *J. Am. Soc. Echocar.*, vol. 11, pp. 803–8, 1998.
- [5] S. P. Turner and M. J. Monaghan, “Tissue Harmonic Imaging for Standard Left Ventricular Measurements: Fundamentally Flawed?” *Eur. J. of Echocar.*, vol. 7, pp. 9–15, 2005.
- [6] T. S. Desser, R. B. Jeffrey, M. J. Lane, and P. W. Ralls, “Tissue Harmonic Imaging: Utility in Abdominal and Pelvic Sonography,” *J. Clin. Ultrasound*, vol. 27, pp. 135–42, 1999.
- [7] F. Tranquart, N. Grenier, V. Eder, and L. Pourcelot, “Clinical Use of Ultrasound Tissue Harmonic Imaging,” *Ultrasound Med. & Biol.*, vol. 28, pp. 889–94, 1999.
- [8] S. J. Rosenthal, P. L. Jones, and L. H. Wetzel, “Phase Inversion Tissue Harmonic Sonographic Imaging: A Clinical Study,” *Am. J. of Roentgenol.*, vol. 176, pp. 1393–8, 2001.
- [9] U. Bartram and K. Darge, “Harmonic vs Conventional Ultrasound Imaging of the Urinary Tract of Children,” *Ped. Radiol.*, vol. 35, pp. 655–60, 2005.

- 
- [10] D. Paladini, M. Vassallo, A. Tartaglione, and P. Martinelli, "The Role of Tissue Harmonic Imaging in Fetal Echocardiography," *Ultrasound Obstet. Gynecol.*, vol. 23, pp. 159–64, 2004.
- [11] W. A. Willinek, M. von Falkenhausen, H. Strunk, and S. H. H, "Tissue Harmonic Imaging in Comparison With Conventional Sonography: Effect on Image Quality and Observer Variability in the Measurement of the Intima Media Thickness in the Common Carotid Artery," *RoFo*, vol. 172, pp. 641–5, 2000.
- [12] C.-L. Yen, H.-Y. Chang, S.-Y. Huang, Y.-C. Huang, and C.-M. Jeng, "Combination of Tissue Harmonic Sonography, Real-Time Spatial Compound Sonography and Adaptive Image Processing Technique for the Detection of Carotid Plaques and Intima-Medial Thickness," *Eur. J. of Radiol.*, vol. 71, pp. 11–6, 2009.
- [13] A. C. Baker, A. M. Berg, A. Sahin, and J. N. Tjøtta, "The Nonlinear Pressure Field of Plane, Rectangular Apertures: Experimental and Theoretical Results," *J. Acoust. Soc. Am.*, vol. 97, pp. 3510–7, 1995.
- [14] Y.-S. Lee and M. F. Hamilton, "Time Domain Modeling of Pulsed Finite-Amplitude Sound Beams," *J. Acoust. Soc. Am.*, vol. 97, pp. 906–17, 1995.
- [15] T. Christopher, "Finite Amplitude Distortion-Based Inhomogenous Pulse Echo Ultrasound Imaging," *IEEE Trans. Ultrason., Ferroelect., Freq. Contr.*, vol. 44, pp. 125–9, 1997.
- [16] M. A. Averkiou and M. F. Hamilton, "Nonlinear Distortion of Short Pulses Radiated by Plane and Focused Circular Pistons," *J. Acoust. Soc. Am.*, vol. 102, pp. 2539–48, 1997.
- [17] T. Christopher, "Experimental Investigation of Finite Amplitude Distortion-Based, Second Harmonic Pulse Echo Ultrasound Imaging," *IEEE Trans. Ultrason., Ferroelect., Freq. Contr.*, vol. 45, pp. 158–62, 1998.
- [18] M. A. Averkiou, "Tissue Harmonic Imaging," in *IEEE Ultrason. Symp. Proc.*, 2000, pp. 1563–72.
- [19] X. Yang and R. O. Cleveland, "Time Domain Simulation of Nonlinear Acoustic Beams Generated by Rectangular Pistons With Application to Harmonic Imaging," *J. Acoust. Soc. Am.*, vol. 117, pp. 113–23, 2005.

- 
- [20] V. A. Khokhlova, A. E. Ponomarev, M. A. Averkiou, and L. A. Crum, "Nonlinear Pulsed Ultrasound Beams Radiated by Rectangular Focused Diagnostic Transducers," *Acoust. Phys.*, vol. 52, pp. 481–9, 2006.
- [21] T. Varslot, S.-E. Måsøy, T. F. Johansen, and B. A. J. Angelsen, "Aberration in Nonlinear Acoustic Wave Propagation," *IEEE Trans. Ultrason., Ferroelect., Freq. Contr.*, vol. 54, pp. 470–9, 2007.
- [22] H. Kaupang, S.-E. Måsøy, T. Varslot, T. F. Johansen, and B. A. J. Angelsen, "Generation and Aberration of Second-Harmonic Ultrasound Beams in Heterogeneous Tissue," in *IEEE Ultrason. Symp. Proc.*, 2006, pp. 2160–3.
- [23] M. Hamilton and D. T. Blackstock, *Nonlinear Acoustics*. San Diego: Academic Press, 1997.
- [24] G. Taraldsen, "A Generalized Westervelt Equation for Nonlinear Medical Ultrasound," *J. Acoust. Soc. Am.*, vol. 109, pp. 1329–33, 2001.
- [25] F. A. Duck, *Physical Properties of Tissue*. London: Academic Press, 1990.
- [26] C. R. Hill, J. C. Bamber, and G. R. ter Haar, *Physical Principles of Medical Ultrasound*, 2nd ed. Chichester, England: John Wiley & Sons, Ltd., 2004.
- [27] *IEC 62359: Ultrasonics - Field Characterization*, 1st ed., International Electrotechnical Commission, Geneva, Switzerland, Apr 2005.
- [28] M. E. Frijlink, H. Kaupang, T. Varslot, and S.-E. Måsøy, "Abersim: A Simulation Program for 3D Nonlinear Acoustic Wave Propagation for Arbitrary Pulses and Arbitrary Transducer Geometries," in *IEEE Ultrason. Symp. Proc.*, 2008, pp. 1282–5.
- [29] T. Varslot and G. Taraldsen, "Computer Simulation of Forward Propagation in Soft Tissue," *IEEE Trans. Ultrason., Ferroelect., Freq. Contr.*, vol. 52, pp. 1473–82, 2005.
- [30] G. F. Pinton and G. E. Trahey, "A Comparison of Time-Domain Solutions for the Full-Wave Equation and the Parabolic Wave Equation for a Diagnostic Ultrasound Transducer," *IEEE Trans. Ultrason., Ferroelect., Freq. Contr.*, vol. 55, pp. 730–3, 2008.

# A Time-Domain Spectral Element Method for Propagation of Pulses in Nonlinear Soft Tissue

Halvard Høiland-Kaupang and Bjørn Angelsen

Department of Circulation and Medical Imaging, NTNU, Trondheim, Norway

## Abstract

A time-domain Spectral Element Method (SEM) for acoustic wave propagation in nonlinear and absorbing media is presented. The presented method seek to combine the spatial convergence of a spectral method with the versatility of an element method for a coupled system of first order equations. Similar SEM are previously reported for linear, elastodynamic models in seismic research. Here, the model is extended to include nonlinear elasticity and power-law frequency dependent absorption. The method is compared with analytic solutions for plane wave propagation and to an existing simulation tool for two-dimensional test cases. For linear propagation, a polynomial order of  $N=8$  and four points per minimum wavelength produce acceptable errors for the frequency dependent absorption and phase speed of the medium. The nonlinear model requires a higher order to resolve harmonic generation up to the maximum desired frequency, and  $N=16$  is found to be sufficient when four points per minimum wavelength is employed. For two-dimensional, nonlinear propagation  $N=16$  ensures adequate accuracy. The nonlinear model is the most prominent source of error, and the error is reduced when both absorption and non-linearity is used.

## C.1 Introduction

Images created with medical ultrasound suffer from the influence of acoustic noise caused by heterogeneities in the tissue.<sup>1</sup> Two main sources of acoustic noise, or clutter, is phase aberrations and reverberations (multiple scattering).<sup>1</sup> These noise contributions degrade the image and conceal important information needed for proper diagnosis.

Numerical models play an important role in understanding acoustic phenomena such as nonlinear elasticity of tissue and effects of heterogeneities.<sup>2-6</sup> Forward effects, such as harmonic generation and phase aberrations can be studied using one-way, or forward, models. Forward models are often integrated in space, *i.e.*, depth, and several tools are available.<sup>7-12</sup> The effect of scattering, however, is not easily incorporated into one-way models for more complex, *i.e.*, realistic, scattering situations. To study back scatter, either first or higher order, a full wave model integrating the model equation(s) in time within a finite spatial domain is preferred.<sup>2,6,13-21</sup>

Full wave numerical models have one aspect in common: The need of a spatial domain discretization. There are several available and well-known spatial discretization schemes such as Finite Differences (FD),<sup>6,16,19,20</sup> Fourier ( $k$ -space) discretizations,<sup>17,18</sup> Finite Elements (FE)<sup>2,21</sup> and Spectral Elements (SE).<sup>14,15</sup> Both Finite Elements and Spectral Elements are based on the element method, and the term “Finite” and “Spectral” often refer to the order of the polynomial used for approximation.

Each of these methods have advantages and disadvantages. Finite difference methods are simple to implement on structured grids, but suffer from numerical dispersion.<sup>15,16,18</sup> Fourier based, or  $k$ -space, methods show rapid convergence and does not suffer from numerical dispersion.<sup>17,18</sup> Boundary conditions can be somewhat troublesome to implement due to the requirement of periodic boundaries in the discrete Fourier transform, and initial conditions are more often used.<sup>17,18</sup>

Low order FE methods have the same disadvantage of numerical dispersion and need of high spatial sampling as FD methods.<sup>15,22-24</sup> Where FD methods are limited to structured grids, FE methods have the advantage of unstructured grids, and the ability to solve for complex geometries.<sup>23</sup> Spectral Element methods are, on the other hand, shown to provide rapid convergence for solutions meeting certain regularity requirements.<sup>24</sup>

The following sections will present a Spectral Element Method (SEM) for acoustic wave propagation in nonlinear absorbing media. A SEM is chosen to combine the spatial accuracy of a spectral method with the ability to match complex geometries and boundary conditions of a general element method. In

this paper, only simple geometries are employed, and the boundary conditions are of standard Dirichlet type. The method is analyzed and verified for plane wave and two-dimensional propagation.

## C.2 Mathematical Model

### C.2.1 Model Equations

Acoustic wave propagation is described by Newton's second law of motion and a constitutive equation as

$$\rho \frac{\partial \mathbf{u}}{\partial t} = -\nabla p \quad (\text{C.1})$$

$$\mathcal{K}(t, p) \underset{t}{*} \frac{\partial p}{\partial t} = -\nabla \cdot \mathbf{u}. \quad (\text{C.2})$$

Here  $\mathbf{u}=[u, v]^T$  denotes particle velocity,  $p$  the local pressure,  $\rho$  the density and  $\mathcal{K}$  the generalized compressibility accounting for (nonlinear) elasticity and absorption.<sup>16,18,25,26</sup> The generalized compressibility of a nonlinear medium with absorption is

$$\mathcal{K}(t, p) = \tilde{K}(p)\delta(t) + \sum_n \frac{\kappa_n}{\tau_n} e^{-t/\tau_n} H(t)$$

where  $\delta$  is the delta distribution,  $\tilde{K}(p)$  a pressure dependent elasticity,  $H$  the Heaviside distribution and  $\kappa_n$  and  $\tau_n$  the relative compressibilities and the time constants for a number of relaxation processes accounting for absorption.<sup>16,25</sup> The elasticity,  $\tilde{K}(p)$ , is implicitly defined such that  $K(t, p)=\tilde{K}(p)\delta(t) \underset{t}{*} p$  where  $K(t, p)$  is the pressure-density relation.<sup>26</sup> Similar approaches for frequency power-law absorption are found in Refs. 6, 20 and 21. A variable substitution  $S_n=\kappa_n/\tau_n e^{-t/\tau_n} H(t) \underset{t}{*} p$  is introduced,<sup>16</sup> where  $S_n$  satisfies the equation

$$\frac{\partial S_n}{\partial t} = -\frac{1}{\tau_n} S_n + \frac{\kappa_n}{\tau_n} p.$$

Substituting this into Eq. (C.2), and using the relation  $f' \underset{t}{*} g=f \underset{t}{*} g'=(f \underset{t}{*} g)'$ , the left hand side of Eq. (C.2) can be expressed in terms of  $p$ ,  $\partial p/\partial t$ , and  $S_n$  as

$$\mathcal{K}(t, p) \underset{t}{*} \frac{\partial p}{\partial t} = K'(t, p) \frac{\partial p}{\partial t} + \sum_n \frac{\kappa_n}{\tau_n} p - \sum_n \frac{1}{\tau_n} S_n \quad (\text{C.3})$$

where  $K'(t, p)$  is the derivative of  $K(t, p)$ .

For aqueous media, a second order Taylor expansion of the pressure–density relation,  $K(t, p) = \kappa_\infty p - \beta_n \kappa_\infty^2 p^2$ , is a natural choice.<sup>26</sup> Using a general elasticity function  $K(t, p)$  yields a pressure dependent speed of sound,  $c(p) = 1/\rho_0 K'(t, p)$ , where  $c_0 = 1/\rho_0 \kappa_0$  for the linear, non-absorbing case.<sup>25</sup> A similar nonlinear model is also proposed in Ref. 2.

Combining Eqs. (C.1)–(C.3), the final equations for acoustic wave propagation are on scaled and dimensionless form:

$$\rho \frac{\partial \mathbf{u}}{\partial t} = -\nabla p + b.c. \quad (\text{C.4})$$

$$\frac{\partial S_n}{\partial t} = -\frac{1}{\tau_n} S_n + \frac{\kappa_n}{\tau_n} p \quad (\text{C.5})$$

$$K'(t, p) \frac{\partial p}{\partial t} = -\nabla \cdot \mathbf{u} - \sum_n \frac{\kappa_n}{\tau_n} p + \sum_n \frac{1}{\tau_n} S_n + b.c. \quad (\text{C.6})$$

where *b.c.* denotes contributions from the boundary conditions.

The boundary is defined by two regions,  $\Gamma_{\text{xd}}$  and  $\Gamma_{\text{abs}}$ , where  $\Gamma_{\text{xd}}$  defines the vibrating transducer surface and  $\Gamma_{\text{abs}}$  an absorbing boundary. The transducer surface,  $\Gamma_{\text{xd}}$ , is assumed to be a line (or surface in three dimensions) with a normal vibration velocity, *i.e.*,  $u(s, t) = g(s, t)$ . Absorbing boundary conditions are modeled using Perfectly Matched Layers (PML).<sup>16,18</sup> These matched layers are introduced as an absorbing padding of the original domain. Within the PML region, the term  $\alpha \mathbf{u}$  is added to the left hand side of the velocity equation (C.4) and  $\alpha p$  to the pressure equation (C.6) such that the left hand side of Eq. (C.2) is re-written as  $\mathcal{K}(p) *_t (\partial p / \partial t + \alpha p)$ .<sup>16,18</sup> The vector  $\alpha = [\alpha_x \ \alpha_y]^T$  are artificial damping constants working in the *x* and *y* direction only, and is equal to zero within the main calculation domain.

For this to be effective, scalar fields, such as  $p$  and  $S_n$ , need to be vectorized as  $p = p_x + p_y$  within the PML region. The subscript denotes the direction of the component. The pressure and state variable equations then modifies to two equations each for the two-dimensional case.<sup>16,18</sup> In future equations,  $\alpha$  and constants dependent on this will, as a reminder, be written as a vector symbol, but the vectorized pressure equation will not be written out. The PML regions will at the outer boundaries be defined as hard walls where the normal velocity  $u_n = 0$ . Using this formulation all outer boundaries are of homogeneous Dirichlet type.<sup>23</sup>

## C.2.2 Spectral Element Discretization

A spectral element discretization based on high order and orthogonal Legendre polynomials is chosen.<sup>14,15,27–29</sup> As for classical finite element methods, the so-

lution of the velocity and pressure is locally defined within each element and required to be continuous over inter-element boundaries. The general framework of the element methods is based on a variational, or weak, formulation of the model problem.<sup>23</sup> The SEM presented by in Refs. 14 and 15 presents a method for an elastodynamic problem formulation with both a second-order spatial and temporal differentiation. The following section will present a similar method for the pressure–velocity formulation presented in Ref. 16.

Assume the solutions of Eqs. (C.4)–(C.6) are to be found in the spaces  $u, v \in V$  and  $p, S_n \in W$  for the velocity and pressure respectively. A two-dimensional variational formulation of Eqs. (C.4)–(C.6) is

$$\frac{\partial}{\partial t} (\rho u, \phi) + (\rho \alpha_x u, \phi) = -\tilde{c}_x(p, \phi) \quad (\text{C.7})$$

$$\frac{\partial}{\partial t} (\rho v, \varphi) + (\rho \alpha_y v, \varphi) = -\tilde{c}_y(p, \varphi) \quad (\text{C.8})$$

$$\frac{\partial}{\partial t} (S_n, \vartheta) + \left( \frac{1}{\tau_n} S_n, \vartheta \right) = \left( \frac{\kappa_n}{\tau_n} p, \vartheta \right) \quad (\text{C.9})$$

$$\begin{aligned} \frac{\partial}{\partial t} (K(t, p), \psi) + (\boldsymbol{\mu}(t, p)p, \psi) &= \sum_n (\boldsymbol{\nu}_n S_n, \psi) \\ &\quad -c_x(u, \psi) - c_y(v, \psi) \end{aligned} \quad (\text{C.10})$$

where  $\boldsymbol{\mu}(t, p) = \sum_n \kappa_n / \tau_n + \tilde{K}(p)\boldsymbol{\alpha}$ ,  $\boldsymbol{\nu}_n = 1/\tau_n - \boldsymbol{\alpha}$ ,  $\phi, \varphi \in V$  and  $\psi, \vartheta \in W$  are general test functions, and  $(\cdot, \cdot)$  and  $c_x(\cdot, \cdot)$  are defined as

$$(\phi, \varphi) = \int_{\Omega} \phi \varphi \, d\Omega \quad (\text{C.11})$$

$$c_x(\phi, \psi) = \int_{\Omega} \frac{\partial \phi}{\partial x} \psi \, d\Omega. \quad (\text{C.12})$$

The abstract convection form  $\tilde{c}_x(\cdot, \cdot)$  is structurally equivalent to  $c_x(\cdot, \cdot)$  in the sense that the first variable is differentiated. The linear form  $(\cdot, \cdot)$  contains an integration over two function from  $V$  (or possibly  $W$ ) and is symmetric in the sense that  $(\phi, \varphi) = (\varphi, \phi)$ . The abstract form  $c_x(\cdot, \cdot)$  takes its first argument from  $V$  and its second from  $W$  (and vice versa for  $\tilde{c}_x(\cdot, \cdot)$ ), and is antisymmetric in the sense that

$$\begin{aligned} c_x(\phi, \psi) &= \int_{\Omega} \frac{\partial \phi}{\partial x} \psi \, d\Omega \\ &= [\phi \psi]_{\Gamma} - \int_{\Omega_e} \phi \frac{\partial \psi}{\partial x} \, d\Omega \\ &= -c_x(\psi, \phi) = \tilde{c}_x(\psi, \phi). \end{aligned} \quad (\text{C.13})$$

Here, the boundary term vanishes because the test function  $\phi \in V$  has to honor the Dirichlet conditions given on  $\Gamma$ .<sup>23</sup>

In Eqs. (C.7)–(C.10), the integrals are computed numerically using Gauss-Lobatto-Legendre (GLL) quadrature as

$$\int_{-1}^1 f(\xi) d\xi \approx \sum_{\alpha=0}^N w_{\alpha} f(\xi_{\alpha}) \quad (\text{C.14})$$

where the quadrature points,  $\xi_{\alpha}$ , are the roots of the polynomial  $(1-\xi^2)P'_{N-1}(\xi)$  where  $P'_{N-1}(\xi)$  is the derivative of the  $(N-1)$ 'th order Legendre polynomial, and  $w_{\alpha}$  the quadrature weights.<sup>28</sup> GLL quadrature is shown to exactly compute integrals for polynomial functions of order  $2N-1$ .<sup>28</sup>

The solutions are approximated with Lagrange interpolation polynomials  $\ell(\xi)$ , where the  $i$ 'th polynomial is defined as

$$\ell_i(\xi) = \prod_{\substack{j=0 \\ i \neq j}}^N \frac{(\xi - \xi_j)}{(\xi_i - \xi_j)}, \quad i = 0, \dots, N,$$

where  $\xi_i$  and  $\xi_j$  are the chosen pole and roots of the Lagrange polynomial.<sup>28</sup> Choosing  $\xi_j$  to be the quadrature nodes  $\xi_{\alpha}$  in the reference interval  $[-1, 1]$  yields  $\ell_i(\xi_{\alpha}) = \delta_{\alpha i}$  where  $\delta_{\alpha i}$  is the Kronecker delta.<sup>28</sup> Each of the solutions for the velocity, pressure and state variable is assumed to have a nodal basis such that  $f_{qr} = f(\xi_q, \eta_r)$ . This formulation is also assumed for material parameters. Each numerical solutions are defined in two dimensions as

$$f(\xi, \eta, t) \approx f_N(\xi, \eta, t) = \sum_e \sum_{q,r=0}^N f_{qr}^e(t) \ell_q(\xi) \ell_r(\eta), \quad (\text{C.15})$$

where  $f_{qr}^e$  are the nodal weights,  $\ell$  the  $k$ 'th and  $l$ 'th Lagrange polynomial. Extension to one or three dimensions follows directly from this by removing or adding one polynomial in the product.

The quadrature in Eq. (C.14) and solution in Eq. (C.15) require each element to be defined as the reference  $\hat{\Omega} = [-1, 1]^d$  where  $d$  denotes the number of dimensions. The full domain is considered to be a multi-element domain defined as  $\Omega = \bigcup \Omega_e$ , where  $\Omega_e$  is each local element domain. The local elements are non-overlapping, and the full integral can be expressed as  $\int_{\Omega} = \sum_e \int_{\Omega_e}$ .<sup>23</sup> A transformation mapping each local element into the reference domain is needed such that variables and solutions can be expressed as  $f(x, y) = f(x(\xi, \eta), y(\xi, \eta)) = \hat{f}(\xi, \eta)$ . Integration over each local element can

be expressed as an integral over the reference domain through the Jacobian  $d\mathbf{x} = \mathbf{J}d\xi$  as

$$\int_{\Omega_e} f(x, y) d\Omega = \int_{\hat{\Omega}_e} \hat{f}(\xi, \eta) J d\hat{\Omega}$$

where  $J$  is the determinant of the Jacobian,  $\mathbf{J}$ , and  $\Omega_e$  and  $\hat{\Omega}_e$  are the physical and reference element domains respectively.<sup>30</sup> The right hand side integral is then computed using GLL quadrature. The Jacobian can be calculated for each internal node in the element domain. For rectangular elements,  $\Omega_e = [0, L_x] \times [0, L_y]$ , the mapping from  $\hat{\Omega}$  to  $\Omega$  is

$$x(\xi) = \frac{L_x}{2}(\xi + 1) \quad \text{and} \quad y(\eta) = \frac{L_y}{2}(\eta + 1), \quad (\text{C.16})$$

and the Jacobian and its determinant are found to be

$$\mathbf{J} = \frac{\partial \mathbf{x}}{\partial \xi} = \begin{bmatrix} \frac{L_x}{2} & 0 \\ 0 & \frac{L_y}{2} \end{bmatrix}, \quad J = \frac{L_x L_y}{4} \quad (\text{C.17})$$

for all nodes within the element.

Maday and Rønquist present a method using over-integration to cope with deformed geometries and heterogeneous materials. This technique is shown to have no effect if the background media is more regular, or smooth, than the solution itself.

The solution spaces for the velocity ( $V$ ) and pressure and state variables ( $W$ ) are denoted with different letters to indicate that they can be different. They can be set as equal, but are in the following sections defined to be different. The space  $V$  is defined to be the set of all  $N$ 'th order Lagrange polynomials,  $\ell(\xi)$ , defined over the  $N+1$  GLL quadrature points in  $[-1, 1]$  (the endpoints included).

In the following sections, the pressure and the relaxation processes are defined only in the interior of each element, and not on local element boundaries. The order of the polynomial is also reduced. The interpolation functions are still Lagrange polynomials, but now denoted  $\tilde{\ell}$  to distinguish them from the polynomials in  $V$ . The space  $W$  is constructed of all Lagrange polynomials of order  $\tilde{N} (< N)$ , and the integrals are computed using *Gauss-Legendre* (GL) quadrature.<sup>28</sup> GL quadrature is constructed similarly to Eq. (C.14), and computes the integral exactly for polynomials of order up to  $2\tilde{N}+1$  where  $\tilde{N}$  is the order of the polynomial. A visualization of the velocity and pressure nodes of one element as well as an example of the Lagrange polynomials  $\ell_i$  and  $\tilde{\ell}_i$  is presented in Fig. C.1. A similar approach is used in fluid mechanics for an order reduction of 2 and is known as the  $P_N \times P_{N-2}$ -method.<sup>31</sup>

For the GL quadrature points,  $\tilde{\xi}$ , each  $\tilde{\ell}_i(\tilde{\xi}_\alpha) = \delta_{\alpha i}$ .<sup>28</sup> In the abstract form  $\tilde{c}_x(\cdot, \cdot)$ , both a function from  $V$  and  $W$  appear, and the integral is solved using GL quadrature with an interpolation operator,  $I$ , such that  $I \cdot \ell(\xi_\alpha) = \ell_i(\tilde{\xi}_\alpha) = I_{\alpha i}$ . Spatial derivatives of  $\ell$  can be found for the *GLL quadrature points* and is denoted  $\ell'_i(\xi_\alpha) = D_{\alpha i}$ , and the derivative  $\ell'(\tilde{\xi}_\alpha)$  is found to be  $I \cdot \ell'_i(\xi_\alpha) = (ID)_{\alpha i}$ .<sup>28,31</sup>

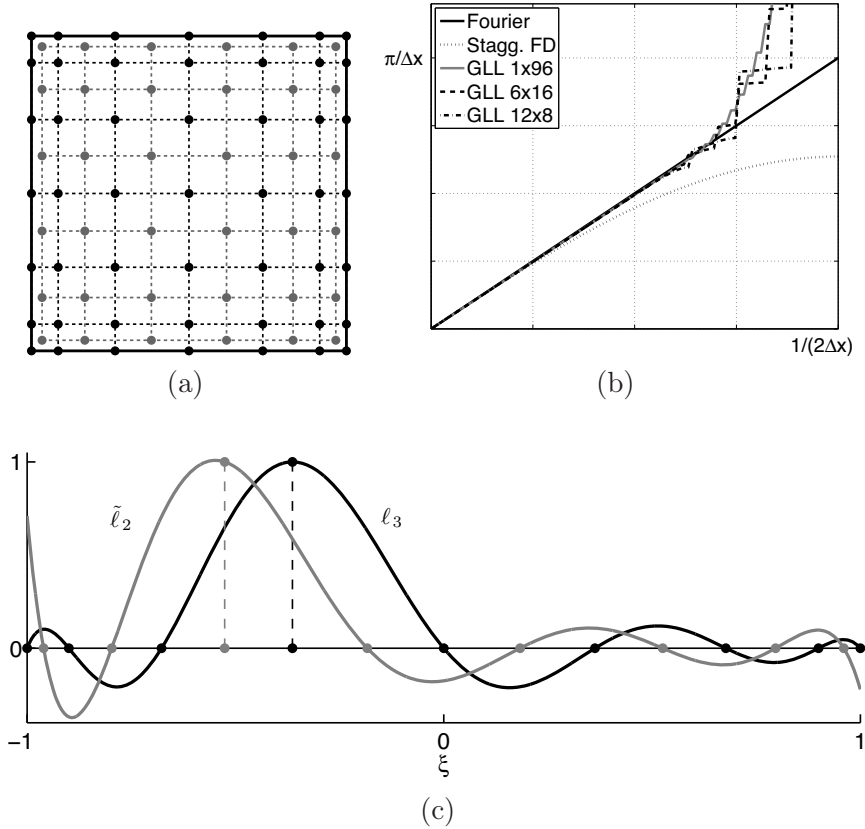


**Figure C.1:** Spectral element discretization. a) Reference element with velocity (black) and pressure (gray) nodes for  $N=6$  b) Spatial frequency response for a Fourier, staggered FD and SE discretization. For the SE case,  $N_e \times N$  denotes the number of elements  $\times$  the polynomial order. c) Example of a Lagrange interpolation polynomial,  $\ell$ , for the velocity space (black,  $N=8$ ) and  $\tilde{\ell}$  for the pressure space (gray,  $\tilde{N}=7$ ).

The left hand side integral of Eq. (C.7) over one local element can be written

as

$$\begin{aligned}
 (\rho u, \phi)_e &= \int_{\Omega_e} \rho u \phi d\Omega \\
 &= \sum_{q,r=0}^N \hat{u}_{qr}(t) \int_{\hat{\Omega}_e} \rho(\xi, \eta) \ell_q(\xi) \ell_r(\eta) \ell_i(\xi) \ell_j(\eta) J d\hat{\Omega} \\
 &\approx \frac{L_x L_y}{4} \sum_{q,r=0}^N \hat{u}_{qr}(t) \sum_{\alpha,\beta=0}^N w_\alpha w_\beta \rho_{\alpha\beta} \delta_{\alpha q} \delta_{\beta r} \delta_{\alpha i} \delta_{\beta j} \\
 &= \frac{L_x L_y}{4} w_i w_j \rho_{ij} \hat{u}_{ij}(t)
 \end{aligned} \tag{C.18}$$

where  $\rho_{\alpha\beta} = \rho(\xi_\alpha, \eta_\beta)$ ,  $\phi$  is chosen to be the product of the Lagrange polynomials  $\ell_i$  and  $\ell_j$  for all  $i$  and  $j$  successively, and the Jacobian from Eq. (C.17) is used. If the linear form is evaluated for two function from  $W$ , GL quadrature is used with quadrature weights,  $\tilde{w}_\alpha$ , and Jacobian,  $\tilde{J}_{ij}$ , evaluated at  $(\tilde{\xi}_i, \tilde{\eta}_j)$ . For the integral in Eq. (C.10),  $K'(t, p)$  introduces a spatially dependent speed of sound. The regularity of the pressure dependent speed of sound is the same as the solution, and the proposed over-integration in Ref. 30 is not employed.

Integration of the abstract form  $c_x^e(\cdot, \cdot)$  introduce differentiation of the second argument, affecting only the Lagrange polynomial from  $V$  due to the nodal basis of the solution. Because all elements are assumed to be rectangular, a full differentiation is not needed. The inverse of the Jacobian,  $\mathbf{J}^{-1} = \partial \boldsymbol{\xi} / \partial \mathbf{x} = \boldsymbol{\xi}_x$  is diagonal and  $\xi_x = 2/L_x$  and  $\eta_y = 2/L_y$ . Both  $\eta_x$  and  $\xi_y$  are zero. Introducing this differentiation to the abstract form in Eq. (C.13), the expression becomes

$$\begin{aligned}
 c_x^e(\phi, p) &= \int_{\Omega_e} \phi_x p d\Omega = \int_{\hat{\Omega}_e} \xi_x \phi \xi p J d\hat{\Omega} \\
 &= \frac{L_x L_y}{4} \sum_{q,r=0}^{\tilde{N}} \hat{p}_{qr}(t) \int_{\hat{\Omega}_e} \tilde{\ell}_q(\xi) \tilde{\ell}_r(\eta) \frac{2}{L_x} \ell'_i(\xi) \ell_j(\eta) d\hat{\Omega} \\
 &\approx \frac{L_y}{2} \sum_{q,r=0}^{\tilde{N}} \hat{p}_{qr}(t) \sum_{\alpha,\beta=0}^{\tilde{N}} \tilde{w}_\alpha \tilde{w}_\beta \delta_{\alpha q} \delta_{\beta r} (ID)_{\alpha i} I_{\beta j} \\
 &= \frac{L_y}{2} \sum_{q,r=0}^{\tilde{N}} \tilde{w}_q \tilde{w}_r (ID)_{qi} I_{rj} \hat{p}_{qr}(t)
 \end{aligned} \tag{C.19}$$

for all  $i, j=1, \dots, N$ . A similar expression for  $c_x^e(u, \psi)$  can be found as

$$c_x^e(u, \psi) \approx \frac{L_y}{2} \tilde{w}_i \tilde{w}_j \sum_{q,r=0}^N (ID)_{iq} I_{jr} \hat{u}_{qr}(t) \quad (\text{C.20})$$

Note that the range of summation of the solution and range of available test functions are switched and that summation in Eq. (C.20) runs over  $q, r=0, \dots, N$  whereas the indices  $i, j=0, \dots, \tilde{N}$ . A similar approach is used for  $c_y^e(\cdot, \cdot)$ .

Applying the presented Spectral Element framework to Eqs. (C.7)–(C.10), some simplifications can be made. Both the quadrature weights and the Jacobian cancel out for Eqs. (C.9) and (C.10) because the space  $W$  is defined such that neither the pressure nor the state variables  $S_n$  are defined on inter-element boundaries.

The final system of semi-discretized equations for one element is

$$w_i w_j \rho_{ij} \left( \frac{\partial \hat{u}_{ij}}{\partial t} + \alpha_{ij}^{(x)} \hat{u}_{ij} \right) = \frac{2}{L_x} \sum_{q,r=0}^{\tilde{N}} \tilde{w}_q \tilde{w}_r (ID)_{qi} I_{rj} \hat{p}_{qr}(t) \quad (\text{C.21})$$

$$w_i w_j \rho_{ij} \left( \frac{\partial \hat{v}_{ij}}{\partial t} + \alpha_{ij}^{(y)} \hat{v}_{ij} \right) = \frac{2}{L_y} \sum_{q,r=0}^{\tilde{N}} \tilde{w}_q \tilde{w}_r (ID)_{qi} I_{rj} \hat{p}_{qr}(t) \quad (\text{C.22})$$

$$\left( \frac{\partial (\hat{S}_n)_{ij}}{\partial t} + \frac{1}{\tau_{ij}^{(n)}} (\hat{S}_n)_{ij} \right) = \frac{\kappa_{ij}^{(n)}}{\tau_{ij}^{(n)}} \hat{p}_{ij} \quad (\text{C.23})$$

$$\left( \hat{K}'_{ij}(t, \hat{p}_{ij}) \frac{\partial \hat{p}_{ij}}{\partial t} + \hat{\mu}_{ij}(t, \hat{p}_{ij}) \hat{p}_{ij} \right) = \sum_n \frac{1}{\tau_{ij}^{(n)}} (\hat{S}_n)_{ij} \quad (\text{C.24})$$

$$- \frac{2}{L_x} \sum_{q,r=0}^N (ID)_{iq} I_{jr} \hat{u}_{qr}(t) - \frac{2}{L_y} \sum_{q,r=0}^N (ID)_{iq} I_{jr} \hat{v}_{qr}(t)$$

where the range of  $i$  and  $j$  are from 0 to  $N$  or  $\tilde{N}$  determined by the the space of the solution on the left hand side of each equation. The final left and right hand side are the elemental mass and stiffness matrices. The final assembly of the full mass and stiffness matrices is not performed in practise, but it is valuable to comment on the left hand side mass matrix that is diagonal for all equations.

### C.2.3 Time Integration

Equations (C.21)–(C.24) all are of the form  $\dot{f}(t) + \dot{a}(t)f(t) = F(g)$ . Yuan *et al.* presents an integrating factor for the case where  $\dot{a}(t) = a$ .<sup>16</sup> Here, the integrating factor,  $e^{a(t)}$ , is used where  $a(t)$  is a general function of time given by  $a(t) = \int \dot{a}(t') dt'$ , such that each equation can be written  $\partial \mathbb{f} / \partial t = \mathbb{F}(t, \mathbb{g})$  with  $\mathbb{f} = e^{a(t)} f$ ,  $\mathbb{g} = e^{b(t)} g$  and  $\mathbb{F}(t, \mathbb{g}) = e^{a(t)} F(e^{-b(t)} \mathbb{g})$ .

If  $\hat{K}'_{ij}(t, \hat{p}_{ij})$  is multiplied over to the right hand side of Eq. (C.24), the integrating factor for the pressure equation becomes

$$\exp \left\{ \int \frac{1}{\hat{K}'_{ij}(t', \hat{p}_{ij})} \sum_n \frac{\kappa_{ij}^{(n)}}{\tau_{ij}^{(n)}} + \frac{\hat{K}_{ij}(\hat{p}_{ij})}{\hat{K}'_{ij}(t', \hat{p}_{ij})} \alpha_{ij} dt' \right\}$$

which is both dependent on time and the pressure. In this case,  $K(t, p)$ , and thus the integrand in the integrating factor, is not explicitly time dependent. For a fixed, given pressure, the integrand reduces to a pressure dependent constant. In Eqs. (C.21)–(C.23) and the linear case of Eq. (C.24), the integrating factors are the same as those reported in Ref. 16.

On abstract autonomous form, Eqs. (C.21)–(C.24) can be written as

$$\frac{\partial \mathbf{y}}{\partial t} = \mathbf{F}(\mathbf{z}) \quad (\text{C.25})$$

$$\frac{\partial \mathbf{z}}{\partial t} = \mathbf{G}(\mathbf{y}, \mathbf{z}) = \mathbf{G}_p(\mathbf{z}) \mathbf{G}_u(\mathbf{y}). \quad (\text{C.26})$$

$$\mathbf{y} = [\mathbf{u} \quad \mathbf{v} \quad \mathbb{S}_n]^\text{T}, \quad \mathbf{z} = [t \quad \mathbb{P}]^\text{T}$$

$$\mathbf{F}(\mathbf{z}) = \begin{bmatrix} \mathbb{F}_x(t, \mathbb{P}) \\ \mathbb{F}_y(t, \mathbb{P}) \\ \mathbb{F}_n(t, \mathbb{P}) \end{bmatrix}, \quad \mathbf{G}(\mathbf{y}, \mathbf{z}) = \begin{bmatrix} \mathbf{G}_p(t, \mathbb{P}) \mathbf{G}_u(\mathbf{u}, \mathbf{v}, \mathbb{S}_n) \\ 1 \end{bmatrix}.$$

The system of equations in Eqs. (C.25)–(C.26) is integrated in time using the leap-frog, or Störmer-Verlet scheme.<sup>16,18,32</sup> The Störmer-Verlet scheme is stable if the step size,  $h$ , fulfill  $h\omega < 2$  where  $\omega = c_{\max} k_{\max}$  and  $c_{\max}$  and  $k_{\max}$  are the maximum speed of sound and spatial wave number produced by the propagation operator. The maximum frequency is equivalent to the largest eigenvalue of the generalized eigenvalue problem  $Kx = Mx\lambda$  where  $K$  and  $M$  are the assembled stiffness and mass matrices from Eqs. (C.21)–(C.24),  $x$  the eigenvector and  $\lambda$  the eigenvalue corresponding to the frequency  $\omega$ .

The spatial wave numbers, *i.e.*, the eigenvalues of the operator, is for the differentiation matrix inversely proportional to the smallest spatial resolution of the domain.<sup>22,32</sup> Because the spatial sampling of the GLL quadrature points are

not equidistant within one element, the minimum  $\Delta x$  decreases for increasing polynomial order. The step size requirement becomes

$$h < \text{CFL} \frac{L_{\min}}{2} \frac{\Delta \xi_N}{c_{\max}} \quad (\text{C.27})$$

where  $L_{\min}/2$  is the transformation of shortest length of one element domain to the reference domain,  $\Delta \xi_N$  the shortest distance between two GLL quadrature points for a polynomial order  $N$  and CFL the Courant–Friedrich–Levy number.<sup>17,28,33</sup> The method is found to be stable for  $\text{CFL} < 0.85$ .

One interpretation of the Störmer-Verlet scheme is a composition of the symplectic Euler method with its adjoint method.<sup>32</sup> The symplectic Euler method integrates a partitioned system as in Eqs. (C.25)–(C.26) with the explicit Euler for the first variable and with the implicit Euler for the second. The explicit and implicit Euler are each other’s adjoint method, and a composition of the symplectic Euler with its adjoint yields<sup>32</sup>

$$\begin{aligned} \mathbf{y}_{n+\frac{1}{2}} &= \mathbf{y}_n + \frac{h}{2} \mathbf{F}(z_n) \\ z_{n+\frac{1}{2}} &= z_n + \frac{h}{2} \mathbf{G}(z_{n+\frac{1}{2}}, \mathbf{y}_{n+\frac{1}{2}}) \\ z_{n+1} &= z_{n+\frac{1}{2}} + \frac{h}{2} \mathbf{G}(z_{n+\frac{1}{2}}, \mathbf{y}_{n+\frac{1}{2}}) \\ \mathbf{y}_{n+1} &= \mathbf{y}_{n+\frac{1}{2}} + \frac{h}{2} \mathbf{F}(z_{n+1}). \end{aligned}$$

where the step for  $z_{n+1}$  is the only implicit term left because  $\mathbf{F}$  is not a function of  $\mathbf{y}$ . Note that implicitness in  $t$  not causes trouble to this formulation because the time only enters the integrating factor  $e^{at}$  within the functions  $\mathbf{F}$  and  $\mathbf{G}$ . If the function  $\mathbf{G}$  is formulated as a function not dependent on the pressure, *i.e.*, the linear case, all steps are fully explicit. Another straight forward extension of the scheme presented above is to not calculate the intermediate steps  $\mathbf{y}_{n+1}$ , but integrate directly to  $\mathbf{y}_{n+\frac{3}{2}}$ .

The nonlinear term in Eq. (C.26) makes the pressure step both nonlinear in and dependent on the future value  $p_{n+1}$ . This nonlinear equation can be solved using Newton iterations, and another advantage of defining the pressure only in the interior of each element, is that such an iteration is possible to do element-wise, and there is no need for a temporary boundary pressure field.

Yet a simpler approach than Newton iterations is to assume that the pressure dependent speed of sound is constant within one time step. The stability requirements of the integrator requires the step size,  $h$ , to correspond to a sampling frequency of the order of hundreds of points per wavelength – far more

than the spatial resolution. The pressure dependent speed of sound is calculated from a constant pressure value,  $p^*$ , such that  $\mathbf{z}_{n+i}^* = [t+ih \mathbb{P}^*]^T$  and the final integration scheme becomes

$$\begin{aligned} \mathbf{y}_{\frac{1}{2}} &= \mathbf{y}_0 + \frac{h}{2} \mathbf{F}(\mathbf{z}_0) \\ \mathbf{z}_{n+1} &= \mathbf{z}_n + h \mathbf{G}(\mathbf{z}_{n+\frac{1}{2}}^*, \mathbf{y}_{n+\frac{1}{2}}) \\ \mathbf{y}_{n+\frac{3}{2}} &= \mathbf{y}_{n+\frac{1}{2}} + h \mathbf{F}(\mathbf{z}_{n+1}). \end{aligned}$$

### C.3 Plane Wave Propagation

Simulation experiments are conducted to verify the presented Spectral Element Method for absorption and nonlinear propagation in a plane wave setup. Komatitsch and Vilotte propose in Ref. 15 that a combination of an eight order polynomial ( $N=8$ ) and five points per minimum wavelength ( $n_\lambda=5$ ) is sufficient, although Faccioli *et al.* earlier proposed that four points per wavelength and  $N=5$  was sufficient for the same test problem.<sup>14</sup>

Nonlinear elasticity cause generation of higher harmonic components. Higher frequencies makes the solutions less smooth. The presented SEM is tested both with polynomials of order  $N=8$  and  $N=16$ , and higher order polynomials are assumed to perform the best.<sup>24</sup> A refinement of eight points per wavelength is also tested and compared with the proposed four. The different test cases are presented in Table C.1.

**Table C.1:** Discretization parameters for the plane wave test cases.

Case	1	1b	2	3	3b	4
Order, $N$	8	8	8	16	16	16
Pts. per $\lambda$ , $n_\lambda$	4	4	8	4	4	8
CFL	0.80	0.40	0.80	0.80	0.80	0.80
Exp. Intv.	1	1	1	1	10	1

#### C.3.1 Absorption

To validate the absorption model for a wide range of frequencies a chirp signal is simulated. The chosen absorption model is described by Nachman *et al.* in Ref. 34, and is shown to be causal and to satisfy the Kramers-Krönig relations. An equation for both the frequency dependent phase velocity [Eq. (44)] and absorption [Eq. (45)] of the medium is presented in the same paper.<sup>34</sup> The

phase velocity and absorption of the SEM are estimated and compared to these theoretical results.

Two different materials are chosen: One standard material with linear-in-frequency absorption and one muscle mimicking material with a frequency dependence of  $f^{1.1}$ . The parameters for the two materials are presented in Table C.2. The presented absorption model is tuned to match general power-law frequency dependent absorption of the form  $\alpha(f)=\alpha_0 f^\beta$ . To resemble this frequency behavior, two relaxation processes are found to be sufficient for both materials. The relaxation times,  $\tau_n$ , were chosen to be the same as in Ref. 18:

$$\tau_1 = \frac{1}{5f_{\max}}, \quad \tau_2 = \frac{2}{f_{\max}}$$

and the relative compressibilities,  $\kappa_n$ , were found through minimizing the estimated frequency dependent absorption from Eq. (45) in Ref. 34 to the desired  $\alpha_0 f^\beta$  using Matlab's built-in function `fminsearch`. The calculated values for the compressibilities for the standard material are  $\kappa_1/\kappa_0=4.778 \cdot 10^{-3}$  and  $\kappa_2/\kappa_0=4.582 \cdot 10^{-3}$ . For the muscle mimicking material the values were found to be  $\kappa_1/\kappa_0=6.217 \cdot 10^{-3}$  and  $\kappa_2/\kappa_0=3.782 \cdot 10^{-3}$ .

**Table C.2:** Material parameters for the standard and muscle mimicking materials.

Material	Standard	Muscle
Wave speed, $c_0$	1540	1550
Density, $\rho_0$	1050	1060
Att. const., $\alpha_0$	0.5	0.52
Att. exp., $\beta$	1	1.1
Coeff. of non-linearity, $\beta_n$	3.5	3.9

The chirp signal is constructed from a linear frequency sweep from 500 kHz to 4 MHz, and a Tukey window with  $R=0.25$  is applied over the pulse to taper the endpoints to zero. The source pulse is presented in Fig. C.2. The maximum frequency of interest is 6 MHz, and the wave is propagated in the domain  $[0, 20]$  cm. The number of elements is 196 for Case 3, 392 (double) for Case 1 and 4 and 584 (quadruple) for Case 2. In the muscle mimicking material the number of elements is 195 (Case 3 only). The two elements closest to the source are half size to improve accuracy close to the boundary. The step size is calculated according to Eq. (C.27) with CFL=0.8.

Figure C.2 shows the attenuated pulse after propagating 15 cm in the standard material in addition to the pulse at the source point. The frequency

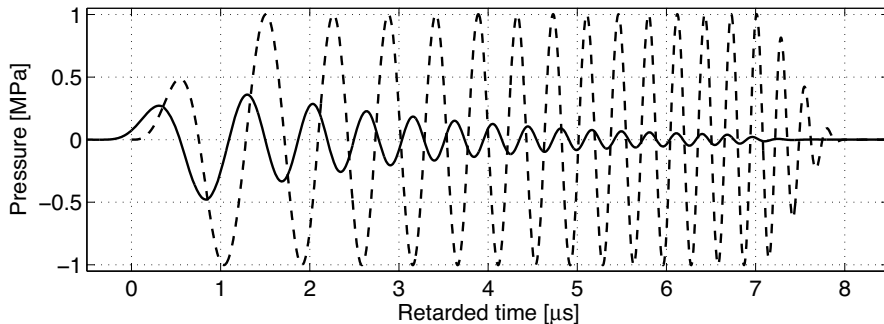


**Figure C.2:** The transmitted chirp signal displayed in retarded time  $\tau=t-z/c_0$  at the vibrating surface (dash) and at 15 cm (solid).

dependence of the absorption is visible in the amplitude, and the shift of the zeros of the pulse show the change in phase velocity due to dispersion.

From the simulated data the frequency dependent absorption can be estimated by comparing the magnitude of the frequency spectra from two depths. The estimated absorption over the interval 10.3–20.5 mm is presented in Fig. C.3 in terms of dB/cm together with the theoretical curve obtained from Ref. 34.

In panels where the difference is visually close to zero, the difference is quantified through the error,  $\epsilon$ , measured in the  $L^2$ -norm as

$$\epsilon = \frac{\|x_{\text{ref}} - x_{\text{sim}}\|_2}{\|x_{\text{ref}}\|_2}. \quad (\text{C.28})$$

In the estimated absorption, the error is estimated in the frequency range to 0–5 MHz. A collection of the  $L^2$ -errors are presented in Table C.3 for the different case and materials. If the step size is reduced with a factor two (Case 1b), the error is reduced with a factor of approximately four, which corresponds well to the second-order Störmer-Verlet scheme.<sup>32</sup> This alone should not be considered as a verification of the order of the integrator. Such a verification should be performed on a spatial grid with negligible discretization errors.

In Case 3b, data is exported at every tenth step. This does not influence the error of the absorption model. The underlying step size is not reduced, only the sampling frequency of the exported data. This behavior is expected, because the underlying signal contains the same information, but is sampled differently. A reduced export sampling frequency reduces the need for free disk space, which is not an issue for plane wave simulations, but can be of interest in higher dimensions.

A similar approach can be used to estimate the phase velocity from the com-

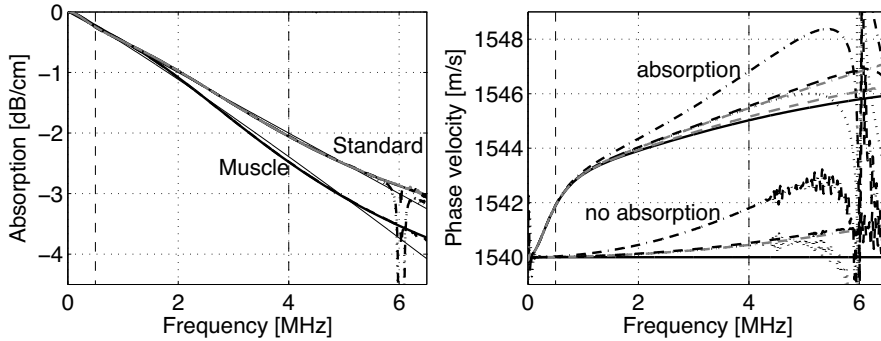


**Figure C.3:** Verification of the absorption model. Left: Magnitude of absorption for the standard and muscle mimicking material. The thin black line indicate the desired absorption  $\alpha_0 f^\beta$ . Right: Phase velocity for the standard material with and without absorption. The line styles are for both panels: Theoretical [Ref. 34] (black solid), Case 1 (black dash-dot), Case 1b (black dot), Case 2 (gray dash-dot), Case 3 (black dash) and Case 4 (gray dash).

plex phase of the simulated data. The estimated phase velocity is presented in the right panel of Fig. C.3, and shows that the error in phase velocity increases for increasing frequency. The results for the muscle material are visually similar to those of the standard material and is not displayed. The  $L^2$ -error measured according to Eq. (C.28) (see Table C.3) is very small when normalized to the wave speed itself.

The error in the phase velocity is either caused by propagation (diffraction) or absorption effects. The simulations run in the standard material is re-run without absorption to eliminate this option. The amplitude of the propagated pulse is constant over the interval as expected, but the estimated phase speed does not match a constant theoretical speed of sound. The source of this error is believed to be the spatial frequency response of the propagation operator [see Fig. C.1(b)], where higher spatial frequencies have too high wave numbers.

A refinement of the step size, polynomial order or spatial sampling reduces the error. It is, however, not clear which of these refinements that is the most prominent cause of error reduction. Increasing the number of points per wavelength is equivalent to increasing the maximum desired frequency in a non-absorbing material, and the frequency response for the band of interest is entirely within the linear region. Another effect of increased spatial sampling is a reduction of the step size in order to meet the stability requirements of the integrator.

In Case 1, the number of points per wavelength within the frequency band

is already higher than four, and should, according to Refs. 14 and 15 be sufficient. Assuming this to be true, the discretization error is assumed to be small compared to the integration error, and a spatial refinement is equivalent to reducing the step size with the same factor of refinement. Comparison of Case 1b and 2 indicate this where the error is approximately four time lower than Case 1. Increasing the order of the polynomial will also have this effect because both the minimum distance between two quadrature nodes and the step size are reduced.

The Störmer-Verlet scheme is also shown to be symplectic (energy preserving), and the total energy change,  $\Delta E$ , in a non-absorbing material after 20 cm is measured in the  $L^2$ -norm and presented in Table C.3. The energy of the signal is found as  $E=1/(\rho c_0) \int |p(t)|^2 dt$ . With absorption,  $\Delta E \approx 900 \cdot 10^{-3}$ , and the errors presented for the non-absorbing case show that the Störmer-Verlet scheme preserves the energy.

**Table C.3:** Error measured in the  $L^2$ -norm for the plane wave test cases. The upper part show errors for the absorption model, and the bottom part for the nonlinear model. All values are of magnitude  $10^{-3}$ .

Case	1	1b	2	3	3b	4
Std., $\alpha(f)$	4.69	1.27	1.29	1.45	1.45	0.59
Std., $c(f)$	0.81	0.19	0.20	0.24	0.24	0.06
Std., $\Delta E$	0.51	0.34	0.04	0.01	0.01	0.02
Std., $c(f)$	0.81	0.19	0.20	0.24	0.24	0.06
Mus., $\alpha(f)$	—	—	—	1.51	—	—
Mus., $c(f)$	—	—	—	0.24	—	—
1. harm.	3.54	1.67	0.54	0.74	0.72	0.15
2. harm.	39.59	7.33	4.85	7.85	7.52	1.07
3. harm.	103.00	261.48	18.96	33.99	33.12	4.05
4. harm.	896.86	829.03	45.82	204.87	209.30	10.34

### C.3.2 Nonlinear Elasticity

Non-linearly elastic materials generate higher harmonic frequencies, and the presented SEM is tested for the cases in Table C.1. For continuous wave (CW) plane wave propagation an analytical solutions for each harmonic component is available through a Fourier series solution given as [Eq. 11-2.6, Ref. 35]

$$p_{n,\text{pk}}(\sigma) = \frac{2P_0}{n\sigma} J_n(n\sigma) \tag{C.29}$$

where  $p_{n,pk}$  are the Fourier coefficient for the  $n$ 'th harmonic frequency,  $P_0$  the amplitude of the transmitted signal, and  $\sigma=z/\bar{z}$  where  $\bar{z}=\rho c^2/\beta_n k P_0$  is the plane wave shock length of the material.

The simulated CW field is propagated on the interval  $[0, 10]$  cm in a standard material without absorption (see Table C.2) and with a source frequency of 3 MHz. The maximum desired frequency is 12 MHz, and the number of elements is 196 for Case 3 (392 for Case 1 and 4 and 584 for Case 2). The two elements closest to the source is half size. For this setup, the shock length is  $\bar{z}=5.81$  cm for a 1 MPa pressure amplitude. At each depth, the field is logged in time, and 32 periods are excerpted for frequency analysis. The step size,  $h$ , was calculated from Eq. (C.27) with CFL=0.8, and adjusted slightly to yield a whole number of samples per wavelength in time.

Visually, the simulated results in Fig. C.4 match the analytic solution well for the first two harmonic components. For Case 1 and 1b ( $N=8$ ,  $n_\lambda=4$ ), the third-harmonic has a too high amplitude and the difference is visible for  $\sigma=z/\bar{z}\gtrsim 0.6$ . A reduction of the step size in Case 1b decreases the error for the first-, second- and fourth-harmonic, but increases the error for the third-harmonic. Why the error increases for the third-harmonic is commented in the next paragraph.

Increasing the polynomial order to  $N=16$  shows an improvement in for both the third- and fourth-harmonic, but the fourth-harmonic is slightly higher than the analytic solution from  $\sigma\gtrsim 0.7$ . Assuming a similar behavior for an eighth-order polynomial – a too high amplitude in the harmonic components closer to the maximum desired frequency – the unexpected error behavior of Case 1 and 1b can be explained by this: In the near field, the visual match with the analytic solution is better for Case 1b than Case 1. The Case 1 curve show a slight clockwise rotation around  $\sigma\approx 0.55$ , and this can lead to a lower global error for the whole curve. Especially because the local error is smaller as the depth and intensity increases.

According to Refs. 14 and 15, a spatial sampling of 4–5 points per wavelength, and a polynomial order  $N\leq 8$  is sufficient for linear propagation. This, however, is not sufficient for the presented nonlinear model, even with CFL=0.4. Increasing the polynomial order, however, has an effect on the alignment with the analytic curves, although the simulated fourth-harmonic is higher than the analytic. Increasing the number of points per wavelength is another option to improve accuracy.

The improvement in accuracy for each frequency after an increase in spatial sampling resolution is best visible in the frequency spectrum where now all harmonics up to the sixth-harmonic is matched well when the analytical value

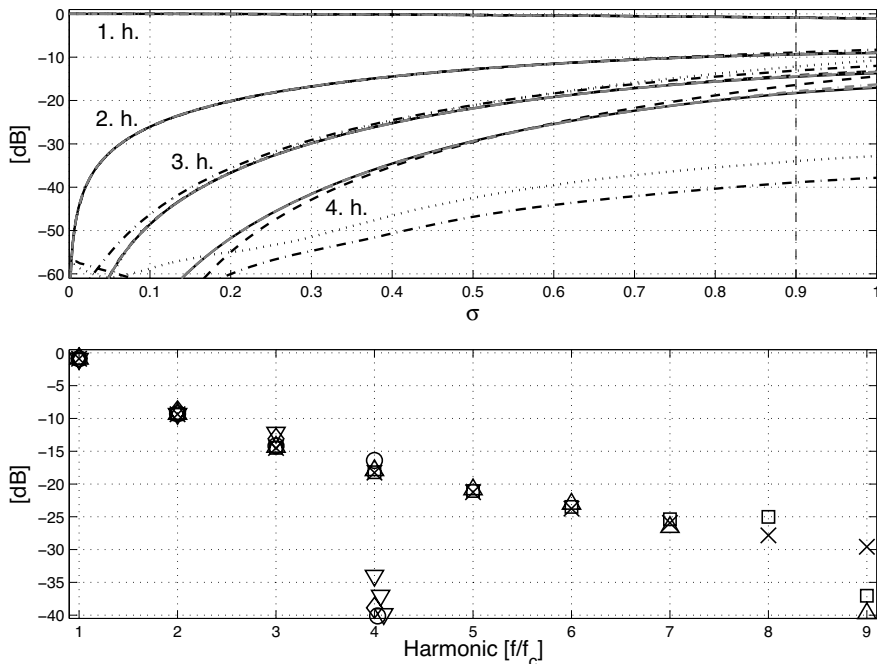


**Figure C.4:** Verification of the nonlinear model. Top: The RMS of the first four harmonic components as a function of depth,  $\sigma=z/\bar{z}$ . Bottom: The frequency components at depth  $\sigma=0.9$ . Line and marker styles are: Analytic solution [Ref. 35] (black solid,  $\times$ ), Case 1 (black dash-dot,  $\diamond$ ), Case 1b (black dot,  $\nabla$ ), Case 2 (gray dash-dot,  $\triangle$ ), Case 3 (black dash,  $\circ$ ) and Case 4 (gray dash,  $\square$ ).

for both  $N=8$  and  $N=16$ . The high order polynomial is still more accurate, both in terms of visual differences and in terms of measured  $L^2$ -error. Increasing the number of elements used reduce the error, but increase the memory consumption. Comparing Case 3 and 3b, a reduction in the export sampling frequency does not influence the error of the model.

## C.4 Two-Dimensional Propagation

Although many aspects of propagation can be covered by plane wave experiments, effects as diffraction, absorption and non-linearity are spatial phenomena. The presented method is tested in a two-dimensional Cartesian domain and compared with an existing simulation tool for forward propagation, Aber-sim.<sup>11,12,36</sup>

All of the transducers specified in Table C.4 have plane transducer surfaces with an infinite extension in the elevation direction, and an azimuth aperture,  $D=2a$ . Focusing is employed using the proper delays for each node in the surface. The radiated pulse is a sinusoidal vibration with amplitude,  $P_0$ , a Gaussian envelope and fractional bandwidth,  $B$ . In order to reduce the amount of output data, the whole pressure field is not exported for each time step. The pressure along the center axis of the transducer is exported and along a transverse line located at a proper depth. Because the pressure is allowed to be discontinuous over inter-element boundaries, the mean value of the two contributions is used.

**Table C.4:** Transducer setup for the two-dimensional test cases.

Case	Mat.	$F$ [mm]	$D=2a$ [mm]	$f_c$ [MHz]	$f_{\max}$ [MHz]	$B$ [%]	$P_0$ [MPa]
A	Std.	$\infty$	17.6	3.5	14.0	20	0.75
B	Std.	61.6	17.6	3.5	14.0	50	0.50
C	Mus.	20.0	8.0	8.0	24.0	60	1.00

The simulations are run with CFL=0.8, and then the step size is adjusted such that the export sampling frequency is  $20f_c$  according to the results of Section C.3. For all the 2D simulations, a polynomial order of  $N=16$  and four points per minimal wavelength is used.

The initial pulse in Abersim is the same as the radiated pulse signal used for the SEM simulations, and the sampling frequency in Abersim is set to the inverse of the step size of the SEM. This results in a temporal sampling using hundreds of points per wavelength. Abersim is considered as the gold standard in this comparison, and has previously been verified in comparison with measurements<sup>11,12</sup> and with other existing simulation tools<sup>36</sup>. In Ref. 11 an error analysis is performed for a nonlinear plane wave setup with absorption, *i.e.*, solving the viscous Burgers' equation.

#### C.4.1 Case A – Unfocused Transducer

Results for the Case A transducer are shown in Fig. C.5. Absorption is switched off for this simulation, and the domain measures  $5 \times 7$  cm ( $104 \times 171$  elements) in the azimuth and depth direction respectively. The medium is homogeneous, and the domain can be split in two symmetric halves in the azimuth direction to reduce the number of azimuth elements to 52. The two rows closest to the vibrating boundary are half size in the depth direction, and two elements on

each side of the edge of the transducer are half size in the azimuth direction to improve accuracy. The maximum depth is somewhat longer than the shock length for plane wave propagation,  $\bar{z}=6.64$  cm, and the results are displayed in terms of the depth  $\sigma=z/\bar{z}$ .

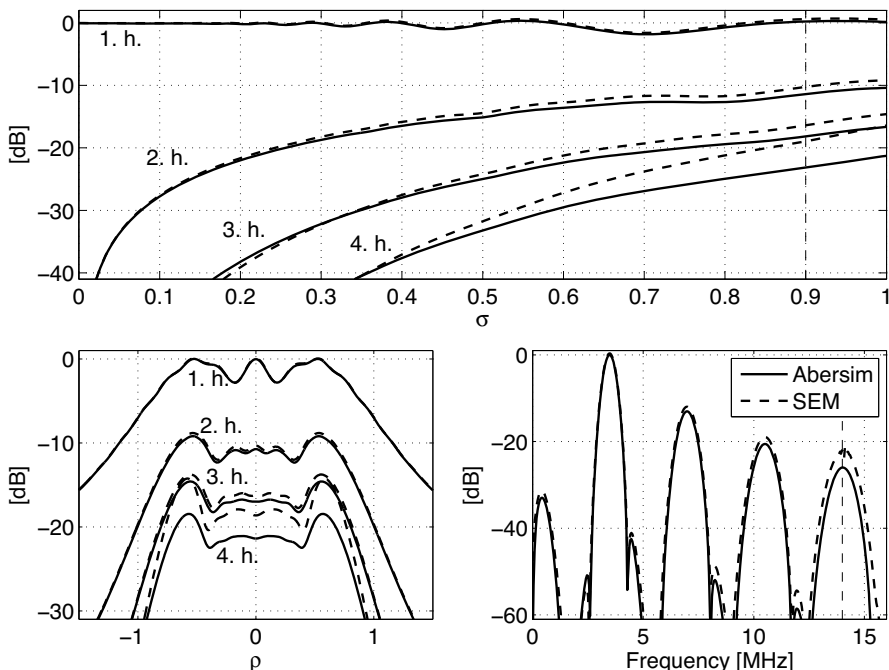


**Figure C.5:** Comparison of Abersim and SEM solution for the unfocused Case A transducer in a standard material. Top: The RMS of the first four harmonic components as a function of depth,  $\sigma=z/\bar{z}$  where  $\bar{z}$  is the plane wave shock length of the medium. Bottom two panels: The azimuth profile as a function of  $\rho=x/a$  (left) and the frequency spectrum (right) of the on-axis signal at depth  $\sigma=0.9$ . The vertical dashed line in the frequency spectrum indicates the maximum desired frequency.

On-axis RMS values match well between the Abersim and SEM solutions. The SEM solution has a higher value for the third-harmonic curve. The discrepancy is quantified in Table C.5. For the nonlinear plane wave problem in Section C.3.2, there is no such difference between the analytic and SEM solution for the third-harmonic, and two causes for the difference seen in the 2D case are suggested in the next paragraph. The cross sectional profiles show the same behavior, and the first two harmonic components align very well across the radiated field.

**Table C.5:** Differences in on-axis RMS value for the Abersim and SEM solutions. The values are the difference  $p_{\text{Ab.}} - p_{\text{SEM}}$  in decibel measured at the vertical line of each depth plot in Figs. C.5, C.7 and C.8. A negative value indicate that the SEM solution has a higher RMS value.

Case	1. harm.	2. harm.	3. harm.	4. harm
Abersim CW	0.07	0.22	0.37	0.50
A	-0.36	-1.05	-1.67	-4.1
B	-0.75	-1.08	-0.67	0.14
C	-0.73	-1.15	-1.69	—

First, although Abersim is considered to be the gold standard in this comparison, it is not an analytic solution. A plane wave CW simulation is performed in Abersim check for the performance of the nonlinear model in Abersim when no absorption is present, *i.e.*, the Burgers' equation without the viscous term. This check shows that the Abersim solution is slightly lower than the analytic solution. The authors of Refs. 11 and 12 comment that a negligible interpolation error is introduced when solving the nonlinear part of the wave equation. The error seen in the CW simulation indicate that the discrepancies between the Abersim and SEM solutions might be reduced with a small factor (10–20%). The discrepancies are, however, for the first three harmonics, within acceptable limits.

The second possible cause is related to the level of the fourth-harmonic. This is for both plane wave and 2D simulations too high, and the error is believed to arise from the numerical dispersion of the propagation operator. This dispersion error will increase with the physical dimension of the problem where the spatial wave numbers for directions not parallel to the Cartesian grid is given as  $k^2 = k_x^2 + k_y^2$ .

The pulse shape and frequency spectrum align well, but the frequency spectrum of the SEM solution is higher for both the higher harmonic and the sub-harmonic component. The pulse shape has a more noisy look for the SEM solution, and this is caused by the limitation in resolvable spatial frequencies. The spectrum is, however, smooth up to  $\sim 16$  MHz which is higher than the maximum desired frequency. Above this, the spectrum becomes chaotic and this introduce the ripple seen in the pulse. Abersim is limited by the Nyquist frequency, and has a smooth spectrum up to this limit. Filtering the Abersim solution such that all frequencies above 16 MHz is set to zero introduces a similar ripple in the Abersim signal. The phase of this ripple is not completely equal, which is suggested to be an effect of the numerical dispersion of the SEM

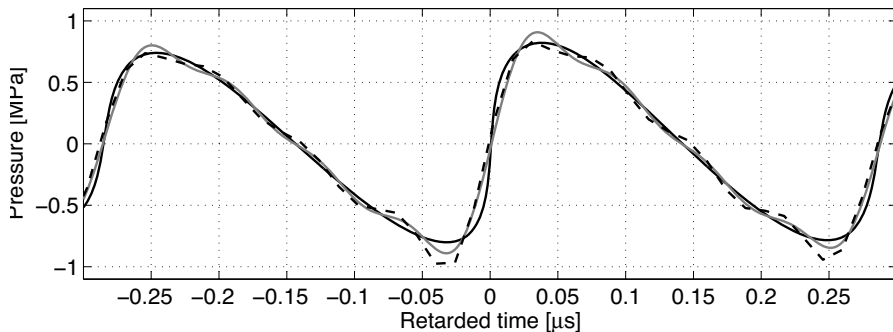


**Figure C.6:** Comparison of the on-axis radiated pulse from the unfocused Case A transducer at depth  $\sigma=0.9$  for the Abersim (black solid line) and SEM (black dash) solutions. The gray solid line indicate the Abersim solution filtered with a rectangular frequency domain lowpass filter limited to  $\pm 16$  MHz.

propagation operator.

#### C.4.2 Case B – Focused Transducer

In Case B, both focusing and absorption are introduced. Figure C.7 presents the on-axis and focal RMS profile, and the match is visually good for the Abersim and SEM solutions. The differences presented in Table C.5 are for Case B lower than for Case A, which indicates that the erroneous behavior of the nonlinear model is reduced when absorption is present.

The focal profile in Fig. C.7 shows that the SEM solutions match the side lobe pattern of the Abersim solution very well for the first two harmonic components. The third-harmonic is slightly higher in level off-axis, but catches the shape of the Abersim solution. For the fourth-harmonic, the SEM solution loses the shape resemblance. The maximum desired frequency is the fourth-harmonic frequency, and this implies that half the band of the fourth-harmonic frequency lobe is not covered by the minimum needed sampling of four points per wavelength. However, as for Case A, the spectrum in Fig. C.7 does not get chaotic up to  $\sim 16$  MHz, but, contradictory to Case A, the bandwidth of Case B is higher and the spectrum becomes chaotic within the fourth-harmonic frequency band.

#### C.4.3 Case C – Diagnostic Transducer

Case C is designed to resemble a diagnostic transducer for imaging of the carotid artery. The center frequency is 8 MHz, the focal point at 20 mm depth and the

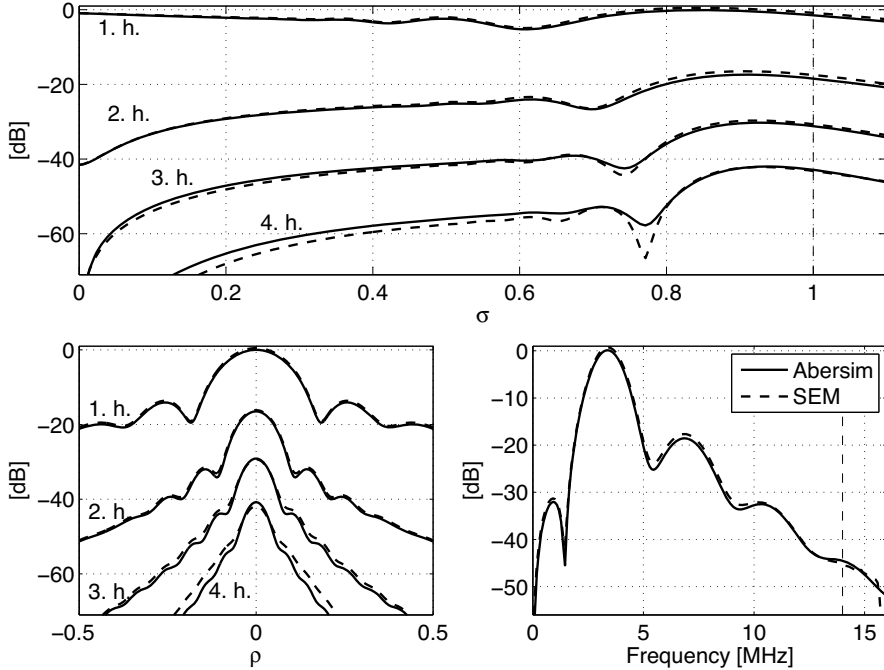


**Figure C.7:** Comparison of Abersim and SEM solution for the focused Case B transducer in a standard material. Top: The RMS of the first four harmonic components as a function of depth,  $\sigma=z/F$  where  $F$  is the focal depth. Bottom two panels: The azimuth focal profile as a function of  $\rho=x/a$  (left) and the frequency spectrum (right) of the focal point signal. The vertical dashed line in the frequency spectrum indicates the maximum desired frequency.

transmit f-number 2.5. Although harmonic imaging at 16 MHz seldom is used, the second-harmonic frequency is said to be of interest. The computational domain covers 25 mm (99 elements) in depth and 16 mm (41 elements for one half-domain) in the azimuth direction. The two rows closest to the vibrating boundary are half size in the depth direction, and two elements on each side of the edge of the transducer are half size in the azimuth direction to improve accuracy. The muscle mimicking material is used to introduce absorption with a general power-law frequency dependence ( $f^{1.1}$ ). The transmit bandwidth is 60%. Results for Case B suggests that the maximum desired frequency is higher than the upper limit of the second-harmonic frequency band. For Case C, the maximum desired frequency is the third-harmonic frequency.

Figure C.8 and Table C.5 show that the the on-axis and focal RMS profiles has similar performance as Case A and B. The differences are of the same

magnitude for the first two harmonic components, but increases for the third. The third-harmonic is said to not be of interest, but is nonetheless included in the figure. The second-harmonic focal profile shows a slightly higher side-lobe level of the SEM solution, but this is within the acceptable range of differences as discussed for Case A.

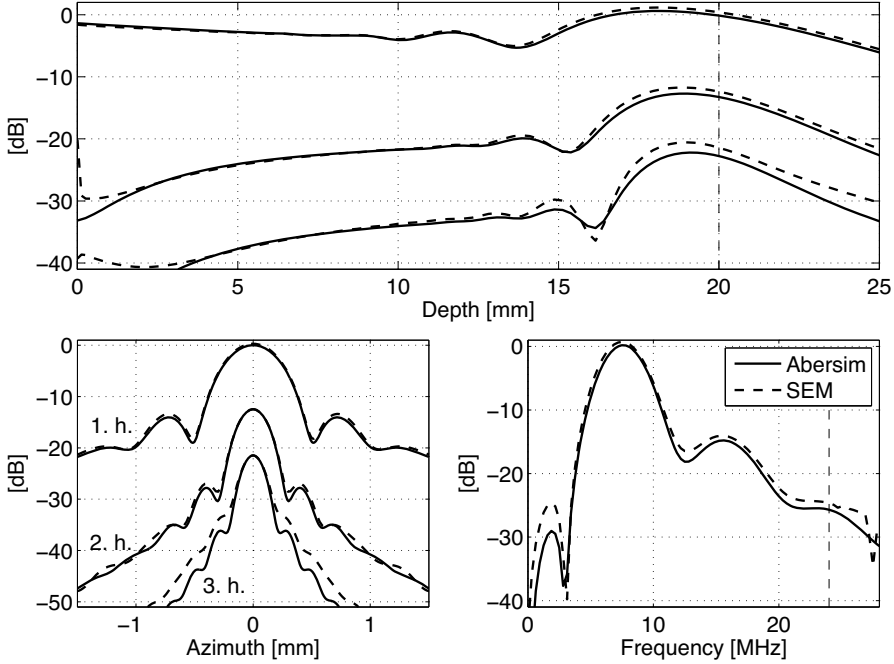


**Figure C.8:** Comparison of Abersim and SEM solution for the focused Case C transducer in a muscle mimicking material. Top: The RMS of the first three harmonic components as a function of depth. Bottom two panels: The focal profile (left) and the frequency spectrum (right) of the focal point signal. The vertical dashed line in the frequency spectrum indicates the maximum desired frequency.

The frequency spectrum at the focal point shows a discrepancy across the frequencies of interest. A reduction in the relative maximum desired frequency, ( $3f_c$  for Case C vs.  $4f_c$  for Case A and B), shifts the region where the SEM discretization is dispersive down such that the frequency range of interest not entirely is contained within the linear region (75% of  $f_{\max}$ ). For Case C, this region covers frequencies up to 18 MHz, which is in the upper region of the second-harmonic band. Still, the second-harmonic is adequately resolved when compared to the Abersim solution.

## C.5 Summary and Conclusion

A time-domain spectral element method is presented and verified for acoustic wave propagation in absorbing and non-linearly elastic materials. Both plane wave propagation and two-dimensional problems are investigated. The results of Section C.3.1 concur with previous reported results on spatial sampling suggesting that a polynomial order of  $N=8$  and four to five points per wavelength is sufficient for linear propagation problems. An error is introduced in the frequency dependent phase-speed, but the error is found to scale with the step size of the time integration scheme.

The presented nonlinear model in Section C.3.2 requires a higher spatial sampling or polynomial order than linear problems. For the presented nonlinear model, a higher polynomial order is chosen to improve spatial accuracy without increasing the memory consumption. The model tends to amplify higher harmonic components, and frequencies closer to the maximum desired frequency are generated at a too high rate when compared to analytic solutions. This effect is also seen for two-dimensional problems. When both absorption and non-linearity is present in the two-dimensional computations, the errors of the nonlinear model become less pronounced.

All in all, the presented SEM is found to work well for acoustic problems in nonlinear and absorbing materials. Harmonic generation is successfully modeled through the SEM, but the error increases for each harmonic component due to a limited spatial frequency range and numerical dispersion introduced by the propagation operator. In order to accurately compute a certain number of harmonic frequency bands, the maximum desired frequency should be set at least 25% higher than the upper limit of the highest desired harmonic band.

Of further work, the authors suggest a verification of the presented SEM for heterogeneous materials and possibly deformed geometries. An extension to three-dimensions would make the tool more versatile.

## Acknowledgements

The work was funded by the Norwegian Research Foundation through the center of research-driven innovation *Medical Imaging Laboratory*. The authors would like to thank Tonni Franke Johansen and Tarjei Rommetveit for fruitful discussions and comments in the process of implementing and testing the presented method.

---

## References

- [1] J. J. Dahl, G. F. Pinton, M. Lediju, and G. E. Trahey, “Simulation and Experimental Analysis of Ultrasonic Clutter in Fundamental and Harmonic Imaging,” in *Proc. of SPIE*, vol. 7265, 726509, 2009, doi:10.1117/12.813782.
- [2] G. L. Wojcik, J. C. Mould, S. Aytex, and L. M. Carcione, “A Study of Second-Harmonic Generation by Focused Medical Transducer Pulses,” in *IEEE Ultrason. Symp. Proc.*, 1998, pp. 1583–8.
- [3] T. D. Mast, L. M. Hinkelman, M. J. Orr, and R. C. Waag, “The Effect of Abdominal Wall Morphology on Ultrasonic Pulse Distortion. Part II. Simulations,” *J. Acoust. Soc. Am.*, vol. 104, pp. 3651–64, 1998.
- [4] T. D. Mast, L. A. Hinkelman, L. A. Metlay, M. J. Orr, and R. Waag, “Simulation of Ultrasonic Pulse Propagation, Distortion, and Attenuation in the Human Chest Wall,” *J. Acoust. Soc. Am.*, vol. 106, pp. 3665–77, 1999.
- [5] T. Varslot, S.-E. Måsøy, T. F. Johansen, and B. A. J. Angelsen, “Aberration in Nonlinear Acoustic Wave Propagation,” *IEEE Trans. Ultrason., Ferroelect., Freq. Contr.*, vol. 54, pp. 470–9, 2007.
- [6] G. F. Pinton, J. Dahl, S. Rosenzweig, and G. E. Trahey, “A Heterogeneous Nonlinear Attenuating Full-Wave Model of Ultrasound,” *IEEE Trans. Ultrason., Ferroelect., Freq. Contr.*, vol. 56, pp. 474–88, 2009.
- [7] Y.-S. Lee and M. F. Hamilton, “Time Domain Modeling of Pulsed Finite-Amplitude Sound Beams,” *J. Acoust. Soc. Am.*, vol. 97, pp. 906–17, 1995.
- [8] M. A. Averkiou and M. F. Hamilton, “Nonlinear Distortion of Short Pulses Radiated by Plane and Focused Circular Pistons,” *J. Acoust. Soc. Am.*, vol. 102, pp. 2539–48, 1997.
- [9] R. J. Zemp, J. Tavakkoli, and R. S. Cobbold, “Modeling of Nonlinear Ultrasound Propagation in Tissue from Array Transducers,” *J. Acoust. Soc. Am.*, vol. 113, pp. 139–52, 2003.
- [10] X. Yang and R. O. Cleveland, “Time Domain Simulation of Nonlinear Acoustic Beams Generated by Rectangular Pistons With Application to Harmonic Imaging,” *J. Acoust. Soc. Am.*, vol. 117, pp. 113–23, 2005.

- [11] T. Varslot and G. Taraldsen, “Computer Simulation of Forward Propagation in Soft Tissue,” *IEEE Trans. Ultrason., Ferroelect., Freq. Contr.*, vol. 52, pp. 1473–82, 2005.
- [12] T. Varslot and S.-E. Måsøy, “Forward Propagation of Acoustic Pressure Pulses in 3D Soft Biological Tissue,” *Mod. Ident. Cont.*, vol. 27, no. 3, pp. 181–200, 2006.
- [13] J. A. Jensen and N. B. Svendsen, “Calculation of Pressure Fields from Arbitrary Shaped, Apodized and Exited Ultrasound Transducers,” *IEEE Trans. Ultrason., Ferroelect., Freq. Contr.*, vol. 39, pp. 262–7, 1992.
- [14] E. Faccioli, F. Maggio, R. Paolucci, and A. Quarteroni, “2D and 3D Elastic Wave Propagation by a Pseudo-Spectral Domain Decomposition Method,” *J. Seism.*, vol. 1, pp. 237–51, 1997.
- [15] D. Komatitsch and J.-P. Vilotte, “The Spectral Element Method: An Efficient Tool to Simulate the Seismic Response of 2D and 3D Geological Structures,” *Bull. Seism. Soc. Am.*, vol. 88, pp. 368–92, 1998.
- [16] X. Yuan, D. Brorup, J. Wisken, M. Berggren, and S. A. Johnson, “Simulation of Acoustic Wave Propagation in Dispersive Media with Relaxation Losses by Using FDTD Method with PML Absorbing Boundary Condition,” *IEEE Trans. Ultrason., Ferroelect., Freq. Contr.*, vol. 46, pp. 14–23, 1999.
- [17] T. D. Mast, L. P. Souriau, D.-L. D. Liu, M. Tabei, A. I. Nachman, and R. Waag, “A k-Space Method for Large-Scale Models of Wave Propagation in Tissue,” *IEEE Trans. Ultrason., Ferroelect., Freq. Contr.*, vol. 48, pp. 341–54, 2001.
- [18] M. Tabei, T. D. Mast, and R. Waag, “A k-Space Method for Coupled First-Order Acoustic Propagation Equations,” *J. Acoust. Soc. Am.*, vol. 111, pp. 53–63, 2002.
- [19] S. Ginter, M. Liebler, T. Dreyer, and R. E. Riedlinger, “Full-Wave Modeling of Therapeutic Ultrasound: Nonlinear Ultrasound Propagation in Ideal Fluids,” *J. Acoust. Soc. Am.*, vol. 111, pp. 2049–59, 2002.
- [20] M. Liebler, S. Ginter, T. Dreyer, and R. E. Riedlinger, “Full-Wave Modeling of Therapeutic Ultrasound: Efficient Time-Domain Implementation of the Frequency Power-Law Attenuation,” *J. Acoust. Soc. Am.*, vol. 116, pp. 2742–50, 2004.

- 
- [21] M. G. Wismer, “Finite Element Analysis of Broadband Acoustic Pulses Through Inhomogeneous Media with Power-Law Attenuation,” *J. Acoust. Soc. Am.*, vol. 120, pp. 3492–502, 2006.
- [22] M. O. Deville, P. F. Fischer, and E. G. Mund, *High-Order Methods for Incompressible Fluid Flow*. Cambridge University Press, 2002, ch. 3, pp. 98–161.
- [23] W. Bickford, *A First Course in the Finite Element Method*. Homewood, IL: Irwin, 1990, ch. 3, 4, pp. 216–481.
- [24] C. Bernardi and Y. Maday, “Spectral Methods,” in *Handbook of Numerical Analysis Volume V: Techniques of Scientific Computing (Part 2)*, P. G. Ciarlet and J. L. Lions, Eds. Elsevier, 1997, pp. 209–486.
- [25] B. A. J. Angelsen, *Ultrasound Imaging*. Trondheim, Norway: Emantec, 2000, vol. 1.
- [26] —, *Ultrasound Imaging*. Trondheim, Norway: Emantec, 2000, vol. 2.
- [27] D. Gottlieb and S. A. Orszag, *Numerical Analysis of Spectral Methods*. Philadelphia: SIAM, 1977, ch. 1–4, pp. 1–54.
- [28] C. Canuto, A. Yousuff Hossaini, Alfio Quarteroni, and J. Thomas A. Zang, *Spectral Methods – Fundamentals in Single Domain*. New York: Springer, 2006, ch. 2, pp. 39–116.
- [29] D. Komatitsch and J. Tromp, “Introduction to the Spectral Element Method for Three-Dimensional Seismic Wave Propagation,” *Geophys. J. Int.*, vol. 139, pp. 806–22, 1999.
- [30] Y. Maday and E. M. Rønquist, “Optimal Error Analysis of Spectral Methods with Emphasis on Non-Constant Coefficients and Deformed Geometries,” *Comp. Meth. Appl. Mech. Eng.*, vol. 80, pp. 91–115, 1990.
- [31] Y. Maday, A. T. Patera, and E. M. Rønquist, “The PN x PN-2 Method for the Approximation of the Stokes Problem,” MIT, Tech. Rep., 1992.
- [32] E. Hairer, C. Lubich, and G. Wanner, “Geometric Numerical Integration Illustrated by the Störmer–Verlet Method,” *Acta Numerica*, pp. 399–450, 2003.
- [33] E. Turkel, “On the Practical Use of High-Order Methods for Hyperbolic Systems,” *J. Comp. Phys.*, vol. 35, pp. 319–40, 1980.

- 
- [34] A. I. Nachman, J. F. Smith, III, and R. C. Waag, “An Equation for Acoustic Propagation in Inhomogeneous Media with Relaxation Losses,” *J. Acoust. Soc. Am.*, vol. 88, pp. 1584–95, 1990.
- [35] A. D. Pierce, *Acoustics - An Introduction to Its Physical Principles and Applications*, 3rd ed. Melville, NY: Acoustical Society of America, 1994.
- [36] M. E. Frijlink, H. Kaupang, T. Varslot, and S.-E. Måsøy, “Abersim: A Simulation Program for 3D Nonlinear Acoustic Wave Propagation for Arbitrary Pulses and Arbitrary Transducer Geometries,” in *IEEE Ultrason. Symp. Proc.*, 2008, pp. 1282–5.

# Analysis of Reverberations in Medical Ultrasound

Halvard Høilund-Kaupang, Jochen Deibele, Thor A. Tangen and Bjørn  
Angelsen

Department of Circulation and Medical Imaging, NTNU, Trondheim, Norway

## Abstract

A mathematical model of reverberations in medical ultrasound is presented along with a classification system. The model shows that all reverberations are constructed from two spatially reciprocal components. For equal transmit and receive beamforming and linearly elastic materials, the two components are equal. If nonlinear elasticity is introduced, the two components are distorted differently. Numerical experiments are conducted to verify the presented model for a setup using plane reflectors. Both a (non-diffracting) plane wave setup and a full three-dimensional transducer setup is investigated. Effects of reverberations are investigated for fundamental and second-harmonic imaging. Second-harmonic suppression of reverberations is discussed, and suggested to be a combined effect of a proposed reverberation weight filter and spatial differences in transmit beam intensity. The first dominates the suppression when the first scatterer is close to the transducer and the other close to the object point. If the two scatterers are close to each other, the suppression is mainly determined by the relative transmit beam intensity of the farthest scatterer and the object point.

## D.1 Introduction

Ultrasound images are created with pulse-echo techniques where the reflected echoes arise from fluctuations in acoustical impedance of the medium, *e.g.*, the human body.<sup>1</sup> Echoes are back scatter from interfaces between different types of tissue and from local random fluctuations within one type of tissue. Images are created under the Born approximation, *i.e.*, each structure or fluctuation only causes first-order scattering.<sup>1</sup> This is a robust and simple approximation, but in reality, sound is scattered multiple times. Multiple echoes, or reflections, are called reverberations and introduce noise and artifacts in the produced images.<sup>2-4</sup>

Reverberations are one source of *clutter* in ultrasound images together with phase aberrations and side-lobe artifacts.<sup>5</sup> Detection of small cysts, hypo-echoic tumors and atherosclerosis is especially vulnerable to clutter noise because the diagnostic information is found in regions where the intensity of the first-order echo is low compared to the surrounding tissue. Phase aberrations and side-lobe artifacts are not investigated in this study. A reverberation can visually be identified as a repetition of a strong scatterer or reflector, or as ghost noise especially seen in the lumen of vessels and cavities.<sup>4</sup>

Second-harmonic imaging is shown to reduce clutter and improve image quality, but the improvement is less pronounced in applications using high frequencies than low.<sup>3,6-8</sup> In high frequency applications, harmonic imaging alone does not provide the best image, and is used in combination with other techniques such as spatial compounding, multiple foci etc.<sup>3,8</sup> Second-harmonic imaging is also shown to be less influenced by phase aberrations in applications where a body wall is present.<sup>9,10</sup> These image enhancements are based on the Born approximation and does not *remove* reverberations, but reduce the effect of them.

To recognize reverberations and reduce the effect of reverberations, an acoustical reverberation model is needed. The following sections present a mathematical model for reverberations and a classification system defining three main classes of reverberations. The two first classes are investigated through numerical experiments. The ability to suppress reverberations with second-harmonic imaging is discussed.

## D.2 Reverberation Model

Sections D.2.1–D.2.3 present a reverberation model using equations of linear acoustics.

The radiated linear field from an ultrasound transducer is described in the frequency domain through the spatial frequency response and the Rayleigh integral as<sup>1</sup>

$$P_t(\mathbf{r}, \omega) = ikP(\omega)H_t(\mathbf{r}, \omega) \quad (\text{D.1})$$

$$H_t(\mathbf{r}, \omega) = \int_{S_t} e^{-i\omega\tau_t(\mathbf{r}_t)} U_n(\mathbf{r}_t) G(\mathbf{r}, \mathbf{r}_t, \omega) d\mathbf{r}_t \quad (\text{D.2})$$

where  $P(\omega)$  is the transmitted temporal pressure in the frequency domain,  $S_t$  the transmit aperture surface,  $H_t$  the spatial frequency response of the transducer,  $\tau_t(\mathbf{r}_t)$  proper transmit focus delays,  $U_n(\mathbf{r}_t)$  the normal surface vibration amplitude and  $G(\mathbf{r}, \mathbf{r}_t, \omega)$  a proper Green's function. The Green's function accounts for both absorption and phase aberrations through the relation  $G(\mathbf{r}, \mathbf{r}_t, \omega) = G_f(\mathbf{r} - \mathbf{r}_t, \omega) S_{ab}(\mathbf{r}_t, \omega)$  where  $G_f$  is the free space Green's function for a homogeneous medium with absorption and  $S_{ab}$  a general phase and amplitude aberration screen.<sup>1,2</sup>

### D.2.1 First-Order Echo

Scattering from a point scatterer is expressed as a convolution in time (or multiplication in frequency) with a Green's function for the scattering coordinate  $\mathbf{r}_{obj}$ . A general scattered field from an object can be expressed as an integration over a set of point scatterers distributed in the volume  $V_{obj}$  as

$$P_s(\mathbf{r}, \omega) = -k^2 \int_{V_{obj}} v(\mathbf{r}_{obj}) G(\mathbf{r}, \mathbf{r}_{obj}, \omega) P_i(\mathbf{r}_{obj}, \omega) d\mathbf{r}_{obj} \quad (\text{D.3})$$

where  $k = \omega/c$ ,  $c$  is the propagation velocity,  $v(\mathbf{r}_{obj})$  is the scattering distribution and  $P_i$  and  $P_s$  the incoming and scattered field respectively. The first-order back scattered pressure is denoted  $P_{s1}$  and use  $P_i = P_t$ .

The total, beamformed receive signal on the receive aperture surface  $S_r$  is found through combination of Eqs. (D.1)–(D.3), and integration over  $S_r$  as

$$\begin{aligned} Y_1(\omega) &= ikH_{rt}(\omega) \int_{S_r} e^{-i\omega\tau_r(\mathbf{r}_r)} P_{s1}(\mathbf{r}_r, \omega) d\mathbf{r}_r \\ &= -k^2 \int_V U(\omega) H_t(\mathbf{r}_1, \omega) v(\mathbf{r}_1) H_r(\mathbf{r}_1, \omega) d\mathbf{r}_1 \end{aligned} \quad (\text{D.4})$$

where  $Y_1$  is the received beamformed signal, the subscript 1 denotes first-order scattering,  $\tau_r(\mathbf{r}_r)$  proper receive focus delays,  $H_r(\mathbf{r}, \omega)$  the spatial frequency response of the receive transducer defined as in Eq. (D.2) with a unit amplitude function, and

$$U(\omega) = ikH_{rt}(\omega)P(\omega), \quad (\text{D.5})$$

where  $H_{rt}(\omega)$  is the electromechanical transfer function of the transducer. Equation (D.5) is assumed to be invariant under the transducer surface coordinate.<sup>1</sup>

### D.2.2 Higher Order Echo

For multiple scattering, Eq. (D.3) is applied multiple times to achieve the  $n$ 'th order scattered pressure field. In directive sound beams, most of the energy is radiated in the forward direction. Specular reflections contribute to strong echoes, and plane structures parallel to the transducer surface are assumed to be a major source of reverberations. Plane structures are not necessarily infinitely large planes, but structures that can be approximated by a plane within the cross-section of the wave field. This assumption implies that received echoes of odd order are more dominant than echoes of even order.

If  $P_{s1}$  is the scattered field from the scatterer  $V_1$ , the second- and third-order scattered field is found equivalently to Eq. (D.3) as

$$P_{s2}(\mathbf{r}, \omega) = \int_{V_2} \sigma(\mathbf{r}_2) G(\mathbf{r}, \mathbf{r}_2, \omega) P_{s1}(\mathbf{r}_2, \omega) d\mathbf{r}_2 \quad (\text{D.6})$$

$$P_{s3}(\mathbf{r}, \omega) = -k^2 \int_{V_3} v(\mathbf{r}_3) G(\mathbf{r}, \mathbf{r}_3, \omega) P_{s2}(\mathbf{r}_3, \omega) d\mathbf{r}_3 \quad (\text{D.7})$$

where  $\sigma$  and  $v$  are point scatter distributions for the volume scatterers  $V_2$  and  $V_3$ . The second scatterer can either be a general volume scatterer  $-k^2 v(\mathbf{r}_2)$ , or a reflective surface with a given reflection coefficient. Both scatterers  $V_1$  and  $V_3$  are assumed to be general volume scatterers.

The transition from the first scatterer in  $V_1$  to  $V_3$  can be found as the second-order scattered field at the coordinate  $\mathbf{r}_3$  (with the  $\omega$  dependence omitted):

$$\begin{aligned} P_{s2}(\mathbf{r}_3) &= \int_{V_2} \sigma(\mathbf{r}_2) G(\mathbf{r}_3, \mathbf{r}_2) P_{s1}(\mathbf{r}_2) d\mathbf{r}_2 \\ &= \int_{V_2} \sigma(\mathbf{r}_2) G(\mathbf{r}_3, \mathbf{r}_2) \int_{V_1} v(\mathbf{r}_1) G(\mathbf{r}_2, \mathbf{r}_1) P_t(\mathbf{r}_1) d\mathbf{r}_1 d\mathbf{r}_2 \end{aligned}$$

where the order of integration can be interchanged to form a reverberation transfer function

$$H_{\text{rev}}(\mathbf{r}_3, \mathbf{r}_1) = \int_{V_2} G(\mathbf{r}_3, \mathbf{r}_2) \sigma(\mathbf{r}_2) G(\mathbf{r}_2, \mathbf{r}_1) d\mathbf{r}_2. \quad (\text{D.8})$$

From spatial reciprocity of the Green's function it is easy to verify that  $H_{\text{rev}}(\mathbf{r}_1, \mathbf{r}_3) = H_{\text{rev}}(\mathbf{r}_3, \mathbf{r}_1)$ . A geometrical interpretation of  $H_{\text{rev}}$  is presented in Fig. D.1.

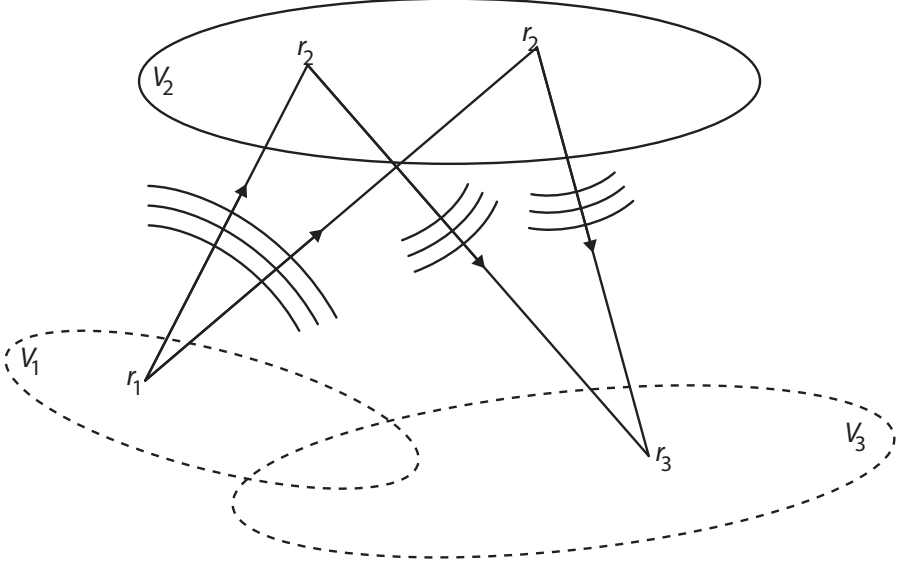


**Figure D.1:** Geometrical interpretation of the reverberation transfer function  $H_{\text{rev}}$  mapping the scattered field from  $\mathbf{r}_1$  through all  $\mathbf{r}_2 \in V_2$  to  $\mathbf{r}_3$ . The reverse path  $\mathbf{r}_3 \rightarrow \mathbf{r}_2 \rightarrow \mathbf{r}_1$  is not drawn for simplicity.

The received third-order signal is found equivalently to Eq. (D.4) through reception of  $P_{s3}$  from Eq. (D.7) as

$$\begin{aligned}
 Y_3(\omega) &= ikH_{\text{rt}}(\omega) \int_{S_r} e^{-i\omega\tau_r(\mathbf{r}_r)} P_{s3}(\mathbf{r}_r, \omega) d\mathbf{r}_r \\
 &= k^4 \int_{V_1} \int_{V_3} v(\mathbf{r}_1) H_{\text{rev}}(\mathbf{r}_1, \mathbf{r}_3, \omega) v(\mathbf{r}_3) \\
 &\quad \times \int_{S_r} e^{-i\omega\tau_r(\mathbf{r}_r)} G(\mathbf{r}_3, \mathbf{r}_r, \omega) d\mathbf{r}_r \\
 &\quad \times U(\omega) H_t(\mathbf{r}_1, \omega) d\mathbf{r}_1 d\mathbf{r}_3 \\
 &= k^4 \int_{V_1} \int_{V_3} v(\mathbf{r}_1) H_{\text{rev}}(\mathbf{r}_1, \mathbf{r}_3, \omega) v(\mathbf{r}_3) \\
 &\quad \times U(\omega) H_t(\mathbf{r}_1, \omega) H_r(\mathbf{r}_3, \omega) d\mathbf{r}_1 d\mathbf{r}_3.
 \end{aligned} \tag{D.9}$$

From this, the received high-order back scattered field can be found in a similar fashion for orders  $N > 3$ .

The total received signal is the sum of the first- and the higher order signal components. The observed reverberation noise in the field point  $\mathbf{r}_{\text{obj}}$  is defined as all high-order signal components where the time-of-flight for the path

$\mathbf{r}_t \rightarrow \mathbf{r}_1 \rightarrow \dots \rightarrow \mathbf{r}_N \rightarrow \mathbf{r}_r$  equals the time-of-flight of the first-order echo  $\mathbf{r}_t \rightarrow \mathbf{r}_{\text{obj}} \rightarrow \mathbf{r}_r$ . None of the scatterers are assumed to be total reflecting, and spatial reciprocity of Eq. (D.8) in (D.9) implies that one pair of scatterers,  $\mathbf{r}_1$  and  $\mathbf{r}_N$ , contributes with two components that always act in pairs where  $\mathbf{r}_1$  is the first scatterer for one component and  $\mathbf{r}_N$  the first for the other. A straight forward expansion of this to include echoes of higher order than three is possible where  $H_{\text{rev}}$  is augmented to include integration over all scatterers  $\mathbf{r}_2$  to  $\mathbf{r}_{N-1}$ .

### D.2.3 Reverberation Classes

For imaging of an object point  $\mathbf{r}_{\text{obj}} \in V_{\text{obj}}$  at depth  $z_{\text{obj}}$ , the noise contribution from reverberations are high-order scattering from the depth interval  $[0, z_{\text{obj}}]$ . The framework presented in the preceding section opens for a classification system for reverberations. Three classes are defined in this section: Class I, II and III. The first two have two sub classes each. A conceptual description follows and Fig. D.2 shows a graphical presentation of the three classes.

**Class I/Ib:** The first scatterer ( $\mathbf{r}_1$ ) is located in the depth interval  $[0, z_{\text{obj}}/2]$ .

For the Class I component, the second scatterer ( $\mathbf{r}_2$ ) is on the transducer surface, and for Class Ib;  $\mathbf{r}_2$  is a general scatterer located closer to the transducer than  $\mathbf{r}_1$ . Note that  $\mathbf{r}_1 \neq \mathbf{r}_2$ . The last scatterer ( $\mathbf{r}_N$ ) is located in the interval  $[z_{\text{obj}}/2, z_{\text{obj}}]$ .

**Class II/IIb:** Reciprocity of  $H_{\text{rev}}$  implies that all reverberations act in pairs.

The Class II/IIb reverberation is the reciprocal of Class I/Ib. The first scatterer in time is now  $\mathbf{r}_N$ . The second scatterer ( $\mathbf{r}_2$ ) is the same for the pairs I/II and Ib/IIb.

**Class III:** Both the first and last scatterer in time are located in the interval  $[z_{\text{obj}}/2, z_{\text{obj}}]$ . Class III reverberations also act in pairs, but the two components are not defined by separate classes and both are recognized as Class III.

Three aspects are worth further comments. First: For a given  $H_{\text{rev}}$ , the two reciprocal components of a reverberation only depend on the first ( $\mathbf{r}_1$ ) and last ( $\mathbf{r}_N$ ) scattering coordinate. This holds for all class contributions from one  $\mathbf{r}_1$  to one  $\mathbf{r}_N$  because a sum over several  $\mathbf{r}_2$  (or more scatterers) in the linear regime can be included in  $H_{\text{rev}}$ .

Second: Reverberations form in the region between the transducer and the object point. Where  $\mathbf{r}_{\text{obj}}$  is found within a scattering object, the first-order echo from  $\mathbf{r}_{\text{obj}}$  generally dominates the back scattered signal because multiple

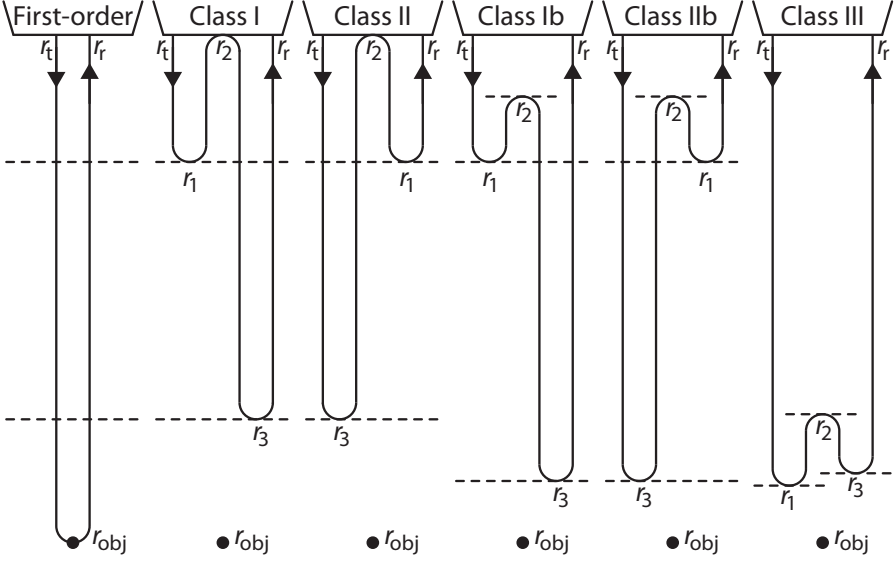


**Figure D.2:** Conceptual presentation of the first-order echo from  $\mathbf{r}_{\text{obj}}$  and the proposed Class I/II pair, Ib/IIb pair and III reverberations. The reverse path of the Class III reverberation is not drawn for simplicity.

scattering reduces the amplitude of the field multiple times. In the case where  $\mathbf{r}_{\text{obj}}$  is found within a hypo-echoic region, and none of the three scatterers,  $\mathbf{r}_1 \rightarrow \dots \rightarrow \mathbf{r}_N$ , are weak scatterers, the high-order back scatter can be of the same magnitude, or higher, than the first-order echo.

Third: The choice of beamforming affects the presented reverberation model. The scatterer  $\mathbf{r}_1$  is located in the near field, and hence outside the focal region, of both the transmit and receive beam. In a dynamically focused receive beam,  $\mathbf{r}_N$  can be close to the focal point ( $\mathbf{r}_{\text{obj}}$ ) of the receive beam, and anywhere in the transmit beam. Because of this, beamforming affects the contribution of the reverberation relative to the first-order echo.

#### D.2.4 Effect of Nonlinear Propagation

If the material is non-linearly elastic, the transmitted field cannot be found directly from the Rayleigh integral or the frequency response as in Eqs. (D.1)–(D.2). Nonlinear distortion generate higher harmonic frequencies as the pulse propagates, and the distortion of the two components of high-order echoes depend on the location of the first scatterer, *i.e.*,  $\mathbf{r}_1$  or  $\mathbf{r}_N$  for the Class I and II component respectively. After the first reflection/scattering, the amplitude

is assumed to be reduced such that further propagation is governed by linear acoustics.

When the first scatterer is close to the transducer, nonlinear distortion effects are weakly pronounced in the Class I/Ib reverberation. The Class II component will, according to the class definition, be more distorted than the Class I component, and when  $\mathbf{r}_N$  and  $\mathbf{r}_{\text{obj}}$  approaches each other, the distortion of the reverberation resemble that of the first-order echo. Both components of the Class III reverberation are distorted similarly to the Class II component.

A nonlinear field is denoted with a subscript  $n$  and is not separable in the sense that  $P_n(\mathbf{r}, \omega) \neq P(\omega)H_t(\mathbf{r}, \omega)$ .<sup>2</sup> Although the transmitted field cannot be found from Eqs. (D.1)–(D.2) directly, it can be simulated using a proper simulation tool. Because the receive beam is assumed to be linear, and the temporal variation is incorporated in the transmit beam, the effect of the transducer transfer function in Eq. (D.5) is accounted for in the transmit beam rather than the receive beam as  $U_{tn}(r, \omega) = ikH_{rt}(\omega)P_{tn}(r, \omega)$ .

### D.2.5 Received Signal Model

From this on, reverberations of higher order than three is neglected. The received signal from a given depth interval is in the frequency domain defined as

$$Y_n(\omega) \approx Y_{1n}(\omega) + \sum Y_{3n}(\omega)$$

where  $Y_{1n}$  is the first-order signal defined in Eq. (D.4), and  $\sum Y_{3n}$  the sum over all third-order signal contributions from different  $V_1$ ,  $V_2$  and  $V_3$  as presented in Eq. (D.9). The reverberation contributions are the ones to be discussed further in detail.

For *one* third-order contribution, the received signal is further split into a Class I and II component as  $Y_{3n} = Y_{3In} + Y_{3II n}$  where the two components each are defined in Eq. (D.9). The two components differ in the sense that the order of the scattering in time, *i.e.*, which coordinate,  $\mathbf{r}_1$  or  $\mathbf{r}_3$ , is the *transmit* field

evaluated in. The Class I and II components are found as

$$Y_{3In}(\omega) = k^4 \int_{V_1} U_{tn}(\mathbf{r}_1, \omega) v(\mathbf{r}_1) \times \int_{V_3} H_{\text{rev}}(\mathbf{r}_1, \mathbf{r}_3, \omega) v(\mathbf{r}_3) H_r(\mathbf{r}_3, \omega) d\mathbf{r}_3 d\mathbf{r}_1 \quad (\text{D.10})$$

$$Y_{3IIIn}(\omega) = k^4 \int_{V_3} U_{tn}(\mathbf{r}_3, \omega) v(\mathbf{r}_3) \times \int_{V_1} H_{\text{rev}}(\mathbf{r}_1, \mathbf{r}_3, \omega) v(\mathbf{r}_1) H_r(\mathbf{r}_1, \omega) d\mathbf{r}_1 d\mathbf{r}_3 \quad (\text{D.11})$$

where  $U_{tn}(\mathbf{r}_i, \omega)$  is the (nonlinear) transmit beam evaluated at  $\mathbf{r}_i$ , and the integral over  $\mathbf{r}_j$  can be interpreted as a (linear) reverberation receive beam defined as

$$H_{r,\text{rev}}(\mathbf{r}_i) = \int_{V_j} H_{\text{rev}}(\mathbf{r}_i, \mathbf{r}_j) v(\mathbf{r}_j) H_r(\mathbf{r}_j) d\mathbf{r}_j$$

where the  $\omega$  dependence is left out.

It is easy to verify that in the linear case, where  $U_t(r, \omega) = U(\omega)H_t(r, \omega)$ , the Class I and II reverberations are equal if  $H_r = H_t$ . If  $V_1 = V_3$ , the order of integration can be interchanged, and the Class I and II components are equal regardless of the non-linearity of the tissue. Because a sum over several  $V_2$  can be included in  $H_{\text{rev}}$ , both of these claims also hold for Class Ib and IIb, or a sum over many  $V_2$  contributions.

The signal model for the reverberation signal is further modified as

$$Y_{3n}(\omega) = \left( \frac{Y_{3In}(\omega)}{Y_{3IIIn}(\omega)} + 1 \right) Y_{3IIIn}(\omega) = (Q_n(\omega) + 1) Y_{3IIIn}$$

where  $Q_n(\omega)$  is a general frequency dependent filter that relates the Class I and II component to each other. If they are equal,  $Q(\omega) = 1$ , and the third-order reverberation is  $Y_{3n} = 2Y_{3IIIn}$ .

In the case where  $Y_{3In} \neq Y_{3IIIn}$ , *i.e.*, when the tissue is nonlinear or when the transmit and receive beams are different, it is interesting to investigate the influence of these two effects on the reverberation contribution. A reverberation weight filter  $W(\omega)$  is constructed such that

$$W_n(\omega) = \frac{Q_n(\omega) + 1}{2}. \quad (\text{D.12})$$

The absolute value of  $W$  defines a modification of the amplitude for one pair of received reverberations caused by beamforming or nonlinear distortion. The

phase of  $W$  is considered to be of less importance, because a summation of many contributions with a random phase and amplitude introduce a reverberation speckle signal in addition to the first-order speckle. Phase differences in  $Q$  will influence  $W$  such that if the Class I and II components are added in-coherently, this will also be reflected in the amplitude of  $W$ .

If  $H_r=H_t$ , the influence from nonlinear propagation will be an amplitude effect within the imaging frequency band. In fundamental imaging, the lost energy to higher harmonic frequencies is lower for the Class I/Ib components than the Class II/Ib components. This implies both  $Q>1$  and  $W>1$ . Compared with the linear case, this indicates that an amplification of the Class I component relative to the Class II component when  $r_1$  approaches the transducer, and  $r_3$  the focal point.

When the distance in depth between the first and third scatterer grows, such effects in  $W_n$  become more pronounced. For a given  $r_1$ , the maximum depth difference to  $r_3$  occur when  $r_2$  is on the transducer surface. This indicates, together with the fact that the transducer surface itself is a plane and strong reflector, that the Class I/II components contribute more than the Class Ib/Ib components. The Class III reverberation is assumed to provide  $W_n \approx 1$  because both components are similarly distorted.

Employing second-harmonic imaging, but still assuming  $H_r=H_t$ , the amplitude of the second-harmonic field increases with depth. When  $r_1$  approaches the transducer, the received (second-harmonic) Class I component approaches zero, and  $|W_n| \rightarrow 1/2$ . From this, it follows that  $W_n$  introduces an amplitude modification in the range 0–6 dB in second-harmonic imaging by, partially or completely, suppressing the Class I relative to the Class II component. The weight filter is less efficient in reducing the amplitude of the Class Ib and Iib components because the first and third scatterer are closer to each other in depth. In the case  $V_1=V_3$ ,  $|W_n|=1$  and the reverberation contribution is dependent on the strength of the Class II reverberation.

### **D.3 Numerical Experiments**

Three numerical experiments are conducted: Two plane wave experiments and one full, three-dimensional (3D) experiment. The plane wave experiments are simulated using a time-domain Spectral Element Method (SEM) and the full 3D experiment is the radiated field from a diagnostic transducer simulated with the program Abersim.<sup>13,11,12</sup>

The time-domain SEM is based on an acoustic model presented in Refs. 14 and 15. The solution is approximated using high-order polynomials ( $N = 16$ ).

Previous presented SEM tools only handle linear propagation,<sup>16,17</sup> and the method used in this paper introduces a modification to account for non-linearity similar to that presented by Wojcik *et al.*<sup>18</sup> The absorption model is based on a theoretical framework presented by Nachman *et al.*<sup>19</sup> which is also employed in Refs. 14 and 15.

The nonlinear and absorption model of the used SEM are separately verified in plane wave experiments through comparison with available analytic solutions. Errors measured in the  $L_2$ -norm are  $0.74 \cdot 10^{-3}$ ,  $7.85 \cdot 10^{-3}$  and  $33.12 \cdot 10^{-3}$  for the first-, second- and third-harmonic component respectively in the non-linear model verification, and  $1.45 \cdot 10^{-3}$  for the absorption and  $0.24 \cdot 10^{-3}$  for the phase velocity measured over a proper frequency range.

### D.3.1 Plane Wave Experiments

Linear and nonlinear plane wave propagation is simulated with the SEM tool in the 180 element interval  $[0, 30]$  mm. The background speed of sound and density are  $c_0=1540 \text{ m s}^{-1}$  and  $\rho_0=1050 \text{ kg m}^{-3}$  respectively. The pressure at the source boundary ( $z=0$ ) is recorded. The source boundary acts as a hard wall when not active. The other boundary is absorbing. The transmitted pulse is a sinusoidal vibration with center frequency 8 MHz and a Gaussian envelope with 50 % fractional bandwidth. The source amplitude is 1 MPa.

Thin layers numbered  $L_1$  to  $L_{10}$  with higher density are introduced at every second millimeter in depth up to 20 mm. A density map of the domain is presented in Fig. D.3. The reflection from thin layers introduce phase changes to the pulse from the summation of the first and second boundary of the layer, and a infinitely thin layer introduce a phase shift of  $\pi/2$ . This implies that multiple reflected pulses add incoherently. The total reflection coefficient will also differ from the reflection coefficient from each of the interfaces.<sup>1</sup>

The first plane wave experiment uses only two layers:  $L_2$  and  $L_8$  (located at 4 and 16 mm respectively). The second reflector is the source boundary. First, the setup is simulated with linear elasticity and no absorption. To verify that the Class I and II reverberations always act in pairs, four separate simulations are performed. The outcome of the first is the total received signal  $Y_{\text{tot}}$ , when both layers are present at all times. To quantify the contribution from high-order ( $N>3$ ) echoes, the second simulation aim to isolate the third-order received signal,  $Y_3$ . This is done through implementation of an event handler that modifies the material of the domain during the simulation such that layers can be introduced or removed during the simulation. The event handler ensures that the number of reflections/transmissions are equal for both components and the total third-order signal. The second simulation produces the

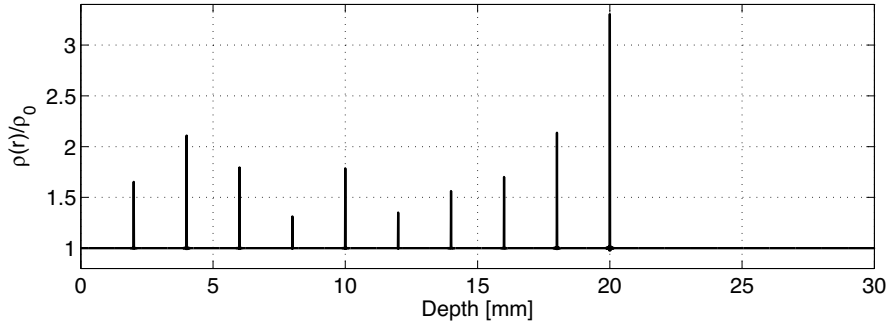


**Figure D.3:** Mass density of the ten layers in the computational domain. The layers  $L_1$  to  $L_{10}$  are the spikes numbered from left to right.

total third-order signal. A similar approach is used to isolate the third-order Class I and II components in the third and fourth simulation. The sum of the two isolated components is denoted  $Y_{3\text{sum}}=Y_{3\text{I}}+Y_{3\text{II}}$ .

Introducing nonlinear elasticity and absorption to the aforementioned setup, the experiment is re-run and the Class I and II reverberation components are isolated. The effects of non-linearity and absorption are investigated. The coefficient of non-linearity is  $\beta_n=3.5$  and the absorption is tuned to  $0.5 \text{ dB cm}^{-1}\text{MHz}^{-1}$  using two relaxation processes with relaxation times  $\tau_1=62.5 \text{ ns}$  and  $\tau_2=6.25 \text{ ns}$ . The relative compressibilities were found using the function `fminsearch` in Matlab (The Mathworks, Natick, CA) to minimize the absorption defined by Eq. (45) in Ref. 19.

Time gain compensation is applied upon receive for simulations with absorption. The total reverberation weight filter  $W$  is found for both fundamental and second-harmonic imaging. For the harmonic setup, the radiated pulse has center frequency 4 MHz and a Gaussian envelope with 40% fractional bandwidth. The harmonic signal is obtained using pulse-inversion for the plane wave experiments.

The second plane wave experiment utilizes all ten layers and compares the reverberation signal for fundamental and second-harmonic imaging. Non-linearity and absorption are the same as described in the preceding paragraph. The first-order received echo is of interest, and in the first simulation, the event handler is used to remove each layer once the transmitted pulse has passed. In a second simulation, the tenth layer ( $L_{10}$ ) is permanently removed and the remaining nine layers are present at all times to compare the first-order and total *reverberation* signal at depth 20 mm for fundamental and harmonic imaging.

### D.3.2 Full 3D Experiment

A full 3D numerical simulation is performed in Abersim to investigate the effects of beamforming on the Class I and II reverberations. An array transducer radiates into a medium with plane reflecting layers similar to the plane wave experiments, but in the full 3D case, all layers have equal reflection coefficient,  $R=0.1$ . The layers are located at every second millimeter in depth up to, but not including, the focal depth (as in the second plane wave experiment). The second scatterer is the transducer surface. The chosen material is a muscle mimicking material with background speed of sound and density  $c_0=1550$  and  $\rho_0=1060$  respectively. The coefficient of non-linearity is  $\beta_n=3.9$  and a power-law absorption model ( $\alpha_0 f^\beta$ ) is employed with  $\alpha_0=0.52 \text{ dB cm}^{-1} \text{ MHz}^{-\beta}$  and  $\beta=1.1$ .

The transducer is a linear array transducer electronically focused in the azimuth direction. A lens is used for focusing in the elevation direction, and both the azimuth and elevation transmit focal depths are  $F_t=20$  mm. Three receive beams are simulated, focused to  $F_r=\{16, 20, 24\}$  mm in the azimuth direction. The elevation receive focus is fixed at 20 mm. The transmitted pulse is an 8 MHz sinusoidal pulse with a Gaussian envelope and 50% fractional bandwidth. For second-harmonic imaging, the center frequency is  $f_c=4$  MHz and the fractional bandwidth 60%.

The spatial resolution is  $\Delta x=100 \mu\text{m}$  and  $\Delta y=97.6 \mu\text{m}$  in the azimuth and elevation directions respectively, and the sampling frequency in time  $F_s=96$  MHz. The transmit beam is set up using 26 transducer elements with  $300 \mu\text{m}$  pitch ( $f/2.56$ ). Transducer elements measure 4 mm in the elevation direction ( $f/5$ ). Two receive aperture settings are investigated for each receive focal depth: One with equal receive and transmit aperture (26 transducer elements) and one tailored to f-number  $f/1.25$ . The latter results in a receive aperture of 44 ( $f/1.21$ ), 54 ( $f/1.23$ ) and 64 ( $f/1.25$ ) transducer elements for the three focal depths 16, 20 and 24 mm respectively.

The layers are combined in pairs such that  $z_1+z_3=F_r$ , and are modeled as pure reflectors. Nonlinear propagation effects are neglected in the reflected field. For simplicity, the phase of the pulse remains unchanged after the reflection. The transducer surface is modeled in the same manner, but the field outside the footprint of the transducer is set to zero, and the field within the extension of the lens (4 mm) is focused twice. The footprint is in the azimuth direction assumed to be wider than the computational domain (25.6 mm) and is set to 8 mm in elevation.

Both linear and nonlinear transmit beams are simulated. Because all scatterers are plane and parallel to the transducer, the field can be propagated

forward up to  $2F_r$ . Receive beamforming is then performed by introduction of proper focusing delays and summation of the pressure field for all spatial points covered by the transducer surface.

## D.4 Results

### D.4.1 Plane Wave Experiments

Figure D.4 presents the results for the linear propagation problem in the first plane wave experiment. The received total signal and two reverberation components are displayed, and the visual match between the Class I and II component is excellent. The right panel shows the difference between the total and third order signal  $\Delta Y_{\text{tot}} = Y_{\text{tot}} - Y_3$ , the third-order signal and the sum of the isolated Class I and II components  $\Delta Y_{\text{sum}} = Y_3 - Y_{3\text{sum}}$ , and difference between the Class I and II component,  $\Delta Y_{\text{iso}} = Y_{3\text{I}} - Y_{3\text{II}}$ . The difference  $\Delta Y_{\text{tot}}$  indicate the presence of higher order echoes in the signal, but the pressure amplitude of these are in the order of Pascal. The differences  $\Delta Y_{\text{sum}}$  and  $\Delta Y_{\text{iso}}$  are very close to zero as expected.

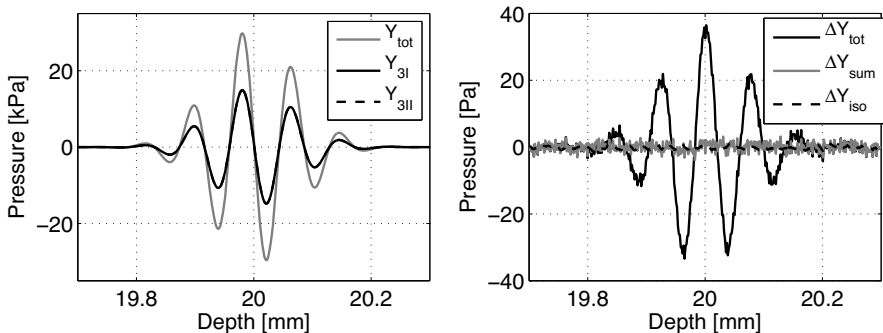


**Figure D.4:** Linear plane wave propagation in the first plane wave experiment. Left: The received reverberation signal. Right: The difference between the simulated signals.

Introducing non-linearity and absorption makes the Class I and II components different. Figure D.5 shows this effect, and it is especially visible in the harmonic case, where the Class I has a lower amplitude than the Class II component.

Results for the second plane wave experiment are presented in Fig. D.6. The first-order signal and the total received signal for the first nine layers are of the same magnitude. Some differences are present, and the total received signal

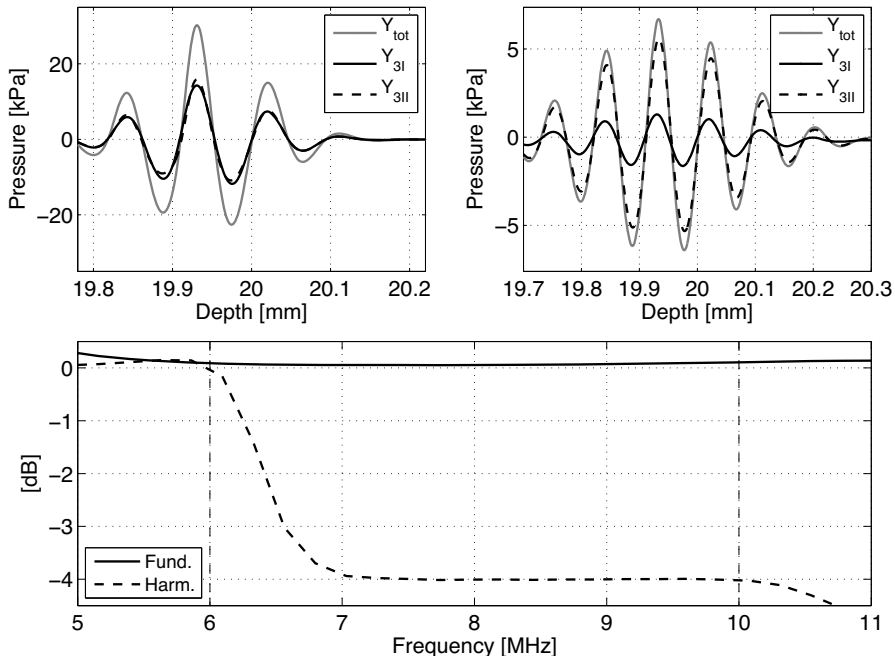


**Figure D.5:** Nonlinear plane wave propagation in the first plane wave experiment. Top two panels: The reverberation signal for fundamental (left) and second-harmonic imaging (right). Bottom: The reverberation weight filter  $W_n$  for the  $L_2$ – $L_8$  layer pair.

for layers  $L_6$  to  $L_9$  is lower than the first order signal. The total reverberation contribution is  $\sim -11$  dB relative to the first-order echo at 20 mm, and second-harmonic imaging suppresses the reverberations  $-5.4$  dB. The total received reverberation signal is a sum over all Class I/Ib, II/IIb and III reverberations, and includes higher order scattering.

#### D.4.2 Full 3D Experiment

In the full 3D experiment, the reverberation weight filter  $W_n$  is presented in Fig. D.7 for the  $F_r=20$  mm setup. In the linear case,  $|W|$  is one. With nonlinear propagation, the shape of  $W_n$  resembles that of the plane wave case, but the magnitude of  $W_n$  is higher in full 3D. The magnitude of  $W_n$  increases for increasing distance between the two layers in a pair. The amplitude modification seen for second-harmonic imaging for the  $L_2$ – $L_8$  layer pair is of the same magnitude as the plane wave case ( $\sim -4$  dB).

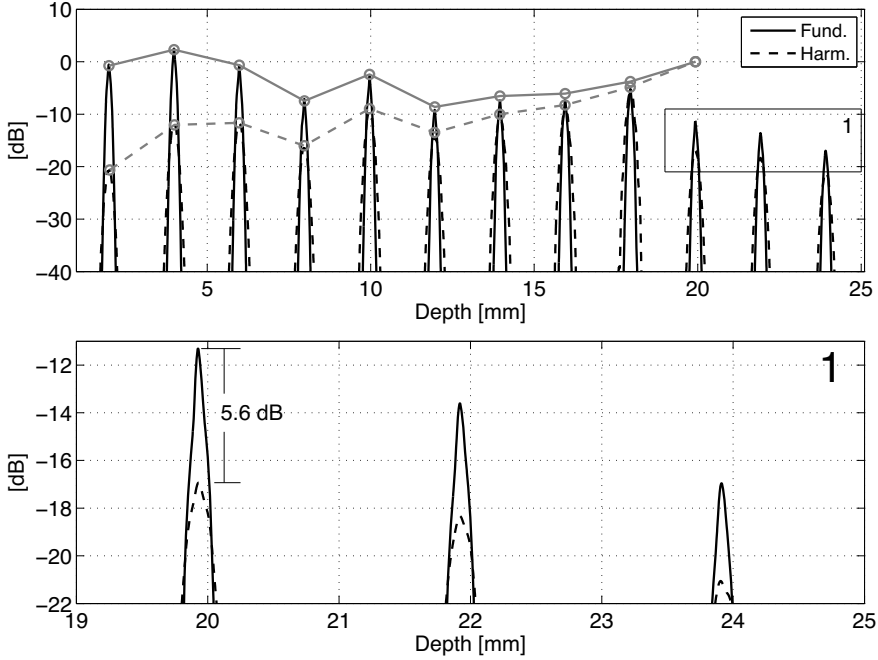


**Figure D.6:** Received first order signal (gray) and total signal (black) from the second plane wave experiment. The simulation for the total signal has removed layer  $L_{10}$  at  $z=20$  mm to only obtain the *reverberation* signal at this depth. The graphs are normalized to the received first order from  $L_{10}$ . The bottom panel is a magnification of the rectangular area denoted 1 in the top panel.

Figure D.8 presents the difference  $\Delta Y_{\text{iso}}$  from linear propagation and the received Class I and II second-harmonic components for the  $L_2$ – $L_8$  layer pair in the full 3D experiment. The normalized error is in the order of  $10^{-6}$ . Similar to the first plane wave experiment, the differences between the Class I and II component are very small for linear propagation, and the Class I component is suppressed relative to the Class II component in second-harmonic imaging.

Figure D.9 presents the absolute value of  $W_n$  for the two cases where  $F_r \neq F_t$ . The phase is of the same magnitude as for  $F_r = F_t$  and is not shown. The shape of  $W_n$  is similar, but the levels differ between the three receive focal settings. The amplitude modification is most prominent when the two layers are far apart.

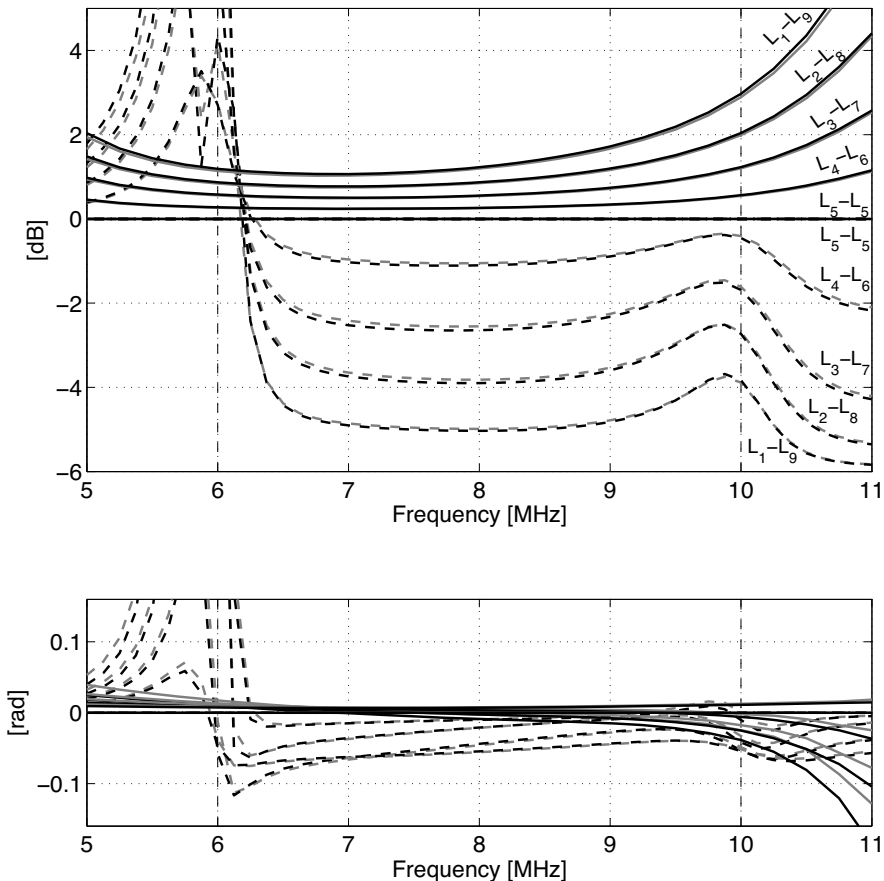


**Figure D.7:** Absolute value (top) and phase (bottom) of  $W_n(\omega)$  when  $F_r = F_t$ . Line colors indicate receive f-number  $f/1.25$  (black) and  $H_r = H_t$  (gray). Line styles indicate second-harmonic imaging (dash) and fundamental imaging with nonlinear (solid) or linear (dash dot at  $\sim 0$  dB and phase) propagation.

## D.5 Discussion

### D.5.1 Plane Wave Experiments

The presented model for reverberations states that Class I and II reverberations always act in pairs. This is verified in the first plane wave experiment. In the linear case, it is stated that the two components are equal, *i.e.*, when the transmit and receive beamforming settings are equal which always is the case in a plane wave environment. Isolating the third order total signal and Class I

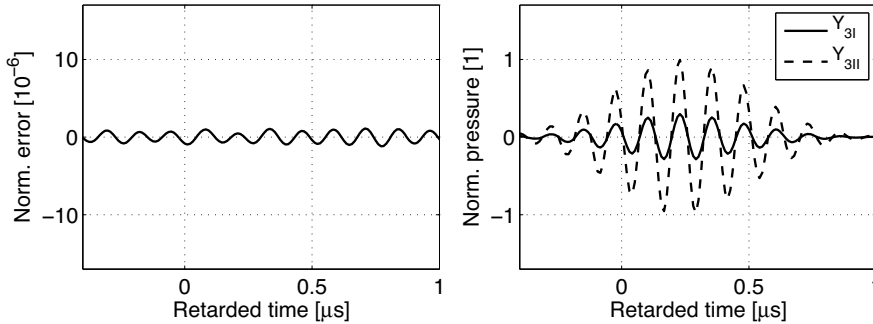


**Figure D.8:** Left: The difference between the Class I and II component with linear propagation. Right: The received second-harmonic Class I and II components. Both panels are normalized to the maximum pressure envelope of the Class II component.

and II components show that the two components are equal, and that the sum of them equals the total third-order reverberation signal.

When non-linearity and absorption are present, the two components become different. Absorption does not cause any differences because it is not a pressure dependent phenomena, and the total propagated distance is equal for the two components. This implies that they are equally attenuated, and non-linearity of the tissue is the only source of differences between the Class I and II components. In fundamental imaging, the difference indicate the amount of fundamental band energy lost to higher harmonics. In second-harmonic imaging it is the difference in energy *gained* in the second-harmonic band. As proposed in Section D.2.5, the maximum possible amplitude modification ( $W_n$ ) of one reverberation pair is  $-6$  dB in second-harmonic imaging when compared with the linear case. The modification arise from partial or complete suppression of the Class I relative to the Class II component, and the results in Fig. D.5 verify this for the  $L_2$ – $L_8$  layer pair.

From the second plane wave experiment the received first-order and total signal align very well for the first layers. As the depth increases, the contribution from reverberation becomes more and more prominent due to more possible combinations of layer pairs in the interval  $[0, z_{\text{obj}}]$ . This introduces a difference visible in the layers  $L_6$  to  $L_9$ . If the first- and third-order signals are added coherently, the total signal should be higher than the first order, but phase differences introduced by reflection/transmission in thin layers and dispersion in the absorption model, cause the contributions to be added incoherently, and the signal can be lower in amplitude.

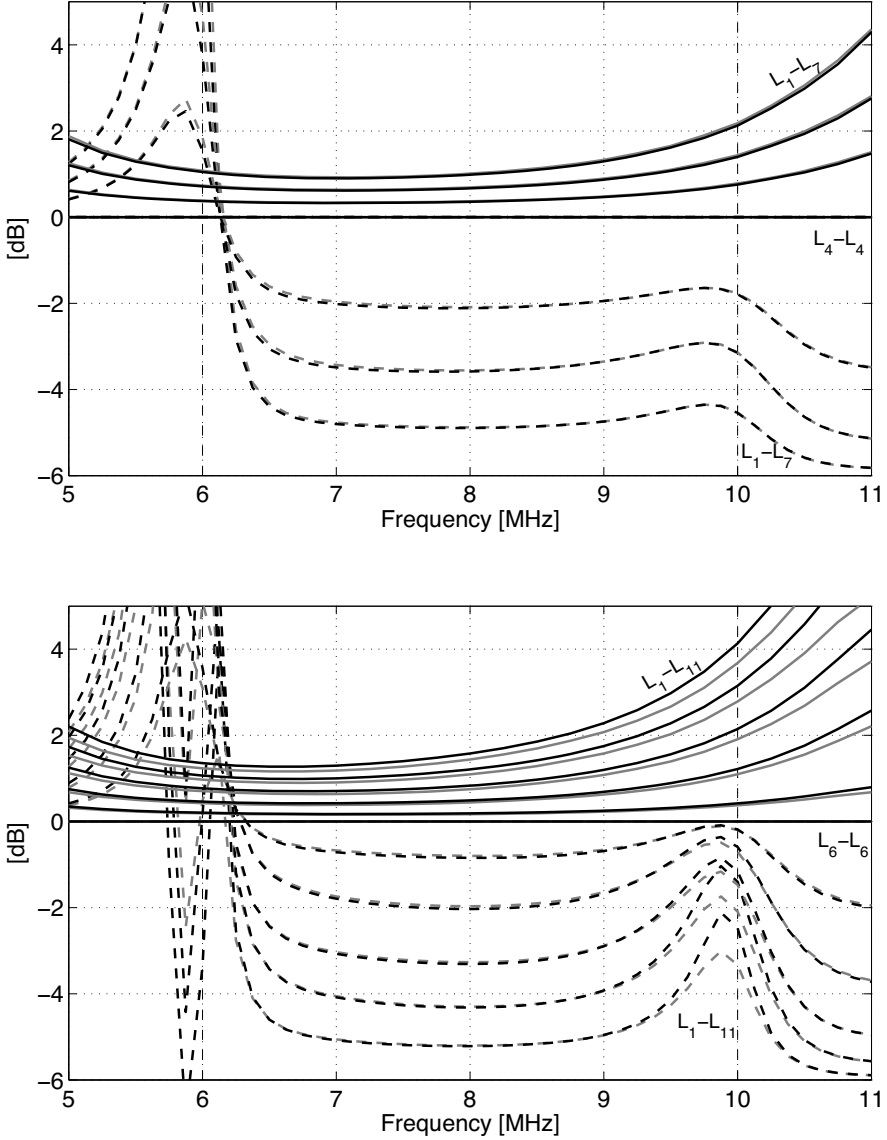


**Figure D.9:** Absolute value of  $W_n$  when  $F_r=16$  mm (top) and  $F_r=24$  mm (bottom). Line colors indicate receive f-number  $f/1.25$  (black) and equal transmit and receive apertures (gray). Line styles are the same as in Fig. D.7.

The  $-5.4$  dB suppression of the reverberation reported for the second-harmonic is measured relative to the (nonlinear) fundamental case and not the linear case.

Because  $W_n$  amplifies the fundamental signal, the suppression obtained through  $W_n$  with second-harmonic imaging increases. However, suppression of reverberations relative to the first-order echoes, are not given by  $W_n$  alone, but also by the differences in transmit beam intensity.

When two layers are far apart, the Class II component is very similar to the first-order echo, *i.e.*, the transmit fields in  $\mathbf{r}_3$  and  $\mathbf{r}_{\text{obj}}$  are similar, and the reverberation suppression is mainly defined through  $W_n$ . In the opposite case, where  $V_1=V_3$  and  $W_n=1$ , the similarity between the Class II component and the first-order echo is at its lowest. Here, the reverberation suppression is given by the transmit beam intensity at  $\mathbf{r}_3$  relative to that in  $\mathbf{r}_{\text{obj}}$ . This will be discussed further in the next section.

### D.5.2 Full 3D Experiment

In the full 3D experiment with linear propagation,  $W=1$  when  $H_r=H_t$  and the medium is linear. This is predicted by the model, and is verified in Fig. D.7, although the lines cannot be distinguished from each other or the rest. When the receive beam is dynamically focused, *i.e.*, has f-number  $f/1.25$  for the three receive focal depths,  $W_n$  is still very close to one for two perfect planes, regardless of the position of the planes. This indicate that beamforming does not play a vital role in suppressing reverberations from perfectly plane reflectors.

If the transducer is modeled as a perfect infinite plane without the lens, the pressure at the receive surface for both the Class I and II components equal the transmit field at depth  $F_t+F_r$ . Geometrically, the curvature of the receive phase fronts equals  $F_r$ , and the receive aperture should not influence the received signal. Diffraction effects, such as edge waves, a finite extension of the transducer surface and the lens, produce different results for different receive f-numbers, but as shown in Figs. D.7 and D.9, such differences are very little pronounced in a setup using plane reflectors.

Compared with the plane wave setup, the amplitude of  $W_n$  increases for fundamental imaging. Generation of harmonic frequencies is a volumetric effect dependent on the local pressure amplitude.<sup>2,9</sup> Diffraction plays an important role in this, and the increased amplitude of  $W_n$  seen in the full 3D experiment compared to the plane wave experiments is believed to arise from higher harmonic generation in focused beams than in plane wave propagation. When  $V_1=V_3$ , Figs. D.7 and D.9 show that  $|W_n|=1$  as predicted for both fundamental and second-harmonic imaging.

The phase of the received signals are zero for the linear case with plane layers and full 3D propagation. Non-linearity introduce a small and smooth phase angle within the frequency band of interest, but different transmit and

receive beamforming does not influence this. In a situation where the scatterers are not perfect planes, the phase is assumed to be less smooth when different transmit and receive beamforming is employed.

The presented model predicts the Class I and II components to be equal if the propagation is linear. The differences shown in Fig. D.8 are in the order of  $10^{-6}$  and is assumed to arise from the numerical experiment rather than the theoretical model. Figure D.8 also shows that the amplitude modification obtained with second-harmonic imaging is a suppression of the Class I component relative to the Class II component.

Different transmit and receive focal depths introduce small differences in the magnitude of  $W_n$  for both fundamental and second-harmonic imaging. The amplitude modification of each layer pair increases if the focal point on receive is deeper than on transmit. The reason for this is that the first layer is located relatively closer to the transducer when the receive focal point moves further away. For all layer pairs and receive focal depths, the amplitude of  $W_n$  is in the range 0—6 dB as predicted by the model, but again; this alone is not a measure on the reverberation suppression.

As discussed in the plane wave experiments: If  $|W_n| < 1$ , this indicate that the Class I component is lower *relative to* the Class II component, and when the Class II component becomes similar to the first-order echo, the reverberation suppression is also given by  $W_n$ . However, the strength of the third-order relative to the first-order signal for one pair is given by the strength of the scatterers  $V_1$ – $V_3$  and  $V_{\text{obj}}$  together with the transmit and receive beam profile. When the Class I and II components become more similar, the similarity of the Class II component to the first-order echo is reduced.

From Eq. (D.11) the weight of the Class II component is the product of the transmit and receive beams evaluated in  $\mathbf{r}_3$  and  $\mathbf{r}_1$  respectively. Even with dynamic focusing,  $\mathbf{r}_1$  will be located closer than half the receive focal depth, and will always be in the near field of the receive beam. On the other hand,  $\mathbf{r}_3$  can be located anywhere in the transmit beam. Assuming low f-numbers on receive,  $H_r(\mathbf{r}_1)$  is assumed to vary slowly when compared with  $H_t(\mathbf{r}_3)$ . Because of this, the suppression of reverberations is assumed to be determined by the combined effect of  $W_n$  and the relative intensity of the transmit beam,  $H_t(\mathbf{r}_3)/H_t(\mathbf{r}_{\text{obj}})$ .

## D.6 Conclusion

A mathematical model of reverberations in medical ultrasound is presented and investigated through numerical experiments. The model claims that reverberations always act in reciprocal pairs, and a classification system is proposed.

The reciprocity of the model is verified in a plane wave experiment. With linear propagation and equal transmit and receive beams ( $H_t=H_r$ ), the two components of the pair, *i.e.*, the Class I and II components will also be equal. This is verified in both a plane wave and full 3D experiment with plane reflectors.

When the propagation is nonlinear, an amplitude modification is introduced through the reverberation weight filter  $W_n$  for each *pair* of reverberations. This introduces an amplification in fundamental imaging and a suppression in second-harmonic imaging when compared with the linear propagation case. Second-harmonic imaging suppresses the Class I component relative to the Class II component, which yields an amplitude modification in the range 0–6 dB. The experiments verify this.

Suppression of reverberations relative to first-order scattering is determined by the combined effects of  $W_n$  and the intensity of the transmit beam. When two layers are far apart the suppression is dominated by  $W_n$ , and when they are close; the relative transmit beam intensity dominates. This applies to *each* pair, and the total reverberation contribution, and suppression, is given through the summation of such pairs.

The previously reported ability to suppress clutter with second-harmonic imaging<sup>3,6-8</sup> is a combined effect of reducing both phase aberrations<sup>9,10</sup> and reverberations. To establish measures for general reverberation suppression in more complex setups, the presented model should be investigated in an experiment accounting for random scatterers and speckle statistics of the received signal.

## References

- [1] B. A. J. Angelsen, *Ultrasound Imaging*. Trondheim, Norway: Emantec, 2000, vol. 1.
- [2] —, *Ultrasound Imaging*. Trondheim, Norway: Emantec, 2000, vol. 2.
- [3] R. Kern, K. Szabo, M. Hennerici, and S. Mairs, “Characterization of Carotid Artery Plaques Using Real-Time Compound B-Mode Ultrasound,” *Stroke*, vol. 35, pp. 870–5, 2004.
- [4] B. D. Sites, R. Brull, V. W. S. Chan, B. C. Spence, J. Gallagher, M. L. Beach, V. R. Sites, and G. S. Hartman, “Artifacts and Pitfall Errors Associated with Ultrasound-Guided Regional Anesthesia. Part I: Understanding the Basic Principles of Ultrasound Physics and Machine Operations,” *Reg. Anesth. Pain Med.*, vol. 32, pp. 412–8, 2007.

- 
- [5] J. J. Dahl, G. F. Pinton, M. Lediju, and G. E. Trahey, "Simulation and Experimental Analysis of Ultrasonic Clutter in Fundamental and Harmonic Imaging," in *Proc. of SPIE*, vol. 7265, 726509, 2009, doi:10.1117/12.813782.
- [6] S. P. Turner and M. J. Monaghan, "Tissue Harmonic Imaging for Standard Left Ventricular Measurements: Fundamentally Flawed?" *Eur. J. of Echocar.*, vol. 7, pp. 9–15, 2005.
- [7] U. Bartram and K. Darge, "Harmonic vs Conventional Ultrasound Imaging of the Urinary Tract of Children," *Ped. Radiol.*, vol. 35, pp. 655–60, 2005.
- [8] C.-L. Yen, H.-Y. Chang, S.-Y. Huang, Y.-C. Huang, and C.-M. Jeng, "Combination of Tissue Harmonic Sonography, Real-Time Spatial Compound Sonography and Adaptive Image Processing Technique for the Detection of Carotid Plaques and Intima-Medial Thickness," *Eur. J. of Radiol.*, vol. 71, pp. 11–6, 2009.
- [9] T. Varslot, S.-E. Måsøy, T. F. Johansen, and B. A. J. Angelsen, "Aberration in Nonlinear Acoustic Wave Propagation," *IEEE Trans. Ultrason., Ferroelect., Freq. Contr.*, vol. 54, pp. 470–9, 2007.
- [10] H. Kaupang, S.-E. Måsøy, T. Varslot, T. F. Johansen, and B. A. J. Angelsen, "Generation and Aberration of Second-Harmonic Ultrasound Beams in Heterogeneous Tissue," in *IEEE Ultrason. Symp. Proc.*, 2006, pp. 2160–3.
- [11] T. Varslot and G. Taraldsen, "Computer Simulation of Forward Propagation in Soft Tissue," *IEEE Trans. Ultrason., Ferroelect., Freq. Contr.*, vol. 52, pp. 1473–82, 2005.
- [12] T. Varslot and S.-E. Måsøy, "Forward Propagation of Acoustic Pressure Pulses in 3D Soft Biological Tissue," *Mod. Ident. Cont.*, vol. 27, no. 3, pp. 181–200, 2006.
- [13] M. E. Frijlink, H. Kaupang, T. Varslot, and S.-E. Måsøy, "Abersim: A Simulation Program for 3D Nonlinear Acoustic Wave Propagation for Arbitrary Pulses and Arbitrary Transducer Geometries," in *IEEE Ultrason. Symp. Proc.*, 2008, pp. 1282–5.
- [14] X. Yuan, D. Brorup, J. Wisken, M. Berggren, and S. A. Johnson, "Simulation of Acoustic Wave Propagation in Dispersive Media with Relaxation

- 
- Losses by Using FDTD Method with PML Absorbing Boundary Condition,” *IEEE Trans. Ultrason., Ferroelect., Freq. Contr.*, vol. 46, pp. 14–23, 1999.
- [15] M. Tabei, T. D. Mast, and R. Waag, “A k-Space Method for Coupled First-Order Acoustic Propagation Equations,” *J. Acoust. Soc. Am.*, vol. 111, pp. 53–63, 2002.
- [16] E. Faccioli, F. Maggio, R. Paolucci, and A. Quarteroni, “2D and 3D Elastic Wave Propagation by a Pseudo-Spectral Domain Decomposition Method,” *J. Seism.*, vol. 1, pp. 237–51, 1997.
- [17] D. Komatitsch and J.-P. Vilotte, “The Spectral Element Method: An Efficient Tool to Simulate the Seismic Response of 2D and 3D Geological Structures,” *Bull. Seism. Soc. Am.*, vol. 88, pp. 368–92, 1998.
- [18] G. L. Wojcik, J. C. Mould, S. Aytex, and L. M. Carcione, “A Study of Second-Harmonic Generation by Focused Medical Transducer Pulses,” in *IEEE Ultrason. Symp. Proc.*, 1998, pp. 1583–8.
- [19] A. I. Nachman, J. F. Smith, III, and R. C. Waag, “An Equation for Acoustic Propagation in Inhomogeneous Media with Relaxation Losses,” *J. Acoust. Soc. Am.*, vol. 88, pp. 1584–95, 1990.

# Bibliography

- Aanonsen, Sigurd I., T. Barkve, J. N. Tjøtta and S. Tjøtta (1984), ‘Distortion and Harmonic Generation in the Nearfield of a Finite Amplitude Sound Beam’, *Journal of the Acoustical Society of America* **75**, 749–68.
- Abersim* — *Ultrasound Simulation Software* (n.d.), Internet page: <http://www.ntnu.no/isb/abersim>. Last visited: 18. January 2011.
- Angelsen, Bjørn A. J. (2000a), *Ultrasound Imaging*, Vol. 1, Emantec, Trondheim, Norway.
- Angelsen, Bjørn A. J. (2000b), *Ultrasound Imaging*, Vol. 2, Emantec, Trondheim, Norway.
- Averkiou, Michaelis A. (2000), Tissue Harmonic Imaging, in ‘IEEE Ultrasonics Symposium Proceedings’, pp. 1563–72.
- Averkiou, Michalakis A., David N. Roundhill and Jeffry E. Powers (1997), A New Imaging Technique Based on the Nonlinear Properties of Tissues, in ‘IEEE Ultrasonics Symposium Proceedings’, pp. 1561–6.
- Averkiou, Michalakis A. and Mark F. Hamilton (1997), ‘Nonlinear Distortion of Short Pulses Radiated by Plane and Focused Circular Pistons’, *Journal of the Acoustical Society of America* **102**, 2539–48.
- Averkiou, Michalakis A. and Robin O. Cleveland (1999), ‘Modeling of an Electrohydraulic Lithotripter With the KZK Equation’, *Journal of the Acoustical Society of America* **106**, 102–12.
- Bæk, D., Jørgen Arendt Jensen and M. Willatzen (2008), Testing of a One Dimensional Model for Field II Calibration, in ‘IEEE Ultrasonics Symposium Proceedings’, pp. 1417–20.

- Baker, Andrew C., Aina M. Berg, Ali Sahin and Jaqueline Naze Tjøtta (1995), 'The Nonlinear Pressure Field of Plane, Rectangular Apertures: Experimental and Theoretical Results', *Journal of the Acoustical Society of America* **97**, 3510–7.
- Bartram, Ulrike and Kassa Darge (2005), 'Harmonic vs Conventional Ultrasound Imaging of the Urinary Tract of Children', *Pediatrics Radiology* **35**, 655–60.
- Bercoff, Jeremy (2008), 'ShearWave Elastography White Paper', Internet page: [http://www.supersonicimagine.fr/product\\_0\\_7\\_white-papers,en.htm](http://www.supersonicimagine.fr/product_0_7_white-papers,en.htm), SuperSonic Imagine, Aix en Provence, France. Last visited: 24. February 2011.
- Bercoff, Jeremy, Michael Tanter and Mathias Fink (2004), 'Supersonic Shear Imaging: A New Technique for Soft Tissue Elasticity Mapping', *IEEE Transactions on Ultrasonics, Ferroelectrics, and Frequency Control* **51**, 396–409.
- Bernardi, Christine and Yvon Maday (1997), Spectral Methods, in P. G.Ciarlet and J. L.Lions, eds, 'Handbook of Numerical Analysis Volume V: Techniques of Scientific Computing (Part 2)', Elsevier, pp. 209–486.
- Berntsen, Jarle (1990), Numerical Calculations of Finite Amplitude Sound Beams, in M. F.Hamilton and D. T.Blackstock, eds, 'Frontiers of Nonlinear Acoustics: Proceedings of 12th ISNA', Elsevier.
- Bickford, William (1990), *A First Course in the Finite Element Method*, Irwin, Homewood, IL, chapter 3, 4, pp. 216–481.
- Bly, S. H. P., D. Lee-Chahal, D. R. Foster, M. S. Patterson, F. Stuart Foster and J. W. Hunt (1986), 'Quantitative Contrast Measurements in B-Mode Images Comparison Between Experiment and Theory', *Ultrasound in Medicine & Biology* **12**, 197–208.
- Bouakaz, Ayache and Nico de Jong (2003), 'Native Tissue Imaging at Superharmonic Frequencies', *IEEE Transactions on Ultrasonics, Ferroelectrics, and Frequency Control* **50**, 496–506.
- Canuto, Claudio, A. Yousuff Hossaini, Alfio Quarteroni and Jr. Thomas A. Zang (2006), *Spectral Methods – Fundamentals in Single Domain*, Springer, New York, chapter 2, pp. 39–116.
- Cherin, Emmanuel, Jeremy Brown, Svein-Erik Måsøy, Hamid Shariff, Raffi Karshafian, Ross Williams, Peter N. Burns and F. Stuart Foster (2008), 'Radial

- 
- Modulated Imaging of Microbubbles Contrast Agents at High Frequency’, *Ultrasound in Medicine & Biology* **34**, 949–62.
- Chiou, See-Ying, Flemming Forsberg, Traci B. Fox and Laurence Needleman (2007), ‘Comparing Differential Tissue Harmonic Imaging With Tissue Harmonic and Fundamental Gray Scale Imaging of the Liver’, *Journal of Ultrasound in Medicine* **26**, 1557–63.
- Choudhry, Sabina, Brian Gorman, J. William Charboneau, Donald J. Tradup, Rebecca J. Beck, James M. Kofler and Debra S. Groth (2000), ‘Comparison of Tissue Harmonic Imaging with Conventional US in Abdominal Disease’, *RadioGraphics* **20**, 1127–35.
- Christopher, Ted P. (1997), ‘Finite Amplitude Distortion-Based Inhomogenous Pulse Echo Ultrasound Imaging’, *IEEE Transactions on Ultrasonics, Ferroelectrics, and Frequency Control* **44**, 125–9.
- Christopher, Ted P. (1998), ‘Experimental Investigation of Finite Amplitude Distortion-Based, Second Harmonic Pulse Echo Ultrasound Imaging’, *IEEE Transactions on Ultrasonics, Ferroelectrics, and Frequency Control* **45**, 158–62.
- Cleveland, Robin O., Mark F. Hamilton and David T. Blackstock (1996), ‘Time-Domain Modeling of Finite-Amplitude Sound in Relaxing Fluids’, *Journal of the Acoustical Society of America* **99**, 3312–8.
- Cobbold, Richard S. C. (2007), *Foundations of Biomedical Ultrasound*, Oxford University Press, Inc., New York, NY.
- Dahl, Jeremy J., Gianmarco F. Pinton, Muyinatu Lediju and Gregg E. Trahey (2009), Simulation and Experimental Analysis of Ultrasonic Clutter in Fundamental and Harmonic Imaging, in ‘Proceedings of SPIE’, Vol. 7265, 726509. doi:10.1117/12.813782.
- Desser, Terry S., R. Brooke Jeffrey, Michael J. Lane and Philip W. Ralls (1999), ‘Tissue Harmonic Imaging: Utility in Abdominal and Pelvic Sonography’, *J. Clin. Ultrasound* **27**, 135–42.
- Deville, Michel O., Paul F. Fischer and Ernest G. Mund (2002), *High-Order Methods for Incompressible Fluid Flow*, Cambridge University Press, chapter 3, pp. 98–161.

- D'hooge, Jan, Johan Nuyts, Bart Bijmens, Bruno De Man, Paul Suetens, Jan Thoen, Marie-Christine Herregods and Frans van de Werf (1997), 'The Calculation of the Transient Near and Far Field of a Baffled Piston Using Low Sampling Frequencies', *Journal of the Acoustical Society of America* **102**, 78–86.
- Duck, Francis A. (1990), *Physical Properties of Tissue*, Academic Press, London.
- Dursun, Safiye, Trond Varslot, Tonni F. Johansen, Bjørn Angelsen and Hans Torp (2005), Fast 3D Simulation of 2nd Harmonic Ultrasound Field From Arbitrary Transducer Geometries, in 'IEEE Ultrasonics Symposium Proceedings'.
- Evans, Lawrence C. (1998), *Partial Differential Equations*, American Mathematical Society, Providence, RI.
- Faccioli, E., F. Maggio, R. Paolucci and A. Quarteroni (1997), '2D and 3D Elastic Wave Propagation by a Pseudo-Spectral Domain Decomposition Method', *Journal of Seismology* **1**, 237–51.
- Field II Ultrasound Simulation Program* (n.d.), Internet page: <http://server.electro.dtu.dk/personal/jaj/field/>. Last visited: 18. January 2011.
- Fink, M., C. Prada, F. Wu and D. Cassereau (1989), Self Focusing in Inhomogeneous Media With Time Reversal Acoustic Mirrors, in 'IEEE Ultrasonics Symposium Proceedings', pp. 681–6.
- Fornberg, Bengt (1996), *A Practical Guide to Pseudospectral Methods*, Cambridge Monographs on Applied and Computational Mathematics, Cambridge University Press.
- Frijlink, Martijn E., David E. Goertz, Ayache Boakaz and Antonius F. W. van der Steen (2006), 'A Simulation on Tissue Harmonic Imaging With a Single-Element Intravascular Ultrasound Catheter', *Journal of the Acoustical Society of America* **120**, 1723–31.
- Frijlink, Martijn E. and Hans G. Torp (2009), Simulation of Acoustic Fields From Arbitrary Transducer Stacks Using a FEM Transducer Model and Nonlinear Wave Propagation, in 'IEEE Ultrasonics Symposium Proceedings', pp. 2340–3.

- 
- Frijlink, Martijn Egbert, Halvard Kaupang, Trond Varslot and Svein-Erik Måsøy (2008), Abersim: A Simulation Program for 3D Nonlinear Acoustic Wave Propagation for Arbitrary Pulses and Arbitrary Transducer Geometries, in ‘IEEE Ultrasonics Symposium Proceedings’, pp. 1282–5.
- Gasquet, Claude and Patrick Witomski (1999), *Fourier Analysis and Applications*, Springer, Berlin, Heidelberg, New York.
- Ginter, Siegfried, Marco Liebler, Thomas Dreyer and Rainer E. Riedlinger (2002), ‘Full-Wave Modeling of Therapeutic Ultrasound: Nonlinear Ultrasound Propagation in Ideal Fluids’, *Journal of the Acoustical Society of America* **111**, 2049–59.
- Golub, Gene H. and Charles F. Van Loan (1996), *Matrix Computations*, 3 edn, Johns Hopkins University Press, Baltimore, London.
- Gottlieb, David and Steven A. Orszag (1977), *Numerical Analysis of Spectral Methods*, SIAM, Philadelphia, chapter 1–4, pp. 1–54.
- Hairer, Ernst, Christian Lubich and Gerhard Wanner (2003), ‘Geometric Numerical Integration Illustrated by the Störmer–Verlet Method’, *Acta Numerica* pp. 399–450.
- Hairer, Ernst and Gerhard Wanner (2002), *Solving Ordinary Differential Equations II*, 2 edn, Springer, Berlin, Heidelberg, New York.
- Hairer, Ernst, Syvert P. Nørsett and Gerhard Wanner (2000), *Solving Ordinary Differential Equations I*, 2 edn, Springer, Berlin, Heidelberg, New York.
- Hamilton, Mark F. and David T. Blackstock (1997), *Nonlinear Acoustics*, Academic Press, San Diego.
- Hann, Lucy E., Ariadne M. Bach, Laura D. Cramer, Donna Siegel, Hyok-Yee Yoo and Rosanna Garcia (1999), ‘Hepatic Sonography: Comparison of Tissue Harmonic and Standard Sonography Techniques’, *American Journal of Roentgenology* **173**, 201–6.
- Hansen, Rune and Bjørn Angelsen (2009), ‘SURF Imaging for Contrast Agent Detection’, *IEEE Transactions on Ultrasonics, Ferroelectrics, and Frequency Control* **34**, 280–90.
- Hansen, Rune, Svein-Erik Måsøy, Tonni F. Johansen and Bjørn Angelsen (2010), ‘Utilizing Dual Frequency Bnad Transmit Pulse Complexes in Medical Ultrasound Imaging’, *Journal of the Acoustical Society of America* **127**, 579–87.

- Hergum, Torbjørn, Stian Langeland, Espen Remme and Hans Torp (2009), 'Fast Ultrasound Imaging Simulation in  $k$ -Space', *IEEE Transactions on Ultrasonics, Ferroelectrics, and Frequency Control* **56**, 1159–67.
- Hill, C. R., J. C. Bamber and G. R. ter Haar (2004), *Physical Principles of Medical Ultrasound*, 2 edn, John Wiley & Sons, Ltd., Chichester, England.
- Hoffelner, Johann, Hermann Landes, Manfred Kaltenbacher and Reinhard Lerch (2001), 'Finite Element Simulation of Nonlinear Wave Propagation in Thermoviscous Fluids Including Dissipation', *IEEE Transactions on Ultrasonics, Ferroelectrics, and Frequency Control* **48**, 779–86.
- Huijssen, Jcaob and M. D. Verweij (2010), 'An Iterative Method for the Computation of Wide-Angle, Pulsed Acoustic Fields of Medical Diagnostic Transducers', *Journal of the Acoustical Society of America* **127**, 33–44.
- Int (2005), *IEC 62359: Ultrasonics - Field Characterization*, 1.0 edn.
- Jensen, Jørgen A. (1991), 'A Model for the Propagation and Scattering of Ultrasound in Tissue', *Journal of the Acoustical Society of America* **89**, 182–90.
- Jensen, Jørgen A. and N. B. Svendsen (1992), 'Calculation of Pressure Fields from Arbitrary Shaped, Apodized and Exited Ultrasound Transducers', *IEEE Transactions on Ultrasonics, Ferroelectrics, and Frequency Control* **39**, 262–7.
- Jing, Yuan and Robin O. Cleveland (2007), 'Modeling the Propagation of Nonlinear Three-Dimensional Acoustic Beams in Inhomogeneous Media', *Journal of the Acoustical Society of America* **122**, 1352–64.
- Ju, Hongbin and K.-Y. Fung (2001), 'Time-Domain Impedance Boundary Conditions with Mean Flow', *AIAA Journal* **39**, 1683–90.
- Kang, Tae-Seob and Chang-Eob Baag (2004), 'An Efficient Finite-Difference Method for Simulating 3D Seismic Response of Localized Basin Structures', *Bulletin of the Seismological Society of America* **95**, 1690–705.
- Kaupang, Halvard, Kristin Helset, Ola M. Rygh, Svein-Erik Måsøy, Vendela Källskog, Christian Nolsøe, Hans Martin Holden and Rune Hansen (2007), 'Contrast Enhanced Ultrasound Sonography of Thyroid Nodules', Symposium of the Norwegian Society of Ultrasound Diagnostics. Original title: Ultralydkontrastavbildning av knuter i skjoldbruskkjertelen.

- 
- Kaupang, Halvard, Svein-Erik Måsøy, Trond Varslot, Tonni F. Johansen and Bjørn. A. J. Angelsen (2006), Generation and Aberration of Second-Harmonic Ultrasound Beams in Heterogeneous Tissue, in 'IEEE Ultrasonics Symposium Proceedings', pp. 2160–3.
- Kaupang, Halvard, Trond Varslot and Svein-Erik Måsøy (2007), Second-Harmonic Aberration Correction, in 'IEEE Ultrasonics Symposium Proceedings', pp. 1537–40.
- Kern, Rolf, Kristina Szabo, Michael Hennerici and Stephen Mairs (2004), 'Characterization of Carotid Artery Plaques Using Real-Time Compound B-Mode Ultrasound', *Stroke* **35**, 870–5.
- Khokhlova, Vera A., A. E. Ponomarev, Michalakis A. Averkiou and Lawrence A. Crum (2006), 'Nonlinear Pulsed Ultrasound Beams Radiated by Rectangular Focused Diagnostic Transducers', *Acoustical Physics* **52**, 481–9.
- Kollmann, Christian (2007), 'New Sonographic Techniques for Harmonic Imaging – Underlying Physical Principles', *European Journal of Radiology* **64**, 164–72.
- Komatitsch, Dimitri, Christophe Barnes and Jeroen Tromp (2000), 'Simulation of Anisotropic Wave Propagation Based upon a Spectral Element Method', *Geophysics* **65**, 1251–60.
- Komatitsch, Dimitri and Jean-Pierre Vilotte (1998), 'The Spectral Element Method: An Efficient Tool to Simulate the Seismic Response of 2D and 3D Geological Structures', *Bulletin of the Seismological Society of America* **88**, 368–92.
- Komatitsch, Dimitri and Jeroen Tromp (1999), 'Introduction to the Spectral Element Method for Three-Dimensional Seismic Wave Propagation', *Geophysical Journal International* **139**, 806–22.
- Kornbluth, Murray, David H. Liang, Allan Paloma and Ingela Schnittger (1998), 'Native Tissue Harmonic Imaging Improves Endocardial Border Definition and Visualization of Cardiac Structures', *Journal of the American Society of Echocardiography* **11**, 693–701.
- Krimholtz, R., D. A. Leedom and G. L. Matthaei (1970), 'New Equivalent Circuits for Elementary Piezoelectric Transducers', *Electronics Letters* **6**, 398–9.
- Kuznetsov, V. P (1970), 'Equations of Nonlinear Acoustics', *Soviet Physics-Acoustics* **16**, 467–70.

- Kwak, Jin Young, Eun-Kyung Kim, Jai Kyung You and Ki Keun Oh (2004), 'Variable Breast Conditions Comparison of Conventional and Real-Time Compound Sonography', *Journal of Ultrasound in Medicine* **23**, 85–96.
- Lee, Yang-Sub and Mark F. Hamilton (1995), 'Time Domain Modeling of Pulsed Finite-Amplitude Sound Beams', *Journal of the Acoustical Society of America* **97**, 906–17.
- Li, Yadong and J. A. Zagzebski (2000), 'Computer Model for Harmonic Ultrasound Imaging', *IEEE Transactions on Ultrasonics, Ferroelectrics, and Frequency Control* **47**, 1259–72.
- Liebler, Marco, Siegfried Ginter, Thomas Dreyer and Rainer E. Riedlinger (2004), 'Full-Wave Modeling of Therapeutic Ultrasound: Efficient Time-Domain Implementation of the Frequency Power-Law Attenuation', *Journal of the Acoustical Society of America* **116**, 2742–50.
- Liu, Qing-Huo (1995), 'Generalization of the  $k$ -Space Formulation to Elastodynamic Scattering Problem', *Journal of the Acoustical Society of America* **97**, 1373–9.
- Liu, Qing-Huo (1998), 'The Pseudospectral Time-Domain (PSTD) Algorithm for Acoustic Waves in Absorptive Media', *IEEE Transactions on Ultrasonics, Ferroelectrics, and Frequency Control* **45**, 1044–55.
- Lockwood, J. C. and J. G. Willette (1973), 'High-Speed Method for Computing the Exact Solution for the Pressure Variations in the Nearfield of a Baffled Piston', *Journal of the Acoustical Society of America* **53**, 735–41.
- Maday, Yvon, Anthony T. Patera and Einar M. Rønquist (1992), The PN x PN-2 Method for the Approximation of the Stokes Problem, Technical report, Massachusetts Institute of Technology.
- Maday, Yvon and Einar M. Rønquist (1990), 'Optimal Error Analysis of Spectral Methods with Emphasis on Non-Constant Coefficients and Deformed Geometries', *Computer Methods in Applied Mechanical Engineering* **80**, 91–115.
- Martinsen, Eli Anne (2007), Detection and Imaging of Micro-Bubbles Using High Frequencies, Master's Thesis, Norwegian University of Science and Technology. Original title: "Deteksjon og avbildning av kontrastbobler ved høye frekvenser.

- 
- Måsøy, Svein-Erik, Bjørn A. J. Angelsen and Trond Varslot (2004), ‘Estimation of Ultrasound Wave Aberration With Signals From Random Scatterers’, *Journal of the Acoustical Society of America* **115**, 2998–3009.
- Måsøy, Svein-Erik, Bjørn A. J. Angelsen and Trond Varslot (2007), ‘Variance Analysis of Arrival Time and Amplitude Estimates From Random Speckle Signal’, *Journal of the Acoustical Society of America* **121**, 286–98.
- Måsøy, Svein-Erik, Øyvind Standal, Peter Näsholm, Tonni F. Johansen, Bjørn Angelsen and Rune Hansen (2008), ‘SURF Imaging: In Vivo Demonstration of an Ultrasound Contrast Detection Technique’, *IEEE Transactions on Ultrasonics, Ferroelectrics, and Frequency Control* **55**, 1112–21.
- Måsøy, Svein-Erik, Tonni F. Johansen and Bjørn Angelsen (2003), ‘Correction of Ultrasonic Wave Aberration With a Time Delay and Amplitude Filter’, *Journal of the Acoustical Society of America* **113**, 2009–20.
- Måsøy, Svein-Erik, Trond Varslot and Bjørn A. J. Angelsen (2005), ‘Iteration of Transmit-Beam Aberration Correction in Medical Ultrasound Imaging’, *Journal of the Acoustical Society of America* **117**, 450–61.
- Mast, T. Douglas, Laura A. Hinkelman, Leon A. Metlay, Micahel J. Orr and Robert Waag (1999), ‘Simulation of Ultrasonic Pulse Propagation, Distortion, and Attenuation in the Human Chest Wall’, *Journal of the Acoustical Society of America* **106**, 3665–77.
- Mast, T. Douglas, Laura M. Hinkelman, Michael J. Orr and Robert C. Waag (1998), ‘The Effect of Abdominal Wall Morphology on Ultrasonic Pulse Distortion. Part II. Simulations’, *Journal of the Acoustical Society of America* **104**, 3651–64.
- Mast, T. Douglas, Laurent P. Souriau, D.-L. Donald Liu, Makoto Tabei, Adrian I. Nachman and Robert Waag (2001), ‘A k-Space Method for Large-Scale Models of Wave Propagation in Tissue’, *IEEE Transactions on Ultrasonics, Ferroelectrics, and Frequency Control* **48**, 341–54.
- Ming Lu, X. and T. L. Proulx (2005), Single Crystals vs. PZT Ceramics for Medical Ultrasound Applications, in ‘IEEE Ultrasonics Symposium Proceedings’, pp. 227–30.
- Moshfeghi, Mehran and Robert C. Waag (1988), ‘In Vivo and In Vitro Ultrasound Beam Distortion Measurements of a Large Aperture and a Conventional Aperture Focused Transducer’, *Ultrasound in Medicine & Biology* **14**, 415–28.

- Mould, John C., Gregory L. Wojcik, Laura M. Carcione, Makoto Tabei, T. Douglas Mast and Robert C. Waag (1999), Validation of FFT-Based Algorithms for Large-Scale Modeling of Wave Propagation in Tissue, *in* ‘IEEE Ultrasonics Symposium Proceedings’, pp. 1551–6.
- Nachman, Adrian I., James F. Smith, III and Robert C. Waag (1990), ‘An Equation for Acoustic Propagation in Inhomogeneous Media with Relaxation Losses’, *Journal of the Acoustical Society of America* **88**, 1584–95.
- Näsholm, Peter, Rune Hansen, Svein-Erik Måsøy, Tonni F. Johansen and Bjørn Angelsen (2009), ‘Transmit Beams Adapted to Reverberation Noise Suppression Using Dual-Frequency SURF Imaging’, *IEEE Transactions on Ultrasonics, Ferroelectrics, and Frequency Control* **56**, 2124–33.
- Oktar, Süna Özhan, Cem Yücel, Hakan Özdemir, Aslı Ulutürk and Sedat Isık (2003), ‘Comparison of Conventional Sonography, Real-Time Compound Sonography, Tissue Harmonic Sonography, and Tissue Harmonic Compound Sonography of Abdominal and Pelvic Lesions’, *American Journal of Roentgenology* **181**, 1341–7.
- Ortega, Dulia, Peter N. Burns, David Hope Simpson and Stephanie R. Wilson (2001), ‘Tissue Harmonic Imaging Is It a Benefit for Bile Duct Sonography’, *American Journal of Roentgenology* **176**, 653–9.
- Paladini, D., M. Vassallo, A. Tartaglione and P. Martinelli (2004), ‘The Role of Tissue Harmonic Imaging in Fetal Echocardiography’, *Ultrasound in Obstetrics and Gynecology* **23**, 159–64.
- Park, Richard D., Thomas G. Nyland, Jimmy C. Lattimer, Charles W. Miller and Jack L. Lebel (1981), ‘B-Mode Gray Scale Ultrasound: Imaging Artifacts and Interpretation Principles’, *Veterinary Radiology* **22**, 204–10.
- Penttinen, A. and M. Luukkala (1976), ‘The Impulse Response and Pressure Nearfield of a Curved Ultrasonic Radiator’, *Journal of Physics D: Applied Physics* **9**, 1547–57.
- Pierce, Allan D. (1994), *Acoustics - An Introduction to Its Physical Principles and Applications*, 3 edn, Acoustical Society of America, Melville, NY.
- Pinton, Gianmarco F. and Gregg E. Trahey (2008), ‘A Comparison of Time-Domain Solutions for the Full-Wave Equation and the Parabolic Wave Equation for a Diagnostic Ultrasound Transducer’, *IEEE Transactions on Ultrasonics, Ferroelectrics, and Frequency Control* **55**, 730–3.

- 
- Pinton, Gianmarco F., Jean-Francois Aubry, Mathias Fink and Michael Tanter (2011), ‘Effects of Nonlinear Ultrasound Propagation on High Intensity Brain Therapy’, *Medical Physics* **38**.
- Pinton, Gianmarco F., Jeremy Dahl, S. Rosenzweig and Gregg E. Trahey (2009), ‘A Heterogeneous Nonlinear Attenuating Full-Wave Model of Ultrasound’, *IEEE Transactions on Ultrasonics, Ferroelectrics, and Frequency Control* **56**, 474–88.
- Prada, C., F. Wu and Mathias Fink (1991), ‘The Iterative Time Reversal Mirror: A Solution to Self-Focusing in the Pulse Echo Mode’, *Journal of the Acoustical Society of America* **90**, 1119–29.
- Rosen, Eric L. and Mary Scott Soo (2001), ‘Tissue Harmonic Imaging Sonography of Breast Lesions Improved Margin Analysis, Conspicuity, and Image Quality Compared to Conventional Ultrasound’, *Journal of Clinical Imaging* **25**, 379–84.
- Rosenthal, Stanton J., Paul L. Jones and Louis H. Wetzel (2001), ‘Phase Inversion Tissue Harmonic Sonographic Imaging: A Clinical Study’, *American Journal of Roentgenology* **176**, 1393–8.
- Rubin, David N., Naji Yazbek, Mario J. Garcia, William J. Stewart and James D. Thomas (2000), ‘Qualitative and Quantitative Effects of Harmonic Echocardiography Imaging on Endocardial Edge Definition and Side-Lobe Artifacts’, *Journal of the American Society of Echocardiography* **13**, 1012–8.
- Sarvazyan, Armen P., Oleg V. Rudenko, Scott D. Swanson, J. Brian Fowlkes and Stanislav Y. Emilianov (1998), ‘Shear Wave Elasticity Imaging: A New Ultrasonic Technology of Medical Diagnostics’, *Ultrasound in Medicine & Biology* **24**, 1420–35.
- Schmidt, Thorsten, Christian Hoht, Patrick Haage, Marcus Blaum, Dagmar Honnef, Claudia Weiß, Gundula Staatz and R. W. Günther (2003), ‘Diagnostic Accuracy of Phase-Inversion Tissue Harmonic Imaging Versus Fundamental B-Mode Sonography in the Evaluation of Focal Lesions of the Kidney’, *American Journal of Roentgenology* **180**, 1639–47.
- Schrope, Beth, Vernon Newhouse and Volkmar Uhlendorf (1992), ‘Simulated Capillary Blood Flow Measurement Using a Nonlinear Ultrasonic Contrast Agent’, *Ultrasonic Imaging* **14**, 134–58.

- Shapiro, Robert S., Jon Wagreich, Rosaleen B. Parson, Agata Stancato Pasik, Hsu-Chong Yeh and Roger Lao (1998), 'Tissue Harmonic Imaging Sonography: Evaluation of Image Quality Compared with Conventional Sonography', *American Journal of Roentgenology* **171**, 1203–6.
- Sites, Brian D., Richard Brull, Vincent W. S. Chan, Brian C. Spence, John Gallagher, Michael L. Beach, Vincent R. Sites, , Sherif Abbas and Gregg S. Hartman (2010), 'Artifacts and Pitfall Errors Associated with Ultrasound-Guided Regional Anesthesia. Part II: A Pictorial Approach to Understanding and Avoidance', *Regional Anesthesia and Pain Medicine* **35**, S81–S92. Supplement 1.
- Sites, Brian D., Richard Brull, Vincent W. S. Chan, Brian C. Spence, John Gallagher, Michael L. Beach, Vincent R. Sites and Gregg S. Hartman (2007), 'Artifacts and Pitfall Errors Associated with Ultrasound-Guided Regional Anesthesia. Part I: Understanding the Basic Principles of Ultrasound Physics and Machine Operations', *Regional Anesthesia and Pain Medicine* **32**, 412–8.
- Szabo, Thomas L. (1994), 'Time Domain Equations for Lossy Media Obeying a Frequency Power Law', *Journal of the Acoustical Society of America* **96**, 491–500.
- Szopinski, Kazimierz T., Anna M. Pajk, Maciej Wysocki, Dominique Amy, Malgorzata Szopinska and Wieslaw Jakubowski (2003), 'Tissue Harmonic Imaging Utiliy in Breast Sonography', *Journal of Ultrasound in Medicine* **22**, 479–87.
- Szopinski, Kazimierz T., Maciej Wysocki, Anna M. Pajk, Rafal Z: Slapa, Wieslaw Jakubowski and Malgorzata Szopinska (2003), 'Tissue Harmonic Imaging of Thyroid Nodules Initial Experience', *Journal of Ultrasound in Medicine* **22**, 5–12.
- Tabei, Makoto, T. Douglas Mast and Robert Waag (2002), 'A k-Space Method for Coupled First-Order Acoustic Propagation Equations', *Journal of the Acoustical Society of America* **111**, 53–63.
- Tam, Christopher K. W. and Laurent Auriault (1996), 'Time-Domaing Impedance Boundary Conditions for Computational Aeroacoustics', *AIAA Journal* **34**, 917–923.
- Tanaka, Sachiko, Osamu Oshikawa, Teruko Sasaki, Tatsuya Ioka and Hideaki Tsukuma (2000), 'Evaluation of Tissue Harmonic Imaging for the Diagnosis of Focal Liver Lesions', *Ultrasound in Medicine & Biology* **26**, 183–7.

- 
- Taraldsen, Gunnar (2001), 'A Generalized Westerwelt Equation for Nonlinear Medical Ultrasound', *Journal of the Acoustical Society of America* **109**, 1329–33.
- Texas KZK Time Domain Code (n.d.), Internet page: <http://people.bu.edu/robinc/kzk/index.html>. Last visited: 18. January 2011.
- Thomas, James D. and David N. Rubin (1998), 'Tissue Harmonic Imaging: Why Does it Work', *Journal of the American Society of Echocardiography* **11**, 803–8.
- Tjøtta, Jaqueline Naze and Sigve Tjøtta (1980), 'An Analytical Mmodel for the Nearfield of a Baffled Piston Transducer', *Journal of the Acoustical Society of America* **68**, 334–9.
- Torp, Hans, Tonni F. Johansen and Jo Stein Haugen (2005), Nonlinear Wave-propagation - A Fast Simulation Method Based on Quasi-Linear Approximation of the Second Harmonic Field, in 'IEEE Ultrasonics Symposium Proceedings'.
- Tranquart, F., N. Grenier, V. Eder and L. Pourcelot (1999), 'Clinical Use of Ultrasound Tissue Harmonic Imaging', *Ultrasound in Medicine & Biology* **28**, 889–94.
- Turkel, Eli (1980), 'On the Practical Use of High-Order Methods for Hyperbolic Systems', *Journal of Computational Physics* **35**, 319–40.
- Turner, Stuart P. and Mark J. Monaghan (2005), 'Tissue Harmonic Imaging for Standard Left Ventricular Measurements: Fundamentally Flawed?', *European Journal of Echocardiography* **7**, 9–15.
- Varslot, Trond, Bjørn A. J. Angelsen and Robert C. Waag (2004), 'Spectral Estimation for Characterization of Acoustic Aberration', *Journal of the Acoustical Society of America* **116**, 97–108.
- Varslot, Trond and Gunnar Taraldsen (2005), 'Computer Simulation of Forward Propagation in Soft Tissue', *IEEE Transactions on Ultrasonics, Ferroelectrics, and Frequency Control* **52**, 1473–82.
- Varslot, Trond, Harald Krogstad, Eirik Mo and Bjørn A. J. Angelsen (2004), 'Eigenfunction Analysis of Stochastic Backscatter for Characterization of Acoustic Aberration in Medical Ultrasound Imaging', *Journal of the Acoustical Society of America* **115**, 3068–76.

- Varslot, Trond, Safiye Dursun, Tonni F. Johansen, Rune Hansen, Bjørn A. J. Angelsen and Hans G. Torp (2003), Influence of Acoustic Intensity on the Second-Harmonic Beam-Profile, in 'IEEE Ultrasonics Symposium Proceedings'.
- Varslot, Trond and Svein-Erik Måsøy (2006), 'Forward Propagation of Acoustic Pressure Pulses in 3D Soft Biological Tissue', *Modeling, Identification and Control* **27**(3), 181–200.
- Varslot, Trond, Svein-Erik Måsøy, Tonni F. Johansen and Bjørn A. J. Angelsen (2007), 'Aberration in Nonlinear Acoustic Wave Propagation', *IEEE Transactions on Ultrasonics, Ferroelectrics, and Frequency Control* **54**, 470–9.
- Verweij, Martin D. and Jacob Huijssen (2009), 'A Filtered Convolution Method for the Computation of Acoustic Wave Field in Very Large Spatiotemporal Domains', *Journal of the Acoustical Society of America* **125**, 1868–78.
- Wallace, Kirk D., Mark R. Holland, Brent S Robinson, Russell J. Fedewa, Christopher W: Lloyd and James G. Miller (2006), 'Impact of Propagation Through an Aberrating Medium on the Linear Effective Apodization of a Nonlinearly Generated Second Harmonic Field', *IEEE Transactions on Ultrasonics, Ferroelectrics, and Frequency Control* **53**, 1260–8.
- Ward, B., A. C. Baker and V. F. Humphrey (1997), 'Nonlinear Propagation Applied to the Improvement of Resolution in Diagnostic Medical Ultrasound', *Journal of the Acoustical Society of America* **101**, 143–54.
- Willinek, W. A., M. von Falkenhausen, H. Strunk and Schild H. H (2000), 'Tissue Harmonic Imaging in Comparison With Conventional Sonography: Effect on Image Quality and Observer Variability in the Measurement of the Intima Media Thickness in the Common Carotid Artery', *RöFo: Fortschritte auf dem Gebiete der Röntgenstrahlen und der Nuklearmedizin* **172**, 641–5.
- Wismer, Margaret G. (2006), 'Finite Element Analysis of Broadband Acoustic Pulses Through Inhomogeneous Media with Power-Law Attenuation', *Journal of the Acoustical Society of America* **120**, 3492–502.
- Wojcik, Gregory L., Bengt Fornberg, Robert C. Waag, John C. Mould, Lisa Nikodym and Tim Driscoll (1997), Pseudospectral Methods for Large-Scale Bioacoustic Models, in 'IEEE Ultrasonics Symposium Proceedings', pp. 1501–6.

- 
- Wojcik, Gregory L., D. K. Vaughan, N. Abboud and John C. Mould (1993), Electromechanical Modeling Using Explicit Time-Domain Finite Elements, in 'IEEE Ultrasonics Symposium Proceedings', pp. 1107–12.
- Wojcik, Gregory L., John C. Mould, F. Lizzi, Jr., N. Abboud, M. Ostromogilsky and D. K. Vaughan (1995), Nonlinear Modeling of Therapeutic Ultrasound, in 'IEEE Ultrasonics Symposium Proceedings', pp. 1617–22.
- Wojcik, Gregory L., John C. Mould, Sevig Aytex and Laura M. Carcione (1998), A Study of Second-Harmonic Generation by Focused Medical Transducer Pulses, in 'IEEE Ultrasonics Symposium Proceedings', pp. 1583–8.
- Wojcik, Gregory L., Thomas L. Szabo, John C. Mould, Laura M. Carcione and Fran Clougherty (1999), Nonlinear Pulse Calculation & Data in Water and a Tissue Mimic, in 'IEEE Ultrasonics Symposium Proceedings', pp. 1521–6.
- Yang, Xinmai and Robin O. Cleveland (2005), 'Time Domain Simulation of Nonlinear Acoustic Beams Generated by Rectangular Pistons With Application to Harmonic Imaging', *Journal of the Acoustical Society of America* **117**, 113–23.
- Yen, Chin-Lan, Hsio-Yun Chang, Shang-Yi Huang, Yung-Chien Huang and Chin-Ming Jeng (2009), 'Combination of Tissue Harmonic Sonography, Real-Time Spatial Compound Sonography and Adaptive Image Processing Technique for the Detection of Carotid Plaques and Intima-Medial Thickness', *European Journal of Radiology* **71**, 11–6.
- Yuan, Xiaojuen, David Brorup, James Wisken, Michael Berggren and Steven A. Johnson (1999), 'Simulation of Acoustic Wave Propagation in Dispersive Media with Relaxation Losses by Using FDTD Method with PML Absorbing Boundary Condition', *IEEE Transactions on Ultrasonics, Ferroelectrics, and Frequency Control* **46**, 14–23.
- Zabolotksaya, E. A and R. V. Khokhlov (1969), 'Quasi-Plane Waves in the Nonlinear Acoustics of Confined Beams', *Soviet Physics-Acoustics* **15**, 35–40.
- Zampieri, Elena and Luca F. Pavarino (2006), 'Approximation fo Acoustic Waves by Explicit Newmark's Schemes and Spectral Element Methods', *Journal of Computational and Applied Mathematics* **185**, 308–25.
- Zemp, Roger J., Jahangir Tavakkoli and Richard S. Cobbold (2003), 'Modeling of Nonlinear Ultrasound Propagation in Tissue from Array Transducers', *Journal of the Acoustical Society of America* **113**, 139–52.



## Dissertations at the Faculty of Medicine, NTNU

### 1977

1. Knut Joachim Berg: EFFECT OF ACETYLSALICYLIC ACID ON RENAL FUNCTION
2. Karl Erik Viken and Arne Ødegaard: STUDIES ON HUMAN MONOCYTES CULTURED *IN VITRO*

### 1978

3. Karel Bjørn Cyvin: CONGENITAL DISLOCATION OF THE HIP JOINT.
4. Alf O. Brubakk: METHODS FOR STUDYING FLOW DYNAMICS IN THE LEFT VENTRICLE AND THE AORTA IN MAN.

### 1979

5. Geirmund Unsgaard: CYTOSTATIC AND IMMUNOREGULATORY ABILITIES OF HUMAN BLOOD MONOCYTES CULTURED *IN VITRO*

### 1980

6. Størker Jørstad: URAEMIC TOXINS
7. Arne Olav Jenssen: SOME RHEOLOGICAL, CHEMICAL AND STRUCTURAL PROPERTIES OF MUCOID SPUTUM FROM PATIENTS WITH CHRONIC OBSTRUCTIVE BRONCHITIS

### 1981

8. Jens Hammerstrøm: CYTOSTATIC AND CYTOLYTIC ACTIVITY OF HUMAN MONOCYTES AND EFFUSION MACROPHAGES AGAINST TUMOR CELLS *IN VITRO*

### 1983

9. Tore Syversen: EFFECTS OF METHYLMERCURY ON RAT BRAIN PROTEIN.
10. Torbjørn Iversen: SQUAMOUS CELL CARCINOMA OF THE VULVA.

### 1984

11. Tor-Erik Widerøe: ASPECTS OF CONTINUOUS AMBULATORY PERITONEAL DIALYSIS.
12. Anton Hole: ALTERATIONS OF MONOCYTE AND LYMPHOCYTE FUNCTIONS IN REACTION TO SURGERY UNDER EPIDURAL OR GENERAL ANAESTHESIA.
13. Terje Terjesen: FRACTURE HEALING AND STRESS-PROTECTION AFTER METAL PLATE FIXATION AND EXTERNAL FIXATION.
14. Carsten Saunte: CLUSTER HEADACHE SYNDROME.
15. Inngard Lereim: TRAFFIC ACCIDENTS AND THEIR CONSEQUENCES.
16. Bjørn Magne Eggen: STUDIES IN CYTOTOXICITY IN HUMAN ADHERENT MONONUCLEAR BLOOD CELLS.
17. Trond Haug: FACTORS REGULATING BEHAVIORAL EFFECTS OF DRUGS.

### 1985

18. Sven Erik Gisvold: RESUSCITATION AFTER COMPLETE GLOBAL BRAIN ISCHEMIA.
19. Terje Espevik: THE CYTOSKELETON OF HUMAN MONOCYTES.
20. Lars Bevanger: STUDIES OF THE Ibc (c) PROTEIN ANTIGENS OF GROUP B STREPTOCOCCI.
21. Ole-Jan Iversen: RETROVIRUS-LIKE PARTICLES IN THE PATHOGENESIS OF PSORIASIS.
22. Lasse Eriksen: EVALUATION AND TREATMENT OF ALCOHOL DEPENDENT BEHAVIOUR.
23. Per I. Lundmo: ANDROGEN METABOLISM IN THE PROSTATE.

### 1986

24. Dagfinn Berntzen: ANALYSIS AND MANAGEMENT OF EXPERIMENTAL AND CLINICAL PAIN.
25. Odd Arnold Kildahl-Andersen: PRODUCTION AND CHARACTERIZATION OF MONOCYTE-DERIVED CYTOTOXIN AND ITS ROLE IN MONOCYTE-MEDIATED CYTOTOXICITY.
26. Ola Dale: VOLATILE ANAESTHETICS.

### 1987

27. Per Martin Kleveland: STUDIES ON GASTRIN.
28. Audun N. Øksendal: THE CALCIUM PARADOX AND THE HEART.
29. Vilhjalmur R. Finsen: HIP FRACTURES

### 1988

30. Rigmor Austgulen: TUMOR NECROSIS FACTOR: A MONOCYTE-DERIVED REGULATOR OF CELLULAR GROWTH.
31. Tom-Harald Edna: HEAD INJURIES ADMITTED TO HOSPITAL.
32. Joseph D. Borsi: NEW ASPECTS OF THE CLINICAL PHARMACOKINETICS OF METHOTREXATE.
33. Olav F. M. Sellevdal: GLUCOCORTICOIDS IN MYOCARDIAL PROTECTION.
34. Terje Skjærpe: NONINVASIVE QUANTITATION OF GLOBAL PARAMETERS ON LEFT VENTRICULAR FUNCTION: THE SYSTOLIC PULMONARY ARTERY PRESSURE AND CARDIAC OUTPUT.
35. Eyvind Rødahl: STUDIES OF IMMUNE COMPLEXES AND RETROVIRUS-LIKE ANTIGENS IN PATIENTS WITH ANKYLOSING SPONDYLITIS.
36. Ketil Thorstensen: STUDIES ON THE MECHANISMS OF CELLULAR UPTAKE OF IRON FROM TRANSFERRIN.

37. Anna Midelfart: STUDIES OF THE MECHANISMS OF ION AND FLUID TRANSPORT IN THE BOVINE CORNEA.
  38. Eirik Helseth: GROWTH AND PLASMINOGEN ACTIVATOR ACTIVITY OF HUMAN GLIOMAS AND BRAIN METASTASES - WITH SPECIAL REFERENCE TO TRANSFORMING GROWTH FACTOR BETA AND THE EPIDERMAL GROWTH FACTOR RECEPTOR.
  39. Petter C. Borchgrevink: MAGNESIUM AND THE ISCHEMIC HEART.
  40. Kjell-Arne Rein: THE EFFECT OF EXTRACORPOREAL CIRCULATION ON SUBCUTANEOUS TRANSCAPILLARY FLUID BALANCE.
  41. Arne Kristian Sandvik: RAT GASTRIC HISTAMINE.
  42. Carl Bredo Dahl: ANIMAL MODELS IN PSYCHIATRY.
- 1989**
43. Torbjørn A. Fredriksen: CERVICOGENIC HEADACHE.
  44. Rolf A. Walstad: CEFTAZIDIME.
  45. Rolf Salvesen: THE PUPIL IN CLUSTER HEADACHE.
  46. Nils Petter Jørgensen: DRUG EXPOSURE IN EARLY PREGNANCY.
  47. Johan C. Ræder: PREMEDICATION AND GENERAL ANAESTHESIA IN OUTPATIENT GYNECOLOGICAL SURGERY.
  48. M. R. Shalaby: IMMUNOREGULATORY PROPERTIES OF TNF- $\alpha$  AND THE RELATED CYTOKINES.
  49. Anders Waage: THE COMPLEX PATTERN OF CYTOKINES IN SEPTIC SHOCK.
  50. Bjarne Christian Eriksen: ELECTROSTIMULATION OF THE PELVIC FLOOR IN FEMALE URINARY INCONTINENCE.
  51. Tore B. Halvorsen: PROGNOSTIC FACTORS IN COLORECTAL CANCER.
- 1990**
52. Asbjørn Nordby: CELLULAR TOXICITY OF ROENTGEN CONTRAST MEDIA.
  53. Kåre E. Tvedt: X-RAY MICROANALYSIS OF BIOLOGICAL MATERIAL.
  54. Tore C. Stiles: COGNITIVE VULNERABILITY FACTORS IN THE DEVELOPMENT AND MAINTENANCE OF DEPRESSION.
  55. Eva Hofslie: TUMOR NECROSIS FACTOR AND MULTIDRUG RESISTANCE.
  56. Helge S. Haarstad: TROPHIC EFFECTS OF CHOLECYSTOKININ AND SECRETIN ON THE RAT PANCREAS.
  57. Lars Engebretsen: TREATMENT OF ACUTE ANTERIOR CRUCIATE LIGAMENT INJURIES.
  58. Tarjei Rygnestad: DELIBERATE SELF-POISONING IN TRONDHEIM.
  59. Arne Z. Henriksen: STUDIES ON CONSERVED ANTIGENIC DOMAINS ON MAJOR OUTER MEMBRANE PROTEINS FROM ENTEROBACTERIA.
  60. Steinar Westin: UNEMPLOYMENT AND HEALTH: Medical and social consequences of a factory closure in a ten-year controlled follow-up study.
  61. Ylva Sahlin: INJURY REGISTRATION, a tool for accident preventive work.
  62. Helge Bjørnstad Pettersen: BIOSYNTHESIS OF COMPLEMENT BY HUMAN ALVEOLAR MACROPHAGES WITH SPECIAL REFERENCE TO SARCOIDOSIS.
  63. Berit Schei: TRAPPED IN PAINFUL LOVE.
  64. Lars J. Vatten: PROSPECTIVE STUDIES OF THE RISK OF BREAST CANCER IN A COHORT OF NORWEGIAN WOMAN.
- 1991**
65. Kåre Bergh: APPLICATIONS OF ANTI-C5a SPECIFIC MONOCLONAL ANTIBODIES FOR THE ASSESSMENT OF COMPLEMENT ACTIVATION.
  66. Svein Svenningsen: THE CLINICAL SIGNIFICANCE OF INCREASED FEMORAL ANTEVERSION.
  67. Olbjørn Klepp: NONSEMINOMATOUS GERM CELL TESTIS CANCER: THERAPEUTIC OUTCOME AND PROGNOSTIC FACTORS.
  68. Trond Sand: THE EFFECTS OF CLICK POLARITY ON BRAINSTEM AUDITORY EVOKED POTENTIALS AMPLITUDE, DISPERSION, AND LATENCY VARIABLES.
  69. Kjetil B. Åsbakk: STUDIES OF A PROTEIN FROM PSORIATIC SCALE, PSO P27, WITH RESPECT TO ITS POTENTIAL ROLE IN IMMUNE REACTIONS IN PSORIASIS.
  70. Arnulf Hestnes: STUDIES ON DOWN'S SYNDROME.
  71. Randi Nygaard: LONG-TERM SURVIVAL IN CHILDHOOD LEUKEMIA.
  72. Bjørn Hagen: THIO-TEPA.
  73. Svein Anda: EVALUATION OF THE HIP JOINT BY COMPUTED TOMOGRAPHY AND ULTRASONOGRAPHY.
- 1992**
74. Martin Svartberg: AN INVESTIGATION OF PROCESS AND OUTCOME OF SHORT-TERM PSYCHODYNAMIC PSYCHOTHERAPY.
  75. Stig Arild Slørdahl: AORTIC REGURGITATION.
  76. Harold C Sexton: STUDIES RELATING TO THE TREATMENT OF SYMPTOMATIC NON-PSYCHOTIC PATIENTS.

77. Maurice B. Vincent: VASOACTIVE PEPTIDES IN THE OCULAR/FOREHEAD AREA.
  78. Terje Johannessen: CONTROLLED TRIALS IN SINGLE SUBJECTS.
  79. Turid Nilsen: PYROPHOSPHATE IN HEPATOCYTE IRON METABOLISM.
  80. Olav Haraldseth: NMR SPECTROSCOPY OF CEREBRAL ISCHEMIA AND REPERFUSION IN RAT.
  81. Eiliv Brenna: REGULATION OF FUNCTION AND GROWTH OF THE OXYNTIC MUCOSA.
- 1993**
82. Gunnar Bovim: CERVICOGENIC HEADACHE.
  83. Jarl Arne Kahn: ASSISTED PROCREATION.
  84. Bjørn Naume: IMMUNOREGULATORY EFFECTS OF CYTOKINES ON NK CELLS.
  85. Rune Wiseth: AORTIC VALVE REPLACEMENT.
  86. Jie Ming Shen: BLOOD FLOW VELOCITY AND RESPIRATORY STUDIES.
  87. Piotr Kruszewski: SUNCT SYNDROME WITH SPECIAL REFERENCE TO THE AUTONOMIC NERVOUS SYSTEM.
  88. Mette Haase Moen: ENDOMETRIOSIS.
  89. Anne Vik: VASCULAR GAS EMBOLISM DURING AIR INFUSION AND AFTER DECOMPRESSION IN PIGS.
  90. Lars Jacob Stovner: THE CHIARI TYPE I MALFORMATION.
  91. Kjell Å. Salvesen: ROUTINE ULTRASONOGRAPHY IN UTERO AND DEVELOPMENT IN CHILDHOOD.
- 1994**
92. Nina-Beate Liabakk: DEVELOPMENT OF IMMUNOASSAYS FOR TNF AND ITS SOLUBLE RECEPTORS.
  93. Sverre Helge Torp: *erbB* ONCOGENES IN HUMAN GLIOMAS AND MENINGIOMAS.
  94. Olav M. Linaker: MENTAL RETARDATION AND PSYCHIATRY. Past and present.
  95. Per Oscar Feet: INCREASED ANTIDEPRESSANT AND ANTIPANIC EFFECT IN COMBINED TREATMENT WITH DIXYRAZINE AND TRICYCLIC ANTIDEPRESSANTS.
  96. Stein Olav Samstad: CROSS SECTIONAL FLOW VELOCITY PROFILES FROM TWO-DIMENSIONAL DOPPLER ULTRASOUND: Studies on early mitral blood flow.
  97. Bjørn Backe: STUDIES IN ANTENATAL CARE.
  98. Gerd Inger Ringdal: QUALITY OF LIFE IN CANCER PATIENTS.
  99. Torvid Kiserud: THE DUCTUS VENOSUS IN THE HUMAN FETUS.
  100. Hans E. Fjøsne: HORMONAL REGULATION OF PROSTATIC METABOLISM.
  101. Eylert Brodtkorb: CLINICAL ASPECTS OF EPILEPSY IN THE MENTALLY RETARDED.
  102. Roar Juul: PEPTIDERGIC MECHANISMS IN HUMAN SUBARACHNOID HEMORRHAGE.
  103. Unni Syversen: CHROMOGRANIN A. Physiological and Clinical Role.
- 1995**
104. Odd Gunnar Brakstad: THERMOSTABLE NUCLEASE AND THE *nuc* GENE IN THE DIAGNOSIS OF *Staphylococcus aureus* INFECTIONS.
  105. Terje Engan: NUCLEAR MAGNETIC RESONANCE (NMR) SPECTROSCOPY OF PLASMA IN MALIGNANT DISEASE.
  106. Kirsten Rasmussen: VIOLENCE IN THE MENTALLY DISORDERED.
  107. Finn Egil Skjeldestad: INDUCED ABORTION: Timetrends and Determinants.
  108. Roar Stenseth: THORACIC EPIDURAL ANALGESIA IN AORTOCORONARY BYPASS SURGERY.
  109. Arild Faxvaag: STUDIES OF IMMUNE CELL FUNCTION *in mice infected with* MURINE RETROVIRUS.
- 1996**
110. Svend Aakhus: NONINVASIVE COMPUTERIZED ASSESSMENT OF LEFT VENTRICULAR FUNCTION AND SYSTEMIC ARTERIAL PROPERTIES. Methodology and some clinical applications.
  111. Klaus-Dieter Bolz: INTRAVASCULAR ULTRASONOGRAPHY.
  112. Petter Aadahl: CARDIOVASCULAR EFFECTS OF THORACIC AORTIC CROSS-CLAMPING.
  113. Sigurd Steinshamm: CYTOKINE MEDIATORS DURING GRANULOCYTOPENIC INFECTIONS.
  114. Hans Stifoss-Hanssen: SEEKING MEANING OR HAPPINESS?
  115. Anne Kvikstad: LIFE CHANGE EVENTS AND MARITAL STATUS IN RELATION TO RISK AND PROGNOSIS OF CANCER.
  116. Torbjørn Grøntvedt: TREATMENT OF ACUTE AND CHRONIC ANTERIOR CRUCIATE LIGAMENT INJURIES. A clinical and biomechanical study.
  117. Sigrid Hørven Wigert: CLINICAL STUDIES OF FIBROMYALGIA WITH FOCUS ON ETIOLOGY, TREATMENT AND OUTCOME.
  118. Jan Schjøtt: MYOCARDIAL PROTECTION: Functional and Metabolic Characteristics of Two Endogenous Protective Principles.
  119. Marit Martinussen: STUDIES OF INTESTINAL BLOOD FLOW AND ITS RELATION TO TRANSITIONAL CIRCULATORY ADAPATION IN NEWBORN INFANTS.
  120. Tømm B. Müller: MAGNETIC RESONANCE IMAGING IN FOCAL CEREBRAL ISCHEMIA.
  121. Rune Haaverstad: OEDEMA FORMATION OF THE LOWER EXTREMITIES.

122. Magne Børset: THE ROLE OF CYTOKINES IN MULTIPLE MYELOMA, WITH SPECIAL REFERENCE TO HEPATOCYTE GROWTH FACTOR.
123. Geir Smedslund: A THEORETICAL AND EMPIRICAL INVESTIGATION OF SMOKING, STRESS AND DISEASE: RESULTS FROM A POPULATION SURVEY.

#### 1997

124. Torstein Vik: GROWTH, MORBIDITY, AND PSYCHOMOTOR DEVELOPMENT IN INFANTS WHO WERE GROWTH RETARDED *IN UTERO*.
125. Siri Forsmo: ASPECTS AND CONSEQUENCES OF OPPORTUNISTIC SCREENING FOR CERVICAL CANCER. Results based on data from three Norwegian counties.
126. Jon S. Skranes: CEREBRAL MRI AND NEURODEVELOPMENTAL OUTCOME IN VERY LOW BIRTH WEIGHT (VLBW) CHILDREN. A follow-up study of a geographically based year cohort of VLBW children at ages one and six years.
127. Knut Bjørnstad: COMPUTERIZED ECHOCARDIOGRAPHY FOR EVALUATION OF CORONARY ARTERY DISEASE.
128. Grethe Elisabeth Borchgrevink: DIAGNOSIS AND TREATMENT OF WHIPLASH/NECK SPRAIN INJURIES CAUSED BY CAR ACCIDENTS.
129. Tor Elsås: NEUROPEPTIDES AND NITRIC OXIDE SYNTHASE IN OCULAR AUTONOMIC AND SENSORY NERVES.
130. Rolf W. Gråwe: EPIDEMIOLOGICAL AND NEUROPSYCHOLOGICAL PERSPECTIVES ON SCHIZOPHRENIA.
131. Tonje Strømholm: CEREBRAL HAEMODYNAMICS DURING THORACIC AORTIC CROSSCLAMPING. An experimental study in pigs.

#### 1998

132. Martinus Bråten: STUDIES ON SOME PROBLEMS RELATED TO INTRAMEDULLARY NAILING OF FEMORAL FRACTURES.
133. Ståle Nordgård: PROLIFERATIVE ACTIVITY AND DNA CONTENT AS PROGNOSTIC INDICATORS IN ADENOID CYSTIC CARCINOMA OF THE HEAD AND NECK.
134. Egil Lien: SOLUBLE RECEPTORS FOR TNF AND LPS: RELEASE PATTERN AND POSSIBLE SIGNIFICANCE IN DISEASE.
135. Marit Bjørgaas: HYPOGLYCAEMIA IN CHILDREN WITH DIABETES MELLITUS
136. Frank Skorpen: GENETIC AND FUNCTIONAL ANALYSES OF DNA REPAIR IN HUMAN CELLS.
137. Juan A. Pareja: SUNCT SYNDROME. ON THE CLINICAL PICTURE. ITS DISTINCTION FROM OTHER, SIMILAR HEADACHES.
138. Anders Angelsen: NEUROENDOCRINE CELLS IN HUMAN PROSTATIC CARCINOMAS AND THE PROSTATIC COMPLEX OF RAT, GUINEA PIG, CAT AND DOG.
139. Fabio Antonaci: CHRONIC PAROXYSMAL HEMICRANIA AND HEMICRANIA CONTINUA: TWO DIFFERENT ENTITIES?
140. Sven M. Carlsen: ENDOCRINE AND METABOLIC EFFECTS OF METFORMIN WITH SPECIAL EMPHASIS ON CARDIOVASCULAR RISK FACTORES.

#### 1999

141. Terje A. Murberg: DEPRESSIVE SYMPTOMS AND COPING AMONG PATIENTS WITH CONGESTIVE HEART FAILURE.
142. Harm-Gerd Karl Blaas: THE EMBRYONIC EXAMINATION. Ultrasound studies on the development of the human embryo.
143. Noëmi Becser Andersen: THE CEPHALIC SENSORY NERVES IN UNILATERAL HEADACHES. Anatomical background and neurophysiological evaluation.
144. Eli-Janne Fiskerstrand: LASER TREATMENT OF PORT WINE STAINS. A study of the efficacy and limitations of the pulsed dye laser. Clinical and morphological analyses aimed at improving the therapeutic outcome.
145. Bård Kulseng: A STUDY OF ALGINATE CAPSULE PROPERTIES AND CYTOKINES IN RELATION TO INSULIN DEPENDENT DIABETES MELLITUS.
146. Terje Haug: STRUCTURE AND REGULATION OF THE HUMAN UNG GENE ENCODING URACIL-DNA GLYCOSYLASE.
147. Heidi Brurok: MANGANESE AND THE HEART. A Magic Metal with Diagnostic and Therapeutic Possibilities.
148. Agnes Kathrine Lie: DIAGNOSIS AND PREVALENCE OF HUMAN PAPILLOMAVIRUS INFECTION IN CERVICAL INTRAEPITELIAL NEOPLASIA. Relationship to Cell Cycle Regulatory Proteins and HLA DQBI Genes.
149. Ronald Mårvik: PHARMACOLOGICAL, PHYSIOLOGICAL AND PATHOPHYSIOLOGICAL STUDIES ON ISOLATED STOMACHS.
150. Ketil Jarl Holen: THE ROLE OF ULTRASONOGRAPHY IN THE DIAGNOSIS AND TREATMENT OF HIP DYSPLASIA IN NEWBORNS.
151. Irene Hetlevik: THE ROLE OF CLINICAL GUIDELINES IN CARDIOVASCULAR RISK INTERVENTION IN GENERAL PRACTICE.

152. Katarina Tunøn: ULTRASOUND AND PREDICTION OF GESTATIONAL AGE.
153. Johannes Soma: INTERACTION BETWEEN THE LEFT VENTRICLE AND THE SYSTEMIC ARTERIES.
154. Arild Aamodt: DEVELOPMENT AND PRE-CLINICAL EVALUATION OF A CUSTOM-MADE FEMORAL STEM.
155. Agnar Tegnander: DIAGNOSIS AND FOLLOW-UP OF CHILDREN WITH SUSPECTED OR KNOWN HIP DYSPLASIA.
156. Bent Indredavik: STROKE UNIT TREATMENT: SHORT AND LONG-TERM EFFECTS
157. Jolanta Vanagaite Vingen: PHOTOPHOBIA AND PHONOPHOBIA IN PRIMARY HEADACHES

## 2000

158. Ola Dalsegg Sæther: PATHOPHYSIOLOGY DURING PROXIMAL AORTIC CROSS-CLAMPING CLINICAL AND EXPERIMENTAL STUDIES
159. xxxxxxxx (blind number)
160. Christina Vogt Isaksen: PRENATAL ULTRASOUND AND POSTMORTEM FINDINGS – A TEN YEAR CORRELATIVE STUDY OF FETUSES AND INFANTS WITH DEVELOPMENTAL ANOMALIES.
161. Holger Seidel: HIGH-DOSE METHOTREXATE THERAPY IN CHILDREN WITH ACUTE LYMPHOCYTIC LEUKEMIA: DOSE, CONCENTRATION, AND EFFECT CONSIDERATIONS.
162. Stein Hallan: IMPLEMENTATION OF MODERN MEDICAL DECISION ANALYSIS INTO CLINICAL DIAGNOSIS AND TREATMENT.
163. Malcolm Sue-Chu: INVASIVE AND NON-INVASIVE STUDIES IN CROSS-COUNTRY SKIERS WITH ASTHMA-LIKE SYMPTOMS.
164. Ole-Lars Brekke: EFFECTS OF ANTIOXIDANTS AND FATTY ACIDS ON TUMOR NECROSIS FACTOR-INDUCED CYTOTOXICITY.
165. Jan Lundbom: AORTOCORONARY BYPASS SURGERY: CLINICAL ASPECTS, COST CONSIDERATIONS AND WORKING ABILITY.
166. John-Anker Zwart: LUMBAR NERVE ROOT COMPRESSION, BIOCHEMICAL AND NEUROPHYSIOLOGICAL ASPECTS.
167. Geir Falck: HYPEROSMOLALITY AND THE HEART.
168. Eirik Skogvoll: CARDIAC ARREST Incidence, Intervention and Outcome.
169. Dalius Bansevicius: SHOULDER-NECK REGION IN CERTAIN HEADACHES AND CHRONIC PAIN SYNDROMES.
170. Bettina Kinge: REFRACTIVE ERRORS AND BIOMETRIC CHANGES AMONG UNIVERSITY STUDENTS IN NORWAY.
171. Gunnar Qvigstad: CONSEQUENCES OF HYPERGASTRINEMIA IN MAN
172. Hanne Ellekjær: EPIDEMIOLOGICAL STUDIES OF STROKE IN A NORWEGIAN POPULATION. INCIDENCE, RISK FACTORS AND PROGNOSIS
173. Hilde Grimstad: VIOLENCE AGAINST WOMEN AND PREGNANCY OUTCOME.
174. Astrid Hjelde: SURFACE TENSION AND COMPLEMENT ACTIVATION: Factors influencing bubble formation and bubble effects after decompression.
175. Kjell A. Kvistad: MR IN BREAST CANCER – A CLINICAL STUDY.
176. Ivar Rossvoll: ELECTIVE ORTHOPAEDIC SURGERY IN A DEFINED POPULATION. Studies on demand, waiting time for treatment and incapacity for work.
177. Carina Seidel: PROGNOSTIC VALUE AND BIOLOGICAL EFFECTS OF HEPATOCYTE GROWTH FACTOR AND SYNDECAN-1 IN MULTIPLE MYELOMA.

## 2001

178. Alexander Wahba: THE INFLUENCE OF CARDIOPULMONARY BYPASS ON PLATELET FUNCTION AND BLOOD COAGULATION – DETERMINANTS AND CLINICAL CONSEQUENCES
179. Marcus Schmitt-Egenolf: THE RELEVANCE OF THE MAJOR HISTOCOMPATIBILITY COMPLEX FOR THE GENETICS OF PSORIASIS
180. Odrun Arna Gederaas: BIOLOGICAL MECHANISMS INVOLVED IN 5-AMINOLEVULINIC ACID BASED PHOTODYNAMIC THERAPY
181. Pål Richard Romundstad: CANCER INCIDENCE AMONG NORWEGIAN ALUMINIUM WORKERS
182. Henrik Hjorth-Hansen: NOVEL CYTOKINES IN GROWTH CONTROL AND BONE DISEASE OF MULTIPLE MYELOMA
183. Gunnar Morken: SEASONAL VARIATION OF HUMAN MOOD AND BEHAVIOUR
184. Bjørn Olav Haugen: MEASUREMENT OF CARDIAC OUTPUT AND STUDIES OF VELOCITY PROFILES IN AORTIC AND MITRAL FLOW USING TWO- AND THREE-DIMENSIONAL COLOUR FLOW IMAGING
185. Geir Bråthen: THE CLASSIFICATION AND CLINICAL DIAGNOSIS OF ALCOHOL-RELATED SEIZURES
186. Knut Ivar Aasarød: RENAL INVOLVEMENT IN INFLAMMATORY RHEUMATIC DISEASE. A Study of Renal Disease in Wegener's Granulomatosis and in Primary Sjögren's Syndrome
187. Trude Helen Flo: RECEPTORS INVOLVED IN CELL ACTIVATION BY DEFINED URONIC ACID POLYMERS AND BACTERIAL COMPONENTS

188. Bodil Kavli: HUMAN URACIL-DNA GLYCOSYLASES FROM THE UNG GENE: STRUCTURAL BASIS FOR SUBSTRATE SPECIFICITY AND REPAIR
189. Liv Thommesen: MOLECULAR MECHANISMS INVOLVED IN TNF- AND GASTRIN-MEDIATED GENE REGULATION
190. Turid Lingaas Holmen: SMOKING AND HEALTH IN ADOLESCENCE; THE NORD-TRØNDELAG HEALTH STUDY, 1995-97
191. Øyvind Hjertner: MULTIPLE MYELOMA: INTERACTIONS BETWEEN MALIGNANT PLASMA CELLS AND THE BONE MICROENVIRONMENT
192. Asbjørn Støylen: STRAIN RATE IMAGING OF THE LEFT VENTRICLE BY ULTRASOUND. FEASIBILITY, CLINICAL VALIDATION AND PHYSIOLOGICAL ASPECTS
193. Kristian Midthjell: DIABETES IN ADULTS IN NORD-TRØNDELAG. PUBLIC HEALTH ASPECTS OF DIABETES MELLITUS IN A LARGE, NON-SELECTED NORWEGIAN POPULATION.
194. Guanglin Cui: FUNCTIONAL ASPECTS OF THE ECL CELL IN RODENTS
195. Ulrik Wisløff: CARDIAC EFFECTS OF AEROBIC ENDURANCE TRAINING: HYPERTROPHY, CONTRACTILITY AND CALCIUM HANDLING IN NORMAL AND FAILING HEART
196. Øyvind Halaas: MECHANISMS OF IMMUNOMODULATION AND CELL-MEDIATED CYTOTOXICITY INDUCED BY BACTERIAL PRODUCTS
197. Tore Amundsen: PERFUSION MR IMAGING IN THE DIAGNOSIS OF PULMONARY EMBOLISM
198. Nanna Kurtze: THE SIGNIFICANCE OF ANXIETY AND DEPRESSION IN FATIGUE AND PATTERNS OF PAIN AMONG INDIVIDUALS DIAGNOSED WITH FIBROMYALGIA: RELATIONS WITH QUALITY OF LIFE, FUNCTIONAL DISABILITY, LIFESTYLE, EMPLOYMENT STATUS, COMORBIDITY AND GENDER
199. Tom Ivar Lund Nilsen: PROSPECTIVE STUDIES OF CANCER RISK IN NORD-TRØNDELAG: THE HUNT STUDY. Associations with anthropometric, socioeconomic, and lifestyle risk factors
200. Asta Kristine Håberg: A NEW APPROACH TO THE STUDY OF MIDDLE CEREBRAL ARTERY OCCLUSION IN THE RAT USING MAGNETIC RESONANCE TECHNIQUES

**2002**

201. Knut Jørgen Arntzen: PREGNANCY AND CYTOKINES
202. Henrik Døllner: INFLAMMATORY MEDIATORS IN PERINATAL INFECTIONS
203. Asta Bye: LOW FAT, LOW LACTOSE DIET USED AS PROPHYLACTIC TREATMENT OF ACUTE INTESTINAL REACTIONS DURING PELVIC RADIOTHERAPY. A PROSPECTIVE RANDOMISED STUDY.
204. Sylvester Moyo: STUDIES ON STREPTOCOCCUS AGALACTIAE (GROUP B STREPTOCOCCUS) SURFACE-ANCHORED MARKERS WITH EMPHASIS ON STRAINS AND HUMAN SERA FROM ZIMBABWE.
205. Knut Hagen: HEAD-HUNT: THE EPIDEMIOLOGY OF HEADACHE IN NORD-TRØNDELAG
206. Li Lixin: ON THE REGULATION AND ROLE OF UNCOUPLING PROTEIN-2 IN INSULIN PRODUCING  $\beta$ -CELLS
207. Anne Hildur Henriksen: SYMPTOMS OF ALLERGY AND ASTHMA VERSUS MARKERS OF LOWER AIRWAY INFLAMMATION AMONG ADOLESCENTS
208. Egil Andreas Fors: NON-MALIGNANT PAIN IN RELATION TO PSYCHOLOGICAL AND ENVIRONMENTAL FACTORS. EXPERIMENTAL AND CLINICAL STUDIES OF PAIN WITH FOCUS ON FIBROMYALGIA
209. Pål Klepstad: MORPHINE FOR CANCER PAIN
210. Ingunn Bakke: MECHANISMS AND CONSEQUENCES OF PEROXISOME PROLIFERATOR-INDUCED HYPERFUNCTION OF THE RAT GASTRIN PRODUCING CELL
211. Ingrid Susann Gribbestad: MAGNETIC RESONANCE IMAGING AND SPECTROSCOPY OF BREAST CANCER
212. Rønnaug Astri Ødegård: PREECLAMPSIA – MATERNAL RISK FACTORS AND FETAL GROWTH
213. Johan Haux: STUDIES ON CYTOTOXICITY INDUCED BY HUMAN NATURAL KILLER CELLS AND DIGITOXIN
214. Turid Suzanne Berg-Nielsen: PARENTING PRACTICES AND MENTALLY DISORDERED ADOLESCENTS
215. Astrid Rydning: BLOOD FLOW AS A PROTECTIVE FACTOR FOR THE STOMACH MUCOSA. AN EXPERIMENTAL STUDY ON THE ROLE OF MAST CELLS AND SENSORY AFFERENT NEURONS

**2003**

216. Jan Pål Loennechen: HEART FAILURE AFTER MYOCARDIAL INFARCTION. Regional Differences, Myocyte Function, Gene Expression, and Response to Cariporide, Losartan, and Exercise Training.
217. Elisabeth Qvigstad: EFFECTS OF FATTY ACIDS AND OVER-STIMULATION ON INSULIN SECRETION IN MAN
218. Arne Åsberg: EPIDEMIOLOGICAL STUDIES IN HEREDITARY HEMOCHROMATOSIS: PREVALENCE, MORBIDITY AND BENEFIT OF SCREENING.

219. Johan Fredrik Skomsvoll: REPRODUCTIVE OUTCOME IN WOMEN WITH RHEUMATIC DISEASE. A population registry based study of the effects of inflammatory rheumatic disease and connective tissue disease on reproductive outcome in Norwegian women in 1967-1995.
220. Siv Mørkved: URINARY INCONTINENCE DURING PREGNANCY AND AFTER DELIVERY: EFFECT OF PELVIC FLOOR MUSCLE TRAINING IN PREVENTION AND TREATMENT
221. Marit S. Jordhøy: THE IMPACT OF COMPREHENSIVE PALLIATIVE CARE
222. Tom Christian Martinsen: HYPERGASTRINEMIA AND HYPOACIDITY IN RODENTS – CAUSES AND CONSEQUENCES
223. Solveig Tingulstad: CENTRALIZATION OF PRIMARY SURGERY FOR OVARIAN CANCER. FEASIBILITY AND IMPACT ON SURVIVAL
224. Haytham Eloqayli: METABOLIC CHANGES IN THE BRAIN CAUSED BY EPILEPTIC SEIZURES
225. Torunn Bruland: STUDIES OF EARLY RETROVIRUS-HOST INTERACTIONS – VIRAL DETERMINANTS FOR PATHOGENESIS AND THE INFLUENCE OF SEX ON THE SUSCEPTIBILITY TO FRIEND MURINE LEUKAEMIA VIRUS INFECTION
226. Torstein Hole: DOPPLER ECHOCARDIOGRAPHIC EVALUATION OF LEFT VENTRICULAR FUNCTION IN PATIENTS WITH ACUTE MYOCARDIAL INFARCTION
227. Vibeke Nossum: THE EFFECT OF VASCULAR BUBBLES ON ENDOTHELIAL FUNCTION
228. Sigurd Fasting: ROUTINE BASED RECORDING OF ADVERSE EVENTS DURING ANAESTHESIA – APPLICATION IN QUALITY IMPROVEMENT AND SAFETY
229. Solfred Romundstad: EPIDEMIOLOGICAL STUDIES OF MICROALBUMINURIA. THE NORD-TRØNDELAGE HEALTH STUDY 1995-97 (HUNT 2)
230. Geir Torheim: PROCESSING OF DYNAMIC DATA SETS IN MAGNETIC RESONANCE IMAGING
231. Catrine Ahlén: SKIN INFECTIONS IN OCCUPATIONAL SATURATION DIVERS IN THE NORTH SEA AND THE IMPACT OF THE ENVIRONMENT
232. Arnulf Langhammer: RESPIRATORY SYMPTOMS, LUNG FUNCTION AND BONE MINERAL DENSITY IN A COMPREHENSIVE POPULATION SURVEY. THE NORD-TRØNDELAGE HEALTH STUDY 1995-97. THE BRONCHIAL OBSTRUCTION IN NORD-TRØNDELAGE STUDY
233. Einar Kjelsås: EATING DISORDERS AND PHYSICAL ACTIVITY IN NON-CLINICAL SAMPLES
234. Arne Wibe: RECTAL CANCER TREATMENT IN NORWAY – STANDARDISATION OF SURGERY AND QUALITY ASSURANCE

#### 2004

235. Eivind Witsø: BONE GRAFT AS AN ANTIBIOTIC CARRIER
236. Anne Mari Sund: DEVELOPMENT OF DEPRESSIVE SYMPTOMS IN EARLY ADOLESCENCE
237. Hallvard Lærum: EVALUATION OF ELECTRONIC MEDICAL RECORDS – A CLINICAL TASK PERSPECTIVE
238. Gustav Mikkelsen: ACCESSIBILITY OF INFORMATION IN ELECTRONIC PATIENT RECORDS; AN EVALUATION OF THE ROLE OF DATA QUALITY
239. Steinar Krokstad: SOCIOECONOMIC INEQUALITIES IN HEALTH AND DISABILITY. SOCIAL EPIDEMIOLOGY IN THE NORD-TRØNDELAGE HEALTH STUDY (HUNT), NORWAY
240. Arne Kristian Myhre: NORMAL VARIATION IN ANOGENITAL ANATOMY AND MICROBIOLOGY IN NON-ABUSED PRESCHOOL CHILDREN
241. Ingunn Dybedal: NEGATIVE REGULATORS OF HEMATOPOIETIC STEM AND PROGENITOR CELLS
242. Beate Sitter: TISSUE CHARACTERIZATION BY HIGH RESOLUTION MAGIC ANGLE SPINNING MR SPECTROSCOPY
243. Per Arne Aas: MACROMOLECULAR MAINTENANCE IN HUMAN CELLS – REPAIR OF URACIL IN DNA AND METHYLATIONS IN DNA AND RNA
244. Anna Bofin: FINE NEEDLE ASPIRATION CYTOLOGY IN THE PRIMARY INVESTIGATION OF BREAST TUMOURS AND IN THE DETERMINATION OF TREATMENT STRATEGIES
245. Jim Aage Nøttestad: DEINSTITUTIONALIZATION AND MENTAL HEALTH CHANGES AMONG PEOPLE WITH MENTAL RETARDATION
246. Reidar Fossmark: GASTRIC CANCER IN JAPANESE COTTON RATS
247. Wibeke Nordhøy: MANGANESE AND THE HEART. INTRACELLULAR MR RELAXATION AND WATER EXCHANGE ACROSS THE CARDIAC CELL MEMBRANE

#### 2005

248. Sturla Molden: QUANTITATIVE ANALYSES OF SINGLE UNITS RECORDED FROM THE HIPPOCAMPUS AND ENTORHINAL CORTEX OF BEHAVING RATS
249. Wenche Brenne Drøyvold: EPIDEMIOLOGICAL STUDIES ON WEIGHT CHANGE AND HEALTH IN A LARGE POPULATION. THE NORD-TRØNDELAGE HEALTH STUDY (HUNT)
250. Ragnhild Støen: ENDOTHELIUM-DEPENDENT VASODILATION IN THE FEMORAL ARTERY OF DEVELOPING PIGLETS
251. Aslak Steinsbekk: HOMEOPATHY IN THE PREVENTION OF UPPER RESPIRATORY TRACT INFECTIONS IN CHILDREN
252. Hill-Aina Steffenach: MEMORY IN HIPPOCAMPAL AND CORTICO-HIPPOCAMPAL CIRCUITS

253. Eystein Stordal: ASPECTS OF THE EPIDEMIOLOGY OF DEPRESSIONS BASED ON SELF-RATING IN A LARGE GENERAL HEALTH STUDY (THE HUNT-2 STUDY)
254. Viggo Pettersen: FROM MUSCLES TO SINGING: THE ACTIVITY OF ACCESSORY BREATHING MUSCLES AND THORAX MOVEMENT IN CLASSICAL SINGING
255. Marianne Fyhn: SPATIAL MAPS IN THE HIPPOCAMPUS AND ENTORHINAL CORTEX
256. Robert Valderhaug: OBSESSIVE-COMPULSIVE DISORDER AMONG CHILDREN AND ADOLESCENTS: CHARACTERISTICS AND PSYCHOLOGICAL MANAGEMENT OF PATIENTS IN OUTPATIENT PSYCHIATRIC CLINICS
257. Erik Skaaheim Haug: INFRARENAL ABDOMINAL AORTIC ANEURYSMS – COMORBIDITY AND RESULTS FOLLOWING OPEN SURGERY
258. Daniel Kondziella: GLIAL-NEURONAL INTERACTIONS IN EXPERIMENTAL BRAIN DISORDERS
259. Vegard Heimly Brun: ROUTES TO SPATIAL MEMORY IN HIPPOCAMPAL PLACE CELLS
260. Kenneth McMillan: PHYSIOLOGICAL ASSESSMENT AND TRAINING OF ENDURANCE AND STRENGTH IN PROFESSIONAL YOUTH SOCCER PLAYERS
261. Marit Sæbø Indredavik: MENTAL HEALTH AND CEREBRAL MAGNETIC RESONANCE IMAGING IN ADOLESCENTS WITH LOW BIRTH WEIGHT
262. Ole Johan Kemi: ON THE CELLULAR BASIS OF AEROBIC FITNESS, INTENSITY-DEPENDENCE AND TIME-COURSE OF CARDIOMYOCYTE AND ENDOTHELIAL ADAPTATIONS TO EXERCISE TRAINING
263. Eszter Vanky: POLYCYSTIC OVARY SYNDROME – METFORMIN TREATMENT IN PREGNANCY
264. Hild Fjærtøft: EXTENDED STROKE UNIT SERVICE AND EARLY SUPPORTED DISCHARGE. SHORT AND LONG-TERM EFFECTS
265. Grete Dyb: POSTTRAUMATIC STRESS REACTIONS IN CHILDREN AND ADOLESCENTS
266. Vidar Fykse: SOMATOSTATIN AND THE STOMACH
267. Kirsti Berg: OXIDATIVE STRESS AND THE ISCHEMIC HEART: A STUDY IN PATIENTS UNDERGOING CORONARY REVASCULARIZATION
268. Björn Inge Gustafsson: THE SEROTONIN PRODUCING ENTEROCHROMAFFIN CELL, AND EFFECTS OF HYPERSEROTONINEMIA ON HEART AND BONE

## 2006

269. Torstein Baade Rø: EFFECTS OF BONE MORPHOGENETIC PROTEINS, HEPATOCYTE GROWTH FACTOR AND INTERLEUKIN-21 IN MULTIPLE MYELOMA
270. May-Britt Tessem: METABOLIC EFFECTS OF ULTRAVIOLET RADIATION ON THE ANTERIOR PART OF THE EYE
271. Anne-Sofie Helvik: COPING AND EVERYDAY LIFE IN A POPULATION OF ADULTS WITH HEARING IMPAIRMENT
272. Therese Standal: MULTIPLE MYELOMA: THE INTERPLAY BETWEEN MALIGNANT PLASMA CELLS AND THE BONE MARROW MICROENVIRONMENT
273. Ingvild Saltvedt: TREATMENT OF ACUTELY SICK, FRAIL ELDERLY PATIENTS IN A GERIATRIC EVALUATION AND MANAGEMENT UNIT – RESULTS FROM A PROSPECTIVE RANDOMISED TRIAL
274. Birger Henning Endreseth: STRATEGIES IN RECTAL CANCER TREATMENT – FOCUS ON EARLY RECTAL CANCER AND THE INFLUENCE OF AGE ON PROGNOSIS
275. Anne Mari Aukan Rokstad: ALGINATE CAPSULES AS BIOREACTORS FOR CELL THERAPY
276. Mansour Akbari: HUMAN BASE EXCISION REPAIR FOR PRESERVATION OF GENOMIC STABILITY
277. Stein Sundstrøm: IMPROVING TREATMENT IN PATIENTS WITH LUNG CANCER – RESULTS FROM TWO MULTICENTRE RANDOMISED STUDIES
278. Hilde Pleyrn: BLEEDING AFTER CORONARY ARTERY BYPASS SURGERY - STUDIES ON HEMOSTATIC MECHANISMS, PROPHYLACTIC DRUG TREATMENT AND EFFECTS OF AUTOTRANSFUSION
279. Line Merethe Oldervoll: PHYSICAL ACTIVITY AND EXERCISE INTERVENTIONS IN CANCER PATIENTS
280. Boye Welde: THE SIGNIFICANCE OF ENDURANCE TRAINING, RESISTANCE TRAINING AND MOTIVATIONAL STYLES IN ATHLETIC PERFORMANCE AMONG ELITE JUNIOR CROSS-COUNTRY SKIERS
281. Per Olav Vandvik: IRRITABLE BOWEL SYNDROME IN NORWAY, STUDIES OF PREVALENCE, DIAGNOSIS AND CHARACTERISTICS IN GENERAL PRACTICE AND IN THE POPULATION
282. Idar Kirkeby-Garstad: CLINICAL PHYSIOLOGY OF EARLY MOBILIZATION AFTER CARDIAC SURGERY
283. Linn Getz: SUSTAINABLE AND RESPONSIBLE PREVENTIVE MEDICINE. CONCEPTUALISING ETHICAL DILEMMAS ARISING FROM CLINICAL IMPLEMENTATION OF ADVANCING MEDICAL TECHNOLOGY
284. Eva Tegnander: DETECTION OF CONGENITAL HEART DEFECTS IN A NON-SELECTED POPULATION OF 42,381 FETUSES

285. Kristin Gabestad Nørsett: GENE EXPRESSION STUDIES IN GASTROINTESTINAL PATHOPHYSIOLOGY AND NEOPLASIA
286. Per Magnus Haram: GENETIC VS. ACQUIRED FITNESS: METABOLIC, VASCULAR AND CARDIOMYOCYTE ADAPTATIONS
287. Agneta Johansson: GENERAL RISK FACTORS FOR GAMBLING PROBLEMS AND THE PREVALENCE OF PATHOLOGICAL GAMBLING IN NORWAY
288. Svein Artur Jensen: THE PREVALENCE OF SYMPTOMATIC ARTERIAL DISEASE OF THE LOWER LIMB
289. Charlotte Björk Ingul: QUANTIFICATION OF REGIONAL MYOCARDIAL FUNCTION BY STRAIN RATE AND STRAIN FOR EVALUATION OF CORONARY ARTERY DISEASE. AUTOMATED VERSUS MANUAL ANALYSIS DURING ACUTE MYOCARDIAL INFARCTION AND DOBUTAMINE STRESS ECHOCARDIOGRAPHY
290. Jakob Nakling: RESULTS AND CONSEQUENCES OF ROUTINE ULTRASOUND SCREENING IN PREGNANCY – A GEOGRAPHIC BASED POPULATION STUDY
291. Anne Engum: DEPRESSION AND ANXIETY – THEIR RELATIONS TO THYROID DYSFUNCTION AND DIABETES IN A LARGE EPIDEMIOLOGICAL STUDY
292. Ottar Bjerkeset: ANXIETY AND DEPRESSION IN THE GENERAL POPULATION: RISK FACTORS, INTERVENTION AND OUTCOME – THE NORD-TRØNDELAG HEALTH STUDY (HUNT)
293. Jon Olav Drogset: RESULTS AFTER SURGICAL TREATMENT OF ANTERIOR CRUCIATE LIGAMENT INJURIES – A CLINICAL STUDY
294. Lars Fosse: MECHANICAL BEHAVIOUR OF COMPACTED MORSELLISED BONE – AN EXPERIMENTAL IN VITRO STUDY
295. Gunilla Klensmeden Fosse: MENTAL HEALTH OF PSYCHIATRIC OUTPATIENTS BULLIED IN CHILDHOOD
296. Paul Jarle Mork: MUSCLE ACTIVITY IN WORK AND LEISURE AND ITS ASSOCIATION TO MUSCULOSKELETAL PAIN
297. Björn Stenström: LESSONS FROM RODENTS: I: MECHANISMS OF OBESITY SURGERY – ROLE OF STOMACH. II: CARCINOGENIC EFFECTS OF *HELICOBACTER PYLORI* AND SNUS IN THE STOMACH

## 2007

298. Haakon R. Skogseth: INVASIVE PROPERTIES OF CANCER – A TREATMENT TARGET ? IN VITRO STUDIES IN HUMAN PROSTATE CANCER CELL LINES
299. Janniche Hammer: GLUTAMATE METABOLISM AND CYCLING IN MESIAL TEMPORAL LOBE EPILEPSY
300. May Britt Drugli: YOUNG CHILDREN TREATED BECAUSE OF ODD/CD: CONDUCT PROBLEMS AND SOCIAL COMPETENCIES IN DAY-CARE AND SCHOOL SETTINGS
301. Arne Skjold: MAGNETIC RESONANCE KINETICS OF MANGANESE DIPYRIDOXYL DIPHOSPHATE (MnDPDP) IN HUMAN MYOCARDIUM. STUDIES IN HEALTHY VOLUNTEERS AND IN PATIENTS WITH RECENT MYOCARDIAL INFARCTION
302. Siri Malm: LEFT VENTRICULAR SYSTOLIC FUNCTION AND MYOCARDIAL PERFUSION ASSESSED BY CONTRAST ECHOCARDIOGRAPHY
303. Valentina Maria do Rosario Cabral Iversen: MENTAL HEALTH AND PSYCHOLOGICAL ADAPTATION OF CLINICAL AND NON-CLINICAL MIGRANT GROUPS
304. Lasse Løvstakken: SIGNAL PROCESSING IN DIAGNOSTIC ULTRASOUND: ALGORITHMS FOR REAL-TIME ESTIMATION AND VISUALIZATION OF BLOOD FLOW VELOCITY
305. Elisabeth Olstad: GLUTAMATE AND GABA: MAJOR PLAYERS IN NEURONAL METABOLISM
306. Lilian Leistad: THE ROLE OF CYTOKINES AND PHOSPHOLIPASE<sub>A<sub>2</sub>S</sub> IN ARTICULAR CARTILAGE CHONDROCYTES IN RHEUMATOID ARTHRITIS AND OSTEOARTHRITIS
307. Arne Vaaler: EFFECTS OF PSYCHIATRIC INTENSIVE CARE UNIT IN AN ACUTE PSYCHIATRIC WARD
308. Mathias Toft: GENETIC STUDIES OF LRRK2 AND PINK1 IN PARKINSON'S DISEASE
309. Ingrid Løvold Mostad: IMPACT OF DIETARY FAT QUANTITY AND QUALITY IN TYPE 2 DIABETES WITH EMPHASIS ON MARINE N-3 FATTY ACIDS
310. Torill Eidhammer Sjøbakk: MR DETERMINED BRAIN METABOLIC PATTERN IN PATIENTS WITH BRAIN METASTASES AND ADOLESCENTS WITH LOW BIRTH WEIGHT
311. Vidar Beisvåg: PHYSIOLOGICAL GENOMICS OF HEART FAILURE: FROM TECHNOLOGY TO PHYSIOLOGY
312. Olav Magnus Søndena Fredheim: HEALTH RELATED QUALITY OF LIFE ASSESSMENT AND ASPECTS OF THE CLINICAL PHARMACOLOGY OF METHADONE IN PATIENTS WITH CHRONIC NON-MALIGNANT PAIN
313. Anne Brantberg: FETAL AND PERINATAL IMPLICATIONS OF ANOMALIES IN THE GASTROINTESTINAL TRACT AND THE ABDOMINAL WALL
314. Erik Solligård: GUT LUMINAL MICRODIALYSIS

315. Elin Tollefsen: RESPIRATORY SYMPTOMS IN A COMPREHENSIVE POPULATION BASED STUDY AMONG ADOLESCENTS 13-19 YEARS. YOUNG-HUNT 1995-97 AND 2000-01; THE NORD-TRØNDELAGE HEALTH STUDIES (HUNT)
316. Anne-Tove Brenne: GROWTH REGULATION OF MYELOMA CELLS
317. Heidi Knobel: FATIGUE IN CANCER TREATMENT – ASSESSMENT, COURSE AND ETIOLOGY
318. Torbjørn Dahl: CAROTID ARTERY STENOSIS. DIAGNOSTIC AND THERAPEUTIC ASPECTS
319. Inge-Andre Rasmussen jr.: FUNCTIONAL AND DIFFUSION TENSOR MAGNETIC RESONANCE IMAGING IN NEUROSURGICAL PATIENTS
320. Grete Helen Bratberg: PUBERTAL TIMING – ANTECEDENT TO RISK OR RESILIENCE ? EPIDEMIOLOGICAL STUDIES ON GROWTH, MATURATION AND HEALTH RISK BEHAVIOURS; THE YOUNG HUNT STUDY, NORD-TRØNDELAGE, NORWAY
321. Sveinung Sørhaug: THE PULMONARY NEUROENDOCRINE SYSTEM. PHYSIOLOGICAL, PATHOLOGICAL AND TUMOURIGENIC ASPECTS
322. Olav Sande Eftedal: ULTRASONIC DETECTION OF DECOMPRESSION INDUCED VASCULAR MICROBUBBLES
323. Rune Bang Leistad: PAIN, AUTONOMIC ACTIVATION AND MUSCULAR ACTIVITY RELATED TO EXPERIMENTALLY-INDUCED COGNITIVE STRESS IN HEADACHE PATIENTS
324. Svein Brekke: TECHNIQUES FOR ENHANCEMENT OF TEMPORAL RESOLUTION IN THREE-DIMENSIONAL ECHOCARDIOGRAPHY
325. Kristian Bernhard Nilsen: AUTONOMIC ACTIVATION AND MUSCLE ACTIVITY IN RELATION TO MUSCULOSKELETAL PAIN
326. Anne Irene Hagen: HEREDITARY BREAST CANCER IN NORWAY. DETECTION AND PROGNOSIS OF BREAST CANCER IN FAMILIES WITH *BRCA1* GENE MUTATION
327. Ingebjørg S. Juel : INTESTINAL INJURY AND RECOVERY AFTER ISCHEMIA. AN EXPERIMENTAL STUDY ON RESTITUTION OF THE SURFACE EPITHELIUM, INTESTINAL PERMEABILITY, AND RELEASE OF BIOMARKERS FROM THE MUCOSA
328. Runa Heimstad: POST-TERM PREGNANCY
329. Jan Egil Afset: ROLE OF ENTEROPATHOGENIC *ESCHERICHIA COLI* IN CHILDHOOD DIARRHOEA IN NORWAY
330. Bent Håvard Hellum: *IN VITRO* INTERACTIONS BETWEEN MEDICINAL DRUGS AND HERBS ON CYTOCHROME P-450 METABOLISM AND P-GLYCOPROTEIN TRANSPORT
331. Morten André Høydal: CARDIAC DYSFUNCTION AND MAXIMAL OXYGEN UPTAKE MYOCARDIAL ADAPTATION TO ENDURANCE TRAINING

## 2008

332. Andreas Møllerløkken: REDUCTION OF VASCULAR BUBBLES: METHODS TO PREVENT THE ADVERSE EFFECTS OF DECOMPRESSION
333. Anne Hege Aamodt: COMORBIDITY OF HEADACHE AND MIGRAINE IN THE NORD-TRØNDELAGE HEALTH STUDY 1995-97
334. Brage Høyem Amundsen: MYOCARDIAL FUNCTION QUANTIFIED BY SPECKLE TRACKING AND TISSUE DOPPLER ECHOCARDIOGRAPHY – VALIDATION AND APPLICATION IN EXERCISE TESTING AND TRAINING
335. Inger Anne Næss: INCIDENCE, MORTALITY AND RISK FACTORS OF FIRST VENOUS THROMBOSIS IN A GENERAL POPULATION. RESULTS FROM THE SECOND NORD-TRØNDELAGE HEALTH STUDY (HUNT2)
336. Vegard Bugten: EFFECTS OF POSTOPERATIVE MEASURES AFTER FUNCTIONAL ENDOSCOPIC SINUS SURGERY
337. Morten Bruvold: MANGANESE AND WATER IN CARDIAC MAGNETIC RESONANCE IMAGING
338. Miroslav Fris: THE EFFECT OF SINGLE AND REPEATED ULTRA VIOLET RADIATION ON THE ANTERIOR SEGMENT OF THE RABBIT EYE
339. Svein Arne Aase: METHODS FOR IMPROVING QUALITY AND EFFICIENCY IN QUANTITATIVE ECHOCARDIOGRAPHY – ASPECTS OF USING HIGH FRAME RATE
340. Roger Almvik: ASSESSING THE RISK OF VIOLENCE: DEVELOPMENT AND VALIDATION OF THE BRØSET VIOLENCE CHECKLIST
341. Ottar Sundheim: STRUCTURE-FUNCTION ANALYSIS OF HUMAN ENZYMES INITIATING NUCLEOBASE REPAIR IN DNA AND RNA
342. Anne Mari Undheim: SHORT AND LONG-TERM OUTCOME OF EMOTIONAL AND BEHAVIOURAL PROBLEMS IN YOUNG ADOLESCENTS WITH AND WITHOUT READING DIFFICULTIES
343. Helge Garåsen: THE TRONDHEIM MODEL. IMPROVING THE PROFESSIONAL COMMUNICATION BETWEEN THE VARIOUS LEVELS OF HEALTH CARE SERVICES AND IMPLEMENTATION OF INTERMEDIATE CARE AT A COMMUNITY HOSPITAL COULD PROVIDE BETTER CARE FOR OLDER PATIENTS. SHORT AND LONG TERM EFFECTS
344. Olav A. Foss: “THE ROTATION RATIOS METHOD”. A METHOD TO DESCRIBE ALTERED SPATIAL ORIENTATION IN SEQUENTIAL RADIOGRAPHS FROM ONE PELVIS

345. Bjørn Olav Åsvold: THYROID FUNCTION AND CARDIOVASCULAR HEALTH
346. Torun Margareta Melø: NEURONAL GLIAL INTERACTIONS IN EPILEPSY
347. Irina Poliakova Eide: FETAL GROWTH RESTRICTION AND PRE-ECLAMPSIA: SOME CHARACTERISTICS OF FETO-MATERNAL INTERACTIONS IN DECIDUA BASALIS
348. Torunn Askim: RECOVERY AFTER STROKE. ASSESSMENT AND TREATMENT; WITH FOCUS ON MOTOR FUNCTION
349. Ann Elisabeth Åsberg: NEUTROPHIL ACTIVATION IN A ROLLER PUMP MODEL OF CARDIOPULMONARY BYPASS. INFLUENCE ON BIOMATERIAL, PLATELETS AND COMPLEMENT
350. Lars Hagen: REGULATION OF DNA BASE EXCISION REPAIR BY PROTEIN INTERACTIONS AND POST TRANSLATIONAL MODIFICATIONS
351. Sigrun Beate Kjotrød: POLYCYSTIC OVARY SYNDROME – METFORMIN TREATMENT IN ASSISTED REPRODUCTION
352. Steven Keita Nishiyama: PERSPECTIVES ON LIMB-VASCULAR HETEROGENEITY: IMPLICATIONS FOR HUMAN AGING, SEX, AND EXERCISE
353. Sven Peter Näsholm: ULTRASOUND BEAMS FOR ENHANCED IMAGE QUALITY
354. Jon Ståle Ritland: PRIMARY OPEN-ANGLE GLAUCOMA & EXFOLIATIVE GLAUCOMA. SURVIVAL, COMORBIDITY AND GENETICS
355. Sigrid Botne Sando: ALZHEIMER'S DISEASE IN CENTRAL NORWAY. GENETIC AND EDUCATIONAL ASPECTS
356. Parvinder Kaur: CELLULAR AND MOLECULAR MECHANISMS BEHIND METHYLMERCURY-INDUCED NEUROTOXICITY
357. Ismail Cüneyt Güzey: DOPAMINE AND SEROTONIN RECEPTOR AND TRANSPORTER GENE POLYMORPHISMS AND EXTRAPYRAMIDAL SYMPTOMS. STUDIES IN PARKINSON'S DISEASE AND IN PATIENTS TREATED WITH ANTIPSYCHOTIC OR ANTIDEPRESSANT DRUGS
358. Brit Dybdahl: EXTRA-CELLULAR INDUCIBLE HEAT-SHOCK PROTEIN 70 (Hsp70) – A ROLE IN THE INFLAMMATORY RESPONSE ?
359. Kristoffer Haugarvoll: IDENTIFYING GENETIC CAUSES OF PARKINSON'S DISEASE IN NORWAY
360. Nadra Nilsen: TOLL-LIKE RECEPTOR 2 –EXPRESSION, REGULATION AND SIGNALING
361. Johan Håkon Bjørngaard: PATIENT SATISFACTION WITH OUTPATIENT MENTAL HEALTH SERVICES – THE INFLUENCE OF ORGANIZATIONAL FACTORS.
362. Kjetil Høydal : EFFECTS OF HIGH INTENSITY AEROBIC TRAINING IN HEALTHY SUBJECTS AND CORONARY ARTERY DISEASE PATIENTS; THE IMPORTANCE OF INTENSITY,, DURATION AND FREQUENCY OF TRAINING.
363. Trine Karlsen: TRAINING IS MEDICINE: ENDURANCE AND STRENGTH TRAINING IN CORONARY ARTERY DISEASE AND HEALTH.
364. Marte Thuen: MANGANASE-ENHANCED AND DIFFUSION TENSOR MR IMAGING OF THE NORMAL, INJURED AND REGENERATING RAT VISUAL PATHWAY
365. Cathrine Broberg Vågbø: DIRECT REPAIR OF ALKYLATION DAMAGE IN DNA AND RNA BY 2-OXOGLUTARATE- AND IRON-DEPENDENT DIOXYGENASES
366. Arnt Erik Tjønnå: AEROBIC EXERCISE AND CARDIOVASCULAR RISK FACTORS IN OVERWEIGHT AND OBESE ADOLESCENTS AND ADULTS
367. Marianne W. Furnes: FEEDING BEHAVIOR AND BODY WEIGHT DEVELOPMENT: LESSONS FROM RATS
368. Lene N. Johannessen: FUNGAL PRODUCTS AND INFLAMMATORY RESPONSES IN HUMAN MONOCYTES AND EPITHELIAL CELLS
369. Anja Bye: GENE EXPRESSION PROFILING OF *INHERITED* AND *ACQUIRED* MAXIMAL OXYGEN UPTAKE – RELATIONS TO THE METABOLIC SYNDROME.
370. Oluf Dimitri Røe: MALIGNANT MESOTHELIOMA: VIRUS, BIOMARKERS AND GENES. A TRANSLATIONAL APPROACH
371. Ane Cecilie Dale: DIABETES MELLITUS AND FATAL ISCHEMIC HEART DISEASE. ANALYSES FROM THE HUNT1 AND 2 STUDIES
372. Jacob Christian Hølen: PAIN ASSESSMENT IN PALLIATIVE CARE: VALIDATION OF METHODS FOR SELF-REPORT AND BEHAVIOURAL ASSESSMENT
373. Erming Tian: THE GENETIC IMPACTS IN THE ONCOGENESIS OF MULTIPLE MYELOMA
374. Ole Bosnes: KLINISK UTPRØVING AV NORSKE VERSJONER AV NOEN SENTRALE TESTER PÅ KOGNITIV FUNKSJON
375. Ola M. Rygh: 3D ULTRASOUND BASED NEURONAVIGATION IN NEUROSURGERY . A CLINICAL EVALUATION
376. Astrid Kamilla Stunes: ADIPOKINES, PEROXISOME PROFILERATOR ACTIVATED RECEPTOR (PPAR) AGONISTS AND SEROTONIN. COMMON REGULATORS OF BONE AND FAT METABOLISM
377. Silje Engdal: HERBAL REMEDIES USED BY NORWEGIAN CANCER PATIENTS AND THEIR ROLE IN HERB-DRUG INTERACTIONS

378. Kristin Offerdal: IMPROVED ULTRASOUND IMAGING OF THE FETUS AND ITS CONSEQUENCES FOR SEVERE AND LESS SEVERE ANOMALIES
379. Øivind Rognmo: HIGH-INTENSITY AEROBIC EXERCISE AND CARDIOVASCULAR HEALTH
380. Jo-Åsmund Lund: RADIOTHERAPY IN ANAL CARCINOMA AND PROSTATE CANCER
- 2009**
381. Tore Grüner Bjåstad: HIGH FRAME RATE ULTRASOUND IMAGING USING PARALLEL BEAMFORMING
382. Erik Søndena: INTELLECTUAL DISABILITIES IN THE CRIMINAL JUSTICE SYSTEM
383. Berit Rostad: SOCIAL INEQUALITIES IN WOMEN'S HEALTH, HUNT 1984-86 AND 1995-97, THE NORD-TRØNDELAG HEALTH STUDY (HUNT)
384. Jonas Crosby: ULTRASOUND-BASED QUANTIFICATION OF MYOCARDIAL DEFORMATION AND ROTATION
385. Erling Tronvik: MIGRAINE, BLOOD PRESSURE AND THE RENIN-ANGIOTENSIN SYSTEM
386. Tom Christensen: BRINGING THE GP TO THE FOREFRONT OF EPR DEVELOPMENT
387. Håkon Bergsens: ASPECTS OF GROUP B STREPTOCOCCUS (GBS) DISEASE IN THE NEWBORN. EPIDEMIOLOGY, CHARACTERISATION OF INVASIVE STRAINS AND EVALUATION OF INTRAPARTUM SCREENING
388. Ronny Myhre: GENETIC STUDIES OF CANDIDATE TENE3S IN PARKINSON'S DISEASE
389. Torbjørn Moe Eggebø: ULTRASOUND AND LABOUR
390. Eivind Wang: TRAINING IS MEDICINE FOR PATIENTS WITH PERIPHERAL ARTERIAL DISEASE
391. Thea Kristin Våtsveen: GENETIC ABERRATIONS IN MYELOMA CELLS
392. Thomas Jozefiak: QUALITY OF LIFE AND MENTAL HEALTH IN CHILDREN AND ADOLESCENTS: CHILD AND PARENT PERSPECTIVES
393. Jens Erik Slagsvold: N-3 POLYUNSATURATED FATTY ACIDS IN HEALTH AND DISEASE – CLINICAL AND MOLECULAR ASPECTS
394. Kristine Misund: A STUDY OF THE TRANSCRIPTIONAL REPRESSOR ICER. REGULATORY NETWORKS IN GASTRIN-INDUCED GENE EXPRESSION
395. Franco M. Impellizzeri: HIGH-INTENSITY TRAINING IN FOOTBALL PLAYERS. EFFECTS ON PHYSICAL AND TECHNICAL PERFORMANCE
396. Kari Hanne Gjeilo: HEALTH-RELATED QUALITY OF LIFE AND CHRONIC PAIN IN PATIENTS UNDERGOING CARDIAC SURGERY
397. Øyvind Hauso: NEUROENDOCRINE ASPECTS OF PHYSIOLOGY AND DISEASE
398. Ingvild Bjellmo Johnsen: INTRACELLULAR SIGNALING MECHANISMS IN THE INNATE IMMUNE RESPONSE TO VIRAL INFECTIONS
399. Linda Tømmerdal Roten: GENETIC PREDISPOSITION FOR DEVELOPMENT OF PREEMCLAMPSIA – CANDIDATE GENE STUDIES IN THE HUNT (NORD-TRØNDELAG HEALTH STUDY) POPULATION
400. Trude Teoline Nausthaug Rakvåg: PHARMACOGENETICS OF MORPHINE IN CANCER PAIN
401. Hanne Lehn: MEMORY FUNCTIONS OF THE HUMAN MEDIAL TEMPORAL LOBE STUDIED WITH fMRI
402. Randi Utne Holt: ADHESION AND MIGRATION OF MYELOMA CELLS– IN VITRO STUDIES –
403. Trygve Solstad: NEURAL REPRESENTATIONS OF EUCLIDEAN SPACE
404. Unn-Merete Fagerli: MULTIPLE MYELOMA CELLS AND CYTOKINES FROM THE BONE MARROW ENVIRONMENT; ASPECTS OF GROWTH REGULATION AND MIGRATION
405. Sigrid Bjørnelv: EATING– AND WEIGHT PROBLEMS IN ADOLESCENTS, THE YOUNG HUNT-STUDY
406. Mari Hoff: CORTICAL HAND BONE LOSS IN RHEUMATOID ARTHRITIS. EVALUATING DIGITAL X-RAY RADIOGRAMMETRY AS OUTCOME MEASURE OF DISEASE ACTIVITY, RESPONSE VARIABLE TO TREATMENT AND PREDICTOR OF BONE DAMAGE
407. Siri Bjørgen: AEROBIC HIGH INTENSITY INTERVAL TRAINING IS AN EFFECTIVE TREATMENT FOR PATIENTS WITH CHRONIC OBSTRUCTIVE PULMONARY DISEASE
408. Susanne Lindqvist: VISION AND BRAIN IN ADOLESCENTS WITH LOW BIRTH WEIGHT
409. Torbjørn Hergum: 3D ULTRASOUND FOR QUANTITATIVE ECHOCARDIOGRAPHY
410. Jørgen Urnes: PATIENT EDUCATION IN GASTRO-OESOPHAGEAL REFLUX DISEASE. VALIDATION OF A DIGESTIVE SYMPTOMS AND IMPACT QUESTIONNAIRE AND A RANDOMISED CONTROLLED TRIAL OF PATIENT EDUCATION
411. Elvar Eyjolfsson: <sup>13</sup>C NMRS OF ANIMAL MODELS OF SCHIZOPHRENIA
412. Marius Steiro Fimland: CHRONIC AND ACUTE NEURAL ADAPTATIONS TO STRENGTH TRAINING
413. Øyvind Støren: RUNNING AND CYCLING ECONOMY IN ATHLETES; DETERMINING FACTORS, TRAINING INTERVENTIONS AND TESTING
414. Håkon Hov: HEPATOCYTE GROWTH FACTOR AND ITS RECEPTOR C-MET. AUTOCRINE GROWTH AND SIGNALING IN MULTIPLE MYELOMA CELLS

- 415. Maria Radtke: ROLE OF AUTOIMMUNITY AND OVERSTIMULATION FOR BETA-CELL DEFICIENCY. EPIDEMIOLOGICAL AND THERAPEUTIC PERSPECTIVES
- 416. Liv Bente Romundstad: ASSISTED FERTILIZATION IN NORWAY: SAFETY OF THE REPRODUCTIVE TECHNOLOGY
- 417. Erik Magnus Berntsen: PREOPERATIV PLANNING AND FUNCTIONAL NEURONAVIGATION – WITH FUNCTIONAL MRI AND DIFFUSION TENSOR TRACTOGRAPHY IN PATIENTS WITH BRAIN LESIONS
- 418. Tonje Strømme Steigedal: MOLECULAR MECHANISMS OF THE PROLIFERATIVE RESPONSE TO THE HORMONE GASTRIN
- 419. Vidar Rao: EXTRACORPOREAL PHOTOCHEMOTHERAPY IN PATIENTS WITH CUTANEOUS T CELL LYMPHOMA OR GRAFT-vs-HOST DISEASE
- 420. Torild Visnes: DNA EXCISION REPAIR OF URACIL AND 5-FLUOROURACIL IN HUMAN CANCER CELL LINES

**2010**

- 421. John Munkhaugen: BLOOD PRESSURE, BODY WEIGHT, AND KIDNEY FUNCTION IN THE NEAR-NORMAL RANGE: NORMALITY, RISK FACTOR OR MORBIDITY ?
- 422. Ingrid Castberg: PHARMACOKINETICS, DRUG INTERACTIONS AND ADHERENCE TO TREATMENT WITH ANTIPSYCHOTICS: STUDIES IN A NATURALISTIC SETTING
- 423. Jian Xu: BLOOD-OXYGEN-LEVEL-DEPENDENT-FUNCTIONAL MAGNETIC RESONANCE IMAGING AND DIFFUSION TENSOR IMAGING IN TRAUMATIC BRAIN INJURY RESEARCH
- 424. Sigmund Simonsen: ACCEPTABLE RISK AND THE REQUIREMENT OF PROPORTIONALITY IN EUROPEAN BIOMEDICAL RESEARCH LAW. WHAT DOES THE REQUIREMENT THAT BIOMEDICAL RESEARCH SHALL NOT INVOLVE RISKS AND BURDENS DISPROPORTIONATE TO ITS POTENTIAL BENEFITS MEAN?
- 425. Astrid Woodhouse: MOTOR CONTROL IN WHIPLASH AND CHRONIC NON-TRAUMATIC NECK PAIN
- 426. Line Rørstad Jensen: EVALUATION OF TREATMENT EFFECTS IN CANCER BY MR IMAGING AND SPECTROSCOPY
- 427. Trine Moholdt: AEROBIC EXERCISE IN CORONARY HEART DISEASE
- 428. Øystein Olsen: ANALYSIS OF MANGANESE ENHANCED MRI OF THE NORMAL AND INJURED RAT CENTRAL NERVOUS SYSTEM
- 429. Bjørn H. Grønberg: PEMETREXED IN THE TREATMENT OF ADVANCED LUNG CANCER
- 430. Vigdis Schnell Husby: REHABILITATION OF PATIENTS UNDERGOING TOTAL HIP ARTHROPLASTY WITH FOCUS ON MUSCLE STRENGTH, WALKING AND AEROBIC ENDURANCE PERFORMANCE
- 431. Torbjørn Øien: CHALLENGES IN PRIMARY PREVENTION OF ALLERGY. THE PREVENTION OF ALLERGY AMONG CHILDREN IN TRONDHEIM (PACT) STUDY.
- 432. Kari Anne Indredavik Evensen: BORN TOO SOON OR TOO SMALL: MOTOR PROBLEMS IN ADOLESCENCE
- 433. Lars Adde: PREDICTION OF CEREBRAL PALSY IN YOUNG INFANTS. COMPUTER BASED ASSESSMENT OF GENERAL MOVEMENTS
- 434. Magnus Fasting: PRE- AND POSTNATAL RISK FACTORS FOR CHILDHOOD ADIPOSITY
- 435. Vivi Talstad Monsen: MECHANISMS OF ALKYLATION DAMAGE REPAIR BY HUMAN AikB HOMOLOGUES
- 436. Toril Skandsen: MODERATE AND SEVERE TRAUMATIC BRAIN INJURY. MAGNETIC RESONANCE IMAGING FINDINGS, COGNITION AND RISK FACTORS FOR DISABILITY
- 437. Ingeborg Smidesang: ALLERGY RELATED DISORDERS AMONG 2-YEAR OLDS AND ADOLESCENTS IN MID-NORWAY – PREVALENCE, SEVERITY AND IMPACT. THE PACT STUDY 2005, THE YOUNG HUNT STUDY 1995-97
- 438. Vidar Halsteinli: MEASURING EFFICIENCY IN MENTAL HEALTH SERVICE DELIVERY: A STUDY OF OUTPATIENT UNITS IN NORWAY
- 439. Karen Lehrmann Ægidius: THE PREVALENCE OF HEADACHE AND MIGRAINE IN RELATION TO SEX HORMONE STATUS IN WOMEN. THE HUNT 2 STUDY
- 440. Madelene Ericsson: EXERCISE TRAINING IN GENETIC MODELS OF HEART FAILURE
- 441. Marianne Klock: THE ASSOCIATION BETWEEN SELF-REPORTED ECZEMA AND COMMON MENTAL DISORDERS IN THE GENERAL POPULATION. THE HORDALAND HEALTH STUDY (HUSK)
- 442. Tomas Ottemo Stølen: IMPAIRED CALCIUM HANDLING IN ANIMAL AND HUMAN CARDIOMYOCYTES REDUCE CONTRACTILITY AND INCREASE ARRHYTHMIA POTENTIAL – EFFECTS OF AEROBIC EXERCISE TRAINING
- 443. Bjarne Hansen: ENHANCING TREATMENT OUTCOME IN COGNITIVE BEHAVIOURAL THERAPY FOR OBSESSIVE COMPULSIVE DISORDER: THE IMPORTANCE OF COGNITIVE FACTORS

444. Mona Løvlien: WHEN EVERY MINUTE COUNTS. FROM SYMPTOMS TO ADMISSION FOR ACUTE MYOCARDIAL INFARCTION WITH SPECIAL EMPHASIS ON GENDER DIFFERENCES
445. Karin Margaretha Gilljam: DNA REPAIR PROTEIN COMPLEXES, FUNCTIONALITY AND SIGNIFICANCE FOR REPAIR EFFICIENCY AND CELL SURVIVAL
446. Anne Byriel Walls: NEURONAL GLIAL INTERACTIONS IN CEREBRAL ENERGY – AND AMINO ACID HOMEOSTASIS – IMPLICATIONS OF GLUTAMATE AND GABA
447. Cathrine Fallang Knetter: MECHANISMS OF TOLL-LIKE RECEPTOR 9 ACTIVATION
448. Marit Følsvik Svindseth: A STUDY OF HUMILIATION, NARCISSISM AND TREATMENT OUTCOME IN PATIENTS ADMITTED TO PSYCHIATRIC EMERGENCY UNITS
449. Karin Elvenes Bakkeland: GASTRIC NEUROENDOCRINE CELLS – ROLE IN GASTRIC NEOPLASIA IN MAN AND RODENTS
450. Kirsten Brun Kjelstrup: DORSOVENTRAL DIFFERENCES IN THE SPATIAL REPRESENTATION AREAS OF THE RAT BRAIN
451. Roar Johansen: MR EVALUATION OF BREAST CANCER PATIENTS WITH POOR PROGNOSIS
452. Rigmor Myran: POST TRAUMATIC NECK PAIN. EPIDEMIOLOGICAL, NEURORADIOLOGICAL AND CLINICAL ASPECTS
453. Krisztina Kunszt Johansen: GENEALOGICAL, CLINICAL AND BIOCHEMICAL STUDIES IN *LRRK2* – ASSOCIATED PARKINSON'S DISEASE
454. Pål Gjerden: THE USE OF ANTICHOLINERGIC ANTIPARKINSON AGENTS IN NORWAY. EPIDEMIOLOGY, TOXICOLOGY AND CLINICAL IMPLICATIONS
455. Else Marie Huuse: ASSESSMENT OF TUMOR MICROENVIRONMENT AND TREATMENT EFFECTS IN HUMAN BREAST CANCER XENOGRAFTS USING MR IMAGING AND SPECTROSCOPY
456. Khalid S. Ibrahim: INTRAOPERATIVE ULTRASOUND ASSESSMENT IN CORONARY ARTERY BYPASS SURGERY – WITH SPECIAL REFERENCE TO CORONARY ANASTOMOSES AND THE ASCENDING AORTA
457. Bjørn Øglænd: ANTHROPOMETRY, BLOOD PRESSURE AND REPRODUCTIVE DEVELOPMENT IN ADOLESCENCE OF OFFSPRING OF MOTHERS WHO HAD PREECLAMPSIA IN PREGNANCY
458. John Olav Roaldset: RISK ASSESSMENT OF VIOLENT, SUICIDAL AND SELF-INJURIOUS BEHAVIOUR IN ACUTE PSYCHIATRY – A BIO-PSYCHO-SOCIAL APPROACH
459. Håvard Dalen: ECHOCARDIOGRAPHIC INDICES OF CARDIAC FUNCTION – NORMAL VALUES AND ASSOCIATIONS WITH CARDIAC RISK FACTORS IN A POPULATION FREE FROM CARDIOVASCULAR DISEASE, HYPERTENSION AND DIABETES: THE HUNT 3 STUDY
460. Beate André: CHANGE CAN BE CHALLENGING. INTRODUCTION TO CHANGES AND IMPLEMENTATION OF COMPUTERIZED TECHNOLOGY IN HEALTH CARE
461. Latha Nruham: ASSOCIATES AND PREDICTORS OF ATTEMPTED SUICIDE AMONG DEPRESSED ADOLESCENTS – A 6-YEAR PROSPECTIVE STUDY
462. Håvard Bersås Nordgaard: TRANSIT-TIME FLOWMETRY AND WALL SHEAR STRESS ANALYSIS OF CORONARY ARTERY BYPASS GRAFTS – A CLINICAL AND EXPERIMENTAL STUDY
- Cotutelle with University of Ghent: Abigail Emily Swillens: A MULTIPHYSICS MODEL FOR IMPROVING THE ULTRASONIC ASSESSMENT OF LARGE ARTERIES

## 2011

463. Marte Helene Bjørk: DO BRAIN RHYTHMS CHANGE BEFORE THE MIGRAINE ATTACK? A LONGITUDINAL CONTROLLED EEG STUDY
464. Carl-Jørgen Arum: A STUDY OF UROTHELIAL CARCINOMA: GENE EXPRESSION PROFILING, TUMORIGENESIS AND THERAPIES IN ORTHOTOPIC ANIMAL MODELS
465. Ingunn Harstad: TUBERCULOSIS INFECTION AND DISEASE AMONG ASYLUM SEEKERS IN NORWAY. SCREENING AND FOLLOW-UP IN PUBLIC HEALTH CARE
466. Leif Åge Strand: EPIDEMIOLOGICAL STUDIES AMONG ROYAL NORWEGIAN NAVY SERVICEMEN. COHORT ESTABLISHMENT, CANCER INCIDENCE AND CAUSE-SPECIFIC MORTALITY
467. Katrine Høyer Holgersen: SURVIVORS IN THEIR THIRD DECADE AFTER THE NORTH SEA OIL RIG DISASTER OF 1980. LONG-TERM PERSPECTIVES ON MENTAL HEALTH
468. Marianne Wallenius: PREGNANCY RELATED ASPECTS OF CHRONIC INFLAMMATORY ARTHRITIDES: DISEASE ONSET POSTPARTUM, PREGNANCY OUTCOMES AND FERTILITY. DATA FROM A NORWEGIAN PATIENT REGISTRY LINKED TO THE MEDICAL BIRTH REGISTRY OF NORWAY
469. Ole Vegard Solberg: 3D ULTRASOUND AND NAVIGATION – APPLICATIONS IN LAPAROSCOPIC SURGERY
470. Inga Ekeberg Schjerve: EXERCISE-INDUCED IMPROVEMENT OF MAXIMAL OXYGEN UPTAKE AND ENDOTHELIAL FUNCTION IN OBESE AND OVERWEIGHT INDIVIDUALS ARE DEPENDENT ON EXERCISE-INTENSITY

471. Eva Veslemøy Tyldum: CARDIOVASCULAR FUNCTION IN PREECLAMPSIA – WITH REFERENCE TO ENDOTHELIAL FUNCTION, LEFT VENTRICULAR FUNCTION AND PRE-PREGNANCY PHYSICAL ACTIVITY
472. Benjamin Garzón Jiménez de Cisneros: CLINICAL APPLICATIONS OF MULTIMODAL MAGNETIC RESONANCE IMAGING
473. Halvard Knut Nilsen: ASSESSING CODEINE TREATMENT TO PATIENTS WITH CHRONIC NON-MALIGNANT PAIN: NEUROPSYCHOLOGICAL FUNCTIONING, DRIVING ABILITY AND WEANING
474. Eiliv Brenner: GLUTAMATE RELATED METABOLISM IN ANIMAL MODELS OF SCHIZOPHRENIA
475. Egil Jonsbu: CHEST PAIN AND PALPITATIONS IN A CARDIAC SETTING; PSYCHOLOGICAL FACTORS, OUTCOME AND TREATMENT
476. Mona Høysæter Fenstad: GENETIC SUSCEPTIBILITY TO PREECLAMPSIA : STUDIES ON THE NORD-TRØNDELAG HEALTH STUDY (HUNT) COHORT, AN AUSTRALIAN/NEW ZEALAND FAMILY COHORT AND DECIDUA BASALIS TISSUE
477. Svein Erik Gaustad: CARDIOVASCULAR CHANGES IN DIVING: FROM HUMAN RESPONSE TO CELL FUNCTION
478. Karin Torvik: PAIN AND QUALITY OF LIFE IN PATIENTS LIVING IN NURSING HOMES
479. Arne Solberg: OUTCOME ASSESSMENTS IN NON-METASTATIC PROSTATE CANCER
480. Henrik Sahlin Pettersen: CYTOTOXICITY AND REPAIR OF URACIL AND 5-FLUOROURACIL IN DNA
481. Pui-Lam Wong: PHYSICAL AND PHYSIOLOGICAL CAPACITY OF SOCCER PLAYERS: EFFECTS OF STRENGTH AND CONDITIONING
482. Ole Solheim: ULTRASOUND GUIDED SURGERY IN PATIENTS WITH INTRACRANIAL TUMOURS
483. Sten Roar Snare: QUANTITATIVE CARDIAC ANALYSIS ALGORITHMS FOR POCKET-SIZED ULTRASOUND DEVICES
484. Marit Skyrud Bratlie: LARGE-SCALE ANALYSIS OF ORTHOLOGS AND PARALOGS IN VIRUSES AND PROKARYOTES
485. Anne Elisabeth F. Isern: BREAST RECONSTRUCTION AFTER MASTECTOMY – RISK OF RECURRENCE AFTER DELAYED LARGE FLAP RECONSTRUCTION – AESTHETIC OUTCOME, PATIENT SATISFACTION, QUALITY OF LIFE AND SURGICAL RESULTS; HISTOPATHOLOGICAL FINDINGS AND FOLLOW-UP AFTER PROPHYLACTIC MASTECTOMY IN HEREDITARY BREAST CANCER
486. Guro L. Andersen: CEREBRAL PALSY IN NORWAY – SUBTYPES, SEVERITY AND RISK FACTORS
487. Frode Kolstad: CERVICAL DISC DISEASE – BIOMECHANICAL ASPECTS
488. Bente Nordtug: CARING BURDEN OF COHABITANTS LIVING WITH PARTNERS SUFFERING FROM CHRONIC OBSTRUCTIVE PULMONARY DISEASE OR DEMENTIA
489. Mariann Gjervik Heldahl: EVALUATION OF NEOADJUVANT CHEMOTHERAPY IN LOCALLY ADVANCED BREAST CANCER BASED ON MR METHODOLOGY
490. Lise Tevik Løvseth: THE SUBJECTIVE BURDEN OF CONFIDENTIALITY
491. Marie Hjelmsæth Aune: INFLAMMATORY RESPONSES AGAINST GRAM NEGATIVE BACTERIA INDUCED BY TLR4 AND NLRP12
492. Tina Strømdal Wik: EXPERIMENTAL EVALUATION OF NEW CONCEPTS IN HIP ARTHROPLASTY
493. Solveig Sigurdardóttir: CLINICAL ASPECTS OF CEREBRAL PALSY IN ICELAND. A POPULATION-BASED STUDY OF PRESCHOOL CHILDREN
494. Arne Reimers: CLINICAL PHARMACOKINETICS OF LAMOTRIGINE
495. Monica Wegling: KULTURMENNESKETS BYRDE OG SYKDOMMENS VELSIGNALSE. KAN MEDISINSK UTREDNING OG INTERVENSJON HA EN SELVSTENDIG FUNKSJON UAVHENGIG AV DET KURATIVE?
496. Silje Alvestad: ASTROCYTE-NEURON INTERACTIONS IN EXPERIMENTAL MESIAL TEMPORAL LOBE EPILEPSY – A STUDY OF UNDERLYING MECHANISMS AND POSSIBLE BIOMARKERS OF EPILEPTOGENESIS
497. Javaid Nauman: RESTING HEART RATE: A MATTER OF LIFE OR DEATH – PROSPECTIVE STUDIES OF RESTING HEART RATE AND CARDIOVASCULAR RISK (THE HUNT STUDY, NORWAY)
498. Thuy Nguyen: THE ROLE OF C-SRC TYROSINE KINASE IN ANTIVIRAL IMMUNE RESPONSES
499. Trine Naalsund Andreassen: PHARMACOKINETIC, PHARMACODYNAMIC AND PHARMACOGENETIC ASPECTS OF OXYCODONE TREATMENT IN CANCER PAIN
500. Eivor Alette Laugsand: SYMPTOMS IN PATIENTS RECEIVING OPIOIDS FOR CANCER PAIN – CLINICAL AND PHARMACOGENETIC ASPECTS

501. Dorthe Stensvold: PHYSICAL ACTIVITY, CARDIOVASCULAR HEALTH AND LONGEVITY IN PATIENTS WITH METABOLIC SYNDROME
502. Stian Thoresen Aspenes: PEAK OXYGEN UPTAKE AMONG HEALTHY ADULTS– CROSS-SECTIONAL DESCRIPTIONS AND PROSPECTIVE ANALYSES OF PEAK OXYGEN UPTAKE, PHYSICAL ACTIVITY AND CARDIOVASCULAR RISK FACTORS IN HEALTHY ADULTS (20-90 YEARS)
503. Reidar Alexander Vigen: PATHOBIOLOGY OF GASTRIC CARCINOIDS AND ADENOCARCINOMAS IN RODENT MODELS AND PATIENTS. STUDIES OF GASTROCYSTOPLASTY, GENDER-RELATED FACTORS, AND AUTOPHAGY
504. Halvard Høilund-Kaupang: MODELS AND METHODS FOR INVESTIGATION OF REVERBERATIONS IN NONLINEAR ULTRASOUND IMAGING